PERFORMANCE OF A NEW PASSIVE DAMPER FOR SEISMIC PROTECTION OF STRUCTURES

KHALED GHAEDI

FACULTY OF ENGINEERING
UNIVERSITY OF MALAYA
KUALA LUMPUR

2020

PERFORMANCE OF A NEW PASSIVE DAMPER FOR SEISMIC PROTECTION OF STRUCTURES

KHALED GHAEDI

THESIS SUBMITTED IN FULFILMENT OF THE REQUIREMENTS FOR THE DEGREE OF DOCTOR OF PHILOSOPHY

FACULTY OF ENGINEERING
UNIVERSITY OF MALAYA
KUALA LUMPUR

2020

UNIVERSITY OF MALAYA

ORIGINAL LITERARY WORK DECLARATION

Name of Candidate: Khaled Ghaedi

Matric No: KHA150015

Name of Degree: Doctor of Philosophy (Ph.D.)

Title of Thesis: PERFORMANCE OF A NEW PASSIVE DAMPER FOR SEISMIC PROTECTION OF STRUCTURES

Field of Study: Structural Engineering and Materials

I do solemnly and sincerely declare that:

(1) I am the sole author/writer of this Work;
(2) This Work is original;
(3) Any use of any work in which copyright exists was done by way of fair dealing and for permitted purposes and any excerpt or extract from, or reference to or reproduction of any copyright work has been disclosed expressly and sufficiently and the title of the Work and its authorship have been acknowledged in this Work;
(4) I do not have any actual knowledge nor do I ought reasonably to know that the making of this work constitutes an infringement of any copyright work;
(5) I hereby assign all and every rights in the copyright to this Work to the University of Malaya ("UM"), who henceforth shall be owner of the copyright in this Work and that any reproduction or use in any form or by any means whatsoever is prohibited without the written consent of UM having been first had and obtained;
(6) I am fully aware that if in the course of making this Work I have infringed any copyright whether intentionally or otherwise, I may be subject to legal action or any other action as may be determined by UM.

Candidate's Signature Date:

Subscribed and solemnly declared before,

Witness's Signature Date:

Name:

Designation:

UNIVERSITI MALAYA

PERAKUAN KEASLIAN PENULISAN

Nama: Khaled Ghaedi

No. Matrik: KHA150015

Nama Ijazah: Doktor Falsafah (Ph.D.)

Tajuk Tesis: PRESTASI DAMPER PASANG BARU UNTUK PERLINDUNGAN SEISMIK STRUKTUR

Bidang Penyelidikan: Kejuruteraan Struktur

Saya dengan sesungguhnya dan sebenarnya mengaku bahawa:

(1) Saya adalah satu-satunya pengarang/penulis Hasil Kerja ini;
(2) Hasil Kerja ini adalah asli;
(3) Apa-apa penggunaan mana-mana hasil kerja yang mengandungi hakcipta telah dilakukan secara urusan yang wajar dan bagi maksud yang dibenarkan dan apa-apa petikan, ekstrak, rujukan atau pengeluaran semula daripada atau kepada mana-mana hasil kerja yang mengandungi hakcipta telah dinyatakan dengan sejelasnya dan secukupnya dan satu pengiktirafan tajuk hasil kerja tersebut dan pengarang/penulisnya telah dilakukan di dalam Hasil Kerja ini;
(4) Saya tidak mempunyai apa-apa pengetahuan sebenar atau patut semunasabahnya tahu bahawa penghasilan Hasil Kerja ini melanggar suatu hakcipta hasil kerja yang lain;
(5) Saya dengan ini menyerahkan kesemua dan tiap-tiap hak yang terkandung di dalam hakcipta Hasil Kerja ini kepada Universiti Malaya ("UM") yang seterusnya mula dari sekarang adalah tuan punya kepada hakcipta di dalam Hasil Kerja ini dan apa-apa pengeluaran semula atau penggunaan dalam apa jua bentuk atau dengan apa juga cara sekalipun adalah dilarang tanpa terlebih dahulu mendapat kebenaran bertulis dari UM;
(6) Saya sedar sepenuhnya sekiranya dalam masa penghasilan Hasil Kerja ini saya telah melanggar suatu hakcipta hasil kerja yang lain sama ada dengan niat atau sebaliknya, saya boleh dikenakan tindakan undang-undang atau apa-apa tindakan lain sebagaimana yang diputuskan oleh UM.

Tandatangan Calon Tarikh:

Diperbuat dan sesungguhnya diakui di hadapan,

Tandatangan Saksi Tarikh:

Nama:

Jawatan:

PERFORMANCE OF A NEW PASSIVE DAMPER FOR SEISMIC PROTECTION OF STRUCTURES

ABSTRACT

Passive energy dissipation devices have been successfully implemented in buildings around the world to reduce structural responses primarily to earthquakes, wind and other dynamic loads. Unlike active and semi-active control systems, passive systems make use of control devices that serve secondary functions. They are connected to structural members to increase structural damping without the use of external forces. The aim of this research is to introduce and investigate the performance of a new passive damper device called bar damper (BD), which is made of a number of solid bars sandwiched between two plates. The concept, placement and material properties of the device are initially presented and described. Subsequently, the test setup and loading procedures are presented and the performance of the proposed damper is assessed. For this purpose, two experimental test stages were implemented with cyclic loading applied. In the first stage, the BD was tested on its own keeping in view a number of design parameters, including the height, diameter and number of solid bars used in the design of the damper device. In the second stage, the bar damper was installed in a structural frame and experimentally tested under cyclic loading to monitor the performance of the device and frame structure equipped with the BD device. The results obtained in the first stage confirmed that the BD specimens exhibited stable hysteretic behavior with a smooth change from elastic to inelastic regime. The experiments also showed that the BD specimens were very efficient in energy dissipation and demonstrated appropriate tolerance in cumulative displacement as well as very ductile performance without significant strength or stiffness degradation. In addition to the experimental study, a finite element (FE) analysis was also done. The analysis results were compared with the experimental results and these were in good agreement. In accordance with the experimental and FE analysis outcomes, a simplified

bilinear model of the BD was proposed to enhance practical use of the device. Moreover, theoretical equations of the damper device were derived based on its plastic mechanism. It is noted that the strength and ductility of the device estimated from the theoretical equations corresponded well with the results obtained from the experiments done in the first stage. It is also interesting to mention that it was possible to achieve suitable performance of the device in terms of increasing energy dissipation level, strength, stiffness and ductility either with the proposed formulas or according to the FE analysis. The results from the experiments on the test frames conducted in the second stage also proved the positive effect of the BD devices on the overall performance of the test frame where strength, stiffness, deformation capacity and energy dissipation level of the frame increased. Moreover, a FE model of the tested frames was developed for further investigation. Overall, it is believed that since the proposed damper achieved excellent performance, it can be adopted for practical use by structural designers to protect new and existing buildings and bridges.

Keywords: Bar damper; Passive system; Structural vibration control; Direction-independent damper; Seismic protection.

PRESTASI PEREDAM BARU UNTUK PERLINDUNGAN SEISMIK BAGI STRUKTUR

ABSTRAK

Peranti pelesapan tenaga pasif telah berjaya dilaksanakan di bangunan di seluruh dunia untuk mengurangkan sambutan struktur terutamanya disebabkan oleh gempa bumi, beban angin dan beban dinamik yang lain. Tidak seperti sistem kawalan aktif dan separuh aktif, sistem pasif menggunakan peranti kawalan yang berfungsi sebagai fungsi sekunder. Ianya disambungkan atau diletakkan pada anggota struktur untuk meningkatkan redaman struktur tanpa menggunakan daya luaran. Tujuan penyelidikan ini adalah untuk memperkenalkan dan menyiasat prestasi peranti peredam pasif baru yang dikenali sebagai peredam bar (BD), yang diperbuat daripada beberapa bar pepejal yang diapit di antara dua plat. Pada mulanya, konsep, perletakan dan sifat bahan bagi peranti ini dibentangkan dan diterangkan. Selepas itu, persediaan ujian dan prosedur pembebanan dibentangkan dan prestasi peredam yang dicadangkan telah dinilai. Untuk tujuan ini, dua tahap ujian eksperimen bebanan telah dilaksanakan dengan menggunakan pembebanan berkitar. Pada peringkat pertama, BD diuji dengan pemantauannya sendiri berdasarkan beberapa parameter reka bentuk, termasuk ketinggian, garis pusat dan bilangan bar padu yang digunakan dalam reka bentuk alat peredam tersebut. Pada peringkat kedua, peredam bar dipasang pada struktur kerangka dan diuji secara eksperimen di bawah pembebanan berkitar untuk memantau prestasi peranti dan struktur kerangka yang dilengkapi dengan peranti BD. Keputusan yang diperoleh pada peringkat pertama mengesahkan bahawa spesimen BD menunjukkan tingkah laku histeris yang stabil dengan perubahan yang lancar dari elastik kepada rejim tidak elastik. Eksperimen ini juga menunjukkan bahawa spesimen BD sangat efisien dalam pelesapan tenaga dan menunjukkan toleransi yang sesuai dalam anjakan kumulatif serta menunjukkan prestasi yang sangat mulur tanpa kemerosotan kekuatan atau kekakuan yang ketara. Sebagai tambahan kepada kajian

eksperimen, analisis unsur terhingga (FE) juga telah dijalankan. Keputusan analisis ini telah dibandingkan dengan keputusan eksperimen dan ianya telah menunjukkan persamaan yang baik. Selaras dengan hasil analisis dari eksperimen dan FE, satu model bilinear yang dipermudahkan untuk BD telah dicadangkan untuk meningkatkan penggunaan praktikal peranti ini. Tambahan pula, persamaan teori bagi peranti peredam ini diperolehi berdasarkan mekanisme plastiknya. Ianya telah menunjukkan bahawa kekuatan dan kemuluran peranti yang dianggarkan dari persamaan teoretikal adalah sepadan dengan hasil yang diperoleh daripada keputusan eksperimen yang dilakukan pada peringkat pertama. Ianya juga menarik untuk dinyatakan bahawa adalah mungkin untuk mencapai prestasi peranti yang sesuai dari segi peningkatan tahap kelesapan tenaga, kekuatan, kekakuan dan kemuluran sama ada dengan formula yang dicadangkan atau menggunakan analisis FE. Hasil daripada eksperimen pada struktur kerangka ujian yang dijalankan pada peringkat kedua juga membuktikan kesan positif peranti BD pada prestasi keseluruhan struktur kerangka ujian apabila kekuatan, kekakuan, kapasiti ubah bentuk dan tahap pelesapan tenaga struktur kerangka itu meningkat. Lebih-lebih lagi, model FE bagi struktur kerangka yang diuji telah dibangunkan untuk penyelidikan lanjut. Secara keseluruhan, memandangkan peredam yang dicadangkan mencapai prestasi yang sangat baik, ia boleh digunakan untuk kegunaan praktikal oleh pereka-bentuk struktur untuk melindungi bangunan dan jambatan yang baru dan sedia ada.

Kata kunci: Peredam damper; Sistem pasif; Kawalan getaran struktur; Peredam bebas pergerakan; Perlindungan seismik.

ACKNOWLEDGEMENTS

I am thankful to Allah Almighty for blessing me with an opportunity to be worthy of such an honorable degree.

I wish to give my special thank to my supervisor, Associate Professor Dr. Zainah Ibrahim for her unconditional support and believing in me throughout my research. Her deep insight into the research area has greatly kept me on the right track of my research work. Through her profound and conscientious discussions offered to me, I have mastered a great deal of knowledge and greatly widened my vision on research. Her logic thinking, research enthusiasm, and deep insight has inspired me and will be of great benefits to my life-long study.

I would further like to thank my cordial friend Dr. Ahad Javanmardi for his kind and various contributions and supports throughout my entire research.

I would like to give my special thanks to my dear wife for her love, encouragement and support during my work towards my PhD degree, which I owe to her every success I have in my life. Special thanks to my beloved parents, brothers and my only sister for all what they did for me throughout my life. It wouldn't have been possible without their help.

I also would like to thank all other friends, especially my dear friends Dr. Usman Hanif and Mr. Meisam Gordan for being helpful and for their energetic help in my thesis writing.

TABLE OF CONTENTS

LIST OF FIGURES

LIST OF TABLES

LIST OF SYMBOLS AND ABBREVIATIONS

A_0	:	Initial area
a	:	Stiffness coefficient
b	:	Width of the bar damper
BD :	:	Bar damper
C	:	Charging time; damping constant
C_k	:	Model parameter
d	:	Diameter of solid bars
d_e	:	Elastic displacement
d_{Max}	:	Maximum displacement in hysteretic curve
d_{Min}	:	Minimum displacement in hysteretic curve
d_y	:	Yield displacement
d_p	:	Yield displacement
E	:	Modulus of elasticity (Young's modulus)
E_D	:	Dissipated energy in each completed cycle
E_{Dt}	:	Total dissipated energy
E_k	:	Tangent stiffness
E_s	:	Stored elastic energy
F	:	Force
FE	:	Finite element
FEM	:	Finite element model
FEA	:	Finite element analysis
F_e	:	Elastic strength

F_D : Damper force

F_P : Plastic strength

F_y : Yield stress

F_{ty} : Yield tensile stress

F_{sy} : Yield shear stress

F_{tu} : Ultimate tensile stress

F_{su} : Ultimate shear stress

f : Amplification factor, frequency

g : Gravitational acceleration

h : Height of solid bars

I_x : Moment of inertia of the solid bar around x axis

K_e : Elastic stiffness

K_P : Plastic stiffness

K_{eff} : Effective stiffness

l : Length

L_d : Length of the bar damper

l_0 : Initial length

M : Maximum bending moment

m : Maximum moment acting at the ends

m_x : Virtual bending moment at the location x

M_p : Plastic bending moment

$M_{(p,x)}$: Plastic moment at location x

$M_{(x)}$: Moment at location x

μ : Ductility

μ_{cum}	:	Cumulative ductility
n	:	Row number of solid bars
N	:	Number of solid bars
N_C	:	Number of cycles
P_{Max}	:	Maximum strength in hysteretic curve
P_{Min}	:	Minimum strength in hysteretic curve
p	:	Horizontal lateral load
P_e	:	Elastic strength
P_y	:	Yield strength
$P_{y\ exp}$	:	Yield strength obtained from experimental test
$P_{y\ FE}$	:	Yield strength obtained from finite element analysis
R_y	:	Reduction factor
S_h	:	Distance between solid bars in horizontal direction
S_v	:	Distance between solid bars in vertical direction
T	:	Time
u	:	Displacement
u_D	:	Relative displacement
$\dot{u}_D$	:	Relative velocity
v	:	Velocity
W	:	Weight
x	:	Distance from neural axis to moment at location x
Z	:	Plastic modulus
Z_x	:	Plastic modulus at location x
δ	:	Displacement
δ_{cum}	:	Cumulative displacement

δ_{max} : Maximum displacement

δ_{min} : Minimum displacement

δ_y : Yield displacement

ξ : Equivalent viscous damping ratio

K' : Cyclic strength hardening factor

$\widetilde{K}$: Cyclic hardening factor of regularization

η : Proportional coefficient

η' : Cyclic strain hardening index

$\Delta\varepsilon_e$: Elastic strain amplitude

$\Delta\varepsilon_p$: Plastic strain amplitude

$\Delta\sigma$: Stable stress

σ : Stress

σ_{nom} : Nominal stress

σ_I : Principal stress at x directions

σ_{II} : Principal stress at y directions

σ_{III} : Principal stress at z directions

σ_y : Yield stress

σ_0 : First point stress

σ_p : End point stress (plastic strain at end point)

$\widetilde{\sigma}$: Stress of regularization

ε : Strain

ε_e : Elastic strain

ε_{nom} : Nominal strain

ε_y	:	Yield strain
ε_0	:	First point strain
ε_p	:	End point strain (plastic strain at end point)
ε_t	:	True strain
$\widetilde{\varepsilon}$	:	Strain of regularization
$\bar{\varepsilon}^{pl}$	:	Equivalent plastic strain
γ_k	:	Model parameter
θp		angle of rotation

CHAPTER 1: INTRODUCTION

1.1 Introduction

Civil structures must be designed appropriately under gravity and lateral loading. This comprises the design of structural elements that can carry applied loads by taking proper safety factors into consideration as well as serviceability conditions. Lateral loads are principally generated by two main sources: wind and ground motions (Elwardany et al., 2019; Ghaedi et al., 2016; Ghaedi et al., 2018; Gordan et al., 2017; Khanzaei et al., 2015; Mashal & Palermo, 2019; Xiang et al., 2019). Structures subjected to such loads not only require systems apt to impede collapse (Carpio. et al., 2019; Elwardany et al., 2018; Pantidis & Gerasimidis, 2018; Seleemah & El-Sharkawy, 2011), but engineers also need to understand more the nature of these loads from a dynamic solution perspective. In other words, dynamic structural responses including damping, vibration and resonant frequency must be understood well.

During wind impacts, structures must tolerate wind pressure by remaining in elastic condition, however, during earthquakes different scenarios may occur. In a ground excitation instance, the inertia, or reaction of a building generates forces of extremely high scale when the base vibrates against neighboring soil. Practically keeping structures in elastic condition is not an easy task and even impossible in many cases, especially during major ground motions. To prevail in such circumstances, increasing the strength of the structure can raise inertia forces on account of varying dynamic properties. In the past, engineers have engaged in changing structural sections and materials, using structural mechanisms like moment-resisting frames and shear walls or modifying structural shapes. Nowadays, a defense system is applied to the basic structural system to increase the ability of a building in the face of earthquake forces. During seismic excitations, a huge portion of seismic input energy that might be conveyed to the structure is dispersed through energy dissipation devices installed. Alongside utilizing such

devices, a problem exists pertaining to the question of how buildings can be designed to act agreeably in these situations. Similarly, supplementary questions to pose are, in what condition does a structure have to be after a seismic event? Does building collapse prevention save lives?

Although several supplementary damping control systems have been presented over the past decades, these structural systems are emerging progressively more in light of new advances in technology. Frequently used energy dissipation systems, including active and semi-active energy dissipation, as well as passive and hybrid vibration control systems have been investigated. Active and semi-active systems can vary based on the external loads applied and need a bulky power supply that may not always be accessible, specifically during an earthquake. However, passive control systems do not require any external power supply alteration in accordance with external load settings, while hybrid control systems can be combinations of active, semi-active and passive systems.

1.2 Problem Statement

Utilizing passive control systems to reduce the dynamic response of structures is gradually becoming dominant, as they do not require external energy sources and are activated upon seismic or dynamic load contact with the structure. Further developments of passive systems from different aspects, such as design, theory, hardware, installation and specification have authorized important applications for industrial plants, bridges and buildings. Such applications are currently evident in any earthquake-prone zone. Although passive devices have been utilized in retrofitting existing buildings and designing new structures of high importance, such as critical bridges, defense installations, hospitals and emergency response services, it is observed that many of the proposed passive devices function as unidirectional systems (Almeida et al., 2017; Fateh et al., 2016; Lee et al., 2016; Lu, 2004; Meng et al., 2019; Ozbulut & Hurlebaus, 2011;

Park & Oh, 2020; Saaed et al., 2015; Titirla et al., 2018; Weber, 2014). . It simply means that besides passive systems other energy dissipation systems must also be placed in both directions to strengthen a structure against dynamic loads.

From an architectural point of view, major structural control systems proposed are designed for installation in specific locations of structures, as many are patterned in X, Z or V form, as shown in different studies (Choi & Kim, 2010; Javanmardi et al., 2019; Ling & Ling, 2012; Maleki & Mahjoubi, 2013; Mualla et al., 2010). It is obvious that using damper devices in such forms occupies space, a matter that should be considered carefully when modelling structures. In addition, a passive damper has to be made of materials that are available, affordable, dissipative and easy to build. The literature indicates that numerous passive devices introduced are made of materials that are either expensive, difficult to obtain or not easy to build.

1.3 Objective of the Research

The main goal of the present work is to introduce and examine a new metallic passive damper for conveying operative control to structures under minor and major dynamic loads ranging from mechanical vibration to wind and earthquakes. The study investigates the performance of the proposed damper subjected to lateral loading. The more specific objectives derived are as follows:

1. To propose a simple and low-cost passive metallic damper with effective energy dissipation capability in a planar direction
2. To investigate and evaluate the performance of the damper through a series of experimental quasi-static cyclic tests
3. To derive constitutive formulas of the device based on its plastic mechanism and compare them with experimental and finite element analysis results

4. To assess the effectiveness of the proposed damper in performance improvement of frame structures under cyclic loading through experimental tests and finite element analysis

1.4 Research Methodology

To attain and verify the research objectives, a new bar damper device (BD) is introduced and related information including its description and placement is presented. To understand the BD's performance, a number of damper device specimens are tested experimentally by subjecting to low-cycle fatigue loading using a 1000kN Universal Test Machine. To satisfy the experimental tests, a benchmark model is numerically investigated by means of the finite element (FE) software ABAQUS and the FE model results are compared with the experiments. Furthermore, mechanical equations of the damper device are also derived and compared to the results obtained experimentally. Later on, the proposed device is installed in a full-scale frame structure at the beam-column site to investigate the effectiveness of the device in improving the frame's response to the applied cyclic loading. Furthermore, FE models of the tested frames equipped with and without BD device are developed and analysed. The results of the FE models are compared with the experimental results. Figure 1.1 demonstrates the BD device tests and FE analysis procedure.

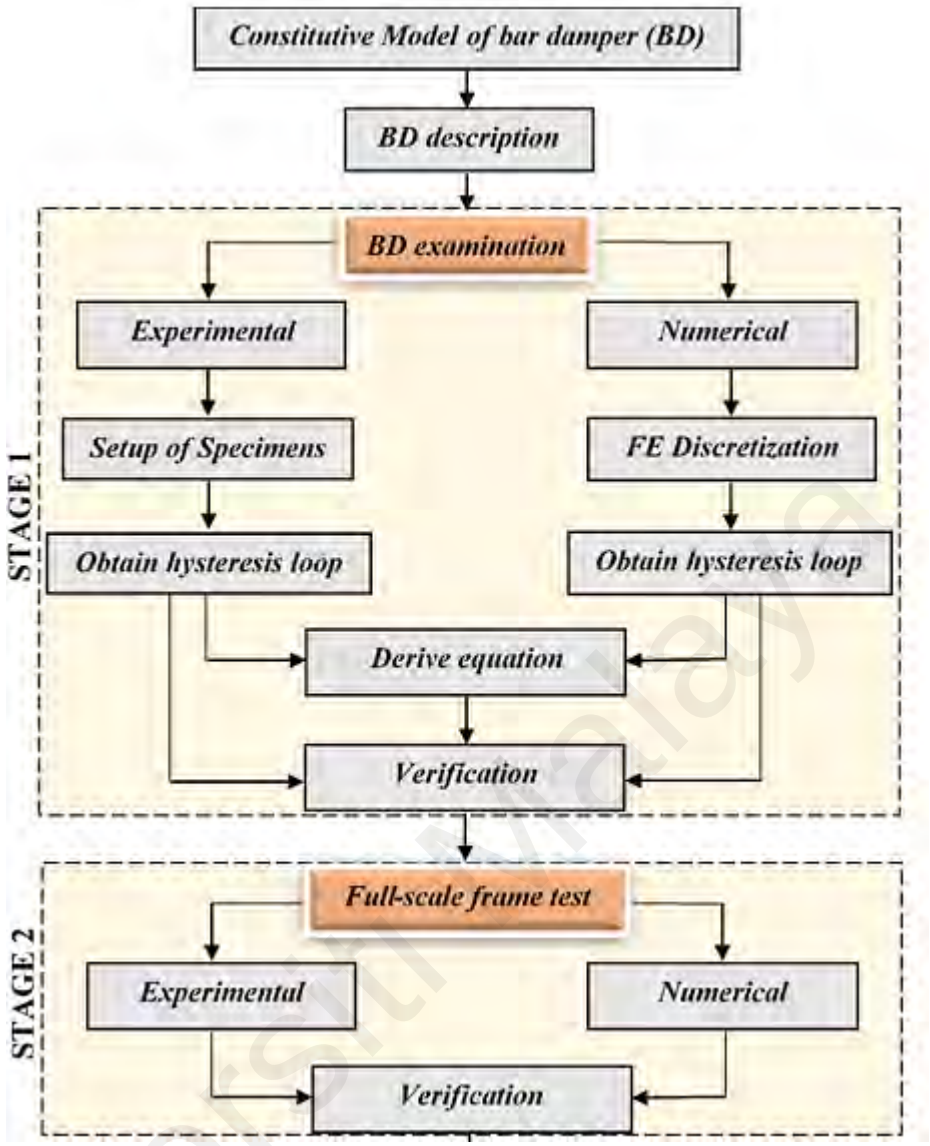

Figure 1.1: Flow chart of the methodology

1.5 Scope and Limitations of the Research

The scope of the present research is divided into two stages. First, the research goes to introduce, develop and test a new passive dissipation system known as a bar damper (BD) device. Several design parameters were established and examined through laboratory tests using full cyclic displacement loading. These were carried out to verify the proposed damper's performance as well as to derive related formulas for the device, i.e. yield force and yield displacement of the damper. Moreover, ABAQUS software was used to

simulate the BD device behavior under cyclic loading and to compare the FE results with the laboratory tests.

In the second stage, the experimental study was limited to two semi-rigid frames, one bare frame and the other was equipped with BD device. Therefore, the effectiveness of the device on response improvement of frame structures was experimentally tested by installing the proposed damper device in a semi-rigid frame structure. The test frames were examined when they were subjected to a series of cyclic displacement loads. The response of the frame equipped with BD devices was compared to the frame without BD device. The behavior of the test frames with and without BD devices was also simulated by means of ABAQUS software for further investigations. The results of these analyses were compared with the experiments. Lastly, by presenting the efficiency of the damper device, appropriate conclusions and recommendations were offered for further future studies.

1.6 Significance of the Research

A number of inventive vibration control devices including active, passive and semi-active systems have been suggested and effectively utilized in the seismic protection of structures. Each of these strategies and systems has positive and negative points. For instance, designing an active or semi-active damper necessitates compliance with numerous restrictions, resulting in limited power source and space, time delays, inadequate measurements of structural responses, incompatibility of the control algorithms with the systems, low strength, etc. On the other hand, interest in the development of passive devices owing to the many advantages compared to active and semi-active control systems has widely increased in recent decades. New developments include using multiple mechanisms like friction, yielding, phase transformation, fluid orificing and viscoelastic material deformation, but there are still some restrictions for

these types of dampers, mainly in practical engineering applications. For example, a shape memory alloy damper or material is very costly to use. Retuning the frequency of a tuned mass damper (TMD) in real time is the main limitation of this device. Furthermore, the high level of damping required and inability to control higher modes productively are other limitations of TMDs, tuned liquid column dampers (TLCDs) and even tuned liquid dampers (TLD). Temperature, small displacement and frequency dependencies are limitations of viscoelastic dampers. The gradual wear of the friction surfaces in friction dampers and permanent displacement are the main disadvantages of this type of dampers. Viscous fluid dampers may confront fluid leakage.

The solution proposed in this work is a type of passive control device called a Bar Damper (BD). The BD is a combination of three typical mild steel materials arranged in such a way to create a unique and innovative device that enhances the strengths and offsets the weaknesses of the individual devices. Specifically, the BD consists of three parts: top and bottom plates and bars arranged in between. The BD, in spite of its simplicity, can be designed in several manners by changing the size, pattern, height, material, etc. It can even be fabricated by incorporating waste materials and no use of advanced technology for assembly. The damper can not only be made of steel material, but also from different dissipative materials such as aluminum, copper and lead. The benefit of utilizing BD is the ability to dissipate energy at all deformation levels. Depending on the situation, it can be designed to dissipate energy from a minor level of lateral loadings like wind forces or minor earthquakes to a high level of loading such as strong ground motions. Increasing the strength and stiffness of the device by changing different parameters enables the BD to dissipate significant amounts of seismic energy. Damper elements permanently damaged in major earthquakes can be replaced without affecting the core structure. The proposed BD device can also be installed at several locations on a structure such as a beam-column connection or in the form of X, Z, V, K,

or it may be used as a base isolation system, etc. Therefore, the proposed BD device opens doors for architects to use all spaces of design. Moreover, the location of the proposed passive damper can be easily changed by varying its main parameters, as seen by the examples in Figure 1.2.

Finally, the proposed BD device is also significant for its applicability to dissipate energy in a planar direction owing to its unique geometry. It is very important to mention this, since most metallic dampers function unidirectional (act in one direction only).

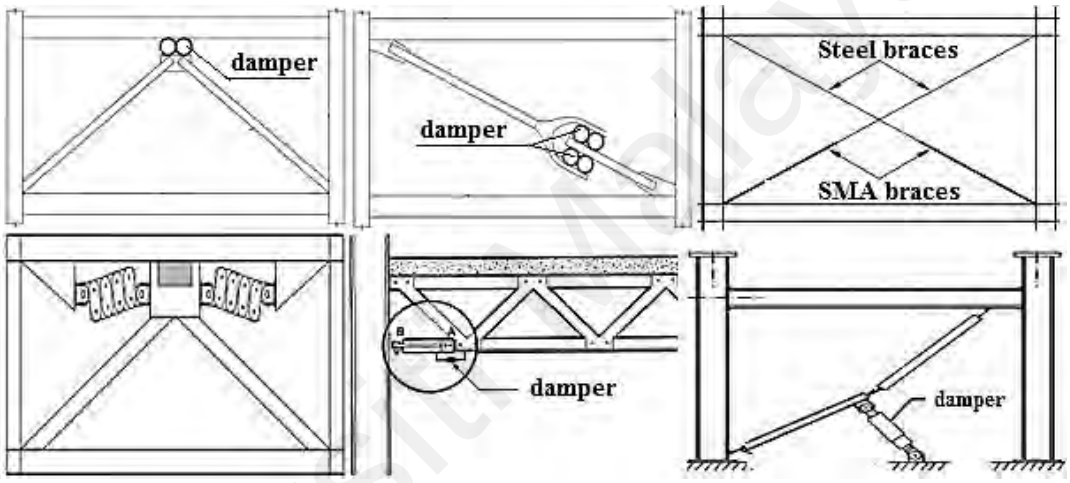

Figure 1.2: Placement of structural control systems in different locations

1.7 Thesis Outline

Chapter 1 presents an introduction to structural vibration control systems. A brief discussion regarding the positive and negative points of different control systems as well as the problem statement on the topic is provided. Subsequently, the objectives, methodology and significance of this study are presented.

Chapter 2 comprises a literature review to deliver a comprehensive background pertaining to the use of different structural control systems. The focus is on the application of such devices in building and bridge structures. It is seen that many articles were

published between the 1990s and 2013 in relation to vibration control systems of structures subjected to ground excitations. Therefore to avoid repetition, an attempt is made in this chapter to review studies more recently carried out, primarily since 2013, on active, passive, semi-active and hybrid vibration control systems for structures under dynamic motions.

Chapter 3 introduces the proposed damper device with a description, its design and potential placements at different locations of a structure. Later in the chapter, the performance of the proposed design parameters is evaluated for the device under experimental cyclic load tests.

Chapter 4 provides details of device. FE modelling and analysis are carried out to verify the damper's performance. Theoretical equations for the damper device are also presented. Finally, the FE study and device equations are validated following a comparison with the experimental results. A bilinear model of the device is presented as well.

Chapter 5 investigates the effects of the device on frame structure performance improvement. To this end, a frame equipped with the proposed device is experimentally tested under cyclic loading and the results are compared with the results of a bare frame. Moreover, related FE models and analyses are implemented and the results are compared with the experimentally tested frame results.

Chapter 6 presents the conclusions of this study and offers appropriate recommendations for further future studies.

CHAPTER 2: LITERATURE REVIEW

2.1 Introduction

Among the numerous natural tragedies, earthquakes can inflict vast damage to a large number of buildings and constructions at the blink of an eye. Privation of awareness on ground motions and their comeback are conspicuous and results in disaster; leading to unpleasant memoirs. Furthermore, it is regrettably agreed that there is no general favourable method to certainly forecast ground motions, yet. Indeed, it may not be promising to define the exact time when a mortal earthquake will happen (Ghaedi & Ibrahim, 2017). Therefore, it is a big concern to civil and structural engineers to design and protect structures against such devastating ground excitations using earthquake-resistant systems.

Principle of conventional earthquake-resistant design has been applied for the last 75 years to ensure an acceptable safety level while avoiding catastrophic failures and life loss (Basu & Reddy, 2016). Numerous researches have been conducted over the last half century for developing innovative earthquake-resistant systems in order to improve seismic performance of structures while keeping the construction costs reasonable. To this end, many works have recently been investigated and published in relation to vibration control systems of structures subjected to ground excitations. This chapter attempts to present the most recent types of proposed seismic energy dissipation systems implemented in building and bridge structures to show the positive progress of the applications of such systems in structural and earthquake engineering area. These systems are active, passive, semi-active and hybrid systems. It should be noted that, since the present study focuses on proposing a passive control system, thereafter, the recent passive systems are extensively reviewed in this chapter.

2.2 Structural Control Systems

Structural control systems are commonly used to decrease unwanted responses of structures due to various sorts of dynamically loadings such as traffic, winds, earthquakes and other service loads. For instance, modern buildings are often susceptible to excessive wind-induced dynamic motion due to their flexibility, lightweight construction, and low inherent damping. As a result, occupants can experience significant tribulation. To reduce its resonant structural response, a building can be equipped with a supplementary damping system, which is installed at appropriate location of the structure to increase the rate of energy dissipation. Vibration control systems are not only used to enhance the structural functionality and safety of buildings against natural and man-made hazards (Ali & Abdel-Ghaffar, 1995; Apostolakis & Dargush, 2009; Aumjaud et. al., 2015; O. Curadelli & Amani, 2014; Dall'Asta & Ragni, 2008; Fu & Cherry, 2000; Hatzigeorgiou & Pnevmatikos, 2014; Karimi, 2012; Li & Wong, 2014; Serror et. al., 2014; Spak et. al., 2015), but they are also used to control any unwanted responses in other fields such as mechanical vibrations. These systems can be categorized into four key groups according to their operative performances. Table 2.1 shows the control systems considering the past and most recent used methods which is investigated in this study.

Table 2.1: Main categories and subcategories of structural control systems

Control mechanisms	Control methods
Active	Active mass driver damper (AMD) Active bracing system (ABS) Active tendon control (ATC) Distributed mass damper (DMD) Active tuned mass damper (ATMD) Active variable stiffness (AVS) Pulse generation system

Table 2.1: Main categories and subcategories of structural control systems (**continued**)

Passive	Fluid viscous damper (FVD) Viscoelastic damper (VED) viscous wall damper (VWD) Friction dampers (FD) Metallic damper (MD) Buckling Restrained Brace (BRB) Self-centring sandwiched BRB (SC-SBRB) Dual-core self-centring brace (DC-SCB) FUSEIS Resetting passive stiffness damper (RPSD) Tuned liquid damper (TLD) Tuned mass dampers (TMD) Tuned mass damper-inerter (TMDI) Tuned-inerter damper (TID) Tuned mass generator (TMG) Particle dampers (PD) Tuned liquid particle damper (TLPD) Particle tuned mass damper (PTMD) Tuned liquid damper with floating roof (TLD-FR) Eddy-Current tuned mass damper (EC-TMD) Nonlinear energy sink damper (NESD) Negative stiffness damper (NSD) Base Isolators ▪ High damping rubber bearing (HDRB) ▪ Lead rubber bearings (LRB) ▪ Elastomeric bearings (EB) ▪ Sliding bearing systems (EBS) ▪ Scissor-like structure (SLS) lever-type isolator ▪ Biologically inspired passive isolator • Variable friction bearings • Pneumatic vibration isolator

Table 2.1: Main categories and subcategories of structural control systems (**continued**)

Semi-active	Semi-active tuned mass damper (STMD) Semi-active resettable variable stiffness TMD (RVS-TMD) Leverage-type stiffness controllable mass damper (LSCMD) Piezoelectric friction damper (PFD) Banded rotary friction device (BRFD) Semi-active bracing systems Variable-stiffness damper Variable-orifice damper Variable-friction damper Viscous fluid damper Controllable fluid damper Electromagnetic dampers (EMD)
Hybrid	Active + Passive Semi-Active + Passive

2.2.1 Active Vibration Control (AVC) Systems

In active control systems, an exterior energy source must be applied to activate the system through suitable signals (Maleki & Mahjoubi, 2013, 2014; Xu & Teng, 2002). In order to generate the signals, appropriate algorithms are used to measure structural dynamic responses.

Several types of AVC systems have been presented and developed. In active control, applied external energy plays the main role to control the system. The essential information of structural behavior under dynamic loading is received by a controller through sensors (see Figure 2.1). Studies on active control are mainly focused on structural safety pertaining to strong wind and seismic loadings, in recent years. However, more investigations in case of functionality are also needed; reduction of environmental

vibration as an essential duty in the serviceability context should be considered as well. Figure 2.2 demonstrates the applications of AVC systems in structural engineering field.

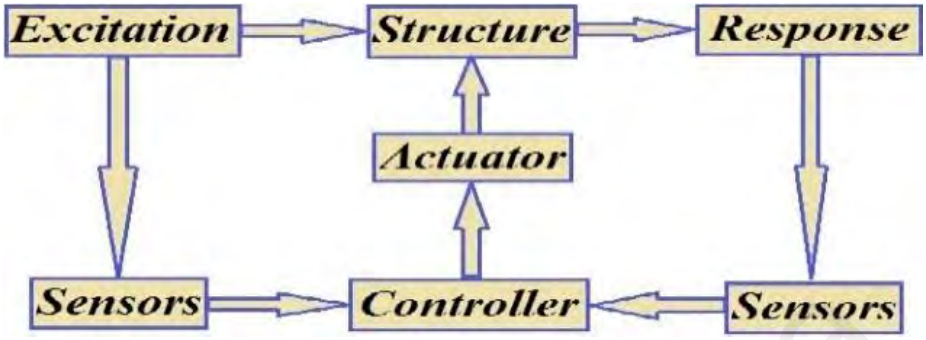

Figure 2.1: Structure of AVC

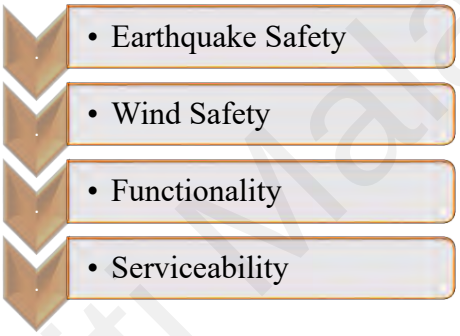

Figure 2.2: Goals of AVC systems in recent years

2.2.1.1 AVC in buildings

In recent years, notable attempts have been devoted to the advancement of the active mass dampers (AMD), active tuned mass dampers (ATMD), active tendon control (ATC), and distributed mass damper (DMD) vibration control systems in order to enhance serviceability and reduce the dynamic responses of civil engineering structures subjected to environmental loads such as wind and ground excitations.

Nigdeli and Boduroğlu (Nigdeli & Boduroğlu, 2013) proposed a system to control torsionally irregular single- and multi-degree-of-freedom (MDOF) structures subjected to near-fault ground excitation through active tendon control (ATC) as shown in Figure 2.3. A numerical algorithm that scanned the peak responses in the time-domain for

arrangements of control coefficients was used to tune proportional-integral-derivative parameters. Based on the investigated results, the ATC system was significantly efficient on mitigation of maximum responses and obtaining a swift steady-state response.

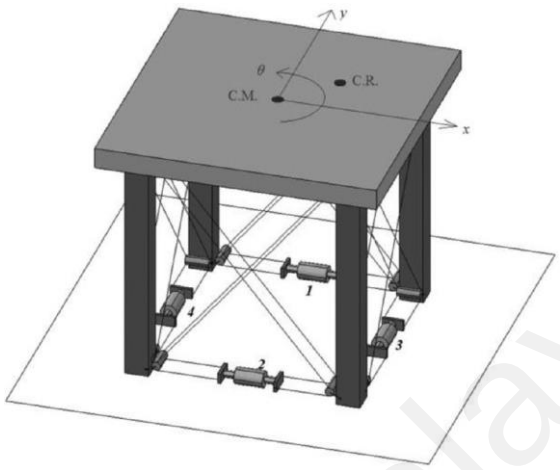

Figure 2.3: Implementation of ATC on a SDOF system (Nigdeli & Boduroğlu, 2013)

A novel control approach was proposed (Amini et al., 2013) for detection of the optimal control forces of ATMD using three control algorithms; particle swarm optimization, discrete wavelet transform (DWT) which was utilized as a strong time-frequency tool for providing time-varying energy in various frequency bands, and Linear-Quadratic-Regulator (LQR) algorithm. After testing the method on a 10-story building subjected to near-fault motions, the results showed that, the proposed approach was effective to reduce the displacement response in real time. Soleymani and Khodadadi (Soleymani & Khodadadi, 2014) proposed a new adaptive ATMD for vibration control of a 76-story building under both seismic and wind motions. A multi-objective genetic-fuzzy algorithm and an adaptive switching-type fuzzy controller was presented to enhance the ATMD performance under the excitations. Tinkir et al. (Tinkir et al., 2013) presented an experimental test in order to control deflection of 2-DOF structure subjected to a scaled earthquake using proportional-integral controlled AMD system. Consequently, deflection

and acceleration response of the two floors were graphically presented for active and passive mode. Muresan et al. (Muresan et al., 2016) proposed an active control system based on fractional order control implemented to a tuned mass damper (TMD) and viscoelastic damper (VED) in order to mitigate seismic vibration of structures by testing the controller in a SDOF laboratory scale structure. The analysed results revealed that the effectiveness of VED in vibration reduction was more than the TMD. Although, the merits of the proposed fractional order controller were noticeable when modelling errors were considered. A filtered sliding mode control method was presented (Wang & Adeli, 2015a) to reduce the wind-induced response of high-rise buildings and the method performance was appraised for a 76-story building using an ATMD installed on the roof. Because of the deletion of high frequency portion of the control force, the actuators, dampers, sensors and structure were less vibrated, and subsequently led to reduce their response in comparison to the unfiltered sliding mode control approach. Ubertini et al. (Ubertini et al., 2015) proposed an innovative AMD system with its modelling and application using a stable collocated sky-hook control algorithm. The system was evaluated by installing the device on the top floor of a 5-story steel structure with reduced-scale under vibration excitation. The presented AMD was made up of an electric torsional servomotor, ball screw, potentiometer and additional carried mass as displayed in Figure 2.4(a) and Figure 2.4(b). Yang et al (Yang et al., 2017) proposed a multi-model negative acceleration feedback control algorithm for a projected AMD system. In the AMD system, as shown in Figure 2.5, the proposed AMD was activated by AC servomotor connected to a portable mass through a ball-screw mechanism, where an accelerometer was installed as a sensor in order to measure vibrations. For the real use of AMDs once the natural frequency (ω_n) amplitude was low, the system could be used as the most applicable mechanism. Teng et al. (2014) proposed recent advanced technologies regarding the design and application of AMDs control on a tall building under wind

loading. Discussions contained overview of real structure, setting up analytical model, the scheme and optimization of a range of energy dissipaters, the time-dependent variable design using feedback control strategy for restricting supplementary mass impact, and the AMDs design and optimization.

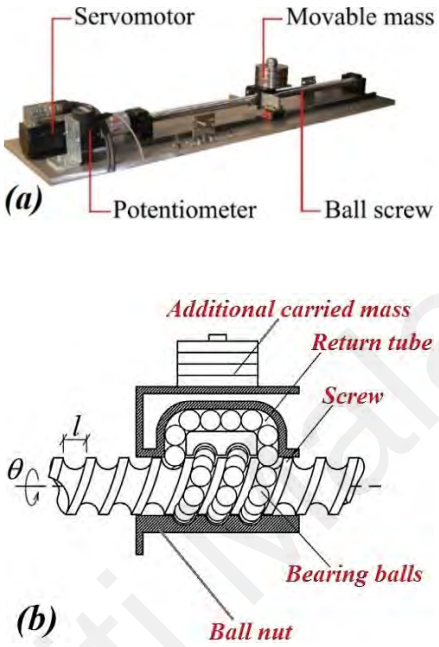

Figure 2.4: Details of (a) Electric torsional servomotor used in AMD system and (b) Components of ball screw (Ubertini et al., 2015)

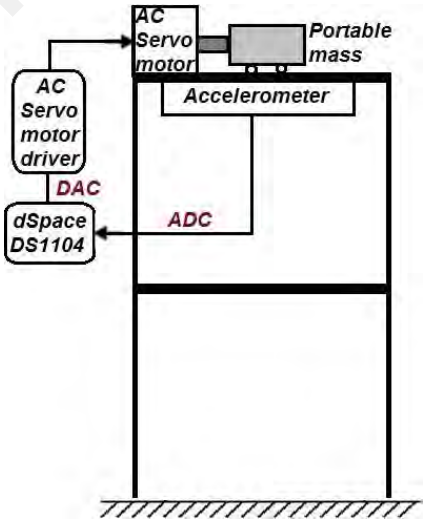

Figure 2.5: Scheme diagram of MDOF using proposed AMD (Yang et al., 2017)

Teng et al. (Teng et al., 2016) also implemented influence time delay analysis on stability and system poles in order to decrease the effect of time delay on the AMD control systems. To ensure the stability of the system, a formula for the maximum time-delay was established for structures with single-DOF (SDOF) and MDOF with resolving the characteristic equation given by (Hu, 2004; Lin, 1996). As a result, a compensation controller was planned and through the numerical and experimental studies, the success of the proposed approach was verified. Fu et al. (Fu & Johnson, 2014) analysed active control techniques for a DMD to demonstrate more structural response mitigations. To this aim, a 20-story building equipped with 20 DMDs was utilized as a test-bed. Accordingly, the presented active DMD technique, considering a single AMD system and a full-active system, could perform better than usual active control systems, while they utilized similar amount of input energy.

In high-rise buildings, the role of stiffness is much significant compared to strength role (Patil & Sangle, 2015). Moment resisting frames because of their flexibility do not meet stiffness criteria, though, concentric braced frames owing to their partial ductility have worthy stiffness. There are numerous manners of making braces to make structures resistant against seismic excitations. In order to enhance the performance of the typical braces installed in structural frames, the active bracing systems (ABS) are implemented. This system can be set in three common forms; X form, K form or V-braced frames (VBF) and in a diagonal form. Nonetheless, other bracing systems can be established such as zipper braced frames (ZBF) and chevron braced frames (CBF) configurations as depicted in Figure 2.6.

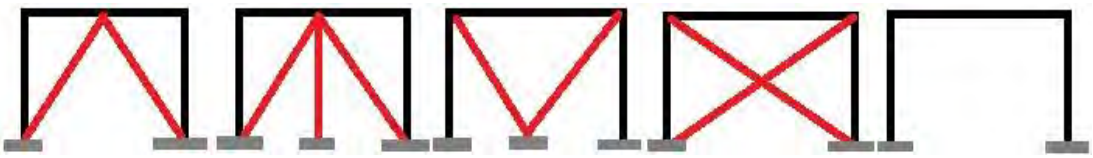

Figure 2.6: Bracing systems in different configurations

By mounting the servo-valve controlling hydraulic actuator, as shown in Figure 2.7, on the bracing systems, a huge control power can be produced (Arias-Montiel et al., 2014; Saaed et al., 2015). This system consists of a hydraulic force supply, an actuator, a servo-valve controller, sensors and a predefined algorithm using a control computer. To measure the sensor processing, the algorithm is used by the control computer and ordering the control signal. The servo-valve will utilize the ordered signal to regulate the intensity and direction of flow. Therefore, the two actuator chambers will be yielded due to the pressure changes. As a result, the vital control power will be generated by pressure changes. Eventually, the power is employed to withstand against severe lateral forces imposed to the structure.

Figure 2.7: F280S servo-valve hydraulic actuator (Arias-Montiel et al., 2014; Saaed et al., 2015)

Many other control algorithms have also been advanced for AVC systems of structures using different methods and devices. Bigdeli and Kim (Bigdeli & Kim, 2014) developed neuro-control algorithm according to modal energy for active nonlinear control of building structures. Amini and Samani (Amini & Samani, 2014) proposed a time-varying wavelet-based pole assignment controller to reduce seismic vibrations in MDOF structures. Discrete wavelet transform was implemented to specify the energy amount of the structural response in real time in a frequency band where the frequency was used in the Big Bang–Big Crunch (BB-BC) algorithm in order to update adaptively the optimal values of the closed loop poles of the system. The proposed wavelet-based pole assignment method was experimentally verified on a 10-story building system, and also through numerical examples under several excitations. Yanik et al. (Yanik et al., 2014) proposed a new AVC performance index considering the mechanical energy minimization of a 3D 6-story building, seismic energies and their control using a fully active tendon system designed by a linear optimal control algorithm. Lack of necessity to solve the nonlinear matrix Riccati equation as well as a theoretical seismic knowledge was the advantageous of the control system. Omidi et al. (Omidi et al., 2016) presented a novel controller, called Multi Positive Feedback (MPF) control, for mitigation of active vibration in piezoelectric-actuated flexible smart structures. The MPF was designed in order to control concurrently the vibrations of single and multi resonant frequency. Nazarimofrad and Zahrai (Nazarimofrad & Zahrai, 2016) developed a mathematical model in order to control the behavior of an irregular buildings subjected to earthquakes by means of active tendons ordered by LQR algorithm, while the soil-structure interaction effect was considered. Liu et al. (Liu et al., 2016) proposed a multiple source multiple harmonic active vibration suppression algorithm considering feedforward structure accordance with conjugate gradient method and reference amplitude rectification. A finite element (FE) model in-loop simulation was also presented for quick algorithm validation.

Yavuz et al. (Yavuz et al., 2016) presented a closed loop control technique for active vibration system to suppress the vibrations of end point. The mathematical of 4DOF system was developed, when the proportional-integral-derivative (PID) control action was integrated to the Newmark method. The PID control algorithm was applied to detect the error signal value of actuator in each time step. An input value was utilized to identify the movements for the following time step. The process was continuing till the steady-state value was roughly touched. Miyamoto et al. (Miyamoto et al., 2016) developed a fresh method to be used in an active control system according to the equivalent input disturbance method and the validation was established through a 10-DOF building model.

2.2.1.2 AVC in bridges

Inordinate and unforeseen cable vibration of bridges is deleterious for the long-term serviceability and safety of bridge structures. It may cause untimely failure of connections as a result of fatigue or collapse of cable-corrosion-protection systems. Furthermore, vibration of stay cables will decrease public confidence. To avoid the destructive vibration for protection of the entire bridge system, application of supplementary devices installed close to the cable anchorages has been broadly accepted. Recently, engineers have, however, proposed novel control approaches to actively suppress vibration of cables; it has temporarily been developed. Pereira et al. (Pereira et al., 2014) proposed a novel active vibration control design methodology to control human vibrations on pedestrian structures based on multi-input multi-output vibration control in order to obtain the sensor location as well as the control law. The method comprised of a performance index minimization that included all the important applied issues involved while accelerometers and inertial-mass actuators were utilized to perform a direct velocity feedback in practice. Wang and Adeli (Wang & Adeli, 2015b) presented an adaptive algorithm to control nonlinear vibration of big structures under seismic loading. They developed the control algorithm according to incorporation of a self-constructing wavelet

neural network, particularly for identification of structural system considering an adaptive fuzzy sliding mode control method. The method was used for mitigation of vibration response of a continuous pre-stressed concrete box girder bridge subjected to dynamic excitations. Mitchell et al. (Mitchell et al., 2015) developed a wavelet-filtered genetic neuro-fuzzy system using aspects of DWTs, implicit redundant representation genetic algorithm-based decentralized output feedback polynomial controls, neural networks, and fuzzy logic theory, in order to control motions of highway bridges under different seismic loads. Crusells-Girona and Aparicio (Crusells-Girona & Aparicio, 2016) proposed an active control system for application of cable-stayed bridges by means of quasi-static approach. The bridge design with active control systems is highly different from the one with no control system. According to this fact, the authors believed the approach must be considered in design codes. It was also noticed that, the study is capable to merge the abilities of the active control for both the quasi-static and dynamic loadings.

2.2.2 Passive Vibration Control (PVC) Systems

Passive strategies are different from active systems in which they are not operated by any external force or source. They are especially worthwhile in circumstances such as ground motions where external source is probable to be disconnected, while it is more urgent than ever. In passive control approach, control devices, as a secondary function, are embedded or connected to the structural members to improve the structural damping or increase the stiffness using a proper method with no use of external force to operate. Therefore, several forms of PVC devices, such as friction dampers, yielding and metallic dampers, have recently been developed for purposes of seismic protection in buildings and bridges. Figure 2.8 shows the general components of PVC systems.

Figure 2.8: Components of PVC system

2.2.2.1 PVC in buildings

Many investigators have considered the effectiveness and advantages of TMDs and have introduced different approaches to develop their robustness and validity. Therefore, TLD, TMD-inerter (TMDI), tuned liquid particle damper (TLPD), TLD with Floating Roof (TLD-FR), Eddy-Current TMD (EC-TMD) and particle TMD (PTMD) have recently been developed.

The inerter system has been earlier used in vibration control through base isolation systems. Recently, Lazar et al. (Lazar et al., 2014) analysed the feasibility of a tuned-inerter damper (TID) control approach as a substitute for TMDs and by consideration of n-DOF systems, general framework for computational response of the structures equipped with proposed TID was developed. Also, Marian and Giaralis (Marian & Giaralis, 2014) proposed an innovative passive device, known as TMD-inerter, to remove the pendulous motion of accidentally support excited primary structural systems compounding the conventional TMD with an inerter device. The inerter in the introduced TMDI configuration was using the "mass amplification effect" as a supplementary connective part between the ground and the TMD pendulous mass for SDOF, and between the primary structure and TMD pendulous mass for chain-like MDOF primary structures. Consequently, Jin et al. (Jin et al., 2016) introduced two configurations of inerter-based passive vibration controls, namely a mass linked to a parallel damper and spring in series with an inerter (Case 1), and a traditional dynamic vibration absorber in

series with an inerter (Case 2) to vibration control of the beam-type structures (see Figure 2.9). The comparison between Case 1 and Case 2 illustrated that for larger mass Case 2 had better performance than the Case 1 while opposite was correct for smaller mass ratio.

Papalou et al. (Papalou et al., 2015) and Papalou and Strepelias (Papalou & Strepelias, 2016) investigated an innovative technique to support multi-drum ancient monuments using particle dampers (PD). The proposed method introduced the utilization of PDs in the form of traditional drums having a hollow section encompassing particles as illustrated in Figure 2.10. The studies proved that, the properly designed PDs were significantly capable to control the response of a multi-drum column with no changing the column appearance.

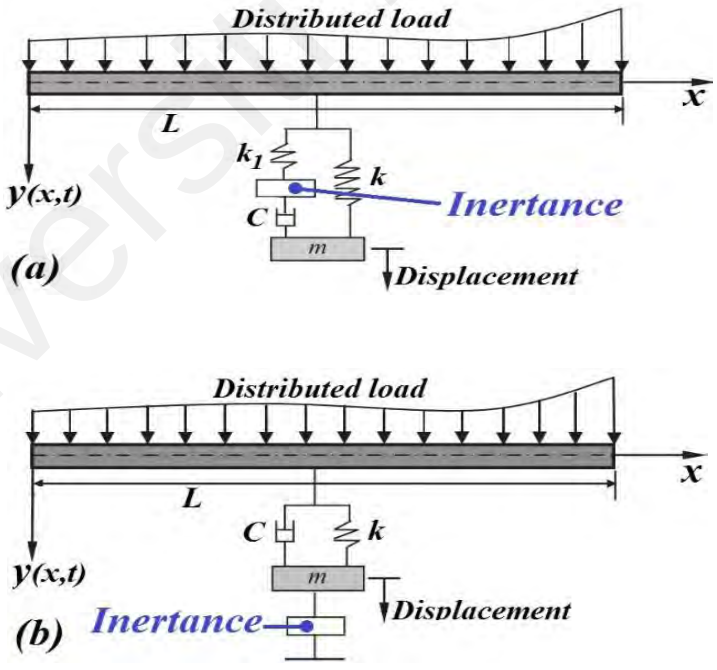

Figure 2.9: Beam-type structure with inerter-based (a) Case 1, and (b) Case 2 vibration control configuration (Jin et al., 2016)

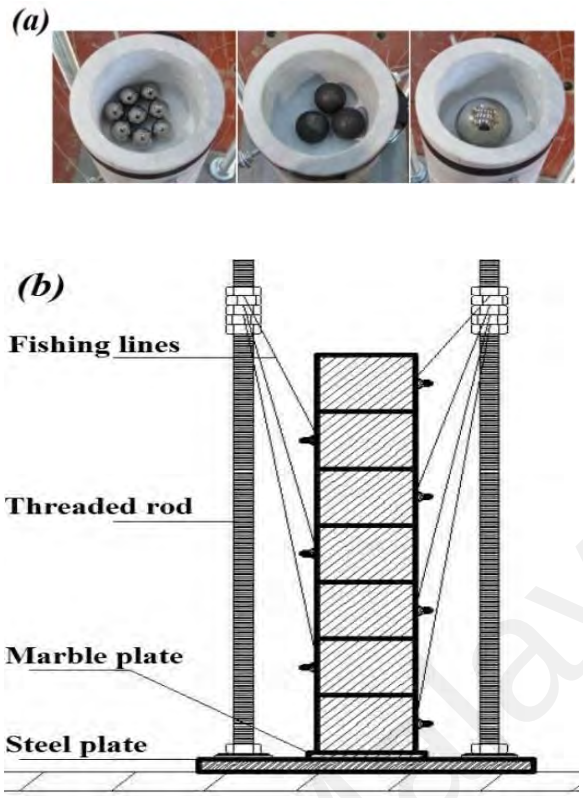

Figure 2.10: (a) PDs inside the drums and (b) schematic of the damper system considering ancient column (Papalou & Strepelias, 2016)

Dai et al. (Dai et al., 2017) presented a new passive vibration control device called tuned liquid particle damper TLPD, which integrates the conventional TLD and PD features as demonstrated in Figure 2.11. The TLPD features in terms of transfer functions and de-tuning settings were studied using shaking table tests and the frequency domain approach was used to discuss the non-linear TLPD performances installed in a 5-story steel frame building under various dynamic motions through shaking table tests. The tests provided the proof of concept results for the advanced passive vibration absorber. Ruiz et al. (Ruiz et al., 2016) proposed an innovative TLD-FR as shown in Figure 2.12, to avoid wave breaking phenomena and provide a linear behavior of liquid. The supplemental damping system was also considered for the TLD-FR by providing a placement for extra damper devices (like viscous damper) to enhance the favourite optimal damping for shaken liquid.

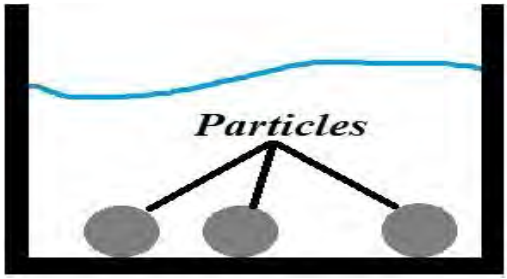

Figure 2.11: Scheme of TLPD (Dai et al., 2017)

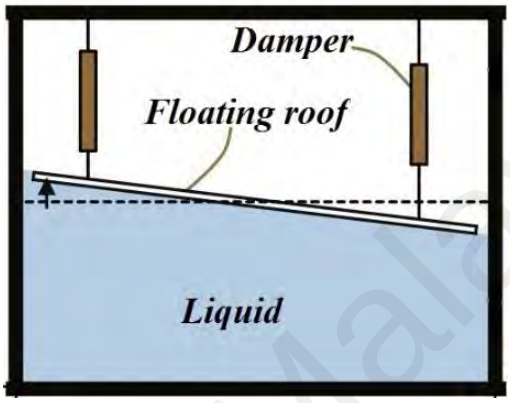

Figure 2.12: TLD-FR (Ruiz et al., 2016)

Lu et.al. (Lu et al., 2017) examined a new EC-TMD on a reduced scale structure to be as a representative for Shanghai Center (SHC) tower with a TMD installed at its 125th floor to evaluate the structural responses due to wind and earthquake excitations. Moreover, the numerical analysis of the SHC equipped with proposed EC-TMD was conducted to verify the results with experimental tests. Figure 2.13 shows the presented EC-TMD, in which *V, I, C* and *B* are velocity, eddy currents, conductive plate and magnetic field, respectively. Lu et al. (Lu et al., 2017) proposed an innovative PTMD, which synthesized several energy dissipation techniques from both particle dampers and TMDs, and its performance was assessed through computational, analytical and experimental methods and an analytical solution based on an equivalent single-particle damper concept was presented. Figure 2.14 shows the PTMD in Lu's study.

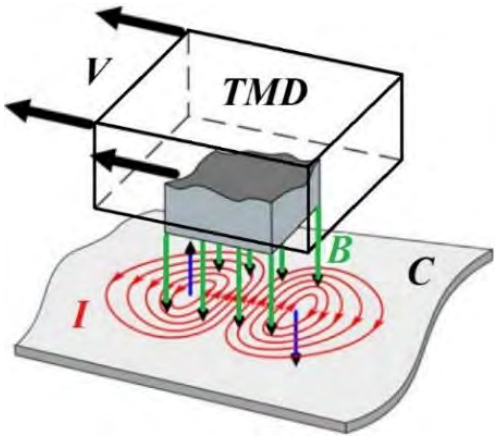

Figure 2.13: Eddy-currents arising from relative motion between conductive metal plate and magnet (Lu et al., 2017)

Figure 2.14: A view of PTMD (Lu et al., 2017)

Min et al. (Min et al., 2014) presented a two-way liquid damper using combination of tuned liquid column damper and tuned sloshing damper, in which its design procedure was developed and verified by installing the damper on a 64-story building structure to show the damper efficiency on reduction of the building response due to wind vibration. Hejazi et al. (Hejazi et al., 2013) proposed a multi-objective optimization technique using genetic algorithm (GA) to modify the performance of passive energy dissipation devices to reduce the damage response of structural members as well as story displacements considering 6-DOF. Hejazi et al. (Hejazi et al., 2016) presented a new FE-based analytical model as well as a constitutive law for viscous wall dampers (VWD) to adapt dampers

with RC structures subjected to seismic loading. They also developed Newmark's algorithm for inelastic analysis in order to detect damage for both the connected VWDs and structural members. Based on the proposed model, a FE program was codified and validated.

Dissipation of energy using devices made of metals such as steel, SMAs, lead and copper have demonstrated their effect on mitigation of the seismic response of structures. As a result, researchers have also used the advantages of such materials to present new solutions for structural vibrations. Qian et al. (Qian et al., 2013) presented an innovative re-centring SMA damper, called RSMAD using nitinol wires as a superelastic components to dissipate energy as indicated in Figure 2.15. Additionally, the constitutive equations for nitinol wires were developed and several cyclic displacement and frequency amplitudes were performed to assess the damper, and based on the obtained results, it was concluded that for a frequency more than 0.5Hz, the damper sensitivity performance was impalpable. Brionce and de la Llera (2014) presented a new copper-based bidirectional energy dissipation damper, where the cyclic device response under demonstrated momentous capacity to dissipate energy in both small and large deformations before failure.

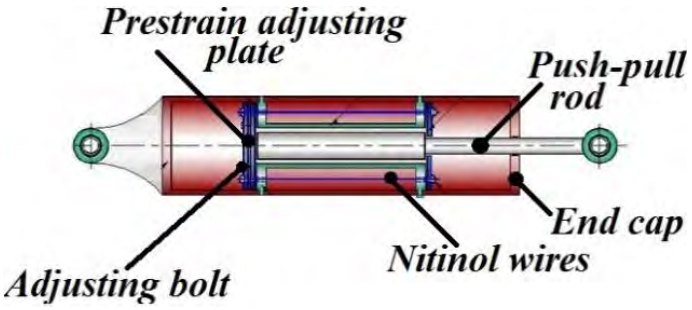

Figure 2.15: RSMAD configuration (Qian et al., 2013)

Fateh et al. (Fateh et al., 2016) presented a novel passive variable stiffness bracing (VSB) system as an adaptive stiffness element to be utilized in structural frames, in which the analytical model of the device was developed to simulate its mechanical performance. Great nonlinear stiffness variety was the most significant feature of the proposed VSB device. Hao et al. (Hao et al., 2014) presented a new H-type steel unbuckling brace (SUB) made of low-yield steel, as depicted in Figure 2.16. The proposed damper was tested and it was affirmed that the damper had great capacity in terms of stable energy dissipation and plastic deformation without any stiffness degradation.

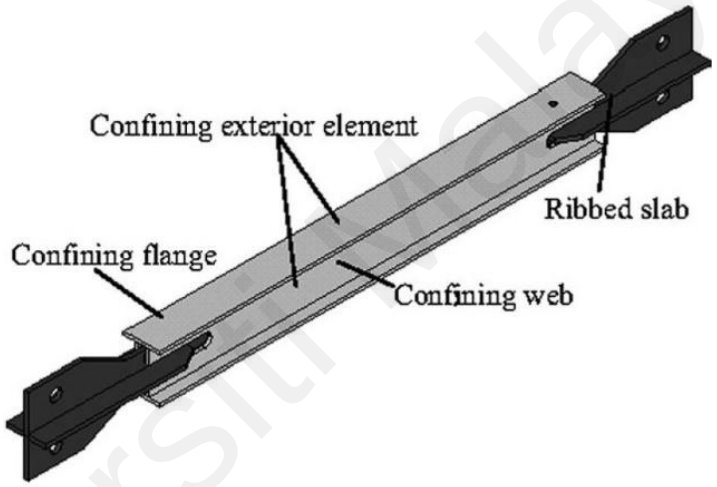

Figure 2.16: Diagram of SUB damper (Hao et al., 2014)

Buckling Restrained Brace (BRB) is categorized as a new type of concentric braced frames (CBFs), where it increase the stiffness and ductility of the frames and simultaneously solves the buckling matter. Chou et al. (Chou et al., 2016) developed BRBs by introducing a dual-core self-centring sandwiched BRB, called SC-SBRB, that merged both the energy dissipation of the SBRB and the self-centring feature of the dual-core self-centring brace (DC-SCB) together. Guerrero et al. (Guerrero et al., 2016) proposed a new approach for preliminary design of short building structures armed by BRBs. It was assumed that a structural frame equipped with BRBs was logically

reinforced by a dual SDOF oscillator to prevent members yielding at the same displacement levels. The method formulation was derived for SDOF buildings. Zhou et al. (Zhou et al., 2017) proposed and replaced a damping outrigger system considering the diagonal BRBs with conventional buckling steel members and a mechanical model of the developed damping outrigger was introduced. The influence of the outrigger system was evaluated on the 124-story SHC tower with 632 m height as the target structure. Dougka et al. (Dougka et al., 2014) and Dimakogianni et al. (Dimakogianni et al., 2015) presented a new passive vibration control system, known as FUSEIS1, which was subdivided into FUSEIS1-1 and FUSEIS1-2 in which the dissipative fuses were beams and short pins, respectively, as demonstrated in Figure 2.17. The fuses were placed between floors connected to two strong rigid columns. Laboratory tests were carried out to evaluate the proposed systems and design recommendations were provided. It was recommended to develop their capacity for self-centring properties. Walsh et al. (Walsh et al., 2017) presented a resetting passive stiffness damper (RPSD) in line with modification of resetting semi-active stiffness damper (RSASD), where the feedback components of RSASD were substituted by a novel rack-lever mechanism, as illustrated in Figure 2.18, to attain damper resetting due to applied force. The numerical and laboratory tests of the RPSD confirm that, control performance of the RPSD was similar to the RSASD.

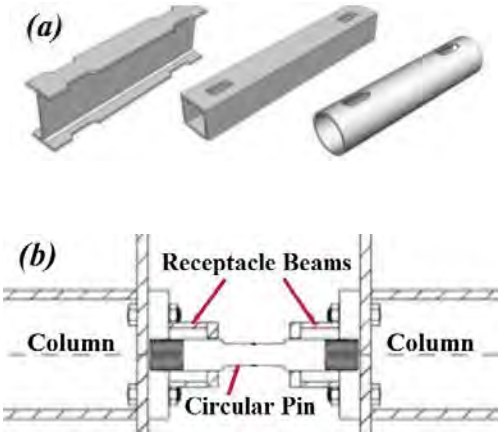

Figure 2.17: (a) FUSEIS1-1 and (b) installed FUSEIS1-2 (Dimakogianni et al., 2015; Dougka et al., 2014)

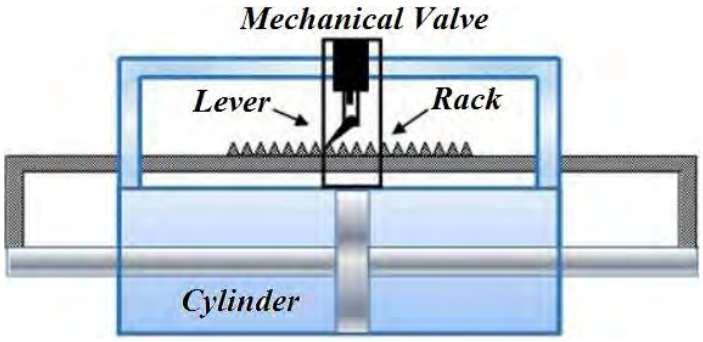

Figure 2.18: RPSD configuration (Walsh et al., 2017)

Viscoelastic passive energy dissipation devices have, however, verified as an effective tool for earthquake-induced vibration control in buildings; a few studies have been progressed for their contribution to vibration control. For example, Yamamoto and Sone (Yamamoto & Sone, 2014) proposed a combination use of metallic yielding component with VED installed in three different frame systems over an inclusive variety of applied displacement amplitudes. The presented vibration control was considered to work as a great capacity of VED during a minor vibration by designing the VE material as thin material to carry the shear strain. Gong and Zhou (Gong & Zhou, 2017) investigated a new form of viscoelastic damper (VED) with robust nonlinear characteristics, presenting both hardening and softening, by designing and testing a 3-srory viscoelastically damped building under dynamic motion using a shaking table to show the control effect of the VED.

A type of nonlinear energy sink damper (NESD) and passive negative stiffness dampers have also been investigated by the engineers as innovative dynamic vibration absorbers. Luo et al. (Luo et al., 2014) introduced a new passive device conducting essentially nonlinear elastomeric springs to reduce response of structures subjected to dynamic loading while the structures remain elastic. To examine the damper, four NESDs were installed on a 9-story building structure where elastomeric springs with pyramidal

shape were implemented to understand the enhanced essentially nonlinear spring elements as presented in Figure 2.19.

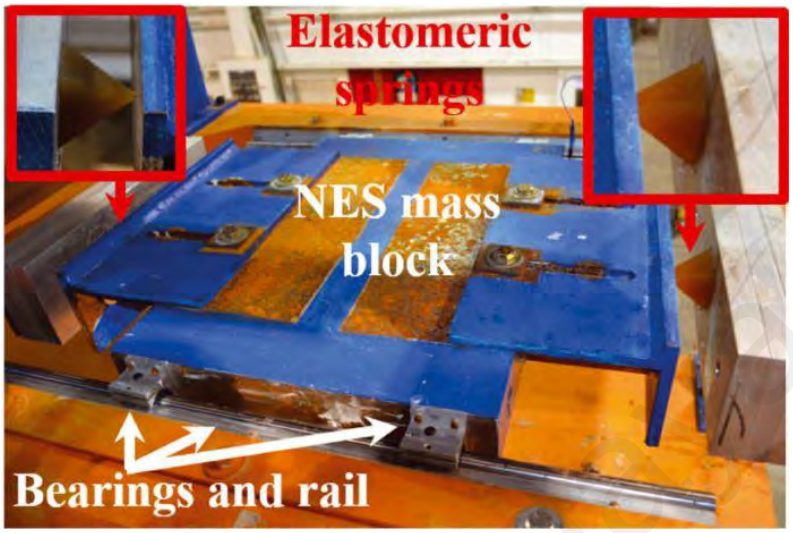

Figure 2.19: NESD used in experimental test (Luo et al., 2014)

Shi and Zhu (Shi & Zhu, 2015) presented two new schemes of passive negative stiffness dampers through magnetism, called magnetic negative stiffness dampers (MNSDs), which were composed of a number of constant magnets set into a conductive pipe as shown in Figure 2.20. The proof of concept laboratory tests were implemented by means of an MTS machine when a cyclic displacement protocol loading was applied to the prototypes.

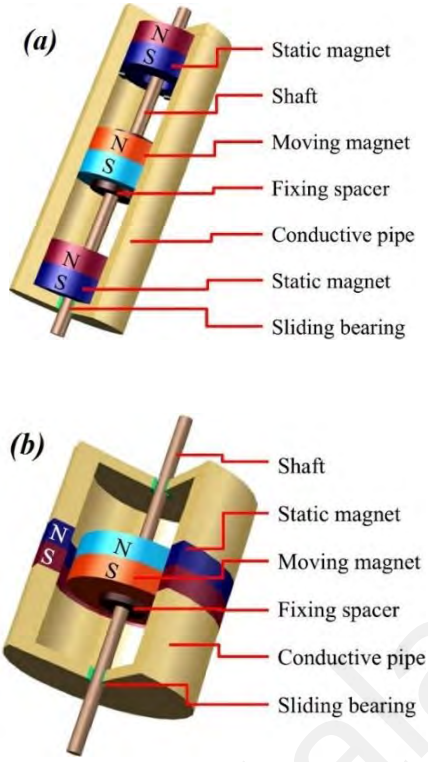

Figure 2.20: MNSD a) type A and b) type B (Shi & Zhu, 2015)

2.2.2.2 PVC in bridges

Applications of passive control systems in bridge engineering has been attracting more attentions, unlike AVC, in terms of proposing innovative control devices and methods. The passive controls have attested to be efficacious in reduction of cable vibration, as the control systems can be favourably adjusted for maximum damping ratio, although, the damper distance to the cable end anchorage is an important matter. Yan et al. (Yan et al., 2014) presented a primary design method for tuned particle dampers (i.e. TPD and PTMD) for continuous viaducts by testing a reduced-scale bridge subjected to ground motions, such that the TPDs were attached to the tested bridge in a dispersed embellishment along the whole bridge length, and an analytic energy approach was conducted for simulation of the damper behavior using a FE model. They showed the proposed preliminary design method for TPDs is a useful tool in response reduction of bridges under seismic motions. Miguel et al. (Miguel et al., 2015) proposed the coincident

optimization of placement and force of friction dampers (FDs) using firefly algorithm. To evaluate the capacity of presented method two footbridges under human-induced vibrations were investigated, in which locations and forces of FDs were the design variables. The results confirmed the capability of the proposed approach for determination of the best placements of the FDs in the structures as well as their optimum forces. Khang et al. (Khang et al., 2016) investigated experimentally and theoretically the influence of TMD on a long-span bridges considering raising the critical flutter wind speed. The equations governing the motion of the bridge deck equipped with TMD were analytically expressed and step-by-step flutter analysis approach was developed using MATLAB program code from 2-DOF system to a 4-DOF system to compute the TMD parameters. Takeya et al. (Takeya et al., 2016) proposed a newly energy harvester device known as tuned mass generator (TMG) consisted of a tuned dual-mass damper system to be used for vibration control of bridges as presented in Figure 2.21. In order to dissipate and use the unused energy reserve of the damper, an electromagnetic transducer was applied. Moreover, TMG was tuned through a new proposed approach, namely multi-domain parameter design approach for both the power generation and energy storage. Based on the analytical study it was shown that, TMG was robust against tuning errors and uncertainties under vibrations. Miguel et al. (Miguel et al., 2016) presented a new application of robust optimal design (ROD) of TMD and Multiple-TMD (MTMD) for vehicle-induced vibration problems of bridges by implementation of a parallel-processing Monte Carlo simulation (MCS) to carry out the high computational complexity. The obtained results showed that by using MTMDs can decrease the maximum vertical displacement at the center of bridges compared to single TMDs solutions.

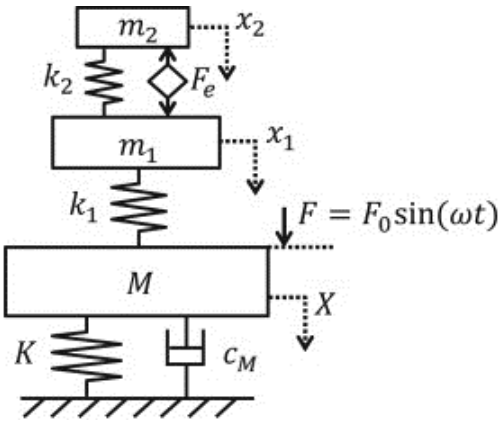

Figure 2.21: Scheme of TMG application on bridges with dual-mass systems (Takeya et al., 2016)

Camara et al. (Camara et al., 2017) proposed a new approach to design optimum yielding dampers (concentrated on TADAS dampers connected between deck and supports) based on equivalent SDOF approximation for short to medium span cable-stayed bridges under seismic excitations in the transverse direction. The results demonstrated that the plastic deformation of dampers causes significant effect to prevent seismic damage of towers in the transverse direction. Attary et al. (Attary et al., 2015a,b) showed the effectiveness of a new passive NSD by implementing the device, which provided negative stiffness, on a scaled down model of a highway bridge subjected to various seismic loads through shaking table test where four different bridge configurations including i) isolated bridge (IB); ii) NSDs+IB; iii) VD+IB; and iv) NSDs+VD+IB was experimentally considered. The proposed NSD is shown in Figure 2.22.

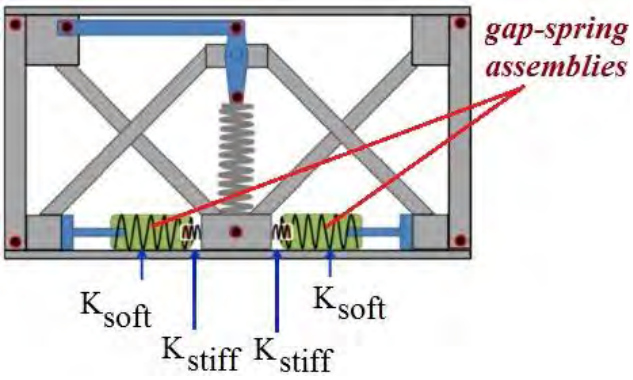

Figure 2.22: Proposed NSD, which dissipates forces with the motion of the device (Attary et al., 2015; Attary et al., 2015)

2.2.3 Semi-active Vibration Control (SVC) Systems

A semi-active damper device is usually defined as a controlled passive device, while it has yet many benefits of an active control system with no need of any large energy input. In other words, a semi-active device is usually defined as an active device with small energy requirement such as that of a battery. A side advantage of this system as well as hybrid control system is providing extra degree of protection through passive control operation when the power sources are failed under extreme excitations, unlike an entirely active system. A close consideration in structural vibration control area gives the detail that, SVC system proposes the adaptability of AVC without requiring the large power supply (see Figure 2.23).

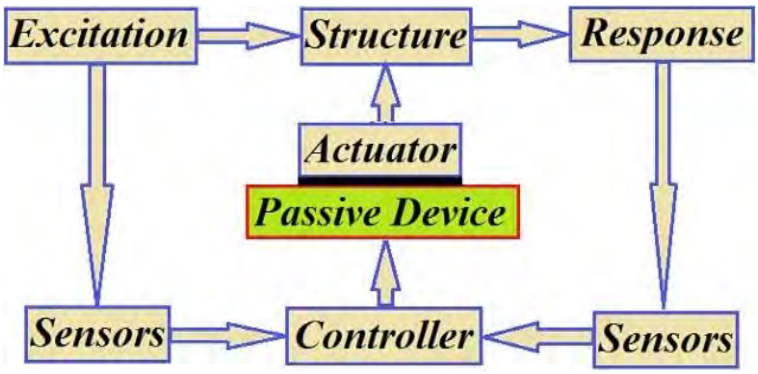

Figure 2.23: SVC components

2.2.3.1 SVC in buildings

Researchers have investigated different stochastic optimal semi-active control algorithms for excited building and bridge structures. One of prevalent SVC system is MR damper, which uses magnetorheological fluids to make adaptable dampers. The damper has been widely considered in vibration control of both the buildings and bridges. Zeinali et al. (Zeinali et al., 2013) employed an adaptive neuro-fuzzy inference system to investigate a phenomenological dynamic model of two types of Lord Corporation MR dampers, a short and a long stroke damper, used in laboratory tests. The obtained results showed that the proposed model was successfully able to predict behavior of both the short and long stroke MR dampers with acceptable accuracy. Cha et al. (Cha et al., 2014) studied four control algorithms including clipped optimal, Lyapunov stability based, passive on and decentralized output feedback polynomial control algorithms using real-time hybrid simulations to validate a MR damper placed in a realistic MRF system, when the frame was subjected to three earthquake excitations. The results in terms of acceleration responses, inter-story drifts, control forces and displacements were presented. Alqado et al. (Alqado et al., 2017) introduced the linear matrix inequality-based closed loop version of the input-shaping control technique for structural vibration control area, where the effectiveness of the presented control method was evaluated by simulation of a 3-story building structure equipped with a MR damper, tightly linked between the ground and the first floor. Khalid et al. (Khalid et al., 2014) examined a reduced scale MR damper model considering the valve mode mechanism through recurrent neural network modelling approach for rehabilitation of the nonlinear hysteretic behavior of MR damper. Besides, an innovative modulated chirp signal (amplitude and frequency range varying input signal) related to supply voltage was introduced for continuous motion of the damper. Xu et al. (Q. Xu et al., 2017) optimized the Back-propagation Artificial Neural Network (BP-ANN) through Artificial Bee Colony (ABC)

algorithm, called ABC BP-ANN as indicated in Figure 2.24, to find the required voltage for SVC of MR dampers (installed in a single and multiple buildings) using Spencer model. It was observed that, the results of MR damper control-forces were close to the LQR active control algorithms. In addition to this, the results revealed that, the proposed algorithm of ABC-BP-ANN was more effective than BP-ANN algorithm to forecast MR damper voltage using the velocity data, displacement and control force. Hashemi et al. (Hashemi et al., 2016) also proposed a wavelet neural network (WNN)-based semi-active control approach for providing precise calculation of input voltage for MR dampers for providing the control parameters imposed to MR dampers installed on a structure. The model was optimized through a localized genetic algorithm and later on, it was applied to a 9-story benchmark building subjected to an increased-scale earthquake. The effectiveness of the controller was also verified under other near-field and far-field earthquake motions. Alqado and Nikolakopoulos (Alqado & Nikolakopoulos, 2016) presented an innovative solution using a semi-active posicast control approach for vibration control of structures with MR dampers and evaluated the approach efficiency numerically using MATLAB code and experimentally testing a 3-storey benchmark structure equipped with a single MR damper. Moreover, a semi-active Bang-Bang (BB) controller and a general feedback LQR algorithm was designed to evaluate the recommended controller performance.

Semi-active TMD (STMD), as an appealing alternative to conventional TMDs, have also been developed considering variable stiffness (VS), having the privilege of incessantly retuning the frequency because of real time control. Consequently, this advantage makes the damper robust to change damping and stiffness of the associated structures. Lin et al. (Lin et al., 2015) proposed an innovative semi-active resettable variable stiffness TMD (RVS-TMD) to improve the TMD control performance. The RVS-TMD was consisted of a RVSD, composed of a control stiffness element and a

resettable element, and an undamped TMD system as shown in Figure 2.25. Based on the numerical analysis, it was shown that the RVS-TMD was capable to evade detuning effect and guarantee the optimal control performance as anticipated while the primary structure frequency was altered.

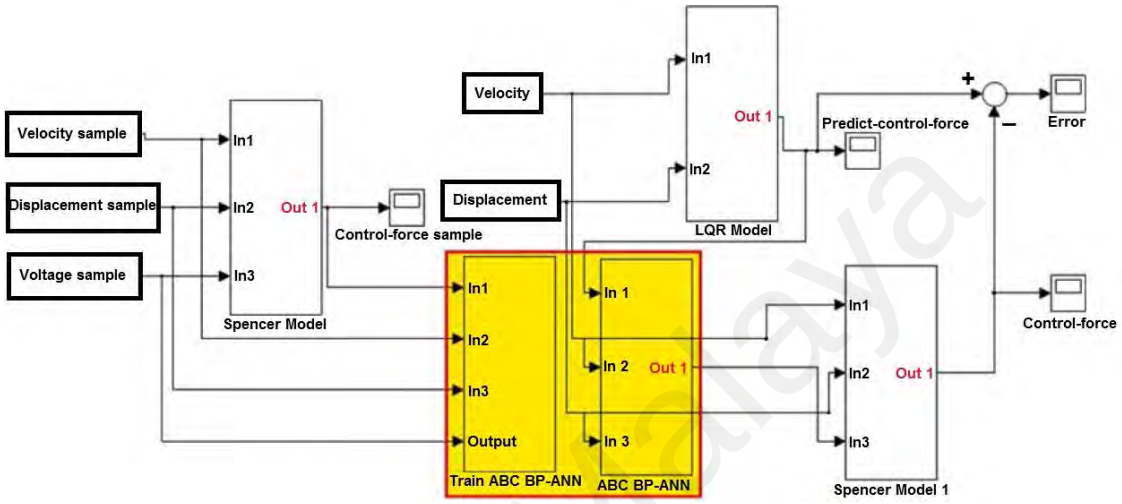

Figure 2.24: Presented ABC-BP-ANN for SVC of MR Dampers (Q. Xu et al., 2017)

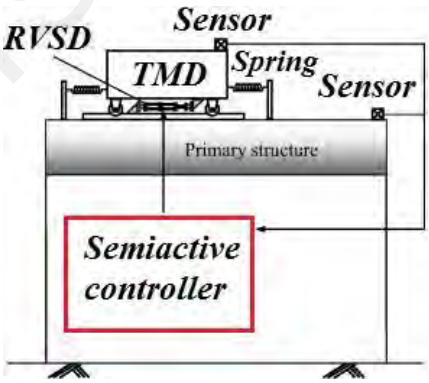

Figure 2.25: Schematic diagram of RVS-TMD (Lin et al., 2015)

Chu et al. (2017) introduced the leverage-type stiffness controllable mass damper (LSCMD) as a semi-active vibration control system to improve the conventional TMD performance. The LSCMD consists of a leverage arm with a portable pivot, allowing

to change the lever arm by changing position of the pivot to restore the force in real time and to control stiffness of the damper as shown in Figure 2.26. The LSCMD effectiveness was evaluated through comparison of the same system equipped with TMDs and hybrid mass damper considering similar control law considered for the LSCMD. Sun and Nagarajaiah (2014) assessed the performance of a semi-active TMD (STMD) by means of frequency and variable damping ratio under seismic motions. The STMD frequency and the damping ratio was conducted by proposing a new short-time Fourier transform-based (STFT-based) control algorithm through tracing the primary structure displacements and the variable stiffness STMD (VS-STMD). The presented results confirmed the effectiveness of the VS-STMD in reduction of the vibrations compared to the optimal TMD under both the near-fault pulse-like and regular ground excitations. Similar study was carried out by Deshmukh and Chandiramani (2014) using LQR algorithm to control a building, equipped with a VS-STMD, under wind excitations.

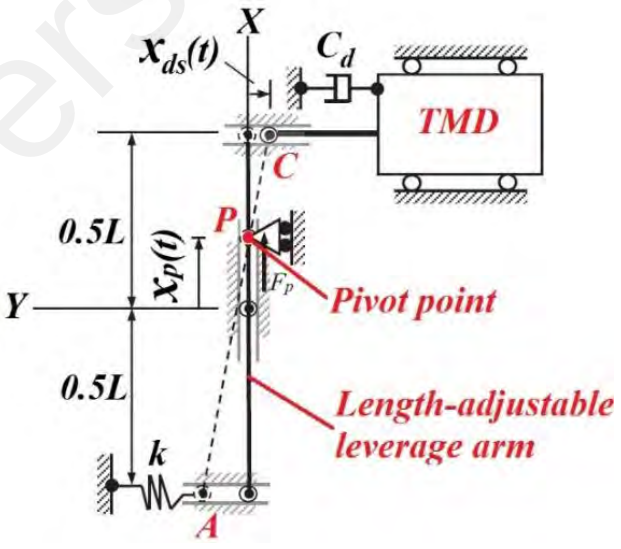

Figure 2.26: LSCMD configuration

Piezoelectric friction dampers (PFD) are classified as intelligent systems aimed at SVC in structures. The PFDs at piezoelectric smart isolation systems (PSIS) are principally considered as variable passive devices. Etedali et al. (Etedali et al., 2013) developed optimal PID controllers of the isolated buildings equipped with PFDs in order to gain semi-active control. The effectiveness of the proposed algorithms was verified via three well-known controllers; LQG control, the maximum passive operation of the FD, and optimal Skogestad's PID method. Using GA, the Skogestad's PID tuning parameter was specified to balance the intension and performance of the closed loop operational systems.

The advancement of semi-active friction dampers has progressively captured attention. Variable friction dampers (VFD) are another solution for vibration control with capability of high-energy dissipation, by converting mechanical energy into heat through friction mechanism that is controllable via an actuator. Cao et al. (Cao et al., 2015) proposed a new semi-active variable friction damper designed based on duo-servo drum brake technology of a vehicle. To evaluate the damper, they fabricated a scaled-down prototype and characterized its dynamic performance. Later, Downey et al. (Downey et al., 2016) proposed a fresh VFD for application of vibration control, named banded rotary friction device (BRFD) as illustrated in Figure 2.27, which was based on the band brake system. The BRFD was analytically presented and experimentally tested by applying harmonic loads to a BRFD prototype. Results confirmed the maximum force capacity of 45 kN when it merely used 267 N actuator force.

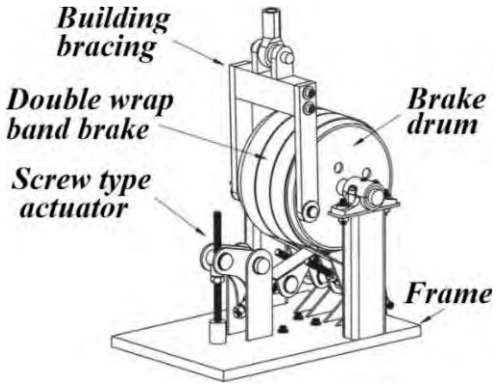

Figure 2.27: BRFD configuration (Downey et al., 2016)

Garrido et al. (Garrido et al., 2016) studied experimentally and theoretically a semi-active friction tendon (SAFT) using two different control laws; simplified quickest-descent control law (SQDCL) based on velocity-feedback and slackening-preventing control law (SPCL) based on force-feedback, to show the effectiveness of proposed system on vibration control of buildings and bridges. Besides using these two lows, the quickest-descent control law (QDCL) was also used to investigate the performance of SAFTs in space structures. Evaluation of hysteretic behavior and displacement response of SAFTs confirmed two important implications; 1) the efficiency of the passive vibration control can continuously be enhanced using semi-active control through three considered control laws and, 2) for very small displacements the SQDCL is more effective, whereas for large displacements the SPCL is more advantageous. Pardo-Varela and Llera (Pardo-Varela & de la Llera, 2015) proposed, designed and tested a semi-active frictional device with piezoelectric actuators in order to control vibration of large scale structures. The presented damper was made of duplex steel plates and leads, to provide an intense frictional capacity, which can be extended for both passive and semi-active modes. Figure 2.28 shows a schematic view of the damper. Choosing the sliding material and clamping system stiffness were two of the main key features in design of the damper.

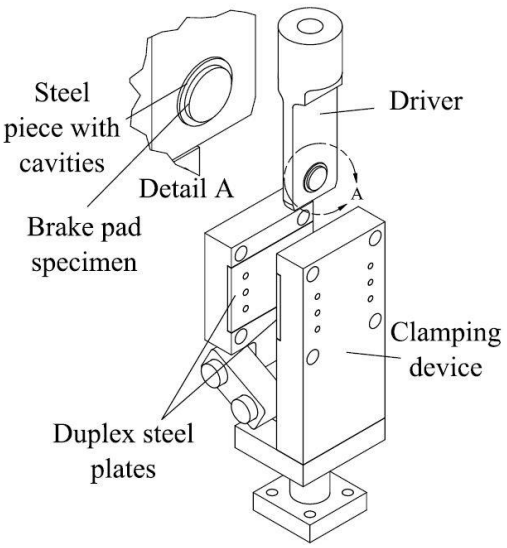

Figure 2.28: Frictional damper (Pardo-Varela & de la Llera, 2015)

Zare and Ahmadizadeh (Zare & Ahmadizadeh, 2014) proposed an alternative methodology for design of optimum viscous fluid dampers by means of stiffness modification and active control (pole assignment) algorithm; adjusted for adaptability with passive systems. In the alternative design approach, the structure poles could relocate to their optimum locations to decrease the vibrational response of the structure. The efficiency of the proposed design method was presented by comparison of a 5-story building controlled through different methods such as LQR algorithm. Shi et al. (Shi et al., 2014) presented a new semi active floor isolation scheme, to be set on the top floor of building structures as depicted in Figure 2.29, to decrease displacement and acceleration under both long- and short-period excitations by adapting LQR control algorithm through frequency-dependent scheduled gain, named LQRSG. The obtained results from the tests demonstrated that the LQRSG approach was outstandingly more efficacious than the traditional LQR control algorithm for structural response reduction due to both long- and short-period motions. Qu et al. (Qu et al., 2017) presented a novel method to optimize the negative stiffness and additional damping values in different floors of building structures.

The formulation was firstly derived to adapt the negative stiffness (NS) and additional damping optimization with the decentralized-static-feedback controller. Afterwards, the controller was explored by homotopy procedure; leading a local optimum solution and lastly, the procedure was verified via numerical analysis of a 20-story benchmark building structure. The results showed that the proposed approach could effectively decrease the inter-story drifts as well as the shear force due to ground accelerations.

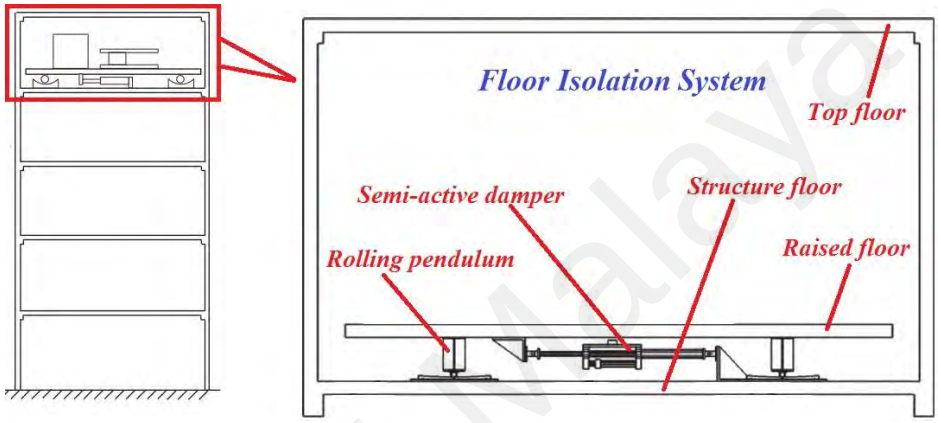

Figure 2.29: Proposed floor isolation system (Shi et al., 2014)

2.2.3.2 SVC in bridges

MR dampers also have been used as a favourable solution in vibration control of cables in bridge structures. It is because of the ability of MR dampers to tune the damping effect of the structural vibration in real time. Therefore, in this regard, Maddaloni et al. (Maddaloni et al., 2013) made some progress to an existing methodology (Brown et al., 2011) to draw out earthquake information by means of a seismic early warning system (SEWS) in the semi-active structural control framework using MR dampers installed on a highway bridge. The methodology also represented an improved form of the one recommended by (Maddaloni et al., 2011). The key idea consisted in varying the MR dampers behavior based on an estimation of the peak ground acceleration (PGA) of an incoming seismic excitation. Luu et al. (Luu et al., 2014) investigated the control

feasibility of vibrations of railway bridges in transverse direction subjected to high-speed traffic through MR dampers installed as shown in Figure 2.30. A H∞ algorithm was derived to control damping forces of MR damper with its inverse model as well as the adaptive neuro-fuzzy inference system technique was built to predict voltages of MR dampers. The suggested model was robust for decreasing resonant vibrations.

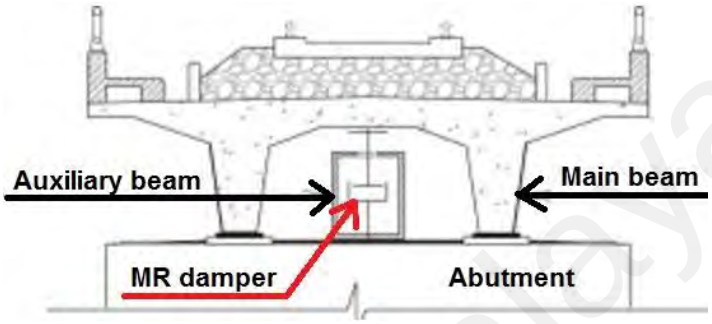

Figure 2.30: Retrofit configuration for bridge (Luu et al., 2014)

Weber (Weber, 2014) presented a new semi-active vibration absorber using MR damper (see Figure 2.31), known as MR-SVA, to show the performance of the un-damped vibration absorber in order to reduce harmonic excitations in which the performance of the proposed device was evaluated by harmonic vibration of the Empa bridge, while the passive absorbers of the MR-SVA were properly adjusted to the target resonance frequency of the bridge once detuning of 10% was implemented. The obtained results were then compared to the behavior of a TMD and showed how the MR-SVA were effective.

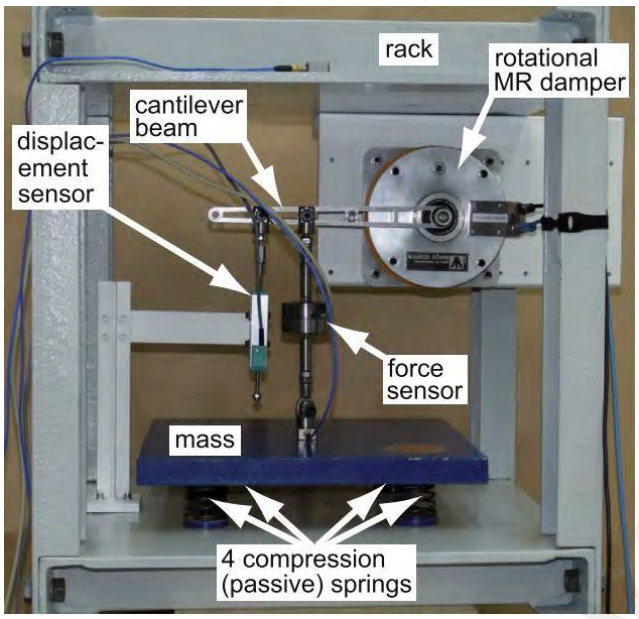

Figure 2.31: Prototype MR-SVA (Weber, 2014)

Arsava and Kim (Arsava & Kim, 2015) proposed two Takagi-Sugeno fuzzy algorithms to investigate nonlinear modelling behavior of MR dampers subjected to different impact forces and control signals. It was proven from the training, testing and validation that, the Output Feedback neuro-fuzzy (OFNF) model was so efficient in nonlinear modelling behavior of MR dampers conducting arbitrary current signals under many extraordinary impact loads. Weber and Distl (Weber & Distl, 2015) presented two control methods, controlled viscous damping and cycle energy control, for MR dampers installed on bridge stay cables and also they solved the force tracking for MR dampers installed on Russky Bridge and Sutong Bridge using a model-based feedforward with no force feedback for decreasing costs, when temperature (-40°C to +60°C) of the bridges' environment was taken into consideration for the damper to guarantee an accurate force tracking of the real MR dampers affected by temperature. The other novelty was minimizing power consumption through real-time decentralized control components with pulse width modulation (PWM) current mounted nearby each damper to prevent DC power lines as shown in Figure 2.32. Weber and Maślanka (Weber & Maślanka, 2014) also

experimentally validated the precise stiffness emulation method with MR dampers for semi-active TMD (MR-STMD) of the Wolgograd Bridge.

Figure 2.32: (a) Russky Bridge, Russia and (b) real-time decentralized controllers with PWM (Weber & Distl, 2015)

Chen et al. (Chen et al., 2016) developed typical LQG control strategy for excellently modifying self-sensing MR dampers in protection of bridge stay cables under extreme vibration as shown in Figure 2.33. With the purpose of real performance, the development took into consideration the limited measurements and a collocated sensing-damping arrangement as well as nonlinear dynamics of the self-sensing damper using a verified Bayesian NARX network approach in order to compensate for nonlinearities of the damper. In condition of running the self-sensing device in semi-active and passive vibration control modes, it was observed that the combination of nonlinear dynamics of the device in the control strategy improved damping force tracing effectively, and attained better performance through the passive control mode and Heaviside step function-based LQG control. Heo et al. (Heo et al., 2017) proposed MR dampers with lumped mass, as shown in Figure 2.34, used in a two-span bridge to reduce its longitudinal vibration under near- and far-filed earthquakes. The mathematical model of damping system was derived and the model was tested under near- and far-field motions through shaking table.

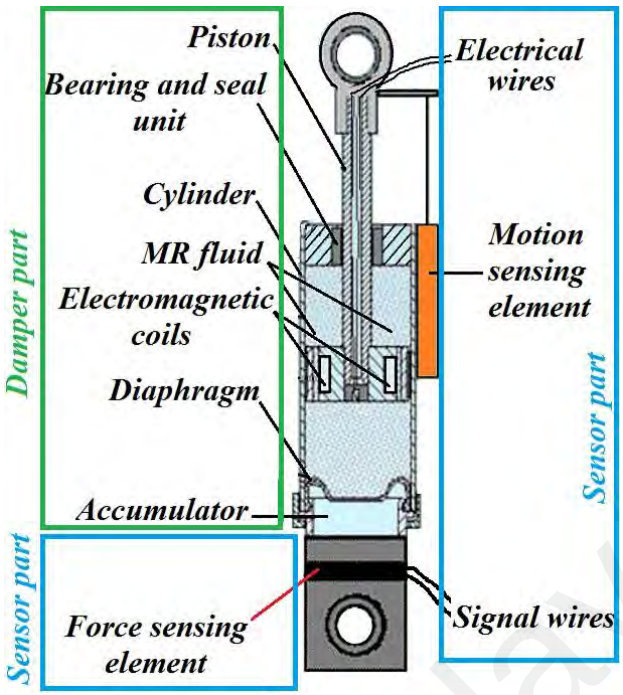

Figure 2.33: Self-sensing MR damper (Chen et al., 2016)

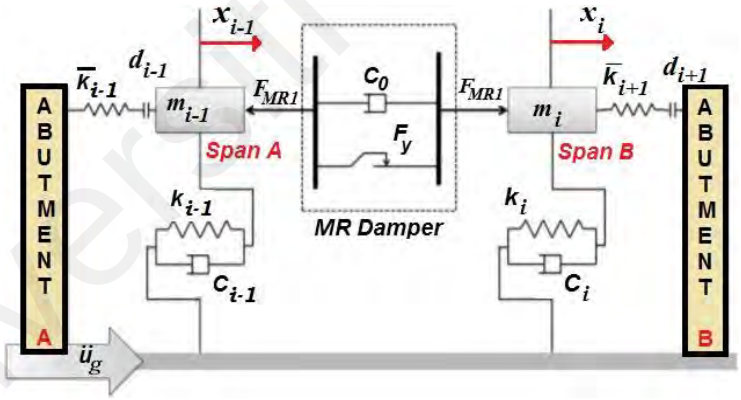

Figure 2.34: MR damper with lumped mass (Heo et al., 2017)

Additionally, to mitigate vibration response of the bridges, a few other devices as well as control approaches have been developed. For instance, Andersson et al. (Andersson et al., 2015) studied external damper systems to mitigate the vibration of railway bridge and, therefore, developed procedures for a VS-STMD by means of tuning frequencies with conducting numerical simulations of the railway bridge as the case study. The

accumulative fatigue damage was computed for different damping systems. Owing to resonant behaviour, it was found that, the results were extremely contingent on the train speed. Weber and Distl (F Weber & Distl, 2015) derived an approximate solution of collocated control by means of corrected optimal modal viscous damping for multimode cable vibration reduction using semi-active damper and negative stiffness according to the control force features of clipped LQR testing numerically and experimentally. Lobo et al. (Lobo et al., 2015) proposed a novel semi-active control device with ability of re-centring made up of a shape memory alloy (SMA) with bar form able to lock or unlock the support condition. The developed system overcame some restrictions addressed by other control systems, whereas, solely relying external force to vary the locked/unlocked state of the support, as harvesting was mobilized through motion of structure alongside with the motion of SMA piston head. Numerical analysis was carried out to evaluate the proposed damper to control a SDOF bridge as well as a similar SDOF model with an added fuse to assess its re-centring ability.

The electromagnetic dampers (EMD) are comparatively a fresh type of dampers that can generate electrical energy from kinetic energy over electromagnetic infusion. Recently, Shen and Zhu (Shen & Zhu, 2015) and Shen et al. (Shen et al., 2016) presented an innovative EMD cum-energy-harvester (EMDEH) comprised of an electromagnetic device attached to a circuit. The proposed damper was tested through a scaled cable-stayed bridge (see Figure 2.35), were it was simultaneously harvesting energy of cable vibration via the energy harvesting circuit (EHC) and was providing necessary damping to the cables.

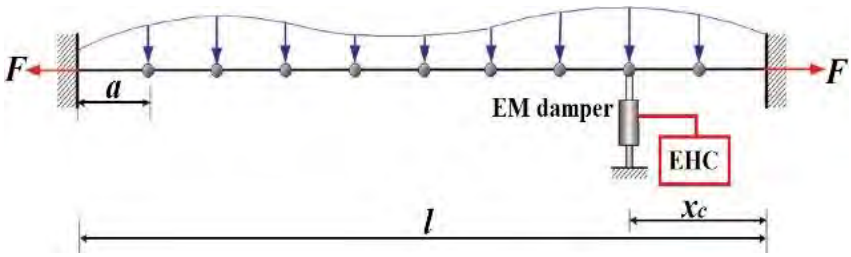

Figure 2.35: Discretized model of a cable-stayed bridge equipped with EMDEH (Shen et al., 2016)

2.2.4 Hybrid Vibration Control (HVC) Systems

A HVC system comprises of utilization of an active control to increase and perfect the PVC performance; requiring less control force. This is a good motivation to work on hybrid control area. In other words, An HVC system operates at the same time with the dangerous vibrations to enhance structural behavior for better safety and service. A HVC system is normally distinct as a combination of active, passive and semi-active dampers. This system can lessen the limitations of active and passive systems when they are implemented alone. Consequently, higher performance may be attained. Furthermore, the HVC system can give a more reliable result compared to a fully AVC system, even though it can be also often more intricate. Figure 2.36 indicate the HVC components.

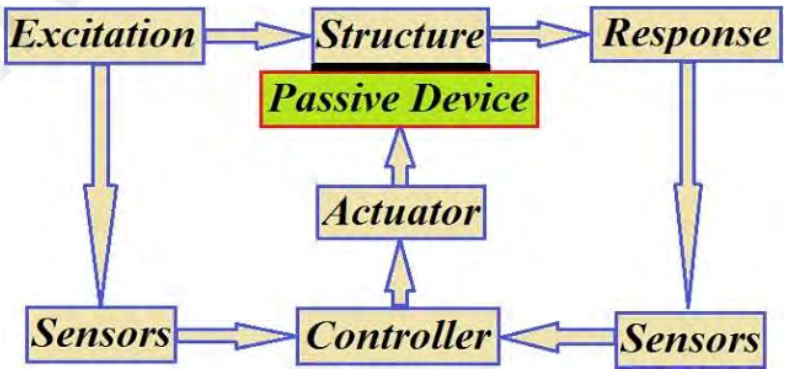

Figure 2.36: Structure of HVC system

2.2.4.1 HVC in buildings

Liquid column dampers (LCDs) have long been used for the seismic vibration control of flexible structures. Tuning Liquid column dampers (LCDs) for short-period structures is not convenient. Several alterations have long been presented on the primary LCD structure to improve its workability in comparatively stiff structures. Gur et al. (Gur et al., 2014) showed that, the efficiency of the LCD can be enhanced by the substitution of a linear spring with a SMA material, called SMA-LCD, for control of short-period structural vibration. The SMA–LCD structure was consisted of the LCD connected to the main structure through the SMA spring, as demonstrated in Figure 2.37. k_s, c_s and m_s are the stiffness, damping and mass of the SDOF structure, and x_l, x_c and x_g are the vertical displacement of the liquid column, liquid container displacement with respect to the SDOF system and the structure displacement relative to the ground, respectively. It was proven that, the system had better control effectiveness compared to the typical LCD and generally understood that the improved behavior of the proposed hybrid system over the compliant liquid column dampers can be reliable to control broadband dynamic-induced vibrations in almost short-period building structures.

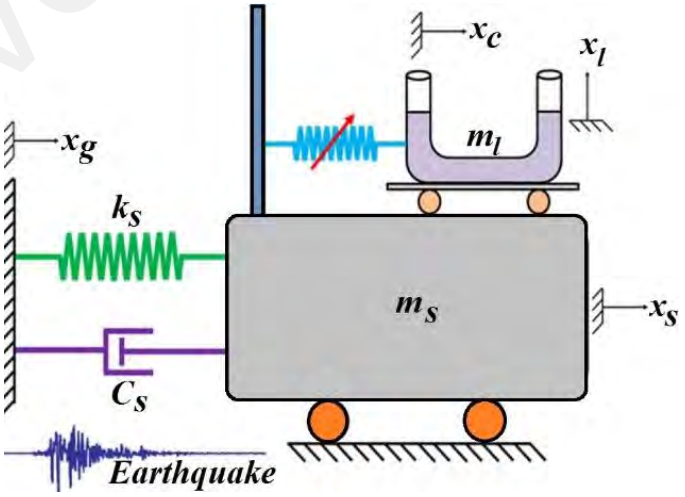

Figure 2.37: SMA–LCD in SDOF system (Gur et al., 2014)

Høgsberg and Brodersen (Brodersen et al., 2016) presented a hybrid viscous damper comprised of a passive dashpot sited in series with a load cell and an active actuator. A filtered integral force feedback approach was used to control the actuator motion, wherein the filter was the key feature, which was designed to decrease damper force. It was shown that in the proposed approach, the control was stable where the force controlled velocity. Thus, a significant energy amount was dissipated through the hybrid dashpot in comparison to a pure viscous damper. Jalaeefar and Asgarian (Jalaeefar & Asgarian, 2014) presented a novel hybrid SMA-based damper, which combined strain recovering systems and energy dissipation. It was recommended to install the device in semi-rigid braced frames. Barmo et al. (Barmo et al., 2015) examined a hybrid system consisting of flat sliding bearings (FSB), lead rubber bearings (LRB) with combination of rotational friction damper (RFD) at the base of a 8-, 12-, 16- and 20-story building to investigate the response of the buildings subjected to ground motions. The results showed that, using such hybrid system can significantly mitigate the base shear and displacement when the height of the buildings is increased. The system had bad effect on drift response when the height (flexibility) was increased. Demetriou and Nikitas (Demetriou & Nikitas, 2016) presented a novel hybrid semi-active mass damper (SA-HMD) for dynamic structural applications as a substitute design for the traditional hybrid ATMD (HATMD). Enabling synthesis of the instant effective system by the consecutive and proper action of semi-active and active elements was the basic innovation of this configuration. To this end, the active elements of the SA-HMD were regulated through an optimal LQR controller, whereas the semi-active elements were controlled by a direct output feedback algorithm, known as displacement based ground-hook (DBG) control algorithm. Moreover, for the coupling of the dampers and the design of the control actions, a mathematical procedure was proposed and the performance of the controllers was assessed on both SDOF and MDOF (76-story) structures of (Yang et al., 2004), as shown in Figure 2.38. Collette and

Chesné (2016) presented a novel vibration control law for a hybrid absorber, called α-HMD, which was guaranteed the closed loop system stability. The α-HMD was compared to a purely AMD and a TMD through 3-DOF model. Eventually, design guidelines were proposed to adjust the control parameter effectively.

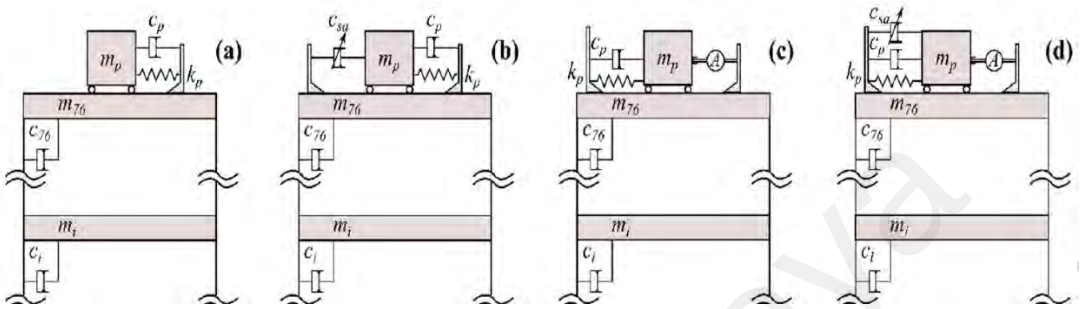

Figure 2.38: Configuration of different control systems (a) TMD, (b) semi-active TMD (SA-TMD), (c) ATMD, (d) SA-HMD for the 76-storey building (Yang et al., 2004)

Kasagi et al. (Kasagi et al., 2016) proposed a new hybrid system where a base-isolated (BI) building was connected to a stiff free wall via oil dampers and to control such a smart hybrid structure, a GA was presented. To show more properties of the system for a wider variety of frequency, a 40-story base isolated building was connected to a 26-story stiff free wall by oil dampers as illustrated in Figure 2.39 was evaluated. However, a similar study was earlier presented by Murase et al. (Murase et al., 2013) to show the effectiveness of the system against long-duration and pulse type dynamic excitations.

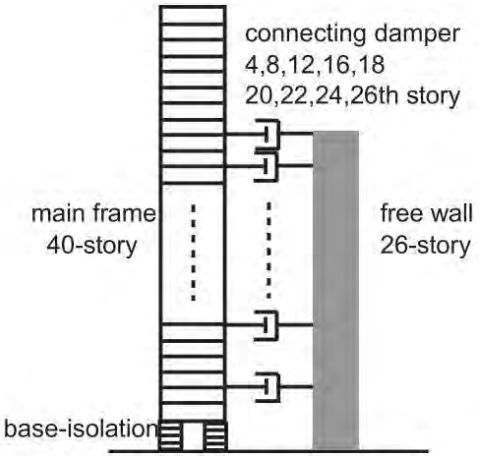

Figure 2.39: Hybrid system of a 40-story base isolated building linked with a 26-story free wall through oil dampers (Kasagi et al., 2016)

Lee et al. (Lee et al., 2016) combined steel strip device with a friction device to propose a new hybrid vibration control in order to improve the performance of structures subjected to multiple level of seismic excitations. Richiedei and Trevisani (Richiedei & Trevisani, 2017) introduced an innovative hybrid technique for assignment of eigenstructure using the concurrent synthesis of active control and passive modifications. The passive modifications changed the eigenvectors through state derivative feedback control. This provided additional DOF in the synthesis of controller. Therefore, overcoming the eigenstructure assignment limitations utilized active control solely. Accordingly, the approach can broadly be applied to vibrating systems including structures.

2.2.4.2 HVC in bridges

Cu and Han (Cu & Han, 2015) proposed an innovative damper type combining TMD with viscous damper in order to increase damping ratio and reduce unfavourable vibration of taut cables of cable-stayed bridges and stadiums. Most recently, a somehow similar idea, i.e., proposing a novel hybrid damper combining TMD with high damping rubber, named TM-HDR damper for the same aims was introduced by Cu et al. (Cu et al., 2017). However, oscillation characteristics of cables with connected dampers were studied

through an analytical solution of the complex eigenvalue problem; experimental investigations are compulsory to support the presented studies. Maddaloni et al. (Maddaloni et al., 2016) proposed a technique of smart passive vibration control for bridges in different seismic zones using variable MR fluid dampers and based on exploitation of a SEWS. As a result, a particular design procedure was presented utilizing regional control algorithms, which was based on the control logic optimized for specific zones specified by homogeneous seismicity.

2.2.5 Base Isolation (BI) Systems

BIs or seismic isolations are a recognized and advantageous method to protect civil structures (Alhamaydeh et al., 2013). The main principle in using BIs is to build a structure with the first mode of vibration beyond an extensive earthquake energy region, which usually causes large movements at the base level that should be lessened (Javanmardi et al., 2017, 2018). For this purpose, researchers have recently presented some sorts of isolations in order to decrease the base displacement and natural frequency of the structures. For instance, Pham and Ahn (Pham & Ahn, 2015) presented a new isolation system, called horizontal active vibration isolator (HAVI), using forces of an EM planar actuator (EPA) in both vertical and horizontal directions. The vertical force was utilized to adjust natural frequency, whereas the horizontal force was applied to banish horizontal disturbance of the isolator. A model of the HAVI was simulated using flexible beam column (FBC), as shown in Figure 2.40, and the efficiency of the proposed isolator was tested through an experimental study.

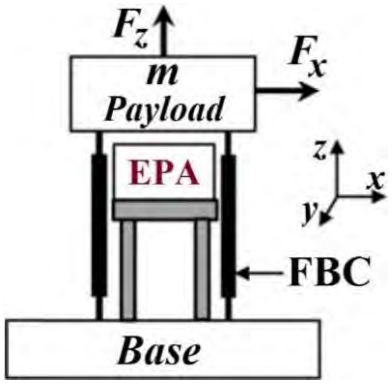

Figure 2.40: HAVI scheme (Pham & Ahn, 2015)

Liu et al. (Liu et al., 2015) introduced an innovative hybrid isolator using an X-shape supporting structure. The hybrid isolator combined the advantageous aspects of both the scissor-like structure (SLS) and lever-type structures, called SLS lever-type isolator, to get perfect ultra-low frequency isolation. In order to enhance the vibration isolation performance in semi-active or passive controls, damping characteristic and essential nonlinear stiffness were detected. Huang et al. (Huang et al., 2014) introduced a new structured ultralow-frequency passive isolator made of a mechanical spring, a knife-edge supports and a sliding beam as shown in Figure 2.41. The analytical analysis was done and confirmed that the isolator was capable to give quasi-zero non-linear stiffness. It was demonstrated that the hybrid isolator could attain remarkable ultra-low frequency vibration isolation and prominently, the system could recognize a uniformly low broadband vibration transmissibility that had never been addressed before. Chen et al. (Chen et al., 2016) presented a biologically inspired (bio-inspired) passive isolation system. The isolator integrated the sacrificial bonds and hidden length idea, given by (Hansma et al., 2005) with a prevalent linear isolator. The effectiveness of the isolation system in decreasing response of seismically isolated structures was demonstrated through several parametric studies when a series of robust earthquake excitations were

applied to the bio-inspired isolators. Figure 2.42 shows the simplified mechanism of the proposed isolation system.

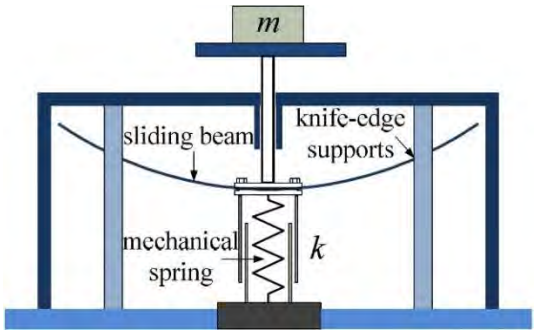

Figure 2.41: Proposed base isolator by (Huang et al., 2014)

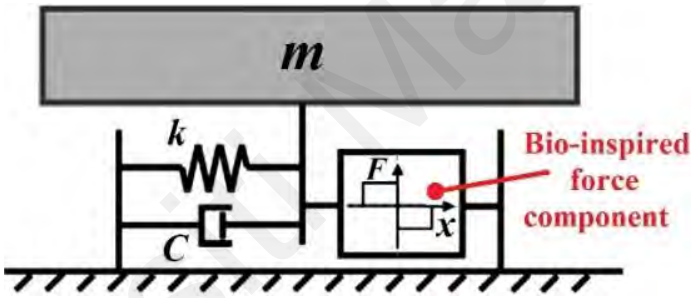

Figure 2.42: The concept of bio-inspired isolator (Chen et al., 2016)

Wu et al. (Wu et al., 2014) proposed the vibration isolator utilizing an innovative magnetic spring (MS) with NS, called MS-NS, in which the isolator integrated the MS-NS with a positive stiffness (PS) spring in parallel where the PS spring comprised of two flexible hinges and a coil spring and the MS-NS was consisted of three cubical magnets arranged in repulsive contact as presented in Figure 2.43. The vibration transitivity of the device was calculated via the equation of motion and measured by an appropriate data acquisition system and finally, the experimental and analytical results illustrated that

combining the MS-NS with a vibration isolator in parallel can extenuate the isolator natural frequency.

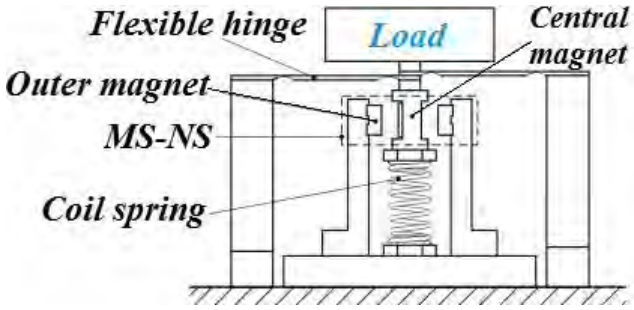

Figure 2.43: Configuration of the proposed vibration isolator (Wu et al., 2014)

Markou and Manolis (Markou & Manolis, 2016) used a fractional derivative zener (FDZ) model linked in parallel to Coulomb friction slider and a linear viscous damper to analyse the mechanical performance of a base isolated building subjected to free vibration. Furthermore, the rheological models and formulations for the BI systems including high damping rubber bearing (HDRB) and low friction sliding bearing (LFSB) are investigated. Consequently, the rheological formulation was presented for the tri-linear model for the first time. The comparison study illustrated that, the FDZ model was able to describe the response of BI systems under complex nonlinear loadings. Calvi et al. (Calvi et al., 2016) introduced two novel variable friction bearings, known as "BowC" (BC) and "BowTie" (BT) as depicted in Figure 2.44. The study concentrated on presenting the concept, basic principles of operation, and formulation of the hysteresis models of the proposed isolation systems by conducting nonlinear time history analyses through direct displacement based design approach.

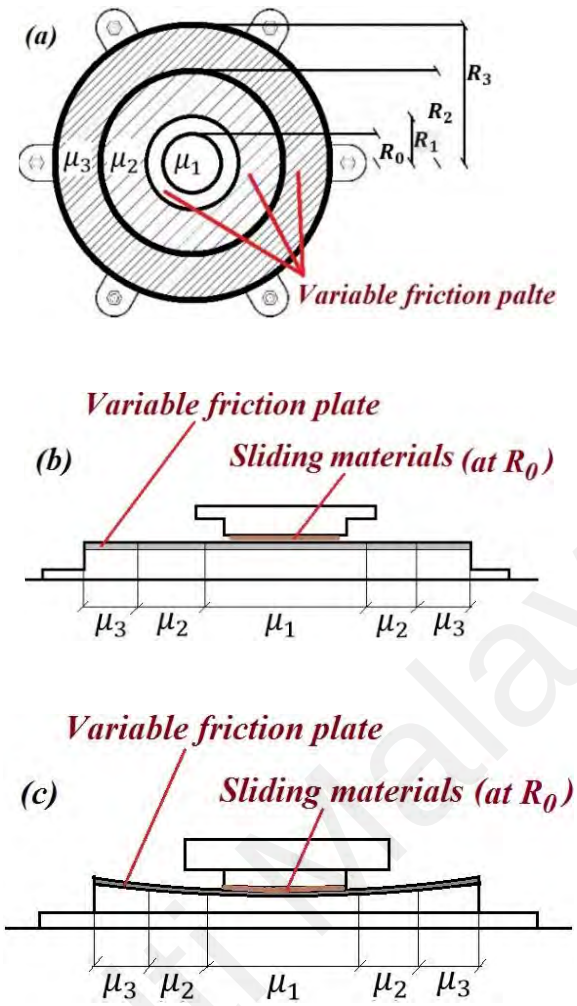

Figure 2.44: Variable frictional device from a) top view and in the form of b) BT and c) BC device in side view (Calvi et al., 2016)

Chen and Liang (Chen & Liang, 2017) proposed an AVC method to boost the performance of a pneumatic isolation systems in low-frequency range. The method applied adaptive wavelet neural network (AWNN) algorithm to capture the time varying and characteristics of nonlinear system as well as to nullify the response payload such that suppression of vibration could be fulfilled. To evaluate the method, a composite control structure scheme, as feedback signals by means of velocity and pressure measurements was conducted and performances of the isolation system, gained from the applied AWNN controller, were assessed with the PID-active technique and a passive

isolator. The results showed that the proposed active AWNN method could effectively tranquilize the vibration disturbance.

In the common laminated steel/rubber isolation bearings, a high vertical stiffness is created by the steel shims, whereas the rubber sheets secure horizontal flexibility. However, this form of BIs is nearly big, weighty and costly. To overcome the problem, Tan et al. (Tan et al., 2014) proposed a new cost-effective and light isolator for low-rise building structures, made of plastic shims and unsaturated fibre reinforced polyester (FRP) between rubber layers. The proposed isolator under both tensile and bending conditions was tested and it was demonstrated that the isolator has great feasibility to replace FRPs in conventional isolators.

2.3 Effectiveness of Damper Installation

Same dampers can have different effects on structural response under vibrations if they are placed differently. A comparison was made theoretically between the different placements of a viscous fluid damper in a single-story steel frame (see Figure 2.45).

Assuming the inter-story drift is denoted by, the relative displacement developed in the damper can be obtained from:

$$u_D = f \times u \tag{2.2}$$

where f is the amplification factor.

The horizontal component of the damper force exerted on the frame is F, where

$$F = f \times F_D \tag{2.3}$$

where F_D is the damper force, which can be obtained from:

$$F_D = C \times \dot{u}_D \tag{2.4}$$

where C is the damping constant of the viscous damper. Then,

$$F_D = C \times f^2 \times \dot{u} \tag{2.5}$$

Hence, the damping ratio can be obtained from:

$$\beta = \frac{Cf^2 gT}{4\pi W} \tag{2.5}$$

where W is the weight of the structure.

Figure 2.45 shows the different amplification factors and damping ratio of the structure with different damper placements (Sigaher & Constantinou, 2003). The calculations were based on assuming 5 % critical damping in the case of horizontal damper (Chevron brace) and the damping ratios of the other systems were calculated relative to this value.

Although toggle-brace configuration has the largest damping ratio, its efficiency may be dropped because of the phase difference between the deformational velocity in the device and the story velocity, to which the device is connected. Accordingly, the damping forces are not 90° out of phase with the structural forces. This leads to developing large axial forces in linkages, which develops high forces in the structure itself. According to this comparison, the placement of the damper in the scissor-jack leads to a significant increase in the damping ratio compared to the conventional configurations (horizontal or diagonal) due to the amplification of the story drift.

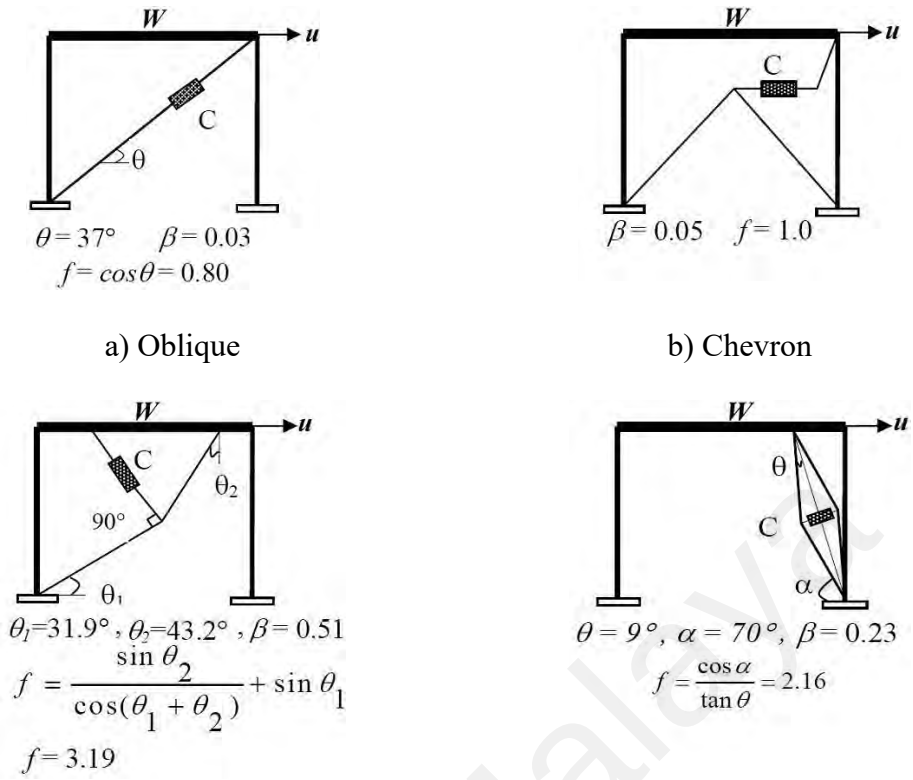

Figure 2.45: Different placements of a damper and its effectiveness (Sigaher & Constantinou, 2003)

2.4 Summary and Conclusions

In the present literature, the most recent structural vibration control systems have widely been reviewed, primarily since 2013, emphasizing on passive control systems. It is observed from the reviewed literature that, significant research has been conducted on the design, development, and verification of novel earthquake-resistant systems for improving seismic performance of building and bridge structures. Although developments in the structural vibration control area are progressed due to advances in new materials, sensors, and computing and information technologies, they have had substantial limitations yet. For instance, active and semi-active control systems have received attention, but they are expensive when the design of these devices required to consider many aspects resulting several difficulties such as power source and space

limitations, time delay effect, measurements of structure responses, compatibility of control algorithms with the systems, strength, etc. Hybrid designs are advanced, but using different techniques in terms of combining characteristics of damping materials and structural systems. Passive control systems are well-accepted and have attracted attention of many researchers, but they have still some restrictions mainly in practical engineering applications such as fabrication, installation, cost and system control. It was also notably observed from the literature that, most of the introduced vibration control systems function in one direction, thus, it is required to install many damper devices in a structure to be protected in both directions, which is not affordable in many cases. Based on the above review, a simple and cost effective passive damper device with bidirectional capability of energy dissipation will be introduced in the next chapter.

CHAPTER 3: DESIGN AND DEVELOPMENT OF BAR DAMPER UNDER EXPERIMENTAL TESTS

3.1 Introduction

Metallic dampers, as a type of passive dampers, were originally manufactured by Bechtel Corporation. Added Damping and Stiffness (ADAS) damper is an evolution of earlier X-plate used as a damping source for piping systems (Stiemer, 1981). The researches in metallic passive energy dissipation devices have been conducted over the last three decades. Triangle Added Damping and Stiffness (TADAS) together with ADAS dampers are the most commonly used metallic dampers in seismic design. Steel plate ADAS dampers have been investigated by many researchers for their capacity in absorbing energy. The aim of using metallic damper devices is to take advantage of the hysteresis of metals to dissipate input seismic energy. Popular metallic dampers include hourglass shape ADAS device, TADAS, Honeycomb damper and buckling restrained brace. These devices are mainly designed to be incorporated into the bracing system of structural frames. Other devices were developed for installation between beams and columns in a frame structure (Koetaka et al., 2005). On the other hand, some researchers have made use of alternative materials in device fabrication, such as lead, low-yield steel, copper and shape memory alloys to improve the dampers performance (Briones & Llera, 2014; Chan & Albermani, 2008; Llera et. al., 2004; He et. al., 2016; Qian et. al., 2013). Figure 3.1 shows a few metallic passive devices proposed and developed by researchers.

(a) U-shaped damper (Dolce et al., 1996)

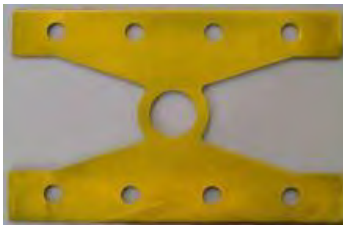

(b) Round-hole damper (Li & Li, 2007)

(c) Slit damper (Kim & Jeong, 2016)

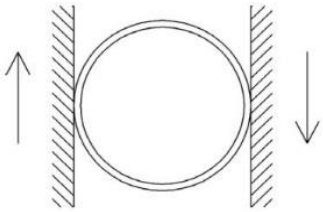

(d) Pipe damper (Maleki & Bagheri, 2010)

(e) Perforated shear panels (Matteis et al., 2016)

(f) Comb-teeth damper (Garivani et al., 2016)

Figure 3.1: Examples of proposed metallic devices

This chapter proposes and describes a metallic bar damper device, known as BD, to be incorporated into building and bridge structures. The BD is a newly proposed device to take advantage of the hysteresis behavior of metals to dissipate seismic input energy with bidirectional function and capability of installation in several locations of a structure to prevent inelastic behavior in the primary gravity and lateral load resisting elements. This device was invented based on the excessive energy-absorbing capabilities to reduce the seismic response of civil structures subjected to earthquakes. To evaluate the damper device, different parametric studies were experimentally conducted on the device subjected to cyclic displacement loading to determine the design parameters and to monitor the behavior of the device in order to enhance its performance. The device was analyzed under quasi-static cyclic loading.

3.2 Device Description

The device is made of a number of solid bars or rods that were sandwiched between two steel plates, the top and bottom plates. The top and the bottom plates can be welded or bolted to the surrounding plates for connecting the device to the structure. A schematic diagram of the device is shown in Figure 3.2. Depending upon the design of the plates, a certain number of bolt holes can be drilled on the plates to attach the bar damper to the target structural member. Energy dissipation by the device is achieved mainly through inelastic cyclic flexural deformation of the bars. In this chapter, the height, diameter and number of the bars were a design variable that can be optimized for desired performance level. Nevertheless, in order to improve the performance of the proposed damper device, several parameters may be operated. These parameters, which are shown in Figure 3.3, are as follows:

- Length of the device (L_d)
- width of the device (b)
- Height of the bars (h)
- Space of the bars (Sh and Sv)
- Diameter of the bars (d)
- Number of the bars (N)
- Row number of the bars (n)
- Arrangement of the bars
- Shape of the bars (solid, hollow tube)
- Materials of the bars (mild steel, high strength steel, composite materials, e.g. hollow tube steel filled by zinc or lead materials)
- Bonding of the bars to the plates (welded and bolted)

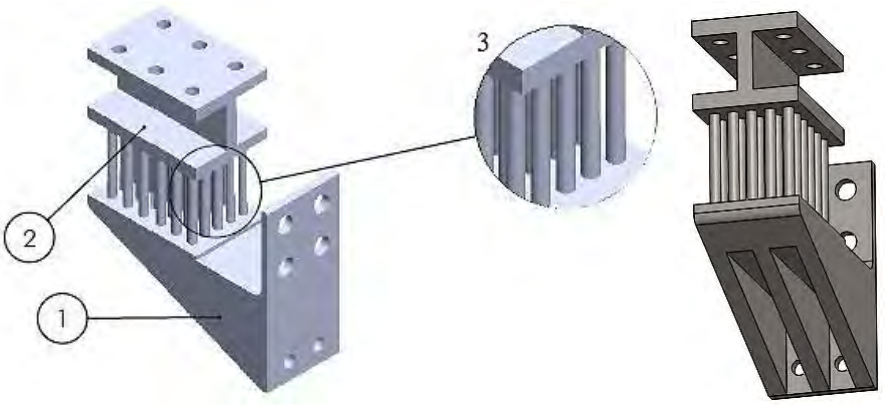

Figure 3.2: Overall view of the BD device with 1) bottom plate 2) top plate 3) solid bars (Patent application No.: PI 2016702928)

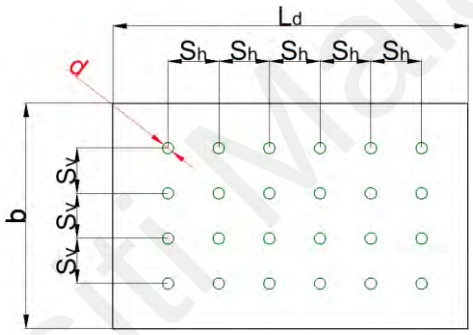

(a) Top view

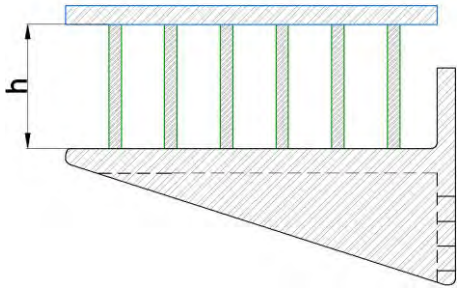

(b) Side view

Figure 3.3: BD parameters

3.3 BD Installation

Although the device was primarily meant to be installed at beam-column joints (see Figure 3.4(a)), but the BD can be installed in any location in buildings and bridges. Some examples of potential installation techniques of BD in buildings are shown in Figure 3.4. For instance, it may be placed on the top flange of a beam to achieve a semi-rigid connection that dissipates energy (Figure 3.4(b)). It may also be mounted on a skewed brace (Figure 3.4(c)), or used as a V or an inverted-V brace system (Figure 3.4(d and e)). Some other configurations are shown in Figure 3.4(f and g)). Figure 3.4(h) also shows the configuration of the BD device in a multi-story building. In structural applications, a dissipative device is placed in both horizontal directions for protection against bidirectional ground motions. The proposed damper can function in both directions and has isotropic energy dissipation; a direction-independent damper.

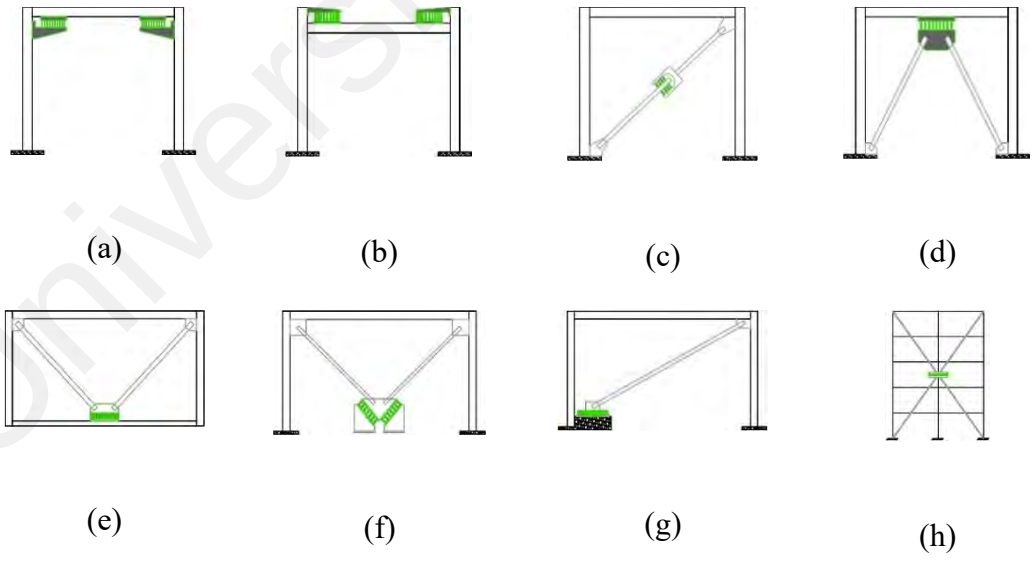

Figure 3.4: Examples of potential application of BD

3.4 Experimental Setup

The objective of the experiments is to verify the structural characteristics as well as the cyclic performance of the proposed device. Attempts were made to identify the key geometric parameters for the largest energy dissipation such as varing stiffness. The device was designed where axial force in the device is less significant; hence no axial force was applied to the specimens in the experiments. To this end, quasi-static load method was used to apply lateral (shear) force to the damper device. Thus, the load was applied in a cyclic procedure using displacement control. The test setup was designed such that the BD device specimens moved down and up after each half cycle of loading and unloading.

3.4.1 Fabrication of Specimens

Overall, twelve specimens similar to Figure 3.5 (middle part) were fabricated at the University of Malaya. To facilitate the of fabrication process, the solid bars as well as plate specimens were cut from the available steel materials; A570 steel grade. Consequently, calculated thicknesses, t, were used for the plates based on the applying load and material properties. In order to adjust the specimens for applying cyclic loading, two different other segments namely, the top segment (loading plate) and the bottom segment (support plate) were designed to be installed to the middle part (the damper) as demonstrated in Figure 3.6. Twenty 15 mm diameter holes were drilled on both the loading and support plates where they were supposed to retain the BD device (Middle part) during experimental tests. Therefore, similar holes were drilled on the BD plates as well. All the segments were welded to each other using full 3 mm rounding weld.

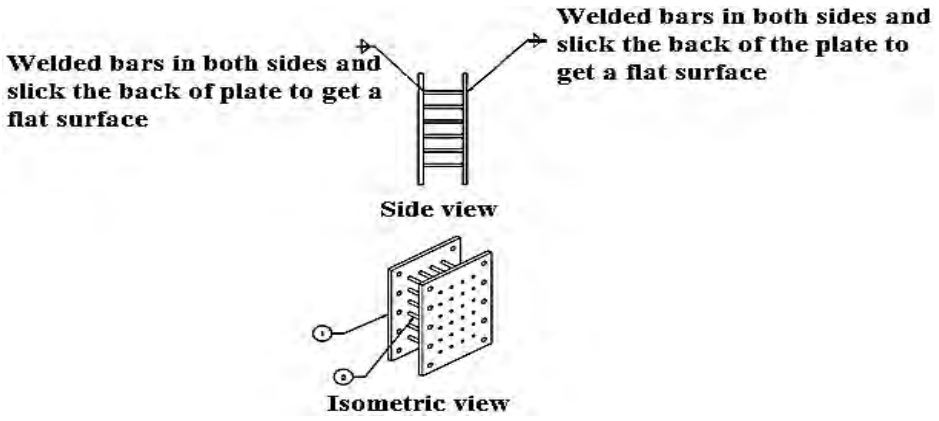

Figure 3.5: Prepared test specimen (middle part) with 24 solid bars

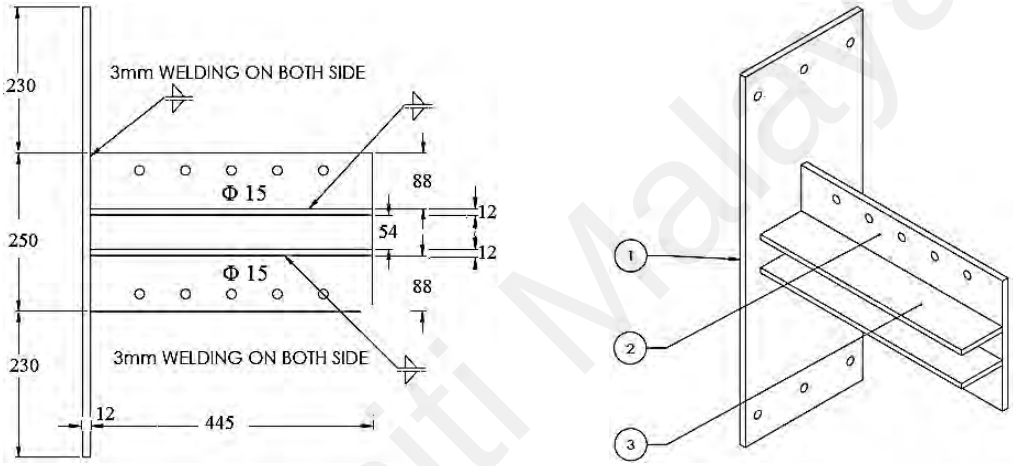

(a) Top segment

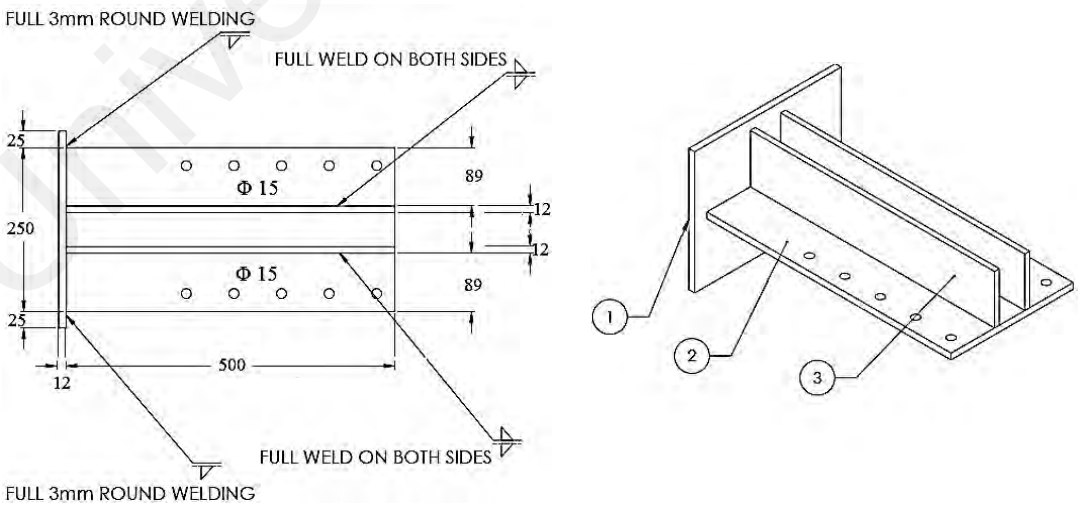

(b) Bottom segment

Figure 3.6: Details of the top and bottom segments in order to place the middle parts (BD specimens) for the test (units: mm)

3.4.2 Test Specimens

Twelve test specimens with different heihgts of 70mm, 100mm, 130mm, 160mm, and different diameters of 8 mm, 10 mm, 12 mm, 14 mm, and different bars numbers of 20, 24, 28, 32 were fabricated at the University of Malaya. These designs were aimed to investigate the capacity changes of the BD device as a function of the aspect ratios h/d (height/diameter) and h/N (height/number of bars) under cyclic loading. The h/d raio was used for variation of bars height and diameter (called BD-HX and BD-DX specimen, in which X stands for specimen index) and h/N ratio was utilized for variation of the bars number (called BD-NY specimen, in which Y stands for number of solid bars)) as indicated in Table 3.1. This table presents the details of the test specimens considering the mentioned variations, i.e., bars height, bars diameter and bars numbers. The W is the total weight of the BD. The gray color shown in the table represents the benchmark specimen (common specimen) in each considered scenario (i.e., BD-H100 = BD-D10 = BD-N24). The detailed drawings of the specimens are illustrated in Figures 3.7, 3.8 and 3.9.

Table 3.1: Details of the test specimens

Specimen	d (mm)	h (mm)	N (No.)	h/d	h/N	W (kg)
BD-H70	10	70	24	7		17.29
BD-H100	10	100	24	10		17.61
BD-H130	10	130	24	13		18.17
BD-H160	10	160	24	16		18.62
BD-D8	8	100	24	12.5		17.20
BD-D10 = BD-H100	10	100	24	10		17.61
BD-D12	12	100	24	8.33		18.38
BD-D14	14	100	24	7.14		19.15
BD-N20	10	100	20	-	5	17.48
BD-N24 = BD-H100	10	100	24	-	4.17	17.61
BD-N28	10	100	28	-	3.57	17.73
BD-N32	10	100	32	-	3.12	18.10

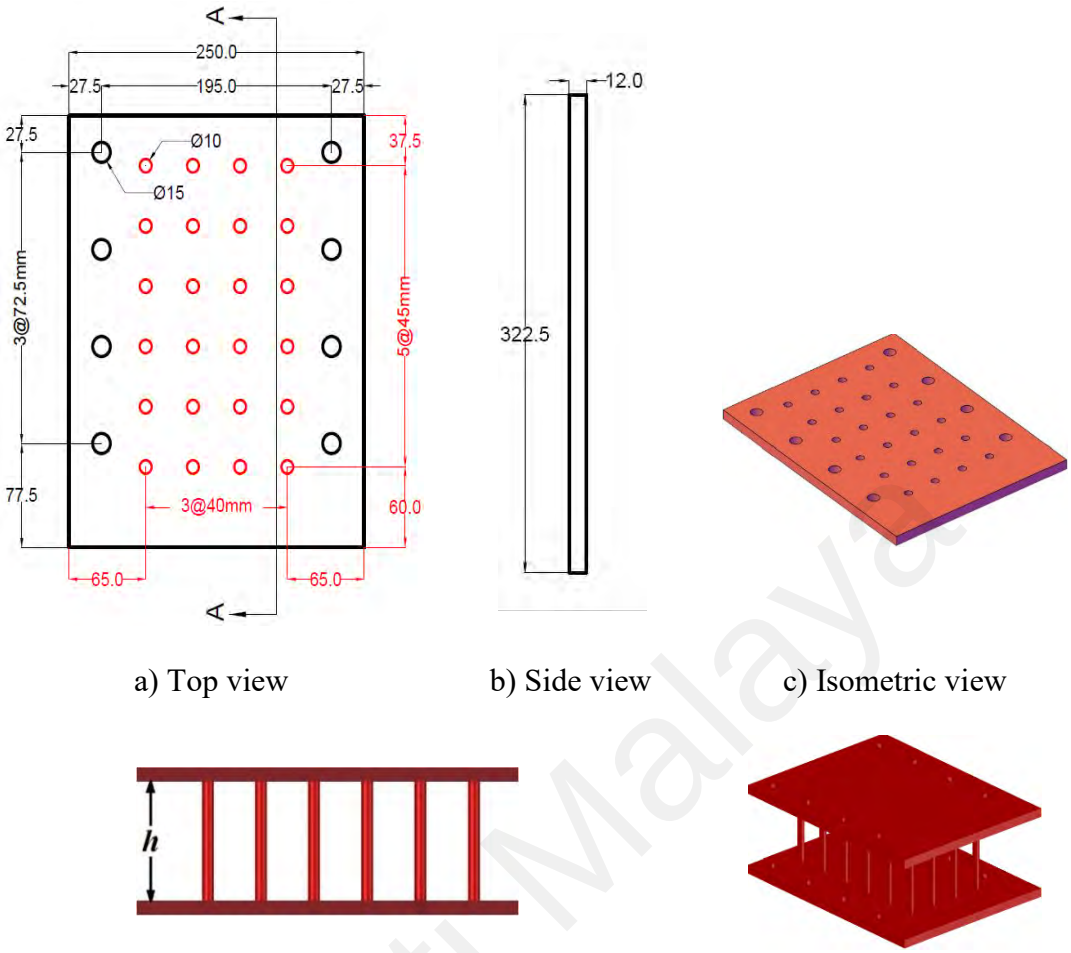

a) Top view b) Side view c) Isometric view

d) Section A-A (h= 70, 100, 130, 160mm) e) Bar Damper

Figure 3.7: : Device used in the experiments considering height effect (units: mm)

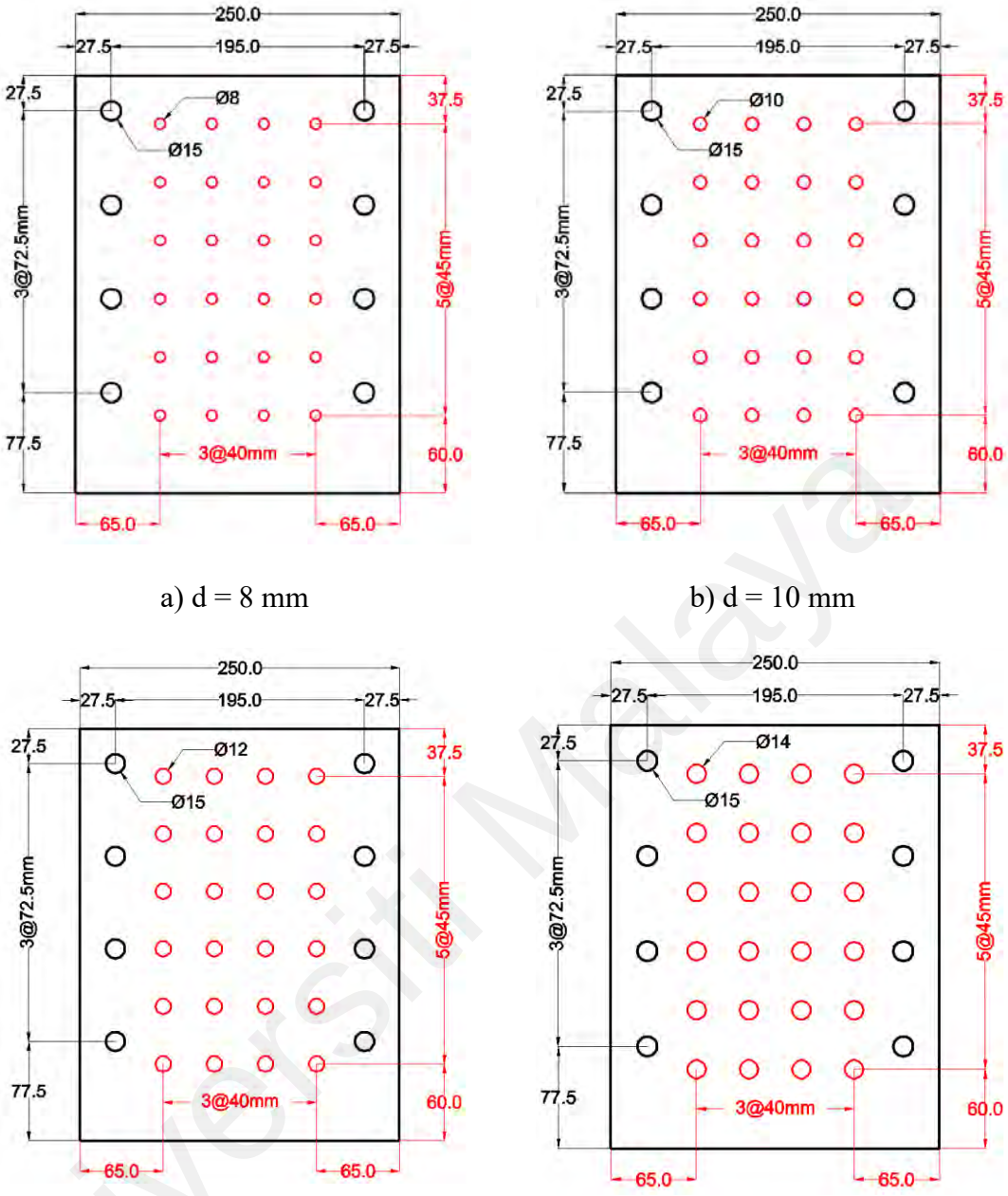

a) d = 8 mm

b) d = 10 mm

c) d = 12 mm

d) d = 14 mm

Figure 3.8: Device specimens considering bars diameters (units: mm)

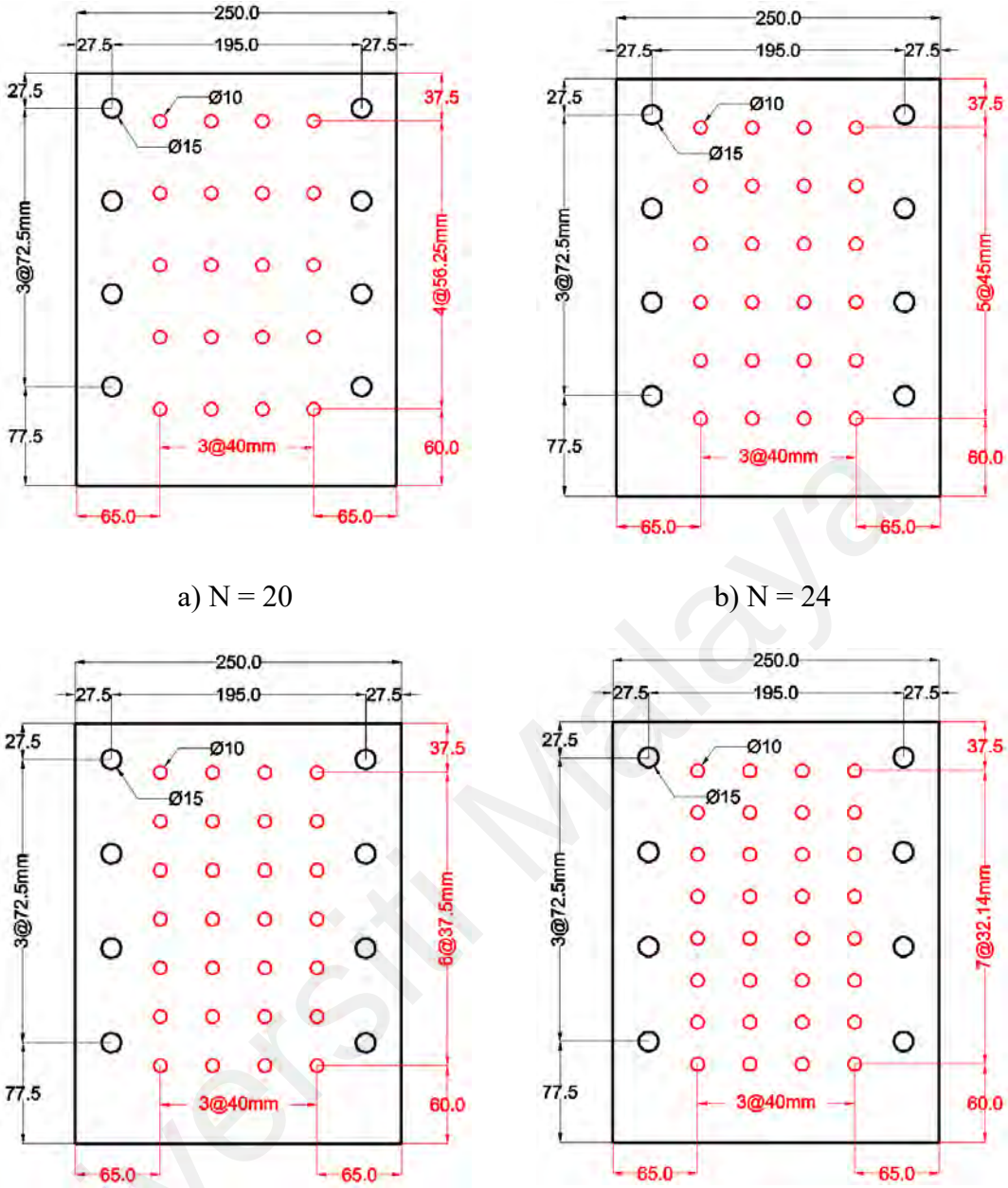

a) N = 20 b) N = 24

c) N = 28 d) N = 32

Figure 3.9: : BD specimens considering different bar numbers (units: mm)

3.4.3 Material Properties

To find material properties with an acceptable approximation, tensile testing in acordance with ASTME8M-00 standard (ASTM E8M-00, 2002) was conducted on steel coupons. The steel used was cut from the available steel materials; ASTM A570 grade 50 (with nominal yield of 345 MPa). Since the solid bars play the main role in the damper device behavior, the coupon samples were chosen from the solid bars. Bars with 10 mm

diameter and overall length of 700 mm were machined to conduct the tests. The yield stress, ultimate stress, Young's modulus and elongation of the steel samples obtained from the tests and reported in Table 3.2. The stress-strain relationship curves obtained through the coupon tests are presented in Figure 3.10. The average yield stress, ultimate strength, and elongation ratio of the steel bars used in the study were determined as 341.174 MPa, 532.35 MPa and 23.8%, respectively.

Table 3.2: Result of tensile test

Sample	Steel grade	σ_y (MPa)	σ_u (MPa)	E_s (MPa)	Elongation (%)
1	A570	342.078	539.248	2.01×10^5	23.33
2	A570	340.271	525.452	2.01×10^5	24.27
Average	A570	341.174	532.35	2.01×10^5	23.80

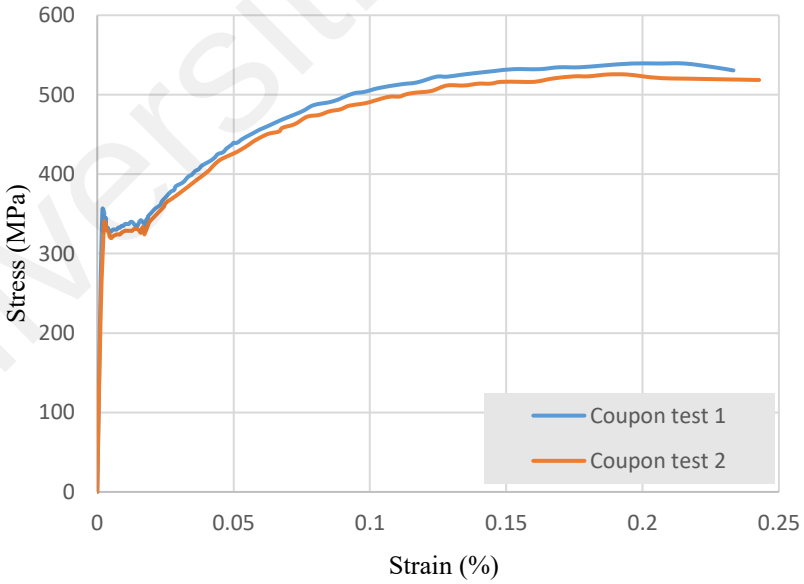

Figure 3.10: Coupon tests of the steel bars used in the present study

3.4.4 Loading Protocol

In order to adjust the specimens for testing, two different segments, namely the top segment (loading plate) and the bottom segment (support plate) were designed to be attached to the BD specimens (see Figure 3.11). Eight 15 mm diameter holes were drilled on both the loading and support segments at the same position as BD middle plate holes for attaching purpose. A progressively increased upturned cyclic displacement accordance with FEMA-461 (FEMA, 2007) was applied to the test specimens (middle parts). As described earlier, the loading was applied at the top of loading segment (loading plate) as depicted in Figure 3.11 and Figure 3.12. The displacement history was designed in quasi-static cyclic procedure such that the amplitude of cyclic displacement was increased from 2 mm to 50 mm. This increase was achieved in 13 steps with displacement amplitudes of 2, 2.5, 3.5, 5, 7.5, 10, 14, 17.5, 22.5, 27.5, 35, 42.5 and 50 mm as indicated in Figure 3.13. Such increasing magnitude was designed to observe a substantial decrease in the stiffness/strength of the specimens as well as destabilize the specimens under the impose displacement conditions. Loading with each of these amplitudes was repeated for 3 cycles in each step. The frequency of the universal test machine (UTM) can be obtained from the following equation:

$$f = 1/\left[\left(4d/v\right)\times 60\right] \tag{3.1}$$

In which d is the displacement (mm) and v is the speed rate (mm/min) of the UTM.

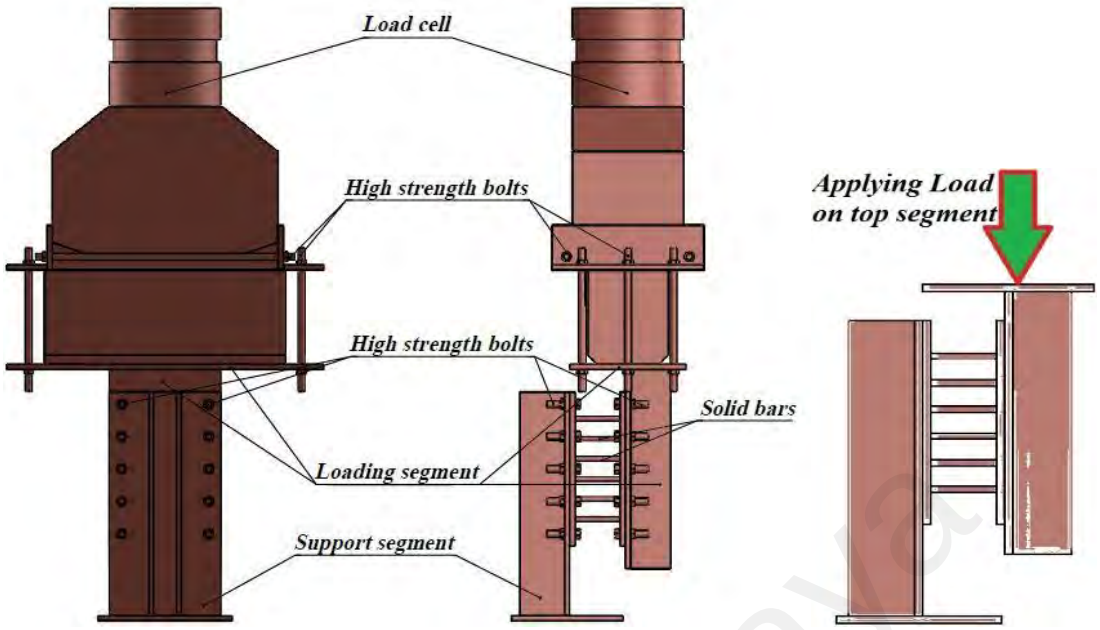

Figure 3.11: BD test setup

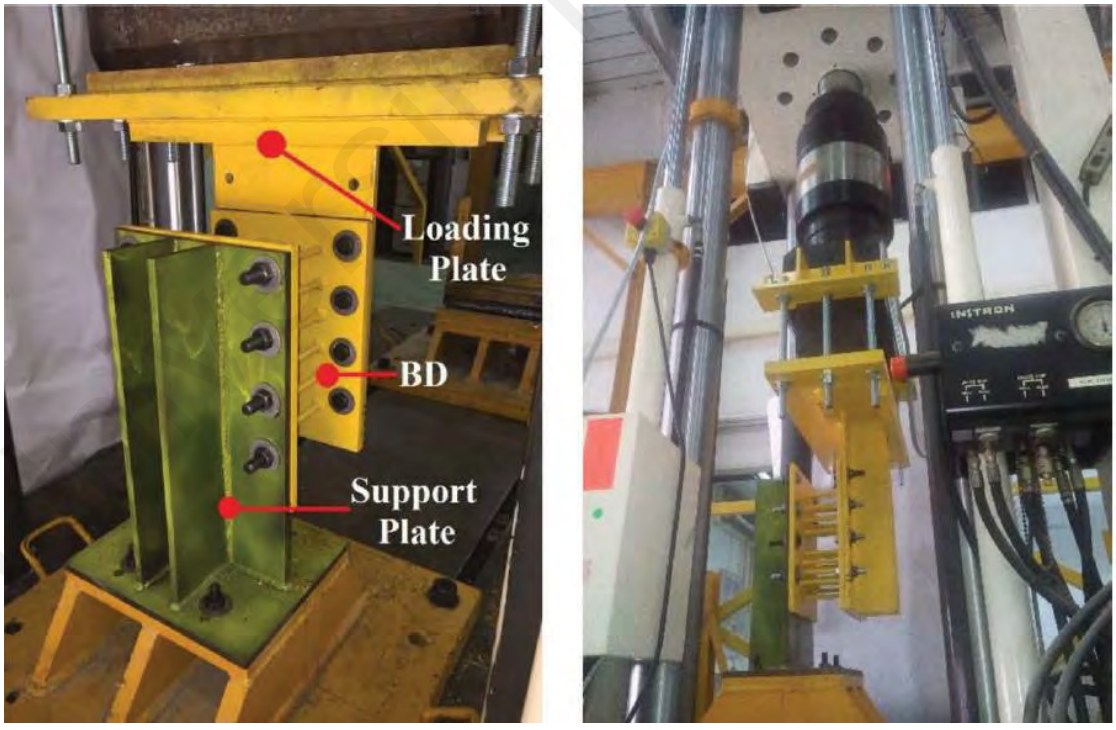

Figure 3.12: Prepared test setup in University of Malaya

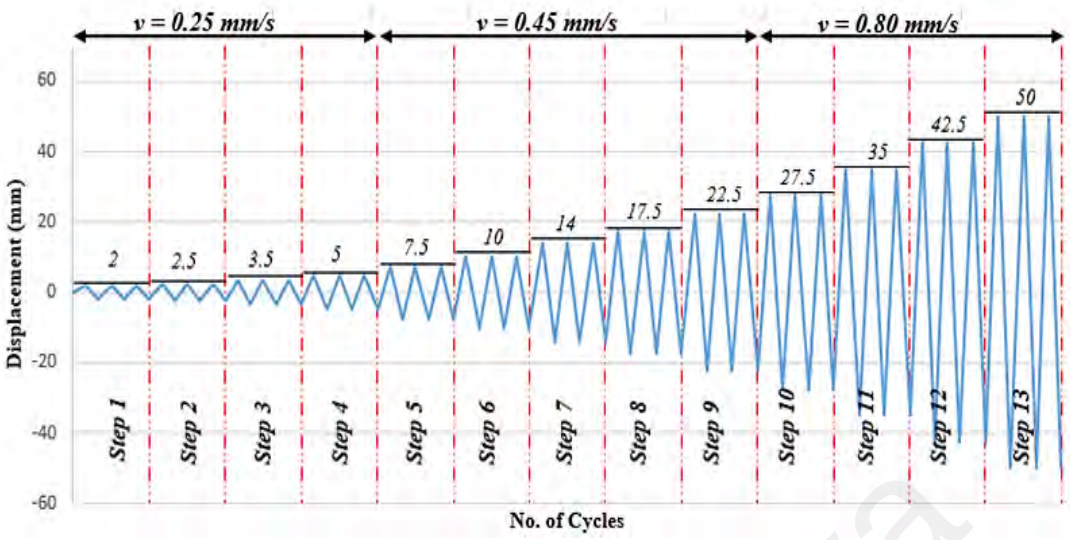

Figure 3.13: Loading procedure of cyclic displacement

3.4.5 Low-cyclic Fatigue (LCF) Life

In LCF, strain control is run by load applied as a dependent variable. In Low-frequency plastic strains, high amplitude is characterized by LCF. LCF is predominantly valuable in those areas that rely on materials in cyclic circumstances including power generation, automotive, architecture, oil and gas, and aerospace sectors. Also, it is fine to use LCF for materials with temperature-varying. The strain variables in the LCF test are commonly defined as:

- Wave Form (trapezoidal/sinusoidal/triangle)
- Frequency (Hz, strain% per second)
- Strain range (%) or Maximum Target Strain (MTS)
- A-Ratio (amplitude/mean)
- Switch point (strain is changed to load control for specimen; increasing frequency)
- Discontinue test (defined counted cycle once test is stopped)

It is noted that, the LCF testing consists of three stages as follows:

a. Crack initiation of intact specimen.
b. Spread life; happens after initiation.
c. Failure; normally specified by dropping load percentage from a constant condition.

In this study, the experimental test was performed using LCF test to determine the maximum load capacity of the specimens. For this purpose, triangular wave shape, as shown in Figure 3.13, was utilized by implementing varying frequency from 0.004 Hz to 0.03125 Hz for different steps (1 to 13).

3.5 Parametric Experimental Study

The performance of the proposed device can be controlled by several parameters. Taking an appropriate choice of each parameter can improve the effectiveness of the BD device. In spite of this fact, herein, three parameters were selected as indicated in Table 3.1 which are:

- Height of the device (solid bars)
- Diameter of the solid bars
- Number of the solid bars

Consequently, by considering the above parameters the related aspect ratios, i.e. height to diameter (h/d) and height to bars numbers (h/N) were discussed in this study. Therefore, the raw data taken from the laboratory tests were analyzed to estimate the following parameters.

- Maximum and minimum shear force, P_{max} and P_{min}
- Yield displacement, δy, that is the value where dissipation starts.

- Cumulative displacement, defined as the summation of the absolute displacement value of the device under cyclic loading up to the failure point, which can be calculated as:

$$\delta_{cum} = \sum_{i=0}^{N} \left(\left| \delta_i^{Max} \right| + \left| \delta_i^{Min} \right| \right) \tag{3.2}$$

- Ductility, μ, defined as the peak displacement to the yield displacement:

$$\mu = \delta_{\max} / \delta_y \tag{3.3}$$

- Cumulative displacement ductility , defined as:

$$\mu_{cum} = \delta_{cum} / \delta_y \tag{3.4}$$

- Effective stiffness, K_{eff} , defined as:

$$K_{eff} = \left| P_{\max} - P_{\min} \right| / \left| \delta_{\max} - \delta_{\min} \right| \tag{3.5}$$

- Equivalent viscous damping ratio expressed in terms of the elastic strain energy (E_s):

$$\xi = \frac{1}{4\pi} \left(E_D / E_s \right) \tag{3.6}$$

The dissipated energy (E_D) in each cycle is the area covered by the hysteresis loop (see Figure 3.14). For a certain lateral load, the harvested energy, E_D, is governed by many factors such as maximum displacement, frequency content of loading, yielding force and duration. Nevertheless, in ordinary circumstances, it can be considered to be controlled by peak displacement and the yield force. This inference is reliant on this hypothesis that the cumulative ductility, $\mu_{cum} = E_D / \left(P_y \delta_y \right)$, and the ductility, μ, are approximately related as $\mu_{cum} = 4(\mu - 1)$ (Akiyama, 1985). Consequently, the energy dissipated per cycle can be calculated as:

$$E_D = \mu_{cum}\left(P_y\delta_y\right) = 4\left(\mu - 1\right)\left(P_y\delta_y\right) \tag{3.7}$$

$$E_D = 4\left(\delta_{\max}/\delta_y - 1\right)\left(P_y\delta_y\right) \tag{3.8}$$

When the ductility is adequately high, i.e., $\mu - 1 \approx \mu$, dissipated energy can be approximated as

$$E_D = 4\left(\delta_{\max}/\delta_y\right)\left(P_y\delta_y\right) \tag{3.9}$$

and can also be expressed in the following form from Equation (3.8):

$$E_D = 4\left(\delta_{\max} - \delta_y\right)P_y \tag{3.10}$$

When the ductility is much larger than 1 (δmax is remarkably larger than δy), the dissipated energy can finally be expressed (see Equation (3.10)) as:

$$E_D = 4\left(P_y\delta_{\max}\right) \tag{3.11}$$

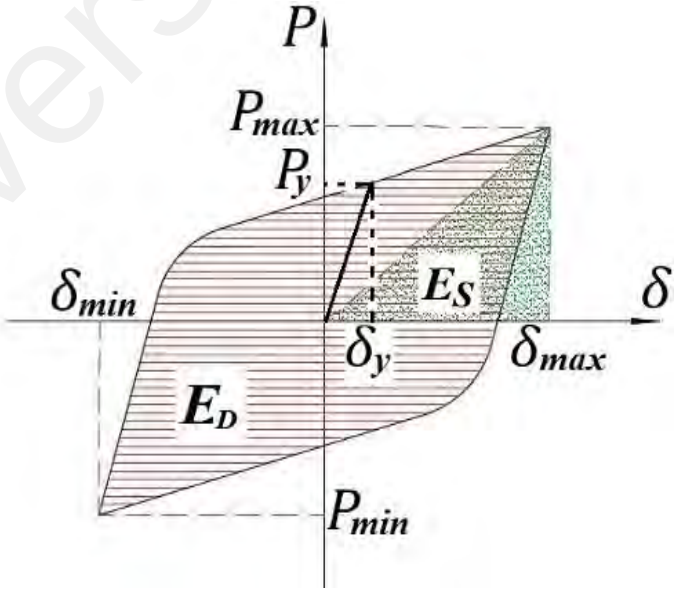

Figure 3.14: Typical hysteresis curve of a steel material per a complete cycle

3.5.1 Height Effect (Case 1)

To investigate the height effect of the solid bars on the overall BD performance, four different heights of the solid bars were selected as listed below and the device specimens were tested under these circumstances.

- BD-H70, h = 70 mm
- BD-H100, h = 100 mm
- BD-H130, h = 130 mm
- BD-H160, h = 160 mm

All four tested specimens were tested and exhibited a stable behavior. The solid bars acted with double curvature deformation under the cyclic displacement tests as expected. The force–displacement hysteretic curves acquired from the experiments are shown through Figures 3.15 to 3.18. Positive indication in the figures refers to upward displacement and load. All devices yielded at relatively small displacement, particularly BD-H70 at 0.25 mm, and revealed very stable hysteresis behavior with a smooth change from elastic to inelastic regime. The displacement response of the specimens was generally smaller than the applied displacement. This was because of small elastic deformation. Specimen BD-H70 with the minimum h/d ratio, endured the highest load capacity while specimen BD-H160 with the maximum h/d ratio, endured the lowest. On the average, the cracking for BD-H70, BD-H100, BD-H130 and BD-H160 occurred after 22, 28, 31 and 37 cycles of loading, respectively (see Table 3.3). With a fine approximation, the specimens sustained four more displacement cycles after formation of cracks. The location of cracks formation and their growth was similar in the four tested specimens. The test was stopped for BD-H100 (the first specimen) after almost all solid bars entirely broke and the resistance of the specimen was considerably decreased as shown in Figure 3.16(a). For other three specimens, the cyclic loading were discontinued

after a few rows of the bars had fully fractured and the resistance was also considerably reduced as shown in Figures 3.15(a), 3.17(a) and 3.18(a). The eight structural bolts connecting the specimens to the loading plates showed a satisfactory performance. No sign of distortion was observed on the bolts and attached plates, at the end of the tests.

3.5.1.1 Shear forces and displacements

The maximum force (P_{max}) and the minimum force (P_{min}) as well as the yield displacements (δ_y) and the peak displacements (δ_{max}) were taken from the experiments as demonstrated in Figures 3.15(a), 3.16(a), 3.17(a) and 3.18(a) for BD-H70, BD-H100, BD-H130 and BD-H160, respectively. The middle section of the cycles shows sliding zones in which load has relatively incremental values. By enlarging the cyclic displacement, the length of these zones was increased. This behavior would be predicted by increasing the h/d ratio under such conditions. The central parts of the cycles exhibited regions of sliding where the force (P) had comparatively constant values. The length of these regions increased when the number of cycles increased up to the value of about 10 to 15 mm. In this case (Case 1), the sliding regions of the obtained hysteresis loops were corrected in the load-displacement curve and plotted in Figures 3.15(b), 3.16(b), 3.17(b) and 3.18(b), respectively. This was done for better presentation of the maximum values of force and displacement as well as to show the rotundity of the hysteresis loop at the end of the tests in order to monitoring dissipated energy. An approximate bi-linear configuration of the tested specimens can be observed through the corrected figures considering h/d ratios. In addition to these, the minimum forces were on an average less than 3% smaller than the maximum forces because of the so-called Bauschinger effect. Altogether, BD-H160, with the highest h/d ratio, tripped the lengthiest displacement before failure. Figure 3.19 shows the strength degradation as soon as the cracks (damage) gradually developed owing to stress concentration at the ends of the solid bars.

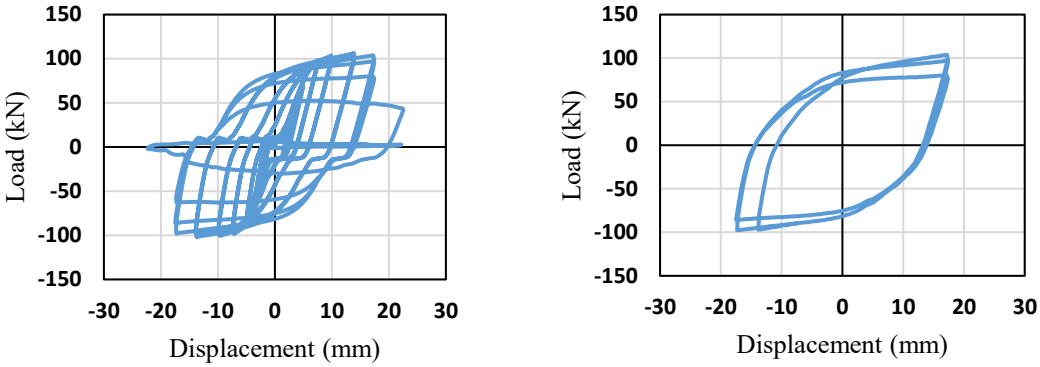

(a) Experiment curves (b) Curves after correction

Figure 3.15: Hysteresis behavior of the specimen BD-H70

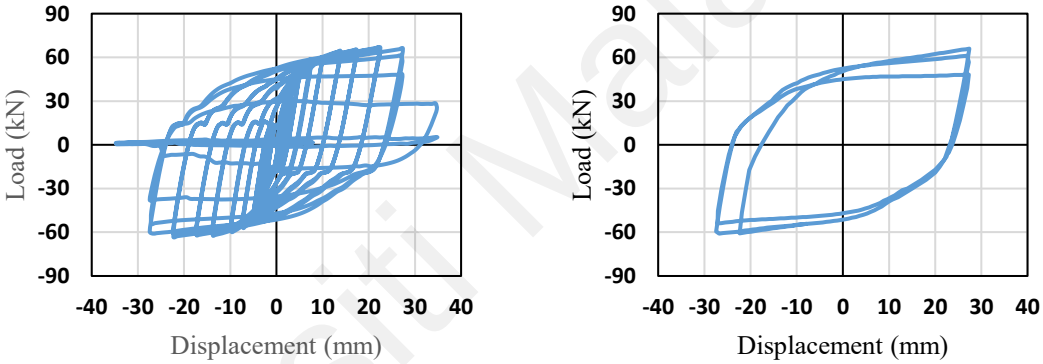

(a) Experiment curves (b) Curves after correction

Figure 3.16: Hysteresis behavior of the specimen BD-H100

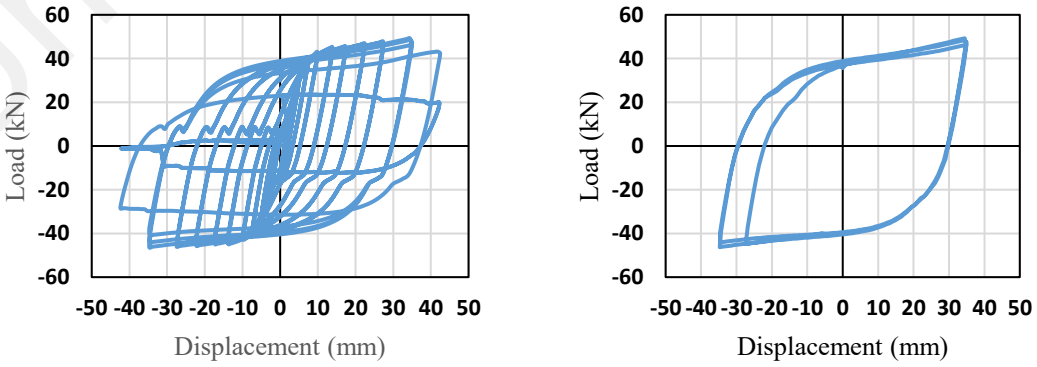

(a) Experiment curves (b) Curves after correction

Figure 3.17: Hysteresis behavior of the specimen BD-H130

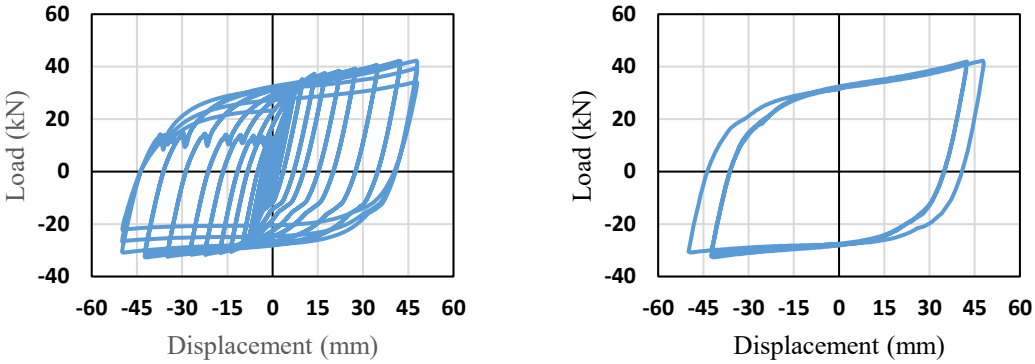

(a) Experiment curves (b) Curves after correction

Figure 3.18: Hysteresis behavior of the specimen BD-H160

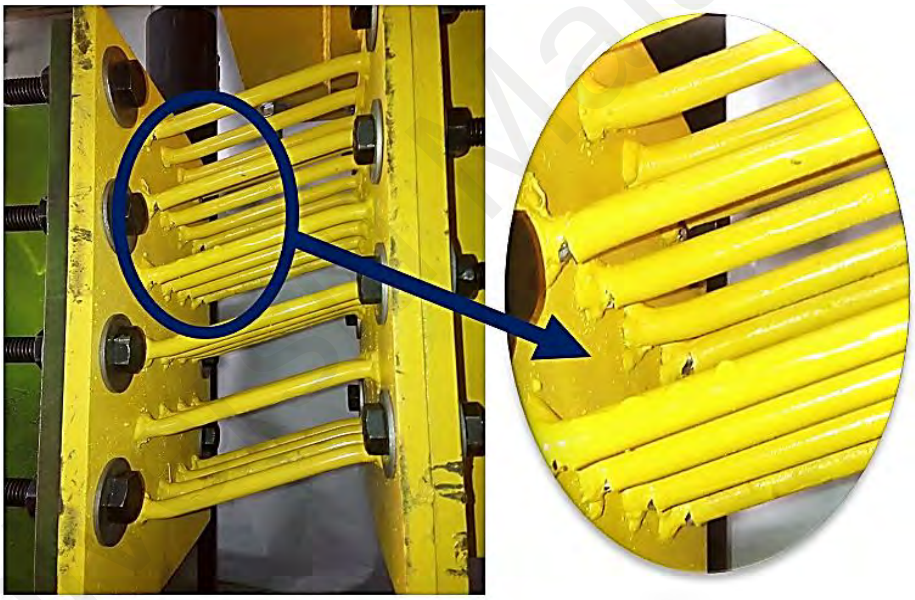

Figure 3.19: Crack formation at the end of the solid bars

3.5.1.2 Effective stiffness and ductility

Yielding dampers are normally categorized as displacement-dependent damping devices. Herein, the device specimens worked in a different fashion as h/d ratio was changed. In other words, the effective stiffness decreased when the h/d ratio was increased. As described earlier, since the devices endured more displacement as h/d ratio

increased, the stiffness of the devices decreased. Figure 3.20 shows the changes of effective stiffness verses h/d ratio. From the figure, the correlation between effective stiffness and considered ratio can be computed as:

$$K_{eff} = 559\ (h/d)^{-2.371} \tag{3.12}$$

In which the determination coefficient, $R^2 = 0.9986$. This means that, the proposed Equation (3.12) can nicely estimate the effective stiffness based on the h/d ratio.

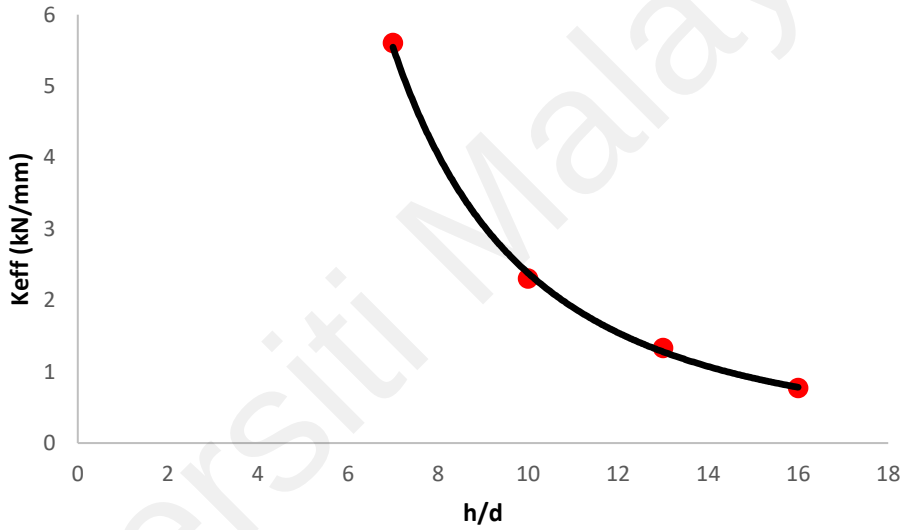

Figure 3.20: Variation of the effective stiffness verses h/d ratio

Figure 3.21 presents the normalized strength (P_{max}/P_y) versus ductility (δ_{max}/δ_y). The tested specimens exhibited an excellent ductility ratio (from 24 to 69) and strength (from 37 to 103 kN) under cyclic loading. This showed that, the strength of the device had improvement of 66 kN from the BD-H160 specimen (37 kN) to BD-H70 specimen (103 kN). These parameters of metallic dampers are generally very important for earthquake resistance capacity. It is noteworthy that, ductility ratio is reliant on the history of applied displacement, thus, it fluctuates once the displacement history was reformed.

Under the cyclic test, a ductility ration near to 69 was achieved for BD-H70 when the test was stopped. It was even anticipated a greater ductility than this could possibility be achieved. Table 3.3 summarizes the performance of the device specimens inferred from the experimental tests.

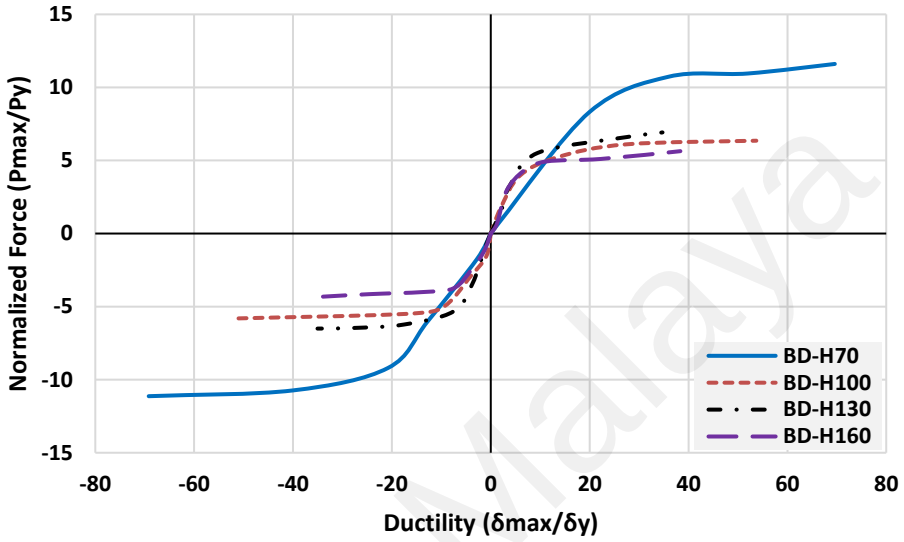

Figure 3.21: Envelope curves of the specimens under applied cyclic loading

Table 3.3: Summary of experimental results, height effect (units: kN, mm)

Specimen	$k_{e,d}$	$\delta_{y\exp}$	$\delta_{\max}$	$P_{y\exp}$	$P_{\max}$	N_c
BD-H70	20.66	0.25	17.37	8.10	102.66	22
BD-H100	7.10	0.50	27.39	8.74	64.84	28
BD-H130	3.23	0.99	34.41	5.64	47.78	31
BD-H160	1.73	1.76	47.95	5.40	37.36	37

Specimen	δ_{cum}	$\mu_{.}$	μ_{cum}	k_{eff}	E_D	E_{Dt}	ζ (%)
BD-H70	742	69	2204	5.6	4508	33492	42
BD-H100	1343	55	2082	2.3	5480	53017	50
BD-H130	1757	35	1392	1.33	5229	52827	51
BD-H160	2849	24	1319	0.77	5658	68166	51

3.5.1.3 Loss factor (viscous damping ratio)

Hysteretic energy dissipation by metals is commonly considered as rate-independent (independent of loading velocity). For practical applications, energy dissipation capacity is predominantly expressed as equivalent viscous damping ratio or loss factor. This damping ratio corresponds to a single degree of freedom oscillator with an effective or equivalent stiffness. Figure 3.22(a) presents the variation of equivalent damping ratio with effective stiffness normalized by the initial elastic stiffness for each individual specimen. Increasing the effective stiffness indicated lower inelastic deformation, and therefore, a lower damping ratio, as it is obvious from the figure. Figure 3.22(b) gives an overall performance trend of the device showing an average relationship between equivalent damping ratio and normalized stiffness considering the trends of all four specimens, where each point represents a feasible stiffness and equivalent damping ratio of the proposed device. The corresponding formula is given by Equation (3.13), accordingly. This confirmed that the bar damper devices were efficient in harvesting seismic energy satisfactorily despite being simple and economical (manufacturing cost only about USD 45; excluding installation and the supporting structure) with a light weight; 17 to 18 kg (see Table 3.1).

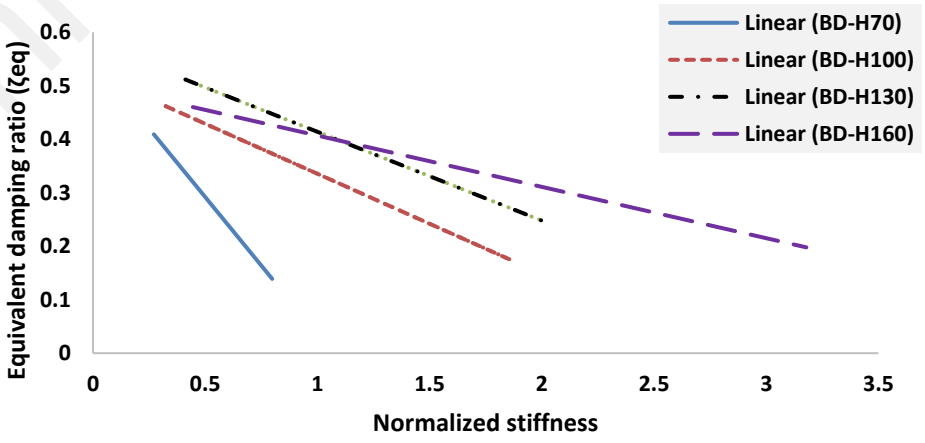

(a) Individual trend

Figure 3.22: Variation of equivalent damping ratio with normalized effective stiffness of the damper device specimens

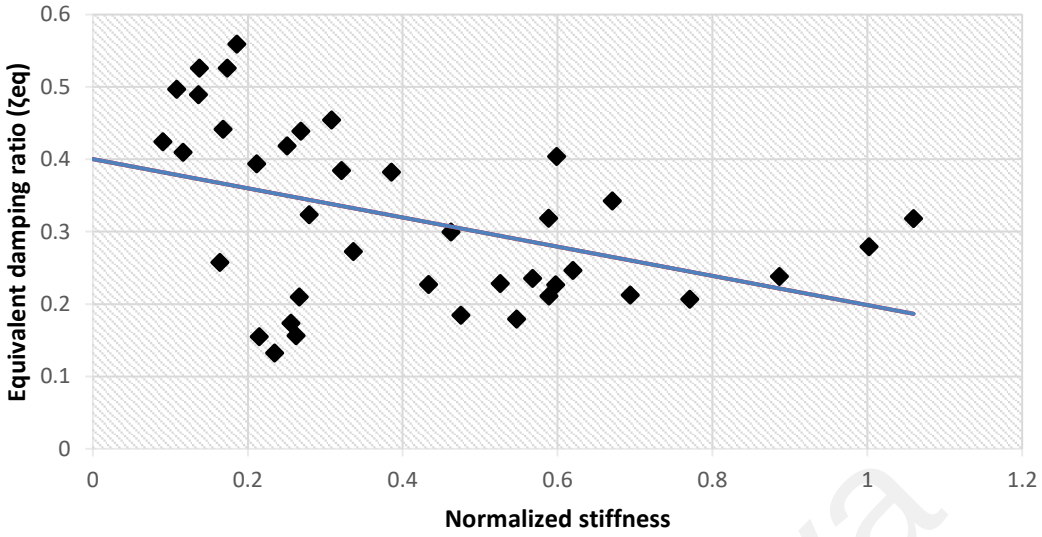

(b) General trend

Figure 3.22: Variation of equivalent damping ratio with normalized effective stiffness of the damper device specimens (**continued**)

$$\xi = -0.202\left(k_{eff}/k_{e,d}\right) + 0.4 \tag{3.13}$$

3.5.1.4 Energy dissipation

For BD-H70 to BD-H160, the energy dissipation started at the second cycle with δ_y= 0.25 mm, δ_y= 0.5, δ_y= 0.99 and δ_y= 1.76 mm, respectively. Figure 3.23 presents the variation of dissipated energy versus numbers of cycles. In the initial stages (first three steps) in which small plastic deformation occurred, energy dissipation varied slowly. With increasing inelastic deformation, energy dissipation increased exponentially. The absorbed energy of the proposed bar dampers ranged from 4508 to 5658 kN.mm in the last cycle, i.e., at failure stage. It is worth noting that, each step included three cycles as stated earlier. For instance, the cyclic dissipated energy in the last step for BD-H70 was calculated as 4508 times three that equals to 13524 kN.mm. The BD-H160 specimen with the highest h/d ratio exhibited largest energy dissipation. Figure 3.24 shows the changes

of total absorbed energy versus cumulative displacement. Experimental tests showed that, the total amount of dissipated energy was 68166 kN.mm in specimen BD-H160. This was approximately 29% higher than the energy dissipated taken from BD-H100 and BD-H130 and two times larger than that dissipated obtained from BD-H70. These differences were associated with different h/d ratios of the devices. The devices had cumulative displacement capacities of 742 mm, 1343 mm, 1757 mm and 2849 mm, which was very attractive. It was evident from the figure that, energy dissipation capacity was strongly related to the aspect ratio of the device. In the figure, the curves had different slopes which denote the effectiveness of the dampers to dissipate energy. The results confirmed that the proposed damper was able to dissipate significant amounts of energy (from 33 x 10^3 kN.mm to 68 x 10^3 kN.mm). It is possible to design the device based on the preferred amount of energy dissipation which can be measured by means of numerical studies such as FE analysis. The given hysteresis behavior showed that the device is reasonably applicable to absorb and dissipate input energy.

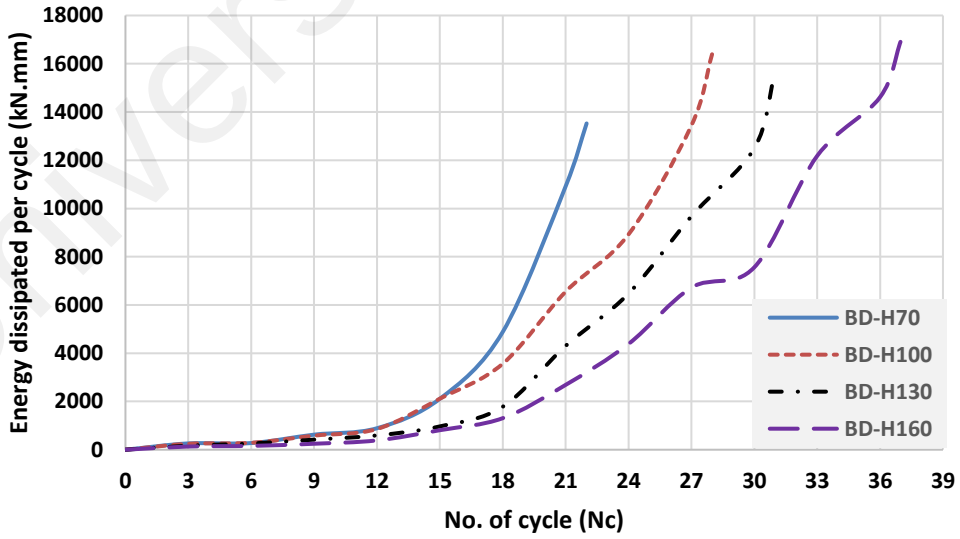

Figure 3.23: Variation of cyclic dissipated energy with number of cycles

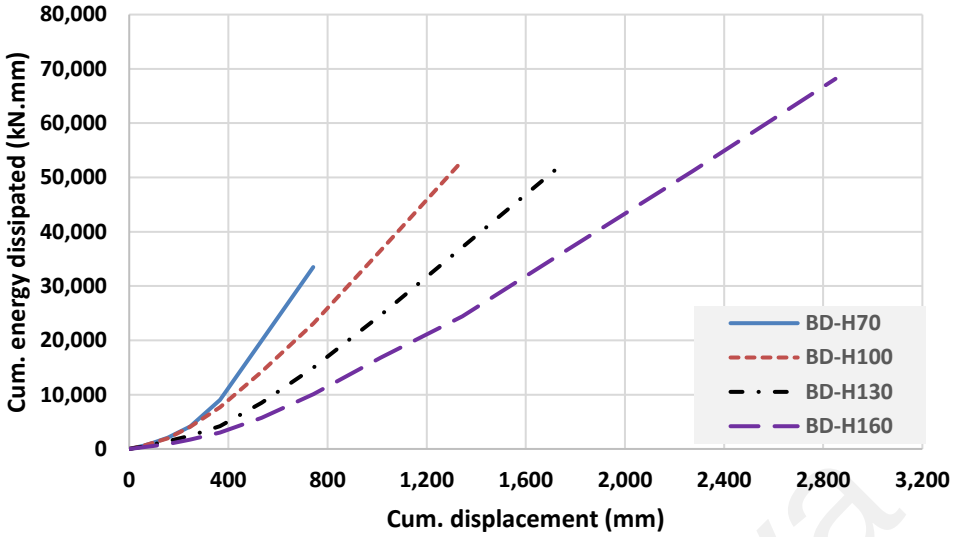

Figure 3.24: Cumulative energy dissipation in the proposed damper specimens

3.5.2 Diameter Effect (Case 2)

To examine the bars diameter effect on the BD performance, four different diameters of the solid bars, as listed below and presented in Figure 3.8, were considered. The BD with bar diameter d = 10 mm was similar to BD-H100 in case 1 under height consideration (see Table 3.1).

- BD-D8, d = 8 mm
- BD-D10 = BD-H100, d = 10 mm
- BD-D12, d = 12 mm
- BD-D14, d = 14 mm

The BD specimens were tested considering diameter variation of solid bars. The device specimens showed stable behavior with similar double curvature deformation under the applied cyclic displacement. The force–displacement hysteretic performance of the specimens attained from the experiments can be observed through Figures 3.25 to 3.27. Similar to previous stage (the height effect), positive indication in the figures refers to

upward displacement and load. The diameter effect of the solid bars on BD performance showed that, the size of the bars had significant effect on BD yielding, in which the yield displacements were relatively smaller compare to the Case 1 (the height effect). These were 0.735 mm, 0.5 mm and 0.49 mm for BD-D8, BD-D12 and BD-D14, respectively. In contrast, the yield forces were relatively greater compared with Case 1.

The specimen BD-D14 with the minimum h/d ratio (= 7.14), endured the highest load while specimen BD-D8 with the maximum h/d ratio (= 12.5), endured the lowest. Strength degradation occurred as cracks (damages) slowly developed owing to stress absorption at the ends of the solid bars (see Figure 3.28). The location of crack formation and growth was similar in all the specimens under diameter effect consideration. Apart from the BD-D10 specimen that was similar to BD-H100 which was discussed in Section 3.5.1, for the other three specimens, the cyclic loading were discontinued after a few rows of the bars had fully fractured and the resistance was considerably reduced as shown in Figures 3.25(a), 3.26(a) and 3.27(a). Once again, the attached structural bolts to the loading plates showed a satisfactory performance. No indication of deformation was seen for the used bolts at the end of the tests. Table 3.4 shows the numbers of cycles undergone by the specimens considering bars diameter effect.

3.5.2.1 Shear forces and displacements

The maximum force (P_{max}) and the minimum force (P_{min}) as well as the maximum displacements (δ_{max}) were taken from the experiments and presented as the hysteresis curves in Figures 3.25(a), 3.26(a) and 3.27(a) for BD-D8, BD-D12 and BD-D14 specimens, respectively. Similar to the previous case (Case 1), the middle section of the cycles shows sliding zones in which the load was relatively increasing. Increase in the cyclic movement enlarges the length of the zone as expected. The hysteresis loops in the last step (step 13) were extracted for each specimen and plotted in Figures 3.25(b), 3.26(b)

and 3.27(b). Unlike Figures 3.15(b), 3.16(b), 3.17(b) and 3.18(b) with sliding regions. These regions were corrected for clarification, while the maximum and minimum force as well as the maximum and minimum displacement of the specimens can clearly be monitored. It was noted that, there was a small difference percentage (about 4%) between the minimum and maximum forces, which was due to the Bauschinger effect as discussed in Case 1. Due to the strain hardening phenomenon, the maximum strengths (P_{max}) were unstably greater than the yield strengths obtained from the experiments (P_{yexp}) for each individual specimen. The BD-D8 specimen, with the highest h/d ratio (= 12.5), tripped the lengthiest displacement before failure.

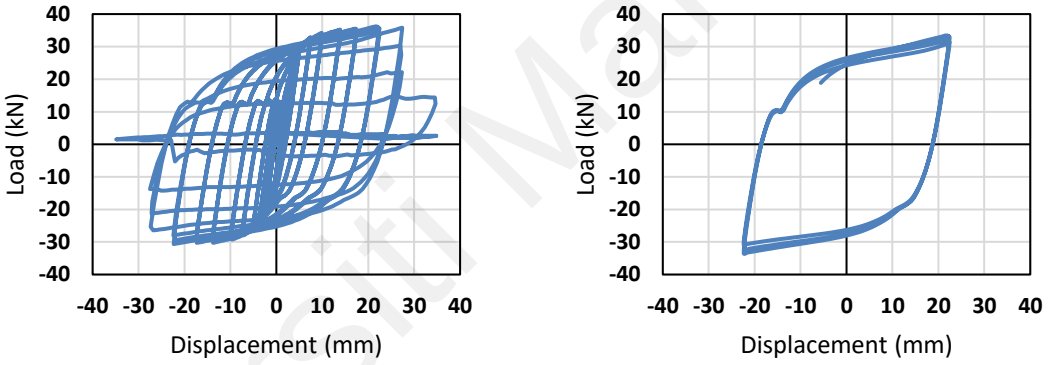

(a) Experiment curves (b) Sliding zones in the last cycle

Figure 3.25: Hysteresis behavior of the specimen BD-D8

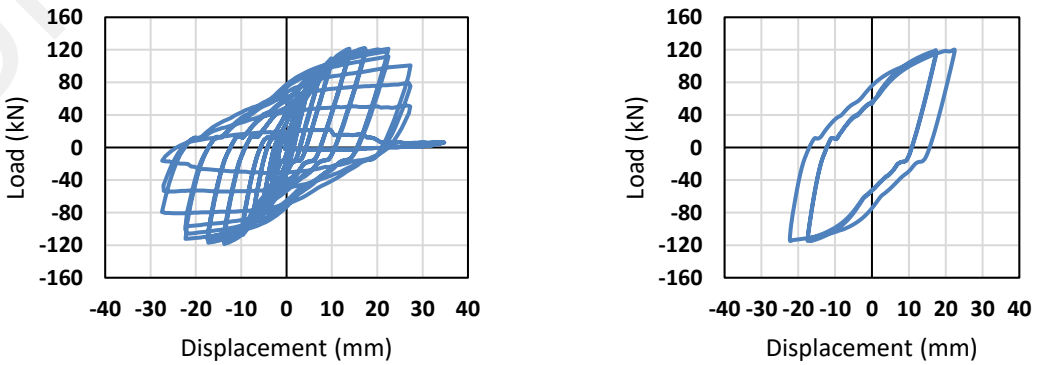

(a) Experiment curves (b) Sliding zones in the last cycle

Figure 3.26: Hysteresis behavior of the specimen BD-D12

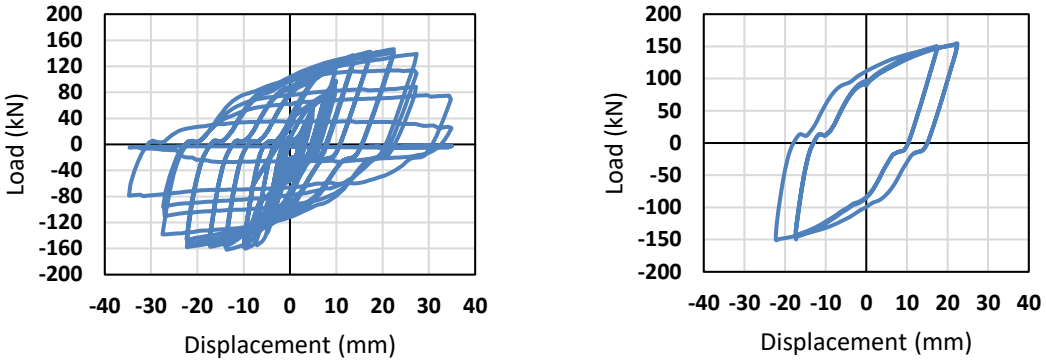

(a) Experiment curves (b) Sliding zones in the last cycle

Figure 3.27: Hysteresis behavior of the specimen BD-D14

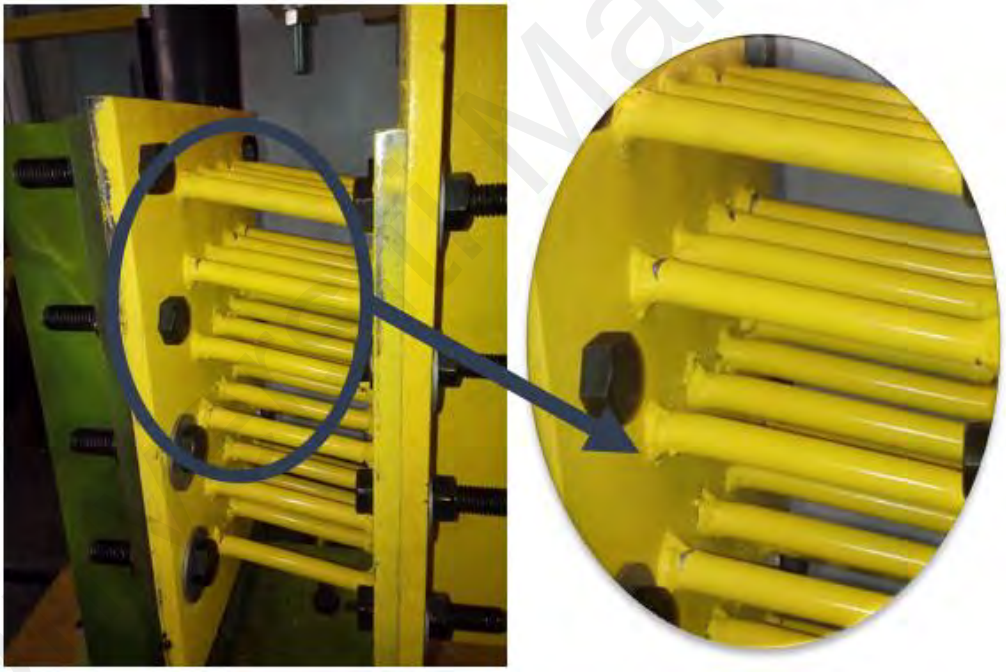

Figure 3.28: Crack formation at the end of the solid bars

3.5.2.2 Effective stiffness and ductility

As mentioned before, the device behaved differently as h/d ratio was changed. In this case and like to Case 1, the effective stiffness decreased when the h/d ratio was increased. Figure 3.29 depicts the effective stiffness verses h/d ratio when the bars diameter effect

was deliberated. From this figure, the correlation between effective stiffness and considered ratio was calculated and stated as the following equation:

$$K_{eff} = 7660(h/d)^{-3.523} \tag{3.14}$$

In which the determination coefficient, $R^2 = 0.98$. This means that, the Equation (3.12) can nicely estimate the effective stiffness based on the h/d ratio.

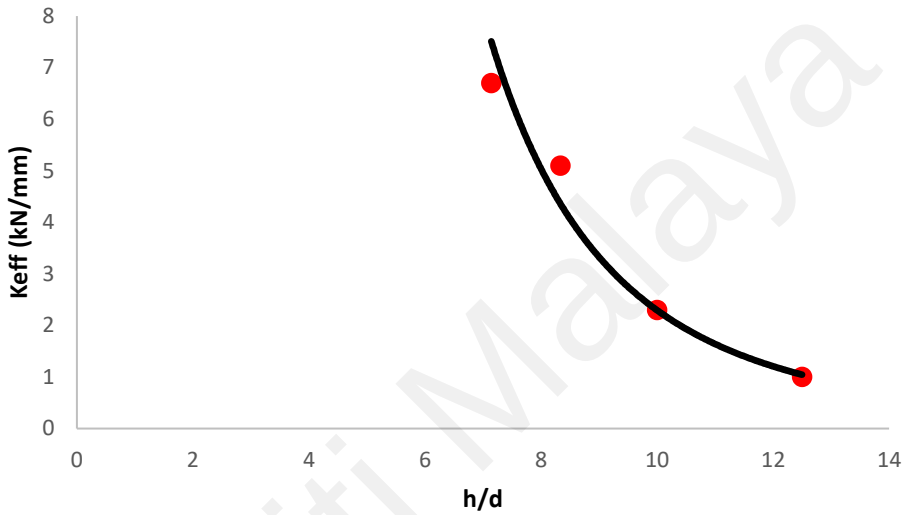

Figure 3.29: Variation of the effective stiffness versus h/d ratio

Figure 3.30 presents the normalized strength (P_{max}/P_y) versus ductility (δ_{max}/δ_y). The tested specimens demonstrate an excellent ductility from 37 to 54.78, as shown in the Figure 3.30, and strength from 33 to 154 kN, as presented in the previous figures, under cyclic loading. This shows that, the strength of the device has a difference of 121 kN from the BD-D8 specimen to BD-D14 specimen. Under applied cyclic displacement, ductility ratio of 55 was observed for BD-D10 when the test was stopped. This ratio for BD-D8, BD-D12 and BD-D14 was 37, 45 and 46, respectively. As it can be seen from the figure, the specimen with smaller bar diameter exhibits a less ductility with less strength. The trend got inversed as the h/d ratio was decreased from 12.5 for BD-D8 to 10, 8.3 and 7.14 for BD-D10, BD-D12 and BD-D14, respectively. Moreover, the

normalized force axis showed that there was a progressive increase of the device strength form BD-D8 to BD-D14. Table 3.4 summarizes the main performance of the device specimens inferred from the experimental tests.

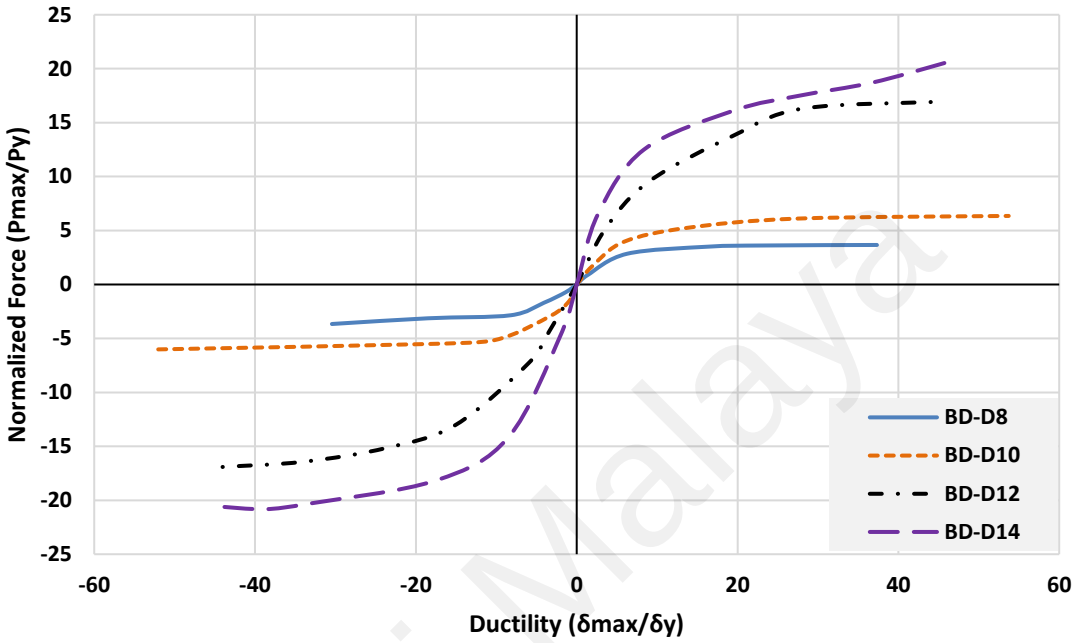

Figure 3.30: Envelope curves of the specimens under applied cyclic loading considering bars diameter effect

Table 3.4 shows that, the specimens endured lesser under applied cyclic load and failed sooner compared to Case 1, however, BD-D8 with bar diameter size of 8 mm showed a good stability up to cycle 28. The maximum number of cycles in Case 1 was recorded as 37 for BD-H160 and 28 for BD-D8 and BD-D10 in Case 2. This showed that, changes in bars diameter had inverse result in terms of the device endurance considering number of cycles.

Table 3.4: Summary of experimental results, bars diameter effect (units: kN, mm)

Specimen	$k_{e,d}$	$\delta_{y\exp}$	$\delta_{\max}$	$P_{y\exp}$	$P_{\max}$	N_c
BD-D8	2.9	0.735	27.44	3.95	33.44	28
BD-D10	7.10	0.50	27.39	8.74	64.84	28
BD-D12	14.66	0.50	22.47	12.85	120.53	27
BD-D14	27.15	0.49	22.43	17.1	154.01	27

Specimen	δ_{cum}	$\mu_{.}$	μ_{cum}	k_{eff}	E_D	E_{Dt}	ζ (%)
BD-D8	1343	37	1416	1	2850	30489	48
BD-D10	1343	55	2082	2.3	5480	53017	50
BD-D12	1013	45	1532	5.1	6570	48090	40
BD-D14	1013	46	1563	6.7	9241	68805	43

3.5.2.3 Loss factor (viscous damping ratio)

Figure 3.31(a) displays the variation of the equivalent damping ratio versus the effective stiffness normalized by the initial elastic stiffness for each individual specimen considering diameter changes of the bars. It was observed that, larger diameter size increased the effective stiffness with lower inelastic deformation, which led to lower damping ratio. Figure 3.31(b) gives an overall trend of the device performance showing an average relationship between equivalent damping ratio and normalized stiffness considering the trends of all four specimens (refer to Figure 3.31(a)). The corresponding formula was presented by Equation (3.15), accordingly. It was approved that the specimens were noticeably capable of dissipating input energy.

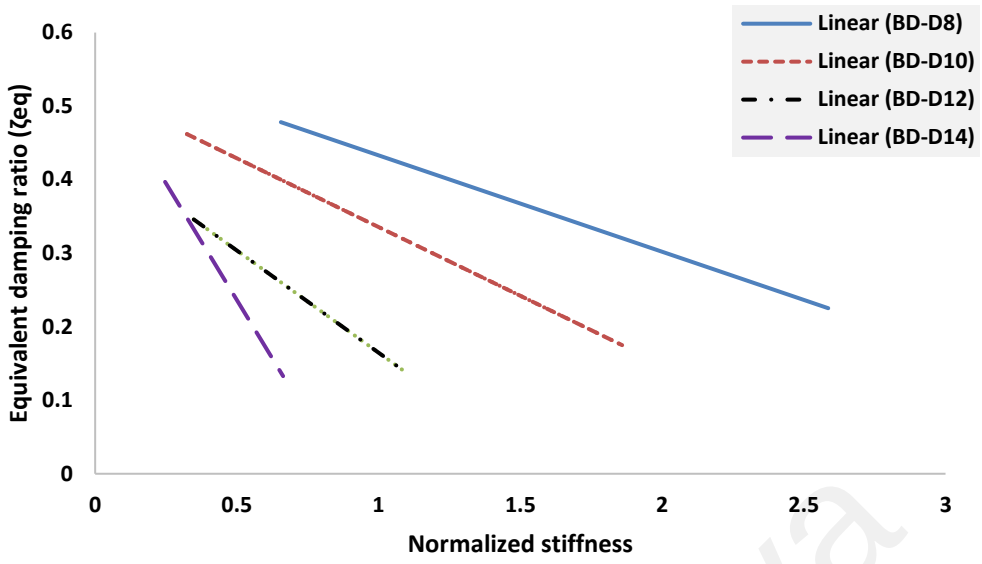

(a) Individual trend

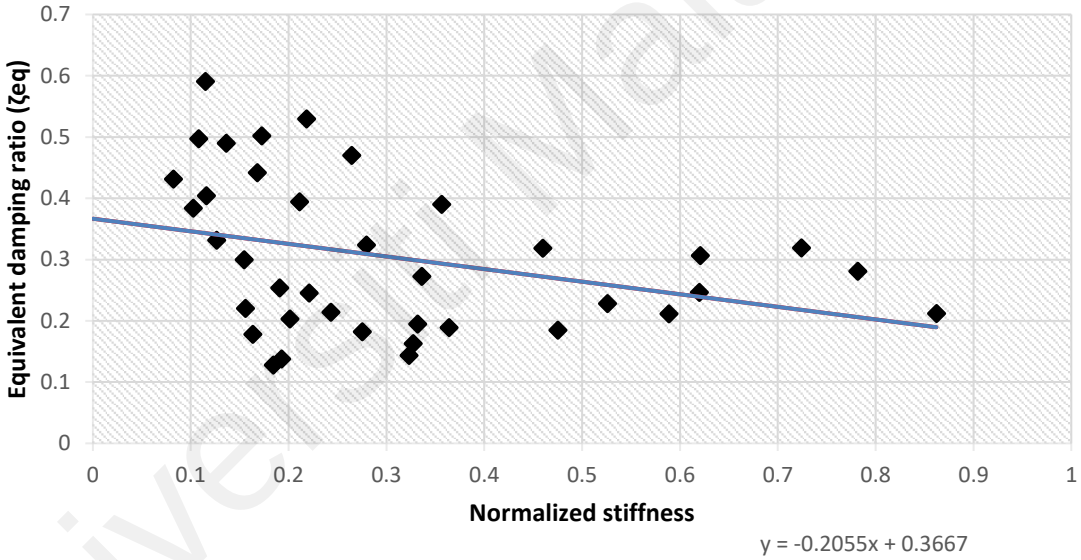

(b) General trend

Figure 3.31: Variation of equivalent damping ratio with normalized effective stiffness of the damper device specimens

$$\xi = -0.2055\left(k_{eff}/k_{e,d}\right) + 0.367 \tag{3.15}$$

3.5.2.4 Energy dissipation

Similar to Case 1, the energy dissipation for BD-D8 to BD-D14 started at the second cycle with δ_y= 0.735 mm, δ_y= 0.5, δ_y= 0.5 and δ_y= 0.49 mm, respectively. Figure 3.32 presents the variation of energy dissipated with number of cycles. In the initial stages (first five steps) in which small plastic deformation occurred, energy dissipation changed gently. The energy dissipation developed exponentially when inelastic deformation increased. In the last cycle, the dissipated energy of the specimens varied from 2850 to 9241 kN.mm at failure point for BD-D8 and BD-D14, respectively. The BD-D14 specimen with lowest h/d ratio exhibited largest energy dissipation (unlike Case 1 for BD-H160 with highest h/d ratio). Figure 3.32 shows the variation of cumulative absorbed energy versus cumulative displacement. Experimental tests exhibited that, the cumulative dissipated energy was 68805 kN.mm for the specimen BD-D14. This was approximately 1.3 times greater than the energy absorbed by BD-D10 and BD-D12 and 2.36 times larger than that one dissipated by BD-D8. It can be seen from the figure that, cumulative displacements for BD-D8 to BD-D14 were pretty lesser considering bars diameter effect in compare to the effect of bars height in Case 1. For instance, the maximum cumulative displacement was related to specimens BD-D8 with about 1343 mm, whereas, the maximum cumulative displacement in Case 1 was for BD-H160 with 2849 mm; more than two times bigger. These showed the effects of diameter changes in dissipating input energy compared to the bars height effects in Case 1. Although, the cumulative displacements for the specimens in this case (Case 2) was smaller than those obtained in Case 1, but the values were still remarkable. This means that, BD-D8 with 1343 mm, BD-D12 and BD-D14 with 1013 mm endured continues displacements. The results shown in Figure 3.33 confirmed the efficiency of the device specimens for dissipating substantial energy amount from 30489 kN.mm for BD-D8 to 68805 kN.mm for BD-D14.

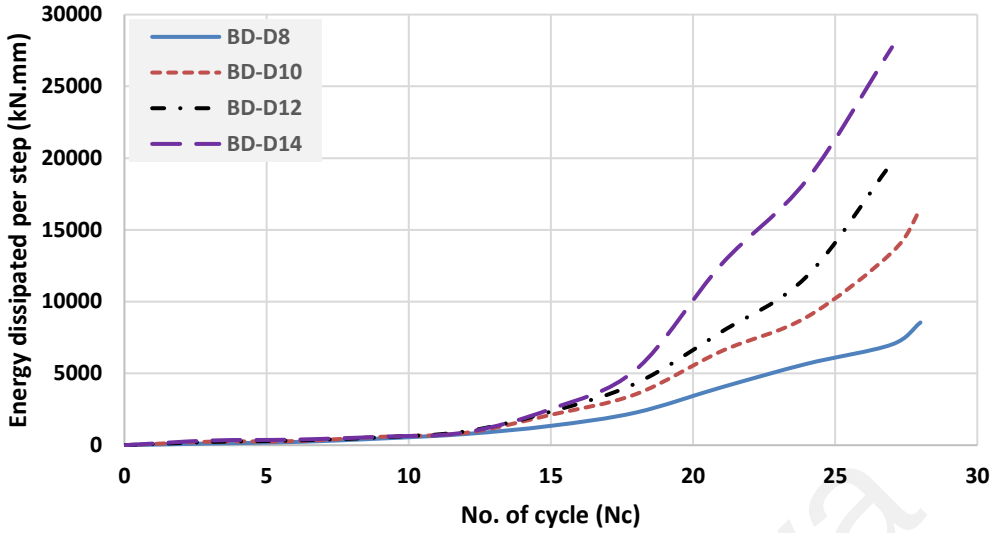

Figure 3.32: Variation of cyclic dissipated energy with number of cycles

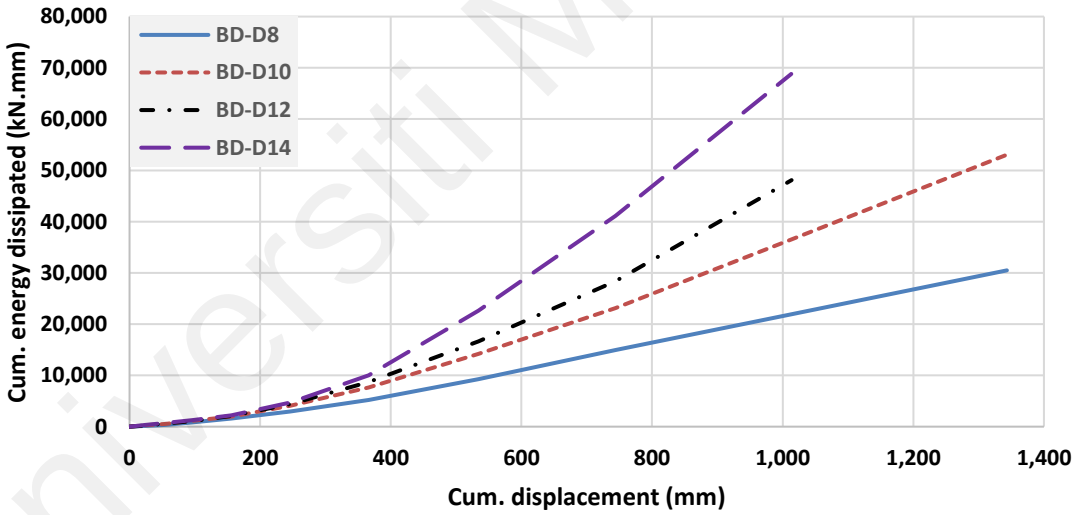

Figure 3.33: Cumulative energy dissipation in the proposed damper specimens

3.5.3 Bars Number Effect (Case 3)

The effect of height and diameter of the solid bars on the damper performance was studied in Case 1 and Case 2. In this section to investigate the effect of the bars numbers

on the BD performance, four different scenarios were also considered as mentioned below (see also Figure 3.9).

- BD-N20, N = 20
- BD-N24 = BD-H100, N = 24
- BD-N28, N = 28
- BD-N32, N = 32

The specimen with 24 number of bars, i.e. BD-N24, was similar to BD-H100 specimen in Case 1 and BD-D10 specimen in Case 2 under the height and dimeter consideration, respectively. Similar to Case 1 and Case 2, the specimens were experimentally tested and they demonstrated acceptable performance. Instead of considering h/d ratio used in previous cases, h/N ratio (height/number of bars) was taken into consideration in this case. Figures 3.34, 3.35 and 3.36 illustrate the hysteretic loop obtained from the specimens under cyclic displacement test. Unlike Case 1 and Case 2, in this case the specimens yielded with the same values, i.e., 0.49 mm, with very stable hysteresis behavior where a smooth transformation can be seen from elastic to inelastic regime. Based on the obtained displacements from four specimens under bars number consideration, it was confirmed that the bars number does not have a noticeable effect on yield displacement.

The h/N ratio for BD-N20, BD-N24, BD-N28 and BD-N32 was 5, 4.17, 3.57 and 3.125, respectively (see Table 3.1). The specimen BD-N32 with the minimum h/N ratio, undergone the highest load while the specimen BD-N20 with the maximum h/N ratio, endured the lowest. Strength degradation arose as cracks (damages) progressively developed due to stress absorption at both ends of the solid bars (see Figure 3.37). In general, the BD-N20, BD-N28 and BD-N32 were failed in cycles 26, 26, 24 of loading, respectively. Also, there was not a principled trend for the device at the failure point

considering number of cycles; however, the location of cracks formation was similar to the tested specimens in Case 1 and Case 2. The structural bolts that attached the specimens to the loading plates also showed an adequate performance as seen in the previous cases.

3.5.3.1 Shear forces and displacements

The maximum force (P_{max}) and the minimum force (P_{min}) as well as the yield displacements (δ_y) and the peak displacements (δ_{max}) were taken from the experiments and illustrated in the form of hysteresis curves in Figures 3.34(a), 3.35(a), and 3.36(a) for BD-N20, BD-N28, and BD-N32, respectively. As discussed in Case 1 and Case 2, the middle section of the cycles showed sliding zones where the load had relatively incremented. By enlarging the cyclic displacement, the length of this zone was increased. This behavior would be predicted by decreasing the h/N ratio from BD-N20 to BD-N32. The last hysteresis curves obtained from the last step (step 13) including their sliding regions were extracted and plotted in Figures 3.34(b), 3.35(b), and 3.36(b). This was shown for better exhibition of the maximum forces and displacements as well as to show the fatness of the hysteresis loop at the end of the tests. Due to the strain hardening phenomenon, the maximum strengths (P_{max}) were unstably greater than the yield strengths obtained from the experiments (P_{yexp}) for each individual specimen.

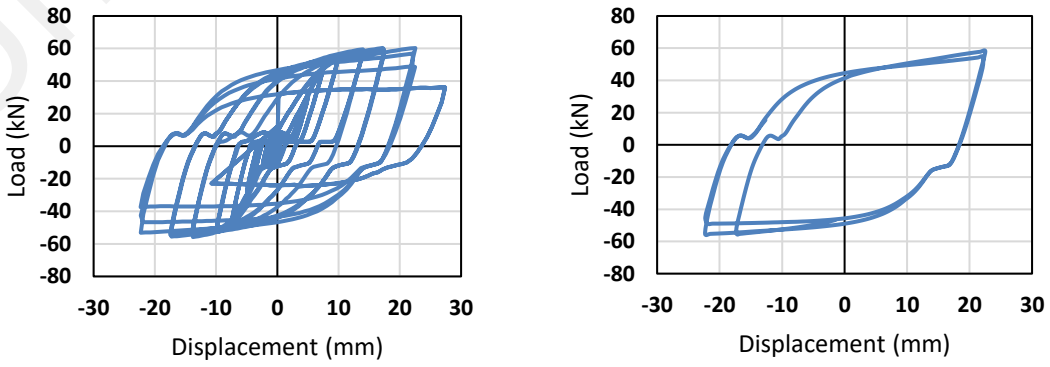

(a) Experiment curves (b) Sliding zones in the last cycle

Figure 3.34: Hysteresis behavior of the specimen BD-N20

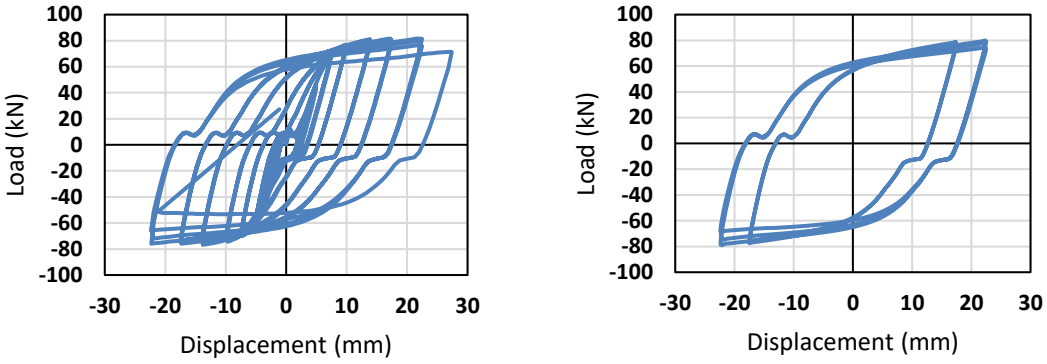

(a) Experiment curves (b) Sliding zones in the last cycle

Figure 3.35: Hysteresis behavior of the specimen BD-N28

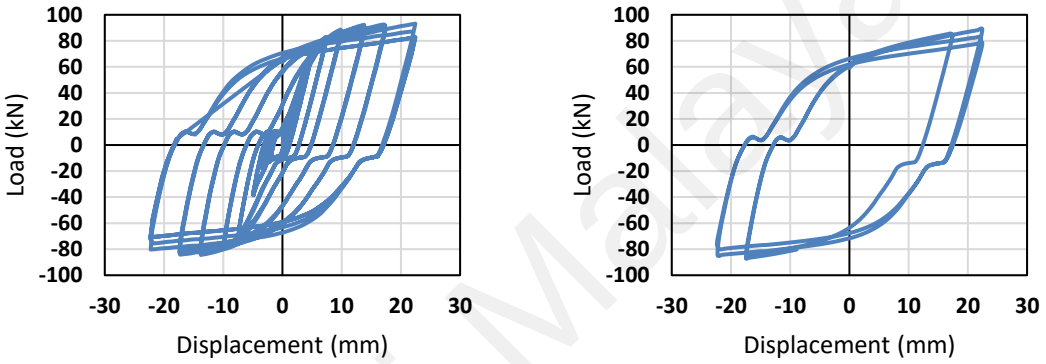

(a) Experiment curves (b) Sliding zones in the last cycle

Figure 3.36: Hysteresis behavior of the specimen BD-N32

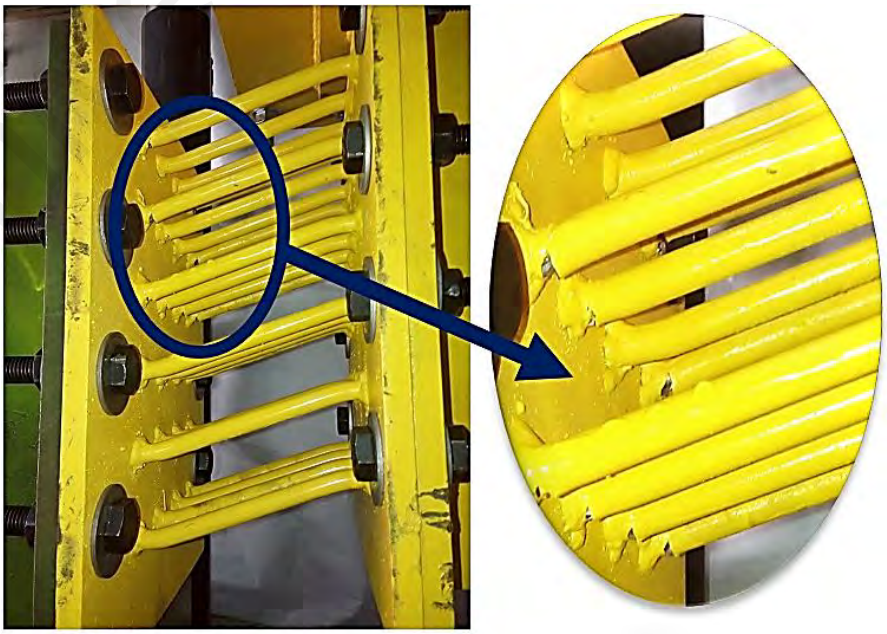

Figure 3.37: Crack formation at the end of the solid bars

3.5.3.2 Effective stiffness and ductility

The effective stiffness decreased when the h/N ratio was increased. Similar to the previous cases, the device worked differently as h/N ratio was altered. Figure 3.38 illustrates the effective stiffness verses h/N ratio under bars numbers effect, in which h=100 mm that is the height of the benchmark specimen (BD-N24). The corresponding equation associated with the effective stiffness and h/N ratios can be proposed as follows:

$$K_{eff} = 86.816(h/N)^{-2.61} \quad (3.16)$$

In which the determination coefficient was $R^2 = 0.92$. This means that, the proposed Equation (3.12) can nicely estimate the effective stiffness based on the h/N ratio.

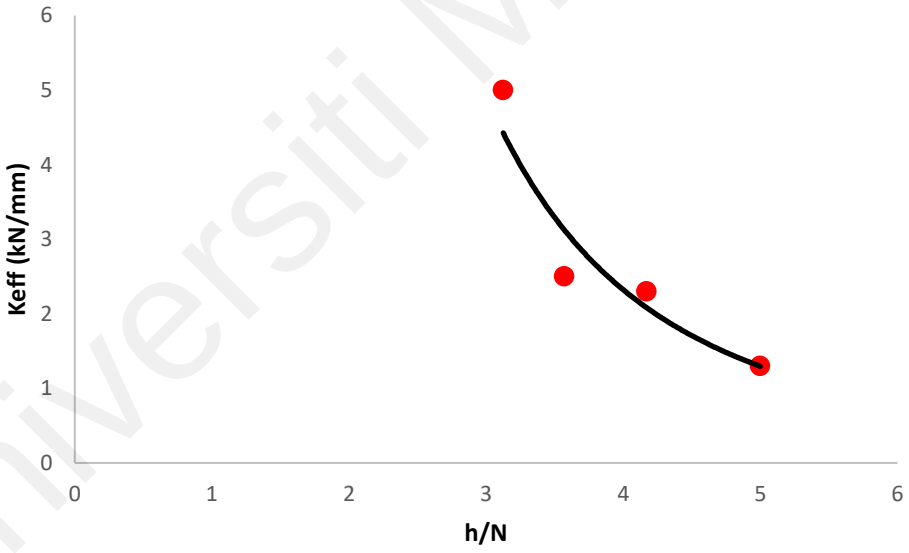

Figure 3.38: Variation of the effective stiffness versus h/N ratio

Figure 3.39 presents the normalized strength (P_{max}/P_y) versus ductility ratio (δ_{max}/δ_y). The tested specimens showed outstanding ductility from 45.7 to 54.78 for BD-N32 and BD-N24, respectively. For strength, the values were obtained from 58 to 89 kN under cyclic loading from BD-N20 to BD-N32. In comparison to Case 1 and Case 2,

the strength values of the specimens were much closer to each other for this case. This showed that, under bars number effect consideration the variance of the strength in Case 1 from BD-H70 to BD-H160 was 66 kN and in Case 2 from BD-D8 to BD-D14 was 121 kN. Nonetheless, the strength variance in this case (Case 3) from BD-N20 to BD-N32 was only 31 kN. It can be concluded from the tests that, changes in the bars number of the device do not have a significant effect on the performance of the proposed damper compared to the bars height and bars diameter effects. In addition, under the applied cyclic load, a ductility of 55 was achieved for BD-N24 when the test was stopped, whereas, this was approximately 46 for BD-N20, BD-N28 and BD-N32. Investigation of the device ductility in different cases shows that, bars diameter has the most effect with the value of 110 for BD-D8, followed by the bars height and the bar number with the value of 69 and 55 for BD-H70 and BD-N24, respectively. Table 3.5 summarizes the main performance of the device specimens inferred from the experimental tests.

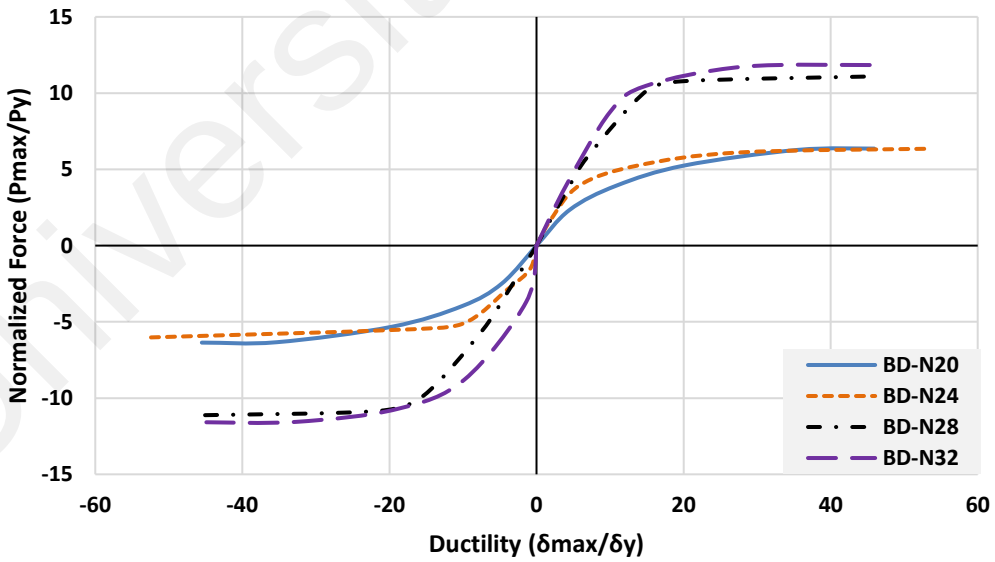

Figure 3.39: Envelope curves of the specimens under applied cyclic loading considering bars number effect

Table 3.5: Summary of experimental results, bars number effect (units: kN, mm)

Specimen	$k_{e,d}$	$\delta_{y\exp}$	$\delta_{\max}$	$P_{y\exp}$	$P_{\max}$	N_c
BD-N20	5.90	0.49	22.50	6.25	58.10	26
BD-N24	7.10	0.50	27.39	8.74	64.84	28
BD-N28	8.25	0.49	22.50	8.80	79.20	26
BD-N32	9.42	0.49	22.43	9.87	88.90	26

Specimen	δ_{cum}	μ	μ_{cum}	k_{eff}	E_D	E_{Dt}	ζ (%)
BD-N20	1014	46	1564	1.3	2790	21306	50
BD-N24	1343	55	2082	2.3	5480	53017	50
BD-N28	1014	46	1564	2.5	4933	40346	41
BD-N32	744	45	1125	5	4340	27984	45

3.5.3.3 Loss factor (viscous damping ratio)

Figure 3.40(a) shows the variation of equivalent damping ratio versus the effective stiffness normalized by the initial elastic stiffness for each individual specimen. It is shown in the figure that, the equivalent damping ratio had indirect relationship with the normalized stiffness such that the increase of the normalized stiffness led less damping ratio. This was because that, increasing the effective stiffness implied lower inelastic deformation, and therefore, a lower damping ratio.

Figure 3.40(b) presents a general performance tendency of the device showing an average relationship between equivalent damping ratio and normalized stiffness considering the trends of all four specimens in which bars numbers effect was taken into account. In the figure, each point represents a feasible stiffness and equivalent damping ratio of the device specimens obtained from Figure 3.40(a). As a result, the corresponding formula was proposed as Equation (3.17), accordingly. Based on the results presented in Figures 3.40 (a) and 3.40(b), the device specimens were appropriately able to harvest energy due to applied external loads, despite this fact that, the bar damper is a simple and

economical device. As mentioned before, manufacturing of the device cost only about USD 45 with a light weight; 17 to 18 kg (see Table 3.1).

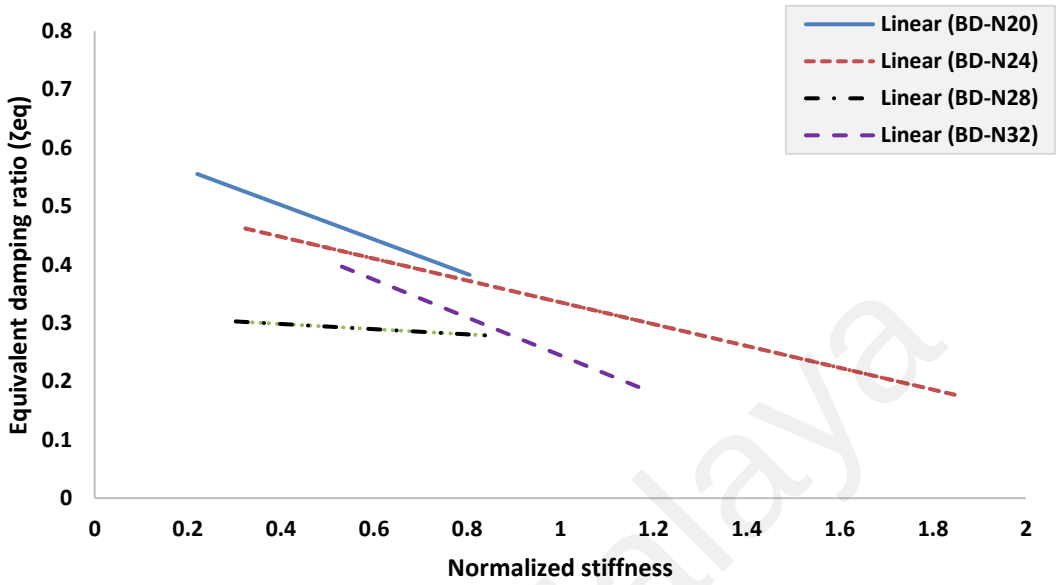

(a) Individual trend

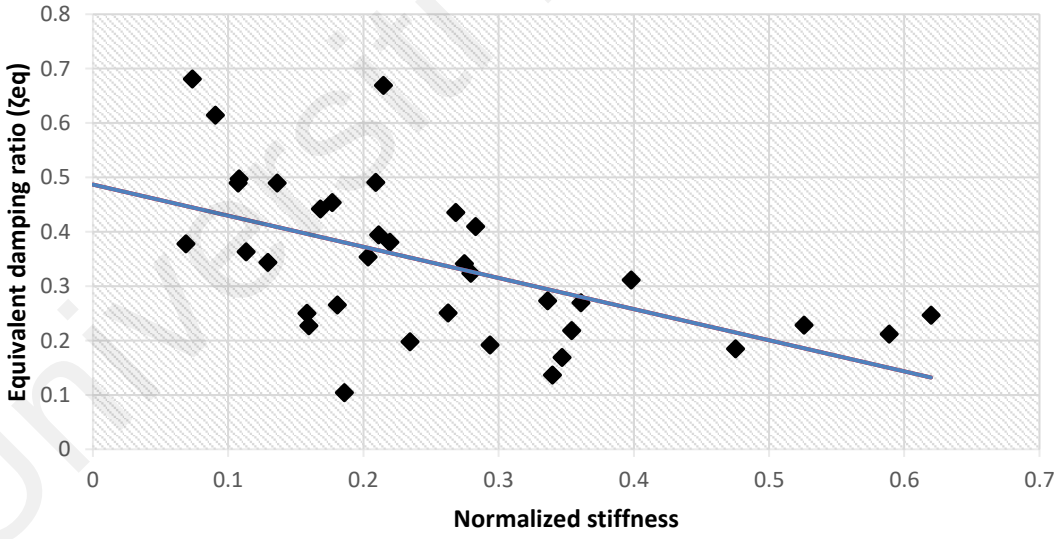

(b) General trend

Figure 3.40: Variation of equivalent damping ratio with normalized effective stiffness of the damper device specimens

$$\xi = -0.572\left(k_{eff}/k_{e,d}\right) + 0.487 \quad (3.17)$$

3.5.3.4 Energy dissipation

Figure 3.41 shows the variation of the energy dissipation versus number of tripped cycles. In the initial stages in which small plastic deformation occurred, energy dissipation varied slowly, up to cycle 13, for all the specimens. Similar to Case 1 and Case 2, with increasing inelastic deformation, energy dissipation upturns exponentially. The absorbed energy of the bar damper specimens ranged from 2790 to 5480 kN.mm in the last cycle (each three cycles equals to one step). It can also be seen from Figure 3.41 that the maximum tripped cycle under bars numbers effect (the present case) and bars diameter consideration (Case 2) was 28, while, under the bars height consideration (Case 1) the maximum continues cycle was 37. This means that, the height parameter had the most effect on dissipating input energy.

Figure 3.42 shows the changes of the cumulative absorbed energy versus cumulative displacement for each specimen. Experimental tests showed that, the total amount of dissipated energy was 53017 kN.mm for the specimen BD-N24. This was approximately 28% lesser than the total energy dissipated by BD-H160 in Case 1 with 68166 kN.mm and 30% smaller than the total energy dissipated by BD-D14 in Case 2 with 68805 kN.mm. Although, these values were remarkably smaller than that obtained from Case 1 for BD-H160 specimen with 2849 mm, but it should be noted that and regardless of these comparisons, the obtained values of the cumulative absorbed energy and displacement for all tested specimens were noticeable.

The results obtained from this case confirmed that, the proposed damper was able to dissipate significant amounts of energy (from 21306 kN.mm to 53017 kN.mm) just by changing the bars numbers. It shows the possibility to design the damper device for different level of earthquake magnitudes based on the preferred amount of energy

dissipation, which can be measured by means of several numerical studies. In short, given the hysteresis behavior makes the device applicable to be utilized as a reasonable energy absorber. Finally, an overall view of the hysteretic performance of the proposed device for each of investigated parameters, i.e. Case 1, Case 2 and Case 3, is presented in Figures 3.43, 3.44 and 3.45, respectively.

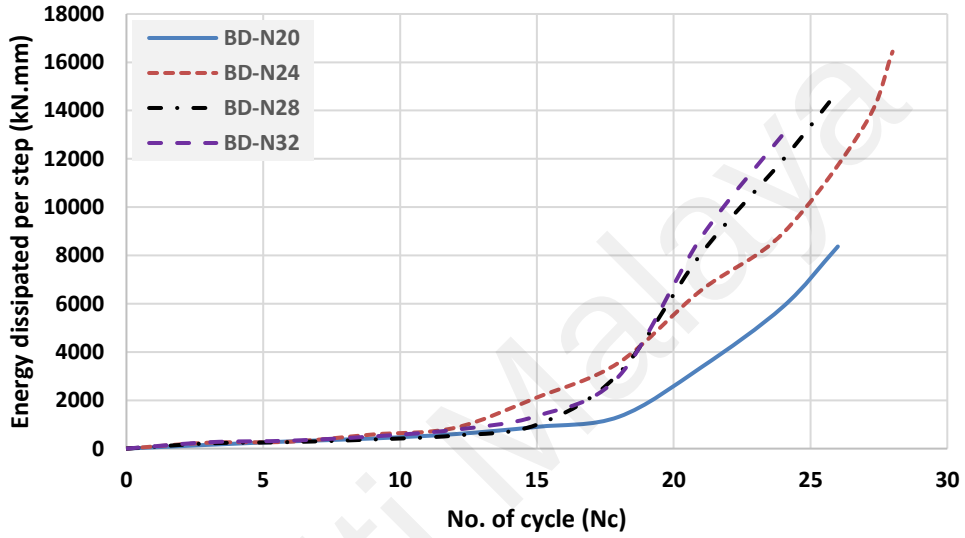

Figure 3.41: Variation of cyclic dissipated energy with number of cycles

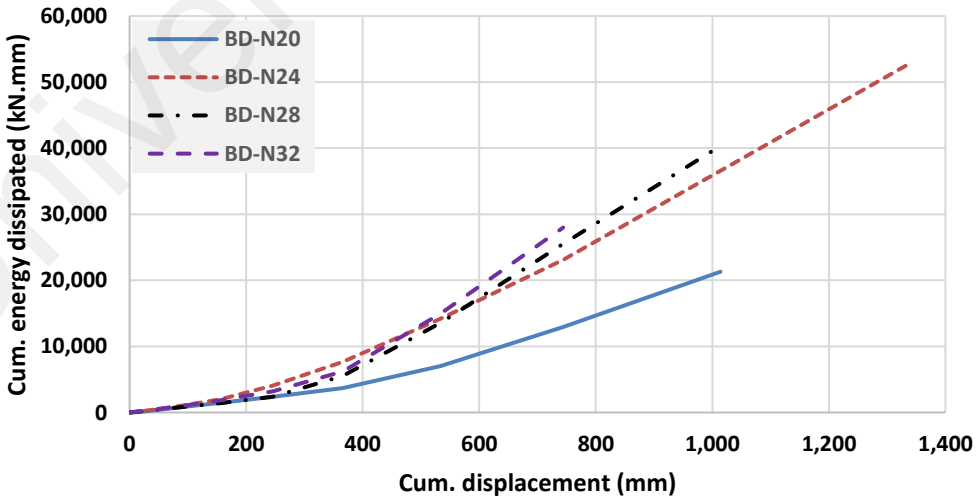

Figure 3.42: Cumulative energy dissipation in the proposed damper specimens

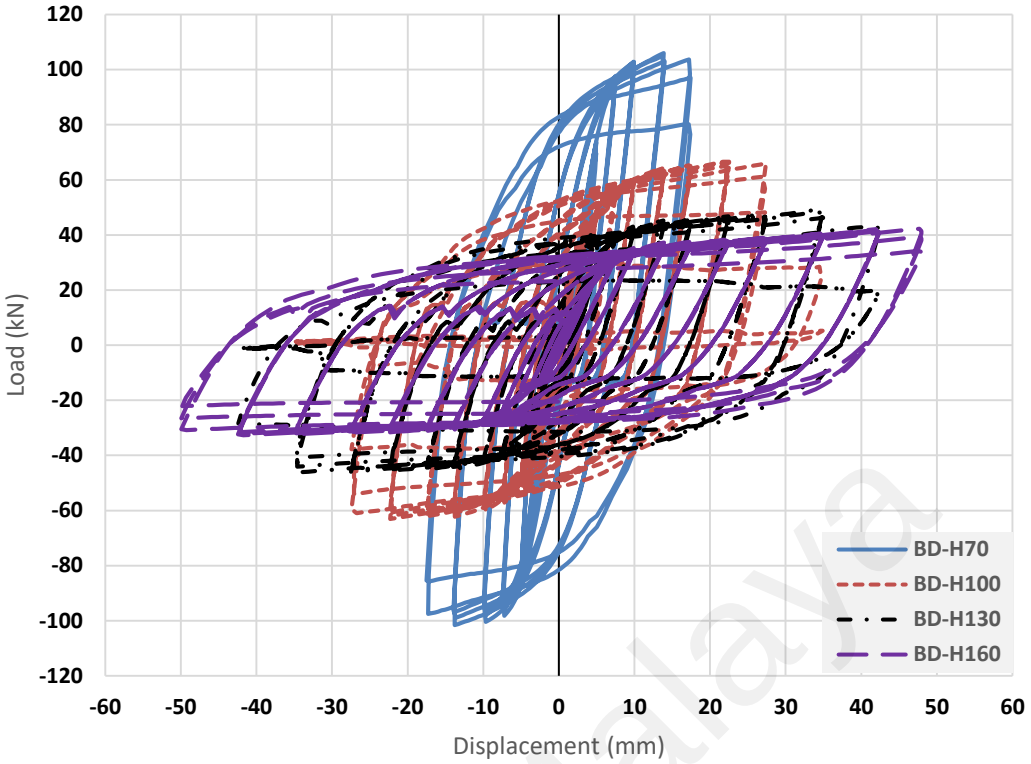

Figure 3.43: Overall view of the device performance considering the bars height effect for BD-H70, BD-H100, BD-H130 and BD-H160 specimens

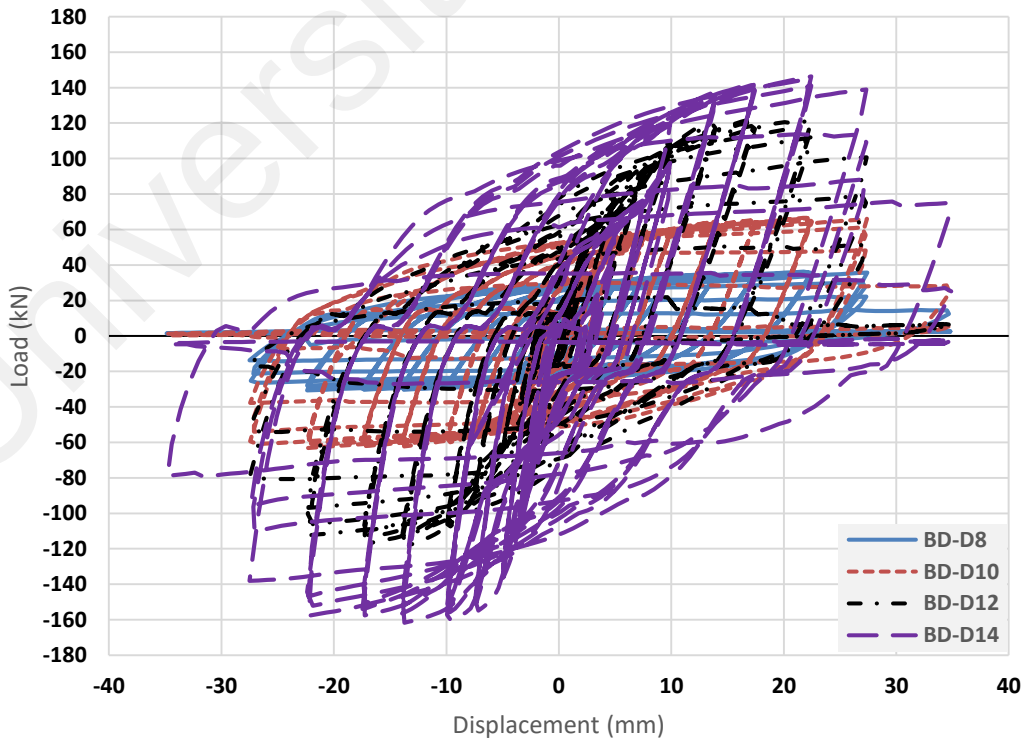

Figure 3.44: Overall view of the device performance considering the bars diameter effect for BD-D8, BD-D10, BD-D12 and BD-D14 specimens

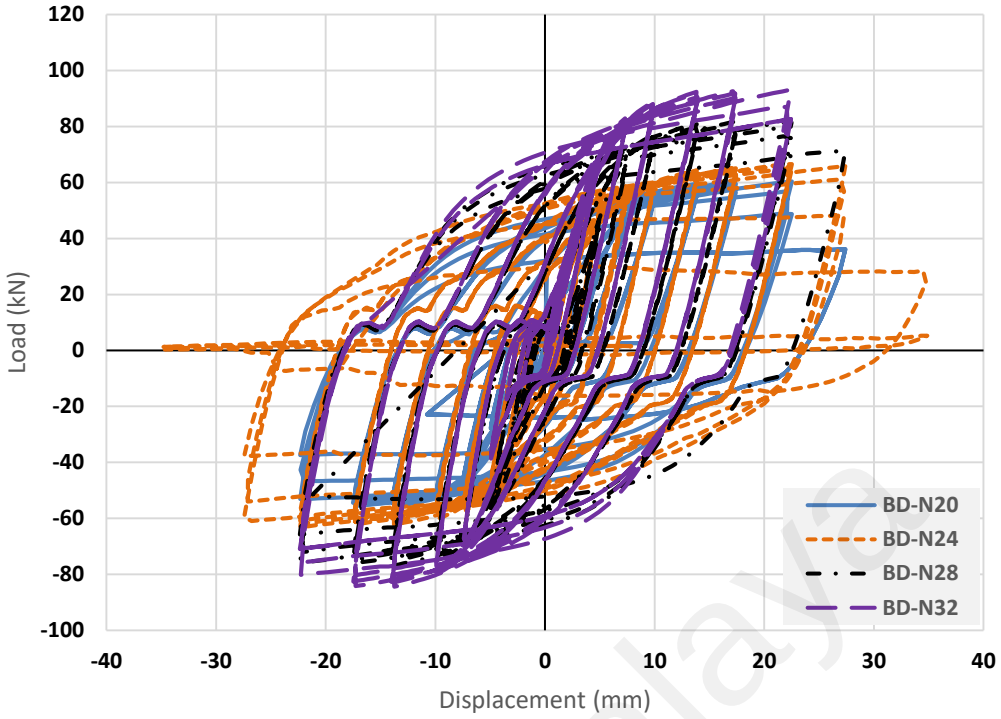

Figure 3.45: Overall view of the device performance considering bars numbers effect for BD-N20, BD-N24, BD-N28 and BD-N32 specimen

3.6 Summary and Conclusions

A new yielding damper, called bar damper (BD), was proposed and tested considering different parameters, i.e. height (Case 1), diameter (Case 2) and numbers (Case 3) of the solid bars. In order to verify the performance of the BD, four specimens for each aforementioned parameter were fabricated and tested under cyclic displacement test; a total of twelve specimens. The proposed devices are quite simple and economical to fabricate and install. Based on the obtained results from experiments, the device specimens exhibited an early energy dissipation due to early plasticity. The experiments showed that BDs were very efficient in energy dissipation, with equivalent viscous damping ratio ranging from 40%, under diameter effect consideration, to 51%, under height effect consideration. The damper also tolerated more than 2849 mm of cumulative displacement, and exhibited very ductile performance. Such high cumulative

displacements indicated good performance of the proposed devices in terms of their robustness against fatigue loading. It should be noted that, the slenderness ratio of these devices was a crucial design variable in Case 1 and Case 2. This was controlling both the effective stiffness and energy dissipation capacity. Lack of local buckling of the solid bars and general buckling in the plates was another advantage of the proposed damper device. Apart from the energy dissipation results, the device specimens exhibited satisfactory performance in terms of maintaining strength and stiffness. It can also be concluded from the experiments that, the bars height parameter has the most effect on dissipating input energy and ductility; however, the bars diameter parameter governed the strength and stiffness capacity. Besides, based on the obtained displacements from four specimens under bars number effect, it was confirmed that the bars number does not have effect on yield displacement of the proposed device. In general, the obtained values of cumulative absorbed energy and displacement for all tested specimens were noticeable.

CHAPTER 4: THEORETICAL APPROACH AND FINITE ELEMENT ANALYSIS OF BAR DAMPER

4.1 Introduction

In the previous chapter, description and concept of the BD device was discussed in detail. Also, test setup of the device along with its loading protocol was intensely presented. In this chapter, theoretical equations of the device were proposed based on the experimental results considering its mechanical mechanism. The values in terms of yield force and yield displacement obtained from the equations were compared to those taken from experimental results to validate the study. Furthermore, a detailed FE analysis was conducted to verify the BD performance. To aid the aim, the benchmark device specimen, i.e,. BD-H100 that was similar to BD-D10 and BD-N24, as shown in the previous chapter, was selected. For FE modelling, the steel elements were modeled using an eight-node linear brick solid element with reduced integration and hourglass control. The inelastic behavior of these elements was considered using the Von Mises yield criterion. The device was modeled when large displacement effects was also taken into consideration. Finally, a simplified bi-linear model of the BD device was proposed to enhance its design and its ease of use for engineers in building and bridge structures.

4.2 Design of the BD

When the BD is subjected to horizontal in-plane force, bending moment and shear force occur simultaneously in the solid bars. However, in cases where the height-to-diameter ratio of the solid bars (which was defined as the aspect ratio) becomes larger, the behavior of the damper was governed by flexure. Herein, the flexure-dominant BD specimen with an aspect ratio of 10 was considered (diameter d = 10 mm and height h = 100 mm) as the benchmark specimen. When the solid bars ends were restrained (fully-welded), horizontal force applied was distributed uniformly for each solid bar.

In order to design the device, the bars were assumed to be fixed at the top and bottom, where they were connected to the plates. In general, the damper mechanical behavior is a double curvature deformation when subjected to relative lateral displacement between the top and bottom plates. This action is illustrated in Figure 4.1(a) and Figure 4.1 (b). The yielding and subsequent formation of plastic hinges occurs at the two ends of the bars. The main design variables were the diameter (d), the height (h), and the number of bars used in the device. With a proper material model and the assumed plastic mechanism (elastic perfectly plastic steel material behavior), the design variables and strength parameters such as yield force (P_y) can be estimated, as explained in the subsequent sections.

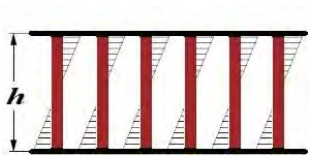

(a) distribution of elastic bending moment

(b) lateral deformation

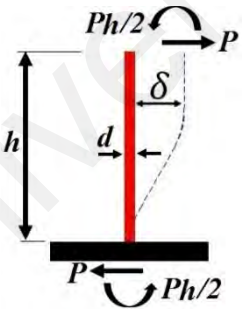

(c) Deformed model

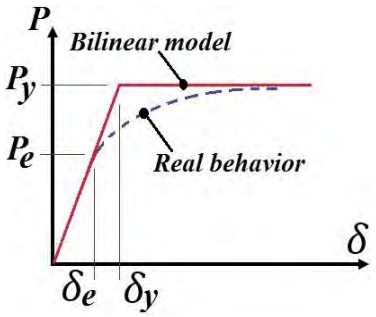

(d) Bilinear mode

Figure 4.1: Dissipative performance of typical flexible steel solid bar

4.2.1 Plastic Mechanism of the BD

To analyze the plastic mechanism of the device, the following proposed adopted with reference to Figure 4.1(c).

The second moment of area (I) of each circular bar is computed as:

$$I = \pi d^4/64 \tag{4.1}$$

With n rows of the bars, the elastic stiffness ($k_{e,d}$) of the device is given by:

$$k_{e,d} = n \times \left(12EI/h^3\right) \tag{4.2}$$

Which, upon substitution of Equation (4.1) becomes:

$$k_{e,d} = n \times \left[0.1875 \times \left(E\pi d^4/h^3\right)\right] \tag{4.3}$$

In which n is the number of rows of the bars, herein is 6, perpendicular to the load direction (see Figure 4.1(b)) and d is the diameter of the bars (10 mm) for the benchmark specimen that is BD-H100/BD-D10/BD-N24. The plastic moment of the bars is given by:

$$M_p = \sigma_y\, d^3/6 \tag{4.4}$$

where σ_y is the yield stress of the material of the bar. Once the displacement is large enough, the bars, upon yielding, form plastic hinges at both ends with a certain angle of rotation, θp. According to Figure 4.1(b) the corresponding plastic displacement of the device is related to the plastic rotation (θp) by the following equation.

$$\delta_p = h \times \tan\theta_p \tag{4.5}$$

For small rotation, $\tan\theta_p \approx \theta_p$, which results in

$$\delta_p = h \times \theta_p \tag{4.6}$$

By considering an elastic perfectly plastic material behavior and based on energy conservation, the following equation can be formulated to estimate the yield strength P_y of the device.

$$P_y \delta_p = 2nM_p \theta_p \tag{4.7}$$

Substituting Equation (4.6) into Equation (4.7) gives

$$P_y = \left(2nM_p / h\right) \tag{4.8}$$

Substituting for the yield moment, the following equation can be derived.

$$P_y = n \times \left(\sigma_y d^3 / 3h\right) \tag{4.9}$$

Therefore the yield displacement can be computed as:

$$\delta_y = \frac{1}{3}\left(\varepsilon_y h^2 / d\right) \tag{4.10}$$

where ε_y is the yield strain of the bar material and is given by σ_y / E, with E being the Young's modulus of elasticity.

4.2.2 Inelastic Modelling of the BD

This section presents the inelastic modelling of the metallic bar damper device considering the behavior of each individual bar. The deformed steel bars and the subsequent force-displacement relation are shown in Figure 4.1(c) and Figure 4.1(d), respectively. In Figure 4.1(c), *d* is the diameter of a steel bar and *h* is the clear height; *P* is the reaction force and *Ph/2* is the moment. The horizontal displacement is denoted by δ. Figure 4.1(d) demonstrates the force-displacement relationship for a single bar of the bar damper device that has a preliminary linear elastic behavior followed with a curved

plastic behavior. δ_e and P_e are the displacement and the force at onset of yielding. The bi-linear model is a simplification of the real behavior. The force and displacement at the formation of plastic hinges are denoted by P_y and δ_y, respectively.

4.3 Finite Element (FE) Model

4.3.1 FE Geometry of the Damper

For geometric modeling of the device, reduced-integration elements were utilized, in which the elements perform one lower integration point in each direction. For such elements, using the reduced integration causes a numerical problem called hour-glassing. To explain this problem, a linear reduced-integration element subjected to bending moment, *M,* due to applied lateral force, *P*, was considered. The steel elements were modeled as 3D8R elements, which are eight-node quadrilateral reduced integration solid elements. Figure 4.2 illustrates an expected deformation mode for the BD device according to the BD design discussed in Chapter 3. The FE model of the device and its deformed shape under lateral loading are shown in Figure 4.3 and Figure 4.4, respectively.

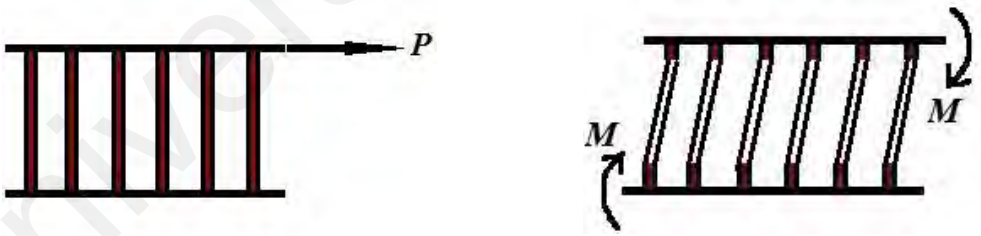

a) before deformation b) after deformation

Figure 4.2: performance mechanism of the BD under applied force

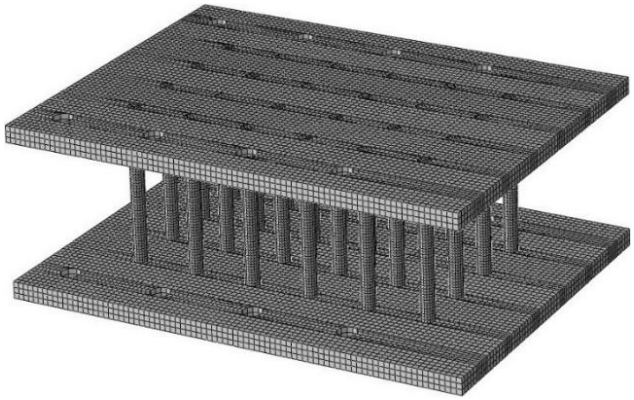

Figure 4.3: BD Model in ABAQUS

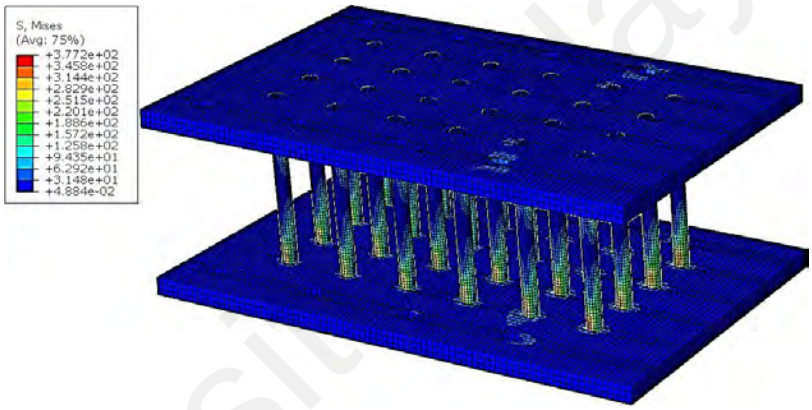

Figure 4.4: BD Deformed shape under Von Mises stress (MPa)

4.3.2 FE Analysis of Steel Deformation using Constitutive Model

A constitutive model of steel material subjected to cyclic loading was adopted and implemented by ABAQUS (ABAQUS, Inc., 2016). The back stress equation of the material model for steel in the software is expressed:

$$\alpha = \sum_{k=1}^{n} \frac{C_k}{\gamma_k}\left(1 - e^{-\gamma_k \bar{\varepsilon}^{pl}}\right) \tag{4.11}$$

in which α is the back stress; shows the yield surface displacement, $\bar{\varepsilon}^{pl}$ represents the equivalent plastic strain (PEEQ). C_k and γ_k stand for model parameters in which

$k = 1,2,3$ and the ultimate kinematic hardening stress is defined by $\sum C_k/\gamma_k$. In this study, A570 steel grade was selected and the coupon tests were performed in accordance with ASTME8M-00 standard (ASTM E8M-00., 2002). The results of the stress-strain relationship curve obtained from the tensile test have been presented earlier in Table 3.2 and Figure 3.10. In the analysis of FE model, the calculated average of yield stress was 341.2 MPa. Poisson's ratio and Young's modulus were 0.3 and 2.01×10^5 MPa, respectively. Consequently, the related C_k and γ_k were specified according to the obtained stress-strain relation curve from the tests. The details of the numerical analysis considering C_k and γ_k parameters are therefore indicated in Table 4.1. The obtained stress-strain curve from the coupon test results and numerical validation are depicted in Figure 4.5, accordingly. As this figure shows, the results from the numerical analysis and that obtained from the coupon test were well agreed. This approved the effect of material model as well as the numerical parameters' accuracy in the present investigation. Hence, in the FE modeling, the properties of the steel grade A570 was used for the damper elements, i.e., solid bars, top and bottom plates.

Table 4.1: Material parameters considered in FE model

C_1 (MPa)	C_2 (MPa)	C_3 (MPa)	γ_1	γ_2	γ_3
8000	15000	3500	270	148	105

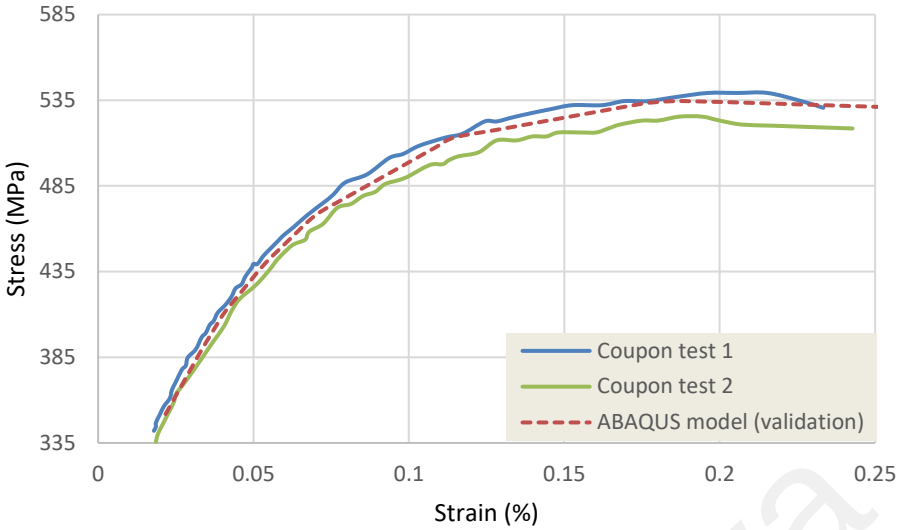

Figure 4.5: Coupon test of steel versus numerical model

Furthermore, for modeling of the steel materials, it was assumed that the material behavior is isotropic and inelastic. Both material and geometry nonlinearities were deliberated in the FE analysis. The BD plates (middle plates) attached to both support and loading plates by means of contact interaction considering normal behavior, hard contact and penalty friction. The experimental test setup (see Figures 3.10 and 3.11) was simulated and its FE discretization with an eight-node linear brick solid element, reduced integration and hourglass control (C3D8R) was implemented.

4.3.3 Stress-strain Curve for Steel Elements

An idealized stress-strain relation curve of steel materials under tension is presented in Figure 4.6. A similar curve from the coupon test, as discussed in Chapter 3, was obtained. The stress in the steel is gained from the applied load to the initial cross-sectional area. This stress is usually called as the nominal or engineering stress which was taken from the coupon test. In the same manner, the strain was taken as the total elongation per initial length of the testing steel under the same test. Similar to the stress, the obtained strain is called the nominal or engineering strain. The nominal stress-strain

relationship curve is proportionate up to the yielding point and the steel acts linearly elastic in this zone (point O to A). The stress-strain ratio in the elastic portion is identified as Young's modulus or modulus of elasticity (E), which is obtained by dividing the stress over the strain in a certain point; approximately equals to 2×10^5 MPa for structural steels. After the yielding point, there is no significant increase in the stress (almost constant), whereas, an increment of 15 to 20 percent compared to the maximum elastic strain is occurred on strain axis. This elongation of the strain is identified as yield plateau in the steel stress-strain relation curve. By increasing the load, the stress again starts to increase with the strain. However, this stress increase is much lesser than the preliminary elastic stress. This phenomenon is recognized as the strain hardening (from point C). Afterward, the stress increase goes on up to its maximum value known as ultimate stress (strength) or tensile stress (strength). After the ultimate stress, steel material loses strength due to the strain increment and it falls off till the rapture happens. The stress-strain relation curve obtained from the coupon tests was utilized in this study and already shown in Chapter 3, Figure 3.10.

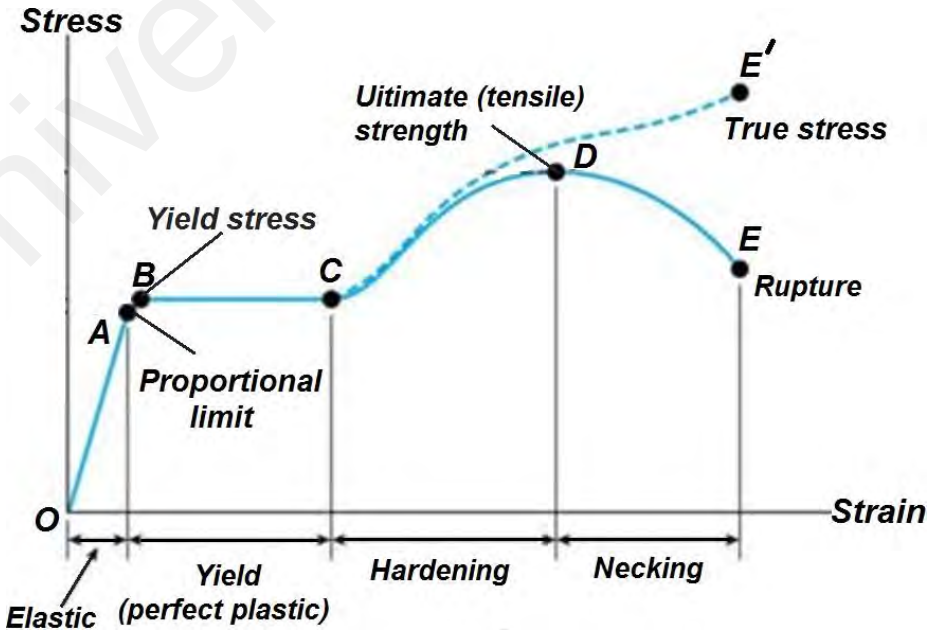

Figure 4.6: Stress-strain relationship curve for steel materials

4.3.4 Von Mises Yield Stress Criterion

In this study, the Von Mises yield stress was used for FE analysis of the damper device to monitor the yield strength of the steel materials including solid bars and their attached plates, loading plate, support plate and bolts. The Von Mises stress, also known as the octahedral shear stress, is a criterion utilized to define the yield or fracture statement of a material under tensile loading. The von Mises stress is commonly utilized for metals or ductile materials, e.g. steel, copper, zinc, etc. The von Mises yield criterion expresses the material yield limit under tension force such that, if the Von Mises stress of the material is smaller than the yield stress of that material, thus, the material does not yield. In the event of plane stress, the envelope of the stress is plotted as an ellipse (see Figure 4.7).

For the Von Mises Criterion, the following expression can be written:

$$F_{ty} = (\sqrt{3})(F_{sy}) \tag{4.18}$$

in which, F_{ty} and F_{sy} are the yield tensile and shear stress, respectively. Similarly, the following equation can be given for a linear material behavior at the failure level:

$$F_{tu} = (\sqrt{3})(F_{su}) \tag{4.19}$$

in which, F_{tu} and F_{su} are the ultimate tensile and shear stress, respectively. The Von Mises criteria are deliberated largely illustrative for ductile materials, where the correlations between F_{tu}/F_{ty} and F_{su}/F_{sy} are significantly close for almost any type of analysis.

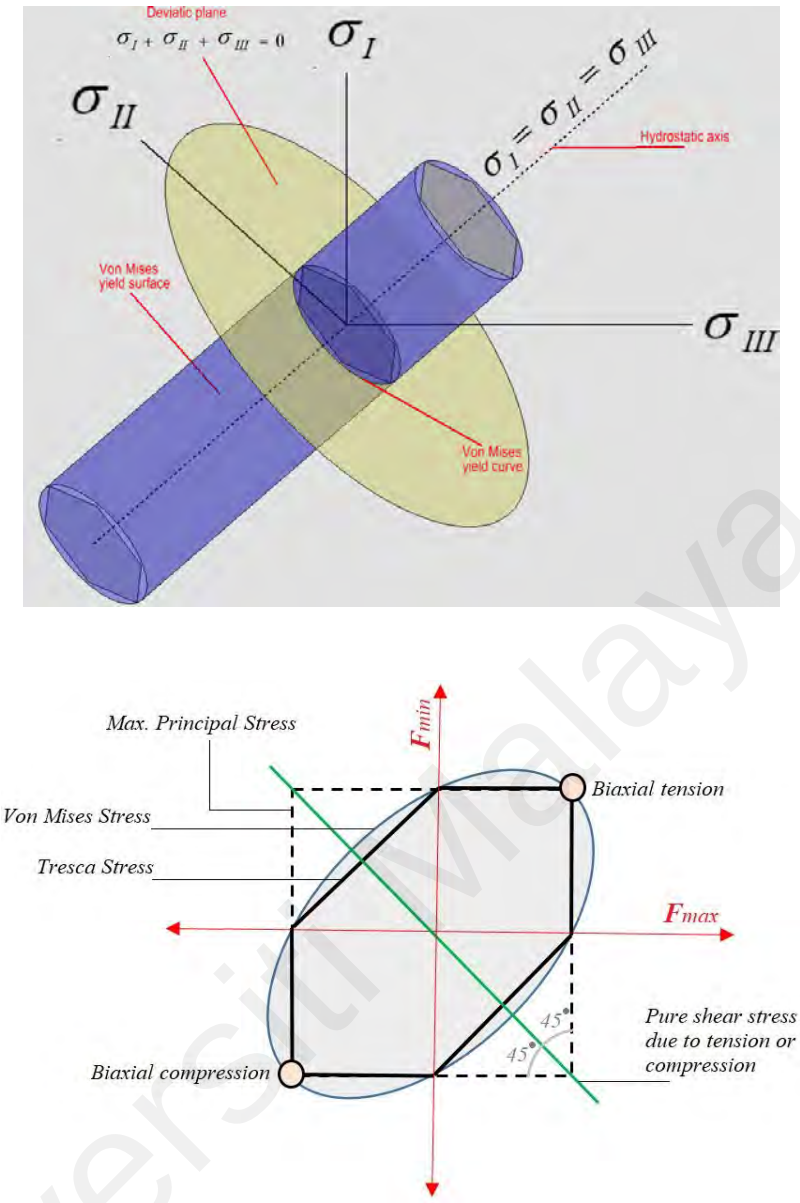

Figure 4.7: Von Mises and Maximum Principal stresses criteria

It is noted that, the maximum distortion energy criterion initiated from the materials, in particular ductile materials, works in a different way once the experiments developed from uniaxial stress to biaxial stress tests. It is observed that, the resistance stresses are much bigger than those of corresponding uniaxial tests. Hence, the criteria engaging a complete stress tensor have been considered.

The uniaxial yield stress can be obtained in terms of the three principal stresses as:

$$\sigma_y^2 = \frac{1}{2}\left[(\sigma_I - \sigma_{II})^2 + (\sigma_{II} - \sigma_{III})^2 + (\sigma_{III} - \sigma_I)^2\right] \tag{4.20}$$

where σ_I, σ_{II} and σ_{III} are the tensile or compressive stresses that act in the three principal directions and σ_y is the yield stress. The principal stresses act in the three mutually perpendicular planes that have zero shear stress. The Von Mises yield surface assumes that the yielding is independent of the equivalent stress. Figure 4.7 demonstrates the Von Mises criterion in 2D and 3D form.

4.3.5 Modeling Inelastic Behavior of Steel

An accurate FE modelling method was utilized by means of ABAQUS software in order to considering the inelastic behavior of the steel elements in the present study. To model the plasticity, true stress and true strain must be used instead of the nominal stress and strain, in which the nominal strain is defined as:

$$\varepsilon_{nom} = \frac{l - l_0}{l_0} = \frac{l}{l_0} - 1 \tag{4.21}$$

Accordingly, the true strain, ε, can be obtained from:

$$\varepsilon = \ln\frac{l}{l_0} = \ln(1 + \varepsilon_{nom}) \tag{4.22}$$

Assuming the incompressibility of the material, its volume remains constant.

$$l_0 A_0 = lA \tag{4.23}$$

So, the actual area, A, is calculated from:

$$A = A_0\left(\frac{l_0}{l}\right) \tag{4.24}$$

By knowing the true stress equation as:

$$\sigma = \frac{F}{A} \tag{4.25}$$

and by substituting the actual area in the true stress, the nominal stress is defined as

$$\sigma_{nom} = \frac{Fl}{A_0 l_0} \tag{4.26}$$

Therefore, for the true and nominal stress relationship, the below expression is defined

$$\sigma = \sigma_{nom}\left(\frac{l}{l_0}\right) \tag{4.27}$$

and by considering the relation between the true strain and nominal strain, for the final relation of the true stress and nominal stress is determined as

$$\sigma = \sigma_{nom}\left(1 + \varepsilon_{nom}\right) \tag{4.28}$$

The true strain calculated from the aforementioned equations is a combination of elastic strain and plastic strain. Accordingly, the plastic strain can be obtained from the following equation:

$$\varepsilon_p = \varepsilon_t - \varepsilon_e = \varepsilon_t - \frac{\sigma}{E} \tag{4.29}$$

In which ε_p and ε_e are the plastic strain and the true elastic strain, respectively. ε_t represents the true total strain. σ and E are also the true stress and modulus of elasticity, respectively. In the coupon test, the nominal stress-strain relation curve was obtained and according to the equations above, the true stress and true strain values as well as the plastic strain for steel elements in ABAQUS were obtained, accordingly. These are tabulated in Table 4.2 and plotted in Figure 4.8.

Table 4.2: True and plastic stress-strain values for steel elements used in FE model

Nominal Strain	Nominal Stress (MPa)	True Strain	True Stress (MPa)	Plastic Strain
0.0179487	342.0785134	0.017789524	348.218378	0
0.0198718	351.5807241	0.019676933	358.5672659	0.017936
0.0314103	389.5895668	0.030927089	401.826692	0.028976
0.0384615	410.9687375	0.037740291	426.7752116	0.035669
0.0512821	439.4753695	0.050010467	462.0125894	0.047768
0.0673077	467.9820016	0.065139309	499.4807938	0.062715
0.111538	513.1172345	0.105744642	570.3493046	0.102976
0.176923	534.4974764	0.162903406	629.0623734	0.15985
0.226282	534.4974764	0.203987	655.4446343	0.200805
0.233333	530.556	0.20972	654.3522231	0.206544

To model the steel hardening, the isotropic hardening model was used. This model assumes that the center of the yield surface remains stationary in the stress space however the size of the yield surface changes uniformly in all directions such that the yield stress varies according to the plastic strains. This model is suitable for dynamic problems with large deformations.

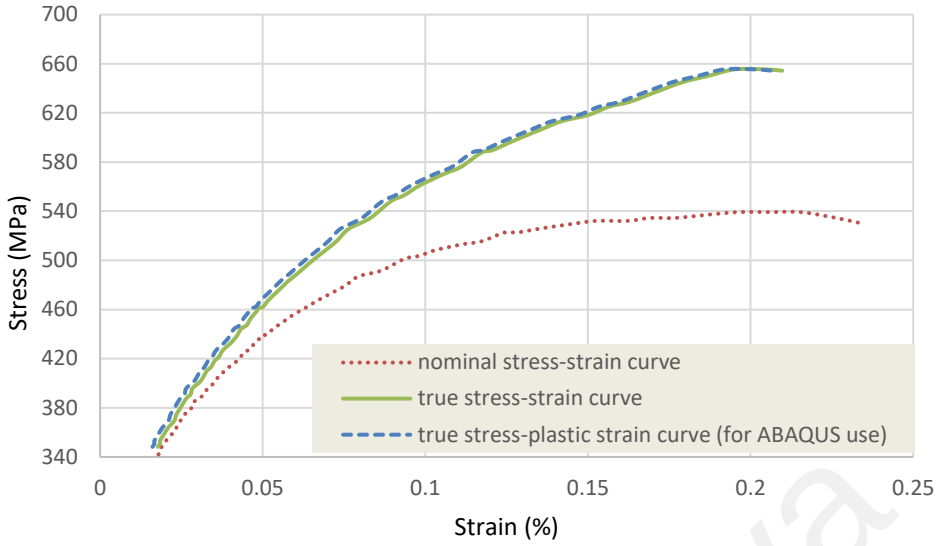

Figure 4.8: Stress-strain relation curves used in ABAQUS for steel elements

4.3.6 Hysteretic Loop of Steel Material

Cyclic loading behavior is strictly correlated with the history of plastic loading and it is progressively developed through the cyclic loading test (Dong & Zhang, 1993). It should be noted that, steel hysteresis loop has a direct relationship with applied loading history. It is accepted that, a hysteresis loop of steel material is categorized into three sections, namely skeleton curve, loading and reloading (softening) curves. The skeleton curve of a hysteresis loop is straightly reflect the response changes under monotonic and cyclic loading. In this regard, Equation (4.30) was proposed by Ramberg and Osgood (NACA-TN-902, 1943) which is related to a skeleton curve model, in which the model is commonly accepted for steel materials under cyclic loading tests. Therefore, the parameters of this model were used as pivotal parameters to express the FE analysis of the steel materials in this study.

$$\frac{\Delta\varepsilon}{2}=\left(\frac{\Delta\varepsilon_e}{2}+\frac{\Delta\varepsilon_p}{2}\right)=\frac{\Delta\sigma}{2E}+\left[\frac{\Delta\sigma}{2K'}\right]^{\frac{1}{\eta'}} \tag{4.30}$$

$\Delta\varepsilon$ is the total strain amplitude and, $\Delta\varepsilon_e$ and $\Delta\varepsilon_p$ are the elastic and plastic strain amplitude, respectively. $\Delta\sigma$ is the stable stress, whereas, K' and η' are the cyclic strength hardening factor and cyclic strain hardening index, respectively. The strain and stress may be adjusted using Equation (4.31) to see the steel yield strength trace as well as to obtain a perfect hardening relationship.

$$\widetilde{\varepsilon}=\widetilde{\sigma}+\left[\frac{\widetilde{\sigma}}{\widetilde{K}}\right]^{\frac{1}{\eta}} \tag{4.31}$$

in which, $\widetilde{\varepsilon}=\varepsilon/\varepsilon_y$ and $\widetilde{\sigma}=\sigma/\sigma_y$. $\widetilde{K}$ is the cyclic hardening factor of regularization and η is the proportional coefficient. It is proved after cyclic loading, the steel ductility declines considerably. In other words, low cycle fatigue causes the weakening and accumulative damage before resulting structural damage.

Four stages are usually considered for steel materials hysteresis criteria include loading curve, unloading curve, reloading direction and reloading curve. These stages of steel hysteretic criteria are expressed below in details.

1. In the first stage, the steel loading passes through the monotonic loading curve with both uniaxial tension and compression.
2. In the second stage, the steel unloading curve passes through the elastic line. In this stage, the initial elastic modulus (E_s) is similar to unloading stiffness.
3. In the third stage, the steel reloading curve goes back to the preceding peak point of the same direction. This hypothesis is posed owing to the test phenomenon. This simplified method has proposed by Légeron et al. (Légeron et. al., 2005) and

it is extensively utilized in consideration of constitutive models which is known as ‘‘peak-orientation model’’.

4. In the fourth stage, the steel reloading curve slope is set between the tangent and unloading stiffness which is from the onset point, i.e. ε_0 and σ_0, to the end point, i.e. ε_p and σ_p, on the ε-axis from the hysteretic curve by means of ‘‘peak-orientation criteria’’. d_1 and d_2, as demonstrated in Figure 4.9, are expressed in Equations (4.32) and (4.33).

$$d_1 = (\varepsilon - \varepsilon_0)E_s \tag{4.32}$$

$$d_2 = (\varepsilon - \varepsilon_0)(E_s - E_k) \tag{4.33}$$

in which, ε_0 is the strain on ε-axis at the start point, E_s and E_k are modulus of elasticity and tangent stiffness, respectively.

The proportional coefficient (η) depends upon the boundary conditions; ($0 \leq \eta \leq 1$). Hence, based on the above analysis, every stress point can be defined for unloading condition in the hysteresis curve as expressed in Equation (4.34) and (4.35).

$$\sigma = d_1 - \eta d_2 = (\varepsilon - \varepsilon_0)E_s - \eta(\varepsilon - \varepsilon_0)(E_s - E_k) + \sigma_0 \tag{4.34}$$

$$E_k = \frac{\sigma_p - \sigma_0}{\varepsilon_p - \varepsilon_0} \tag{4.35}$$

where σ_0 is the first point stress and ε_0 is the first point strain. σ_p and ε_p are the end point stress and strain, respectively. By taking the above expressions, the basic procedure of an incremental step for generating steel material hysteretic loop in ABAQUS software can be presented in Figure 4.10, where ε and ε_y are the elastic and yield strain, respectively.

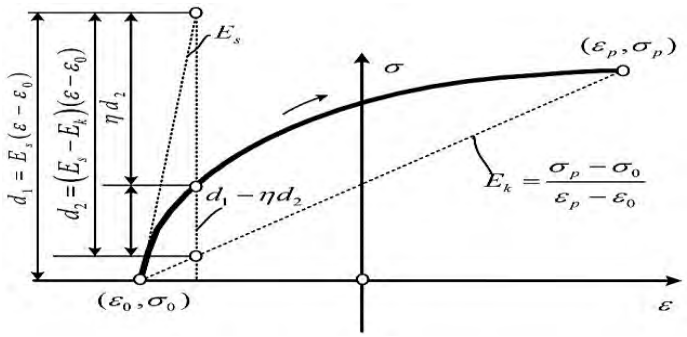

Figure 4.9: Reloading criteria for a steel hysteresis curve (Yongjiu et al., 2011)

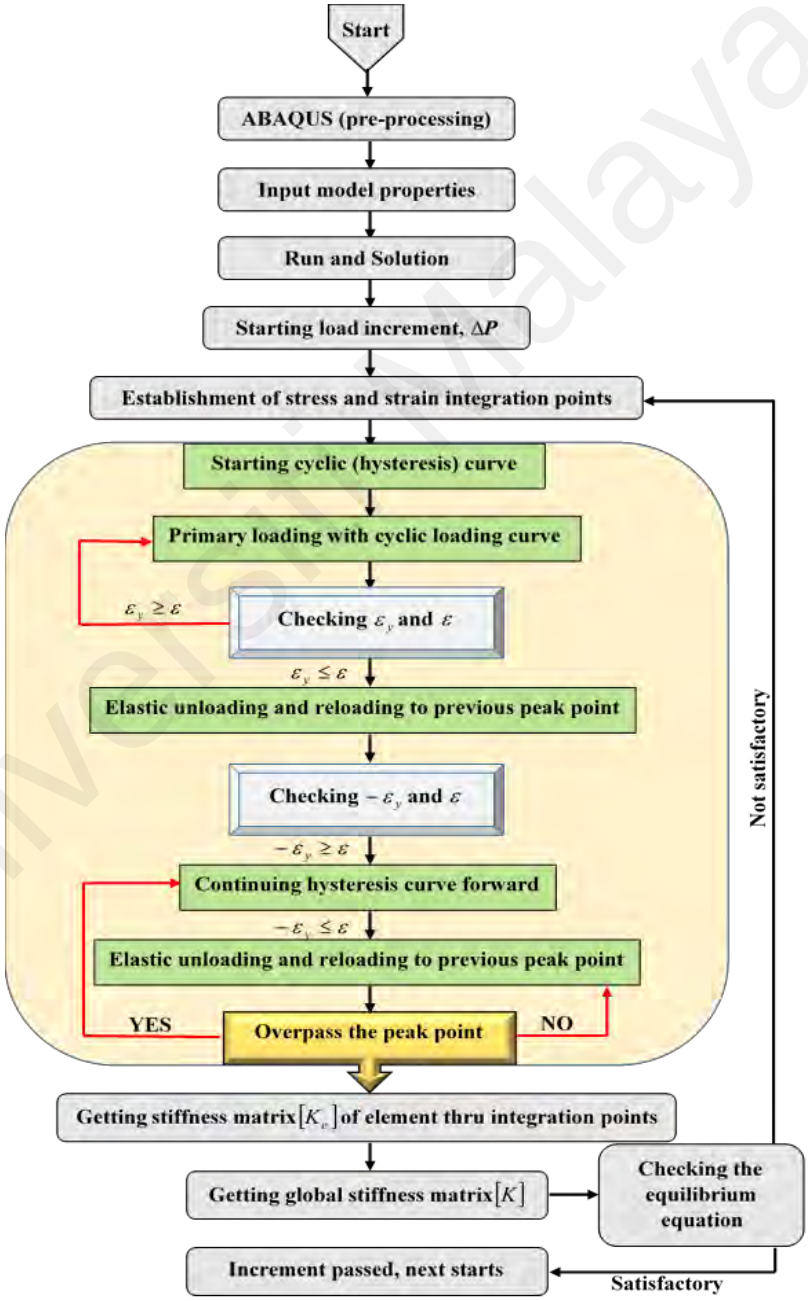

Figure 4.10: Incremental procedure of a hysteretic loop for each element in ABAQUS (Yongjiu et al., 2011)

4.4 Comparison of Experimental, Theoretical and FE Results

In general, metallic damper devices dissipate energy through plastic deformation. Since damage is inevitable after yielding, it is necessary to design the dampers in such a way that they remain elastic under service loads. In this regard, an accurate estimation of yield strengths is crucial. The obtained values from the proposed formulas show that, yield force of the devices was reasonably well estimated by the theoretical models, shown as P_y (Theoretical yield force). It is worth mentioning that, because of the strain hardening phenomenon the maximum strengths (P_{max}) were unstably greater than the yield strengths obtained from the experiments (P_{yexp}) for each individual specimen. The results of experimental (all specimens) and FE results (benchmark specimen only) were compared to the theoretical values as indicated in Table 4.3, Table 4.4 and Table 4.5 considering height, diameter and number of solid bars, respectively.

Table 4.3: Experimental, theoretical and FE results, height effect (units: kN, mm)

Specimen	$k_{e,d}$	δ_y	$\delta_{y\exp}$	$\delta_{y\,FE}$	P_y	$P_{y\exp}$	$P_{y\,FE}$	$P_y / P_{y\exp}$
BD-H70	20.66	0.28	0.25	-	9.74	8.10	-	1.20
BD-H100/BD-D10/BD-N24	7.10	0.56	0.50	0.52	6.82	8.74	9.46	0.78
BD-H130	3.23	0.96	0.99	-	5.25	5.64	-	0.93
BD-H160	1.73	1.45	1.76	-	4.26	5.40	-	0.79

Table 4.4: Experimental, theoretical and FE results, diameter effect (units: kN, mm)

Specimen	$k_{e,d}$	δ_y	$\delta_{y\exp}$	$\delta_{y\,FE}$	P_y	$P_{y\exp}$	$P_{y\,FE}$	$P_y / P_{y\exp}$
BD-D8	2.90	0.71	0.73	-	3.50	3.95	-	0.88
BD-H100/BD-D10/BD-N24	7.10	0.56	0.50	0.52	6.82	8.74	9.46	0.78
BD-D12	14.66	0.47	0.50	-	11.79	12.85	-	0.92
BD-D14	27.15	0.41	0.49	-	18.72	17.10	-	1.09

Table 4.5: Experimental, theoretical and FE results, number effect (units: kN, mm)

Specimen	$k_{e,d}$	δ_y	$\delta_{y\exp}$	$\delta_{y\,FE}$	P_y	$P_{y\exp}$	$P_{y\,FE}$	$P_y / P_{y\exp}$
BD-N20	5.90	0.56	0.50	-	5.68	6.25	-	0.91
BD-H100=BD-D10=BD-N24	7.10	0.56	0.50	0.52	6.82	8.74	9.46	0.78
BD-N28	8.25	0.56	0.49	-	7.96	8.80	-	0.90
BD-N32	9.42	0.56	0.48	-	9.10	9.87	-	0.92

As it can be observed from the tables, prediction of yield displacement was satisfactory. In general, the yield force was slightly underestimated by the theoretical model, hence the design was expected to be conservative. However, this was not the case for BD-H160 and BD-D14, where the theoretical model slightly overestimated the yield force.

For FE model and analysis, the BD-H100 specimen with a height of 100 mm and 24 numbers of solid bars was selected. Specimens BD-H100, BD-D10 and BD-N24 had similar characteristics. Therefore, these specimens were chosen as the benchmark one. Verification of the proposed theoretical equations was made with the experimental results of all BD specimens. Further verification of proposed equations was also carried out through the FE analysis for the benchmark model. Specifications of Section 4.3 were used to carry out the FE model. Figure 4.11 shows the FE model of the benchmark specimen considering the entire experimental test setup including loading and support plates as well as the attached bolts. Figure 4.12 displays the discretization of the BD specimen with its all related parts in the FE model, accordingly.

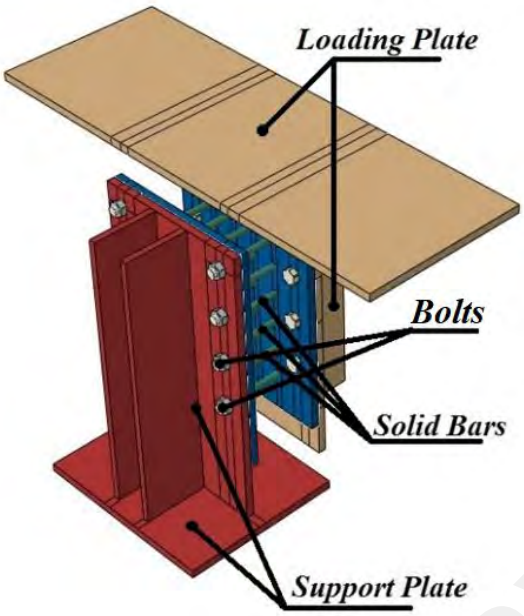

Figure 4.11: Model of test setup in ABAQUS for the FE analysis

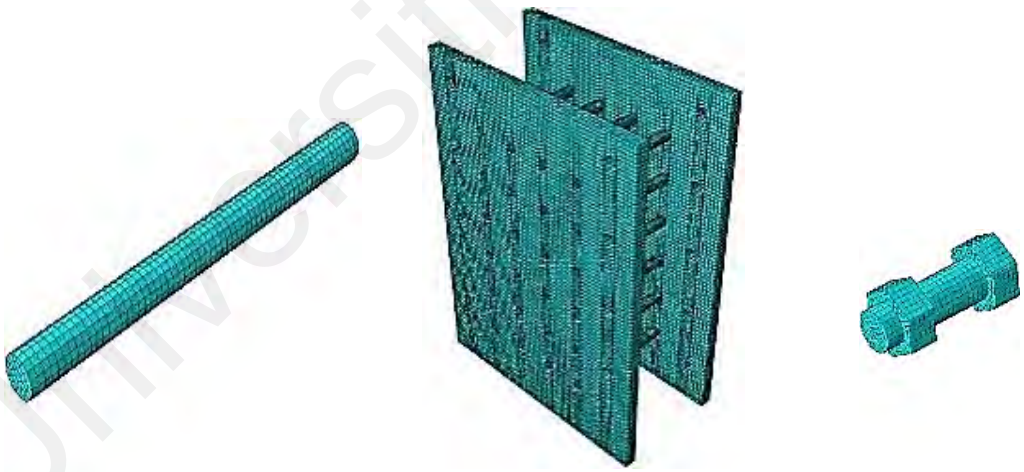

(a) Solid bar (b) BD (c) bolt and nut

Figure 4.12: FEM of the BD including bolts, stiffeners, support and loading plates

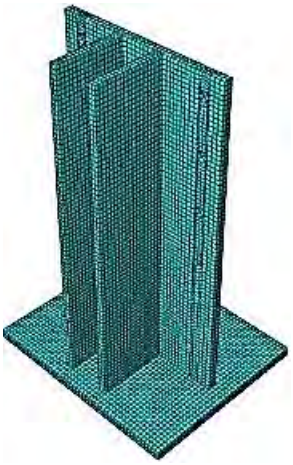

(d) Support plate

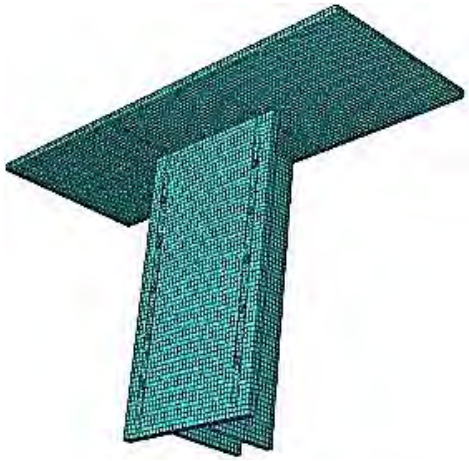

(e) Loading plate

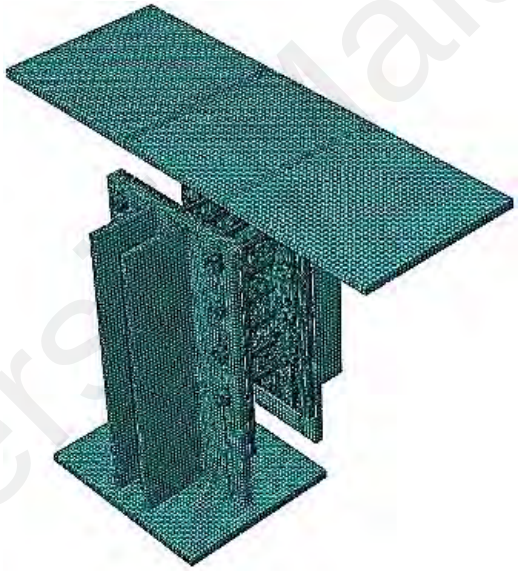

(f) FE discretization of the entire test setup in ABAQUS

Figure 4.12: FE model of the BD including bolts, stiffeners, support and loading plates (**continued**)

Figure 4.13 shows the hysteresis loop of the benchmark specimen obtained from the experimental test and FE analysis. Referring to Table 3.3 in Chapter 3, BD-H100 specimen was failed at cycle 28 in step 9 under the experimental test. It was observed from the table that, the maximum strength and displacement for BD-H100 specimen were

64.84 kN and 27.39 mm, respectively. These values were compared to the FE analysis and a good agreement was found between experimental and FE results, in which the maximum strength and displacement in the FE analysis were 66.58 kN and 27.17 mm, respectively. Figure 4.14 and Figure 4.15 show the deformed shape of the specimen at the end of the test in experimental study and FE analysis, respectively. It can be seen from Figure 4.15 that, the Von Mises stress values for solid bars in FE analysis exceeded the ultimate stress (fracture statement) which was 532.35 MPa obtained from the coupon test. This stress infringement occurred at both ends of the solid bars after deformation, which represents the cracks (damage). No fracture statement was observed for other parts under the test.

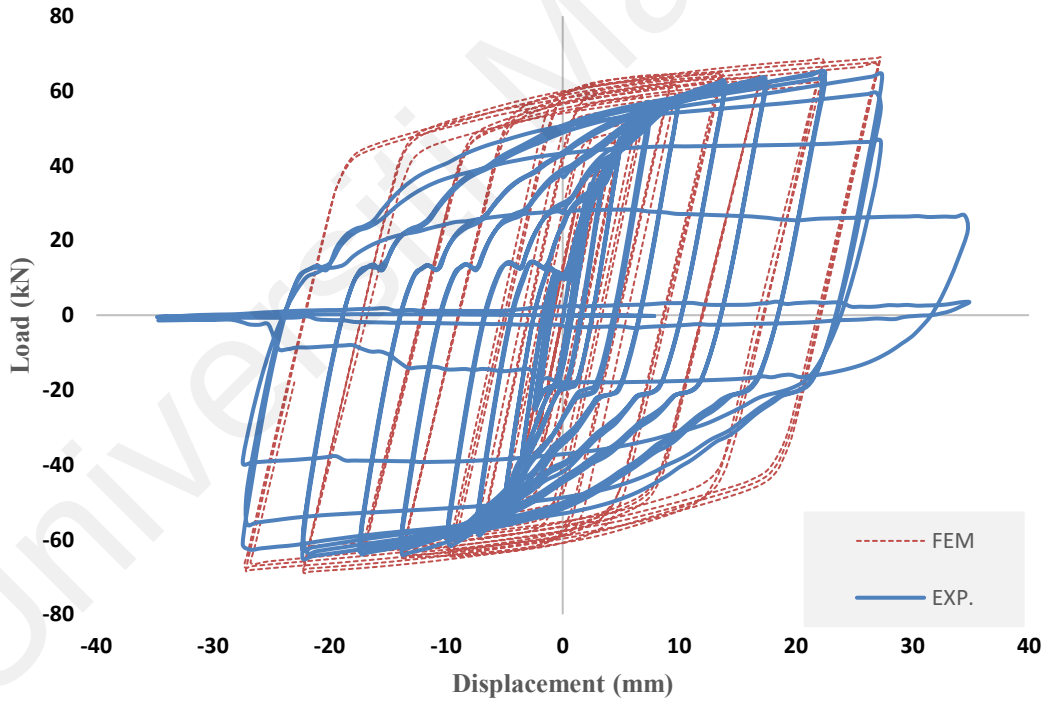

Figure 4.13: Hysteresis loops for the benchmark specimen under cyclic loading for experimental and FE model

Figure 4.14: Overall deformation of benchmark specimen under applied cyclic loading

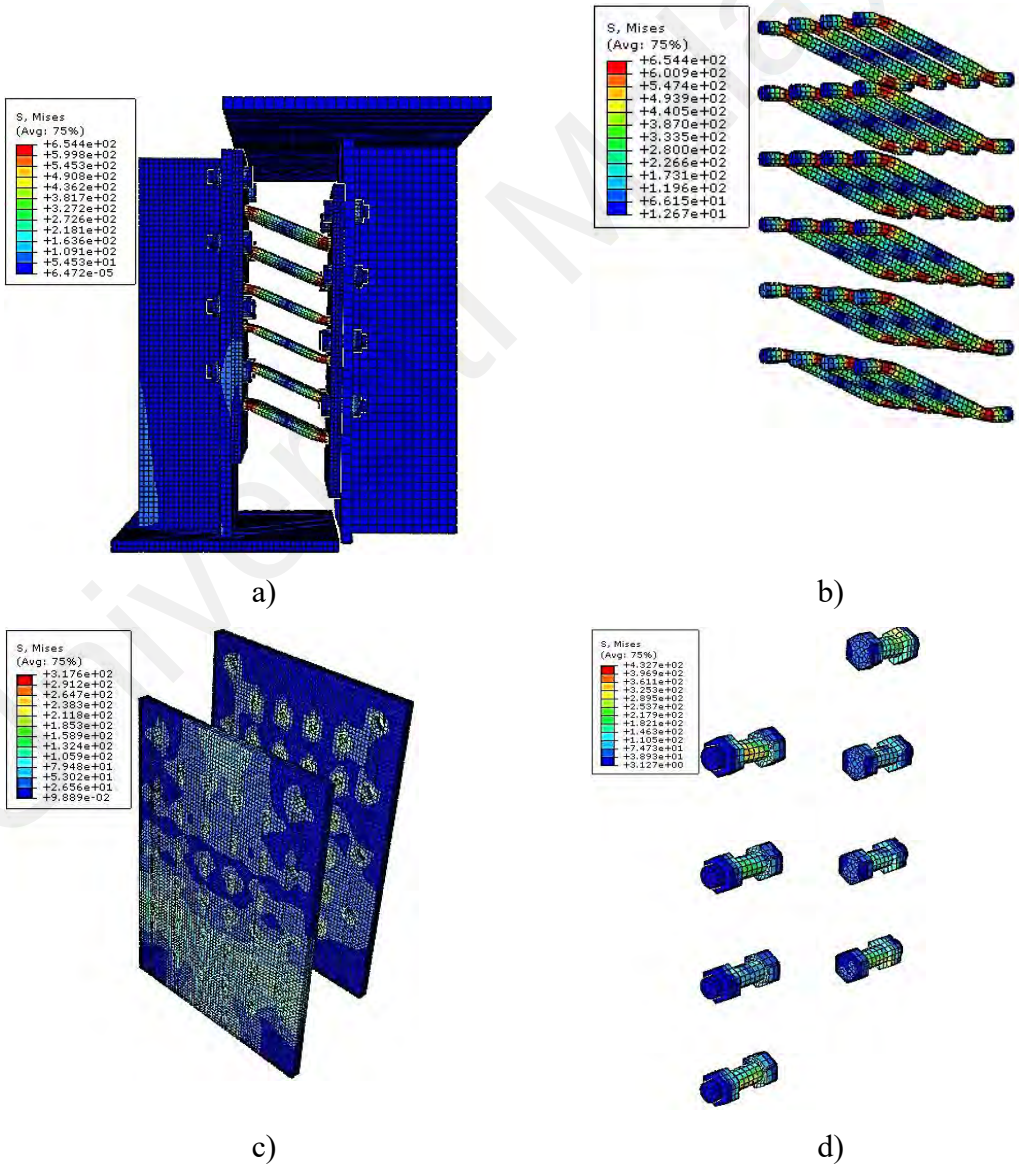

Figure 4.15: Distribution of Von Mises stress on (a) whole model, (b) solid bars, (c) damper plates and (d) bolts and nuts under cyclic deformation (unit: MPa)

4.5 Bi-linear Model

To utilize the proposed BD device as a yielding damper in building and bridge structures, a streamlined nonlinear spring model of the device can be proposed to be implemented in those structural analysis and design software like CSi products, e.g. ETABS, SAP2000 and CSiBridge where they have the facilities to use such spring models. In other words, for a simplified model, the yield displacement and force as well as the initial stiffness were the key parameters, which need to be determined. To this end, the load–displacement curve was estimated with a bi-linear model from the hysteresis loop obtained from the experimental and FE studies. To tune the bi-linear curve with the experimental and numerical results, several device specimens may be chosen. Therefore, the correlation between the stiffness and strength of the devices considering investigated parameters can be obtained. Based on the obtained hysteresis behavior results from experimental and FE studies, the bi-linear model of the BD-H100 specimen, which was similar to BD-D10 and BD-N24 specimens, was given and illustrated in Figure 4.16. To present a clear trend of the proposed bi-linear model given in Figure 4.16(a) and its zoomed view is also shown in Figure 4.16(b). This simplified bi-linear model can be employed in modeling of the performance of bar dampers utilized as passive yielding damper devices. Based on this figure, the yield force and displacement were approximated as 9.10 kN and 0.54 mm for the benchmark specimen, respectively. This bi-linear model was obtained from the benchmark specimen with its unique geometry. Thus, the result obtained for this model might be different when using other device specimens or other BD-type devices with different geometry, material, bars size, bars arrangement, etc.

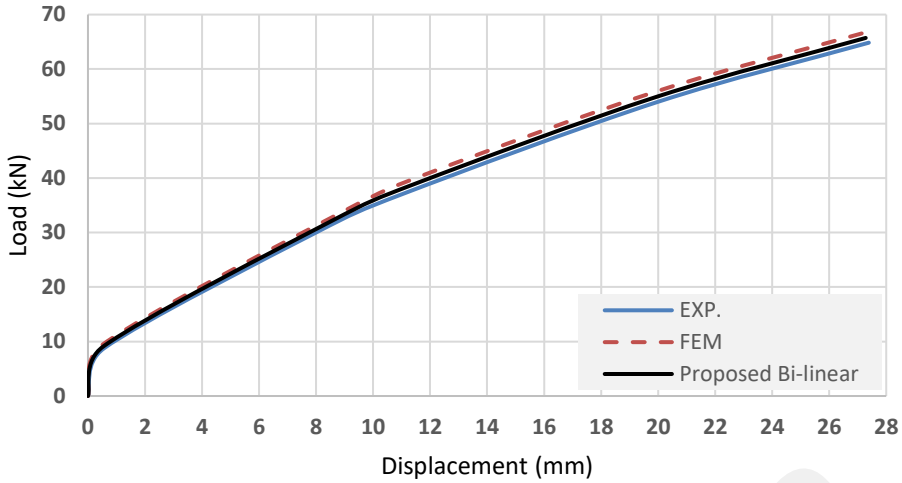

a)

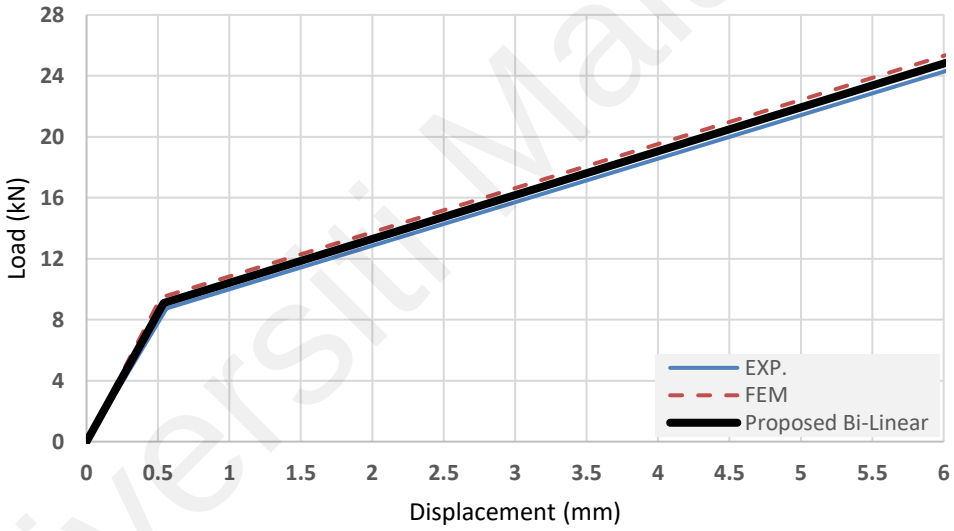

b)

Figure 4.16: Proposed bi-linear model for benchmark specimen a) overall view and b) zoomed view

A detailed explanation of the proposed bi-linear model for the BD device is given in Figure 4.17. In this figure, α is the dimensionless parameter known as stiffness ratio with a value less than one. Also, μ is the ductility parameter which is expressed as a ratio of

the maximum displacement ($d_{\max}$ or d_p) with respect to the yield displacement (d_y) of the damper device. Strength reductions are commonly defined from the elastic strength, P_e , using reduction factor, R_y . Thus, ductility demand, μ , in an inelastic range is applied on structural elements. Ductility is measured as a structural deformation capacity (range from d_y to d_p) before the rapture, when the structure reaches to its yield strength, P_y. The strength reduction is because of nonlinear hysteretic behavior of the system. Therefore, the component of R_y is determined as:

$$R_y = \frac{P_e}{P_y} = \frac{d_e}{d_y} \tag{4.36}$$

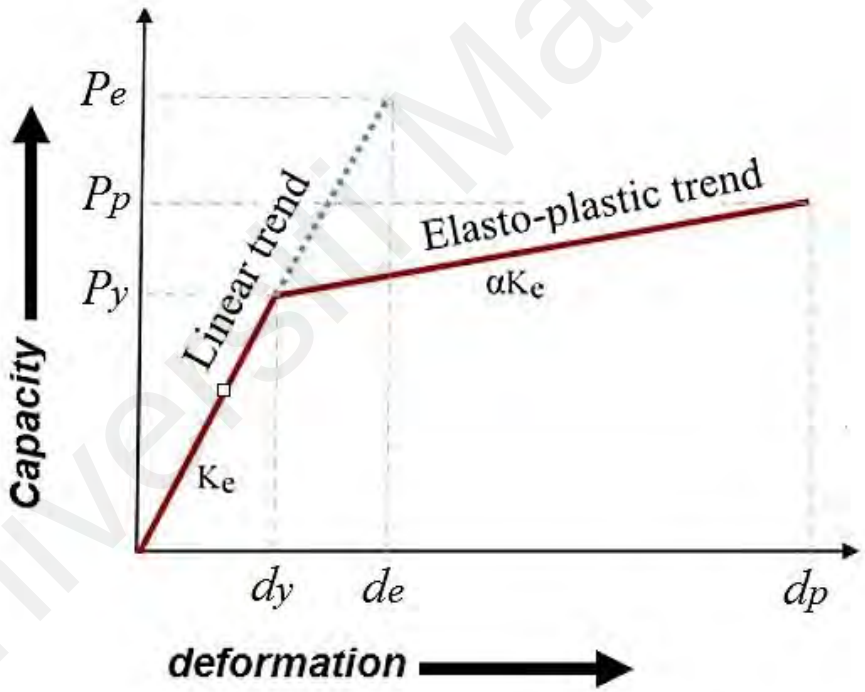

Figure 4.17: Theoretical background of the bi-linear model for BD dampers

4.6 Summary and Conclusions

The experimental tests for the proposed bar damper were carried out and discussed in Chapter 3. In this chapter, it was attempted to propose the theoretical formulas of the

device and validate them by comparing them with the experiments and a FE analysis. For this purpose, the theoretical equations of the damper device were derived based on its plastic mechanism. Later on, a full-scale FE model of the benchmark specimen, i.e. BD-H100, BD-D10, BD-N24, consists of loading and support plates was modeled and analyzed. The steel elements were modeled using an eight-node linear brick solid element with reduced integration and hourglass control. The inelastic behavior of these elements was considered through Von Mises yield criterion. To have the real performance of the device, geometric and material nonlinearities of the steel elements were taken into account considering large displacement effect. As a result, the FE analysis was compared and validated with the experimental results and a notable agreement was found between the results. According to the experimental and FE analyses, a simplified bi-linear model of the BD device was proposed to enhance the practical use of the device for structural engineers in order to implement the device in design of building and bridge structures. Based on the obtained results from the experiments, FE results and derived equations, it was shown that the performance of the device can acceptably be predicted through the proposed equations, in which the predicted yield force and displacement taken from the equations were well-agreed with the experimental and FE results.

CHAPTER 5: PERFORMANCE ASSESSMENT OF STRUCTURAL FRAMES WITH BAR DAMPER

5.1 Introduction

Rigid structural frames are widely considered in the construction of buildings and bridges in seismically active zones (Apostolakis & Dargush, 2009; Chou et al., 2016; Meng et al., 2019; Tafsirojjaman et al., 2019). As a result, these systems are frequently used in the seismic resistant design of structures. Nevertheless, unwarranted deformation owing to the loss of stiffness and strength restricts the efficiency of the system. This is because of the ruptures of welds in the beam-column connection under severe ground motions. Substantial stress absorption by the welds leading to early brittle failure (notable strength and stiffness reduction), results in performance loss (Silwal et al., 2015).

Semi-rigid frames are also typically assembled with bolted connections and used for the beam-column connections. This system of construction shows suitable ductility when exposed to dynamic loadings. The adequate deformation capability significantly decreases the chance of brittle failure in the connections, although, extreme ductility due to the loss of stiffness and energy dissipation capacity in the bolts keep on structural distress. Therefore, design alteration for beam-column connections to keep structural strength, stiffness and energy dissipation is vitally needed (Briones & Llera, 2014; Domenico & Ricciardi, 2019; Dougka et al., 2014; Franco et al., 2010; B. Qu et al., 2019; Ranaei & Aghakouchak, 2019; Ras & Boumechra, 2016; Soong & Spencer Jr, 2002).

The present study concentrates on performance improvement of such structural frames by incorporating semi-rigid frames equipped with the BD device in the beam-column corner connections. To aid the aim, a bar damper (BD) device, as introduced and verified in the previous chapters, was used to improve the performance of structural frames. To this end, a BD specimen was made with its real form considering the full scale.

SolidWorks program was used for preparing accurate details and drawing in order to manufacture the BD device using laser-cut technique. Figures 5.1 and 5.2 show the detailed dimensions and rendered view of the BD device, respectively. The BD device was placed at the location of beam-column connection in the prepared frame as shown in Figure 5.3. To evaluate the performance of the BD device, a quasi-static cyclic loading was applied to the bare frame and the frame equipped with the dampers. Two BD devices were attached to the beam-column connection at each side of the frame to facilitate the design. It was observed that, the BD devices simply deformed under the applied load and they started to dissipate energy as soon as the bars yielding began at early stage of the frame bending. Test results obtained from the bare frame and the one equipped with the BD was compared to each other in terms of strength, stiffness, deformation capacity and harvested energy to assess the efficiency of the design proposal and to justify the possibility of using BD-type devices in design of engineering structures exposed to vibration or dynamic loads.

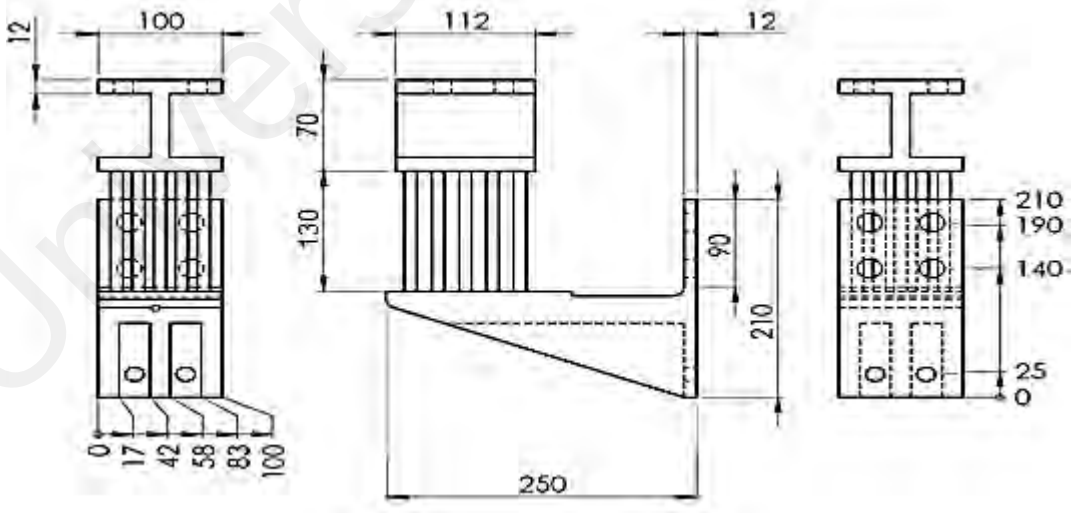

Figure 5.1: Detailed dimensions of the BD installed to in the test frame (units: mm)

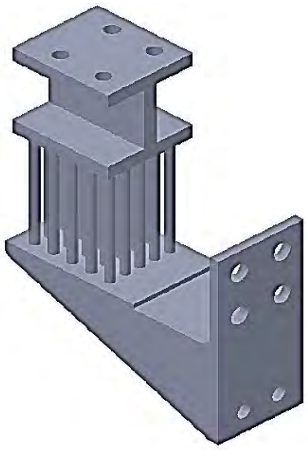

Figure 5.2: Rendered view of the BD

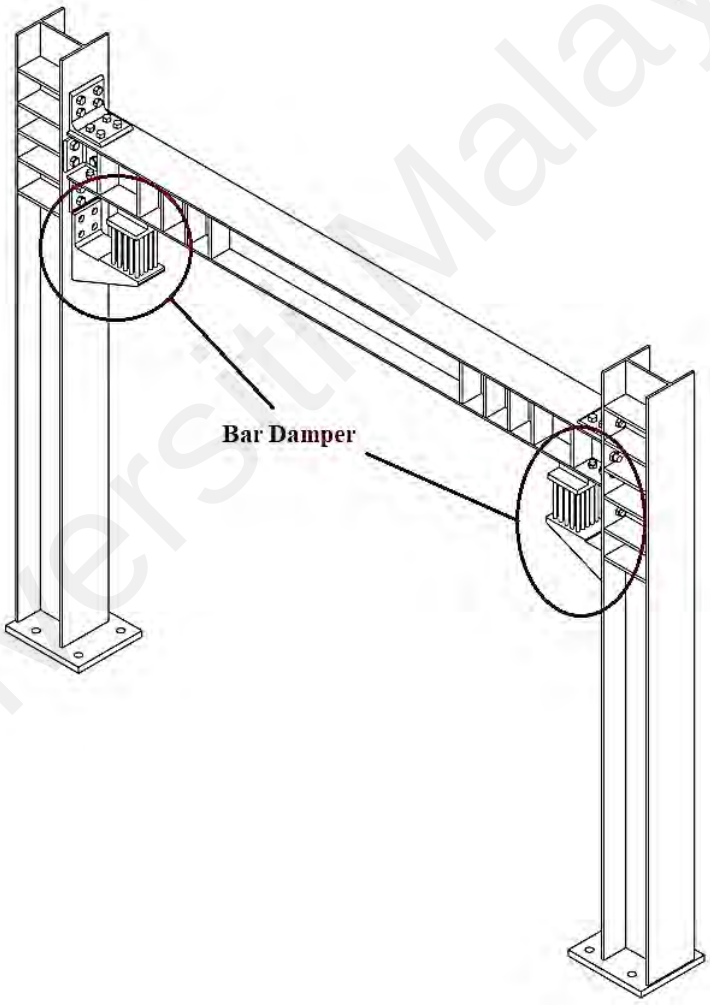

Figure 5.3: Proposed design of the frame equipped with the BD

5.2 Primary Assessment using Pushover Analysis

In order to investigate the effect of BD on the frame responses for the experimental assessment, a preliminary pushover analysis on rigid and semi-rigid frames without damper and a semi-rigid frame with dampers was performed by means of numerical analysis. General purpose Finite Element Software, ABAQUS (Abaqus Inc., 2014), was employed for modeling and analysis of the frames. It should be noted that, the detail of the FE model is described in section 5.5. H175x175x7.5 and H150x150x7 sections were used as columns and beams, respectively for all the three frames. To show the ease of use of the BD device in a structure, two similar BD devices consisting of 25 number of solid bars with 130 mm height and 10 mm diameter were selected and deployed in a semi-rigid frame to evaluate its effect on the response enhancement of frame structures subjected to lateral loading. For the pushover analysis, all of the frames were subjected to a progressively increasing lateral displacement control loading up to 5% drift ratio of the frames, which was 100 mm.

Figure 5.4 shows the stress distribution of all the frames under applied pushover load. It can be seen from the figure that, in the rigid and semi-rigid frames the critical stress occurred at the beam-column connection (panel zone) as well as the column base. Utilizing the BD devices in the semi-rigid frame showed a favorable effect on distribution of these concentrated stresses to other regions of the test frame, as expected. A comparison of the load-displacement curves of the analyzed frames was shown in Figure 5.5. This figure shows that, the strength performance of the frame equipped with BD devices was remarkably improved as compared to the rigid and semi-rigid frames. The maximum load of the rigid and semi-rigid frames was 243 kN and 234 kN, respectively, while for the semi-rigid frame with BD devices it was 290 kN. Consequently, the feasibility of using the BD device in design of frame structures was justified. Moreover,

it is important to mention that, the BD design can be effectively changed to achieve a substantial seismic performance as required.

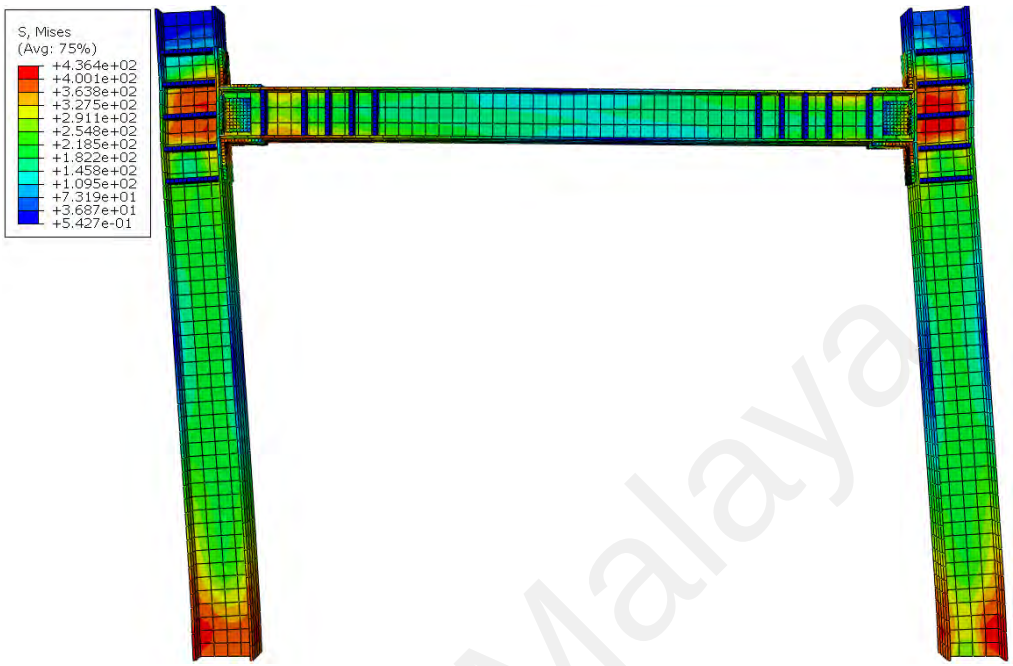

a)

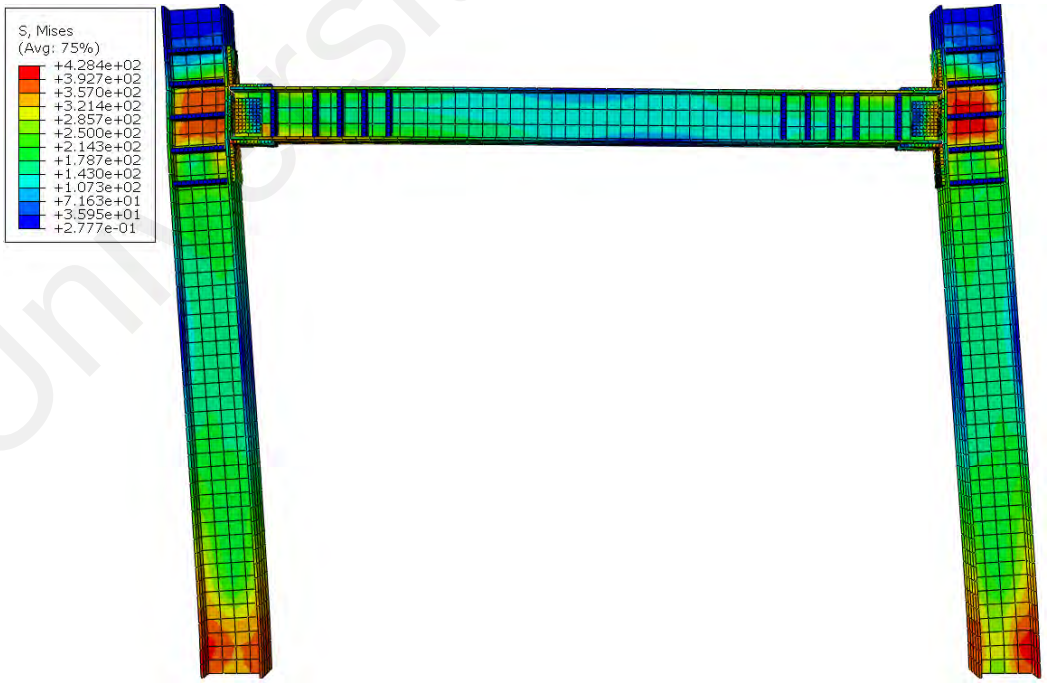

b)

Figure 5.4: Stress concentration in a) moment frame b) semi-rigid frame (unit: MPa)

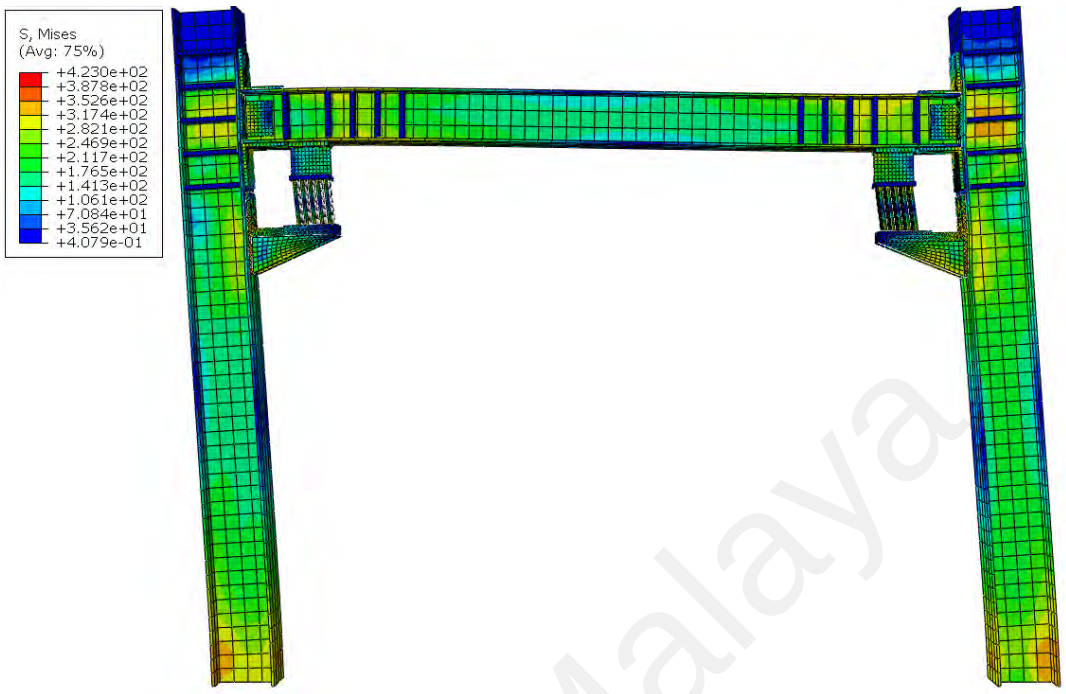

c)

Figure 5.4: Stress concentration in c) semi-rigid frame with BD devices (unit: MPa) (**continued**)

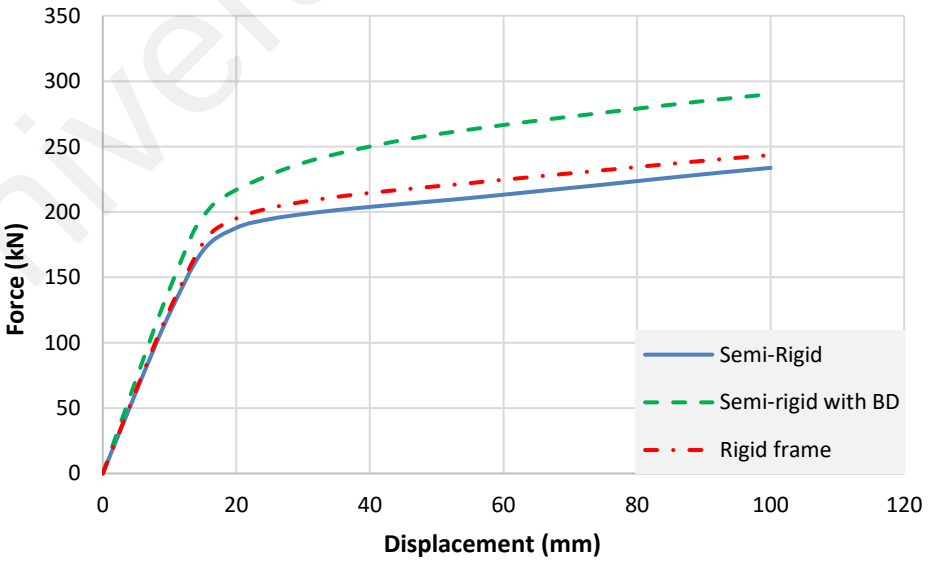

Figure 5.5: Comparison of load-displacement curve for moment frame (MF), semi-rigid frame and semi-rigid frame with BD

5.3 Experimental Study

5.3.1 Test Specimens

To assess the efficiency of the proposed BD device in overall seismic performance of the semi-rigid frames, two semi-rigid frames were designed and fabricated for testing at where one of the semi-rigid frame was equipped with BD devices installed at its beam-column connections. The bare semi-rigid frame and semi-rigid frame with BD devices were utilized in order to make a comparison and examine the performance improvement of the frame where the BD were implemented in design of structural frames. Therefore, the test frames were fabricated with the frame height of 1610 mm and span of 2215 mm. The columns and beams sections of the frames were H175x175x7.5 and H150x150x7, respectively. This combination was used to meet the strong-column weak-beam concept. To attain the semi-rigid connections in the frames, the beam was connected to both the columns by angle sections. Thus, in each side of the beam two equal leg angle sections i.e. L120x120x12, sitting on the top and bottom of the beam flange, was used to connect the beam to columns by four number of 15 mm diameters bolts. Two other web angle sections, i.e. L80x100x12, were also bolted to both sides of the beam web using 20 mm diameter bolts. The other legs of these angle sections were connected to the columns' flange to fulfil the shear connection between the columns and beam considering a 5 mm gap. An assembaly attachment was mountaned to the side of the frames to accumalate the actuator head for applying the push and pull loads. The materials used for columns, beams and BD devices were all made of ASTM A570 with nominal yield strenght of 341 Mpa (see Chapter 3, Table 3.2). Structrual blots garde 8.8 for all the connections. Figures 5.6 and 5.7 illustrate the detailing of the designed test frames with and without damper devices.

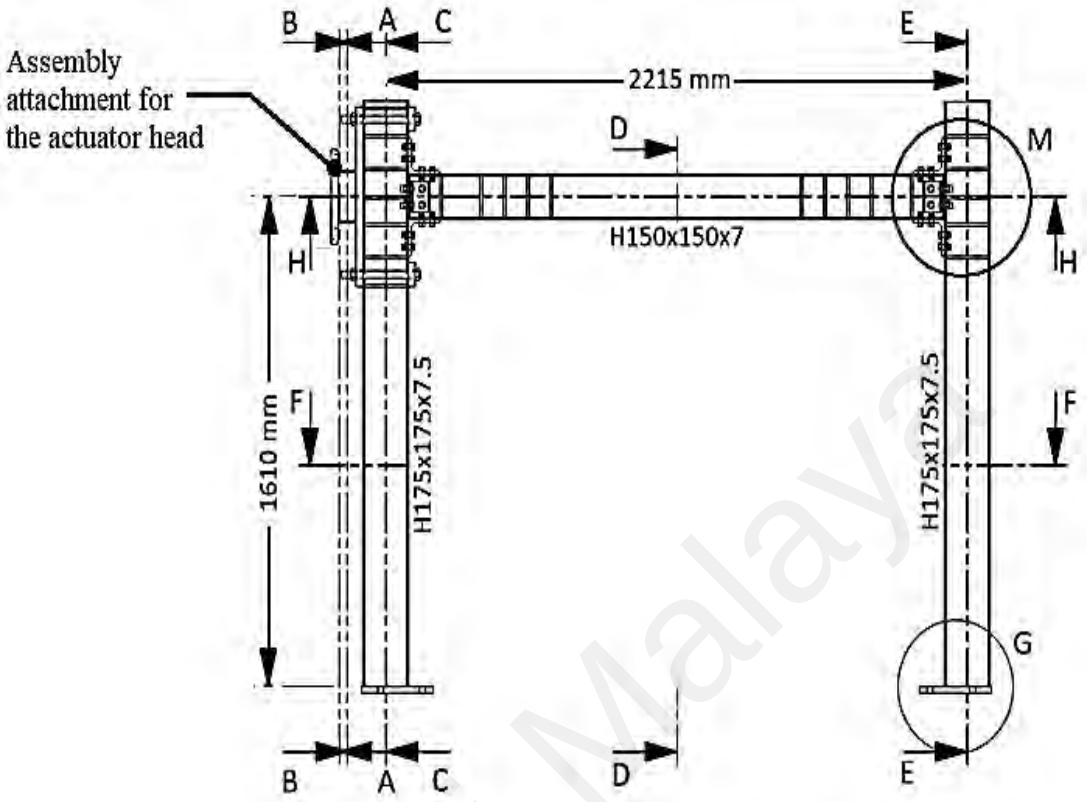

a) Test frames and its related sections (front view)

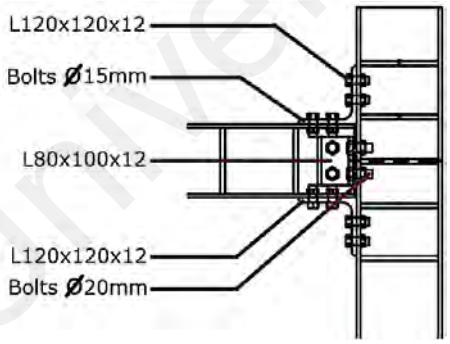

b) Detail M

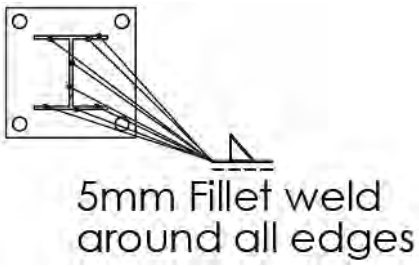

c) Section A-A

Figure 5.6: Details of the test frames

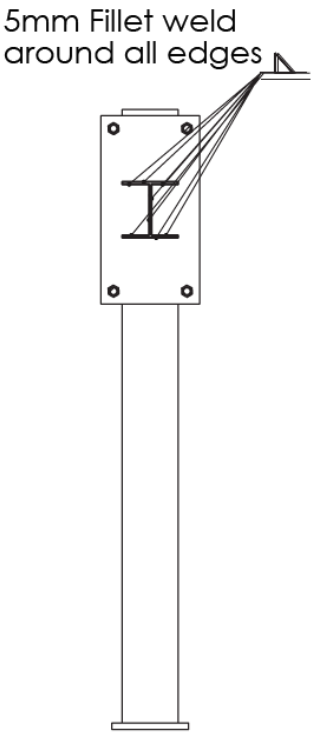

d) Section B-B

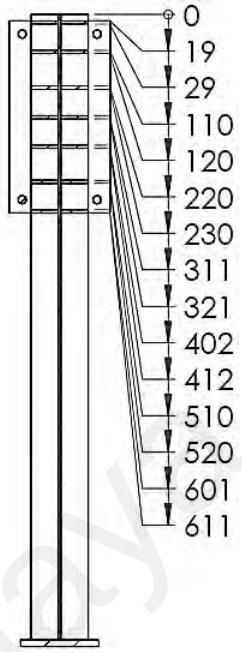

e) Section C-C

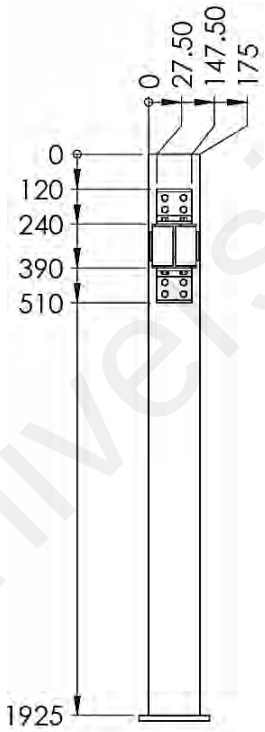

f) Section D-D

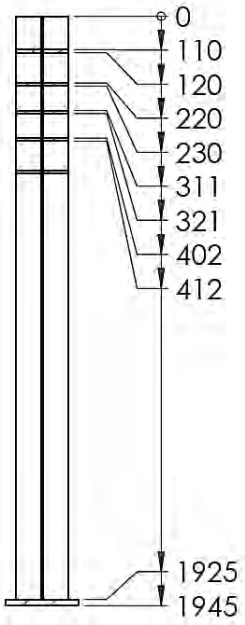

g) Section E-E

Figure 5.6: Details of the test frames (**continued**)

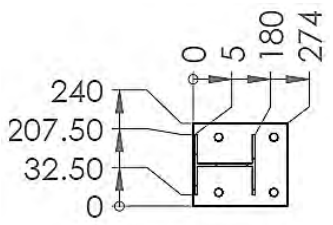

h) Section F-F

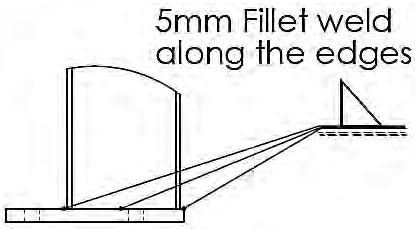

i) Detail G

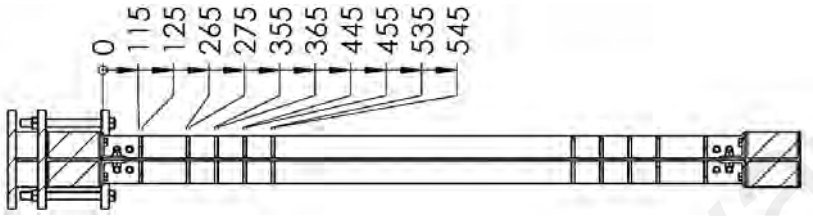

j) Section H-H

Figure 5.6: Details of the test frames (**continued**)

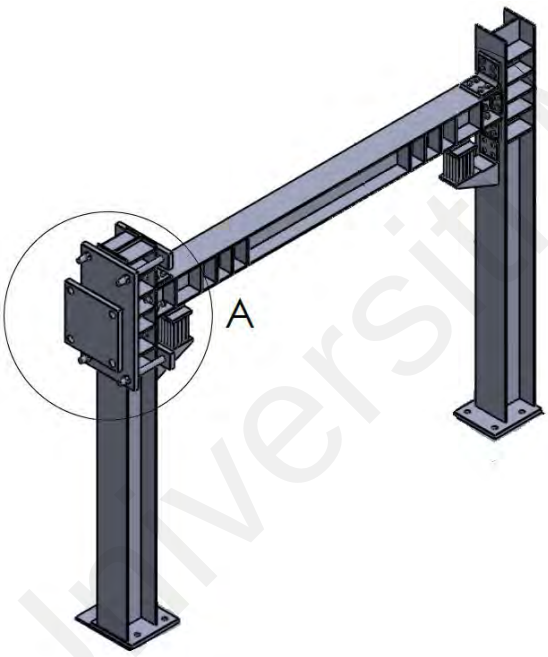

a) Frame with BD

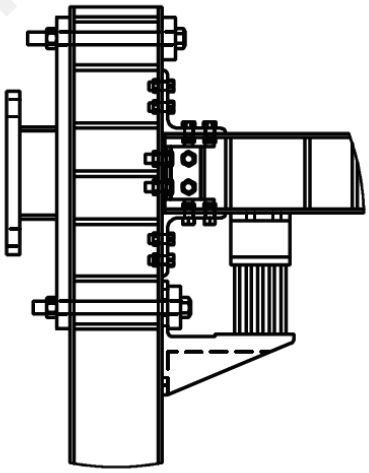

b) Detail A

Figure 5.7: Frame with BD device

5.3.2 Test Setup and Loading

Test frames were designed in such a way that, the columns were pinned to a stiffened plate at their base, where one of the columns was attached to a hydraulic actuator, MTS

Flex test 60 machine, with 500kN capacity sustained by a reaction column. The frame test setup is illustrated in Figure 5.8 and Figure 5.9 for the bare frame and the frame with BD devices, respectively. The quasi-static cyclic loading was applied to both the test frames. The cyclic load was designed considering an incremental displacement continued up to 85 mm, as shown in Figure 5.10. As shown in the figure, the cyclic loading protocol included six steps where each step comprised of three cycles. Therefore, a total number of 18 cycles was designed to displace the test frames up to 85 mm. The quasi-static cyclic test in accordance with FEMA-461 (FEMA, 2007) was performed on the test frames. Since the span of the tested frames was not large, thus, prior to install any lateral support instrument for out-of-plane movement control, a FE analysis was carried out to measure this effect. It was observed from the FE analysis that, the percentage of difference for the frame with and without lateral support was 4% only. Therefore, the lateral support was ignored for testing the frames. The obtained structural response for the tested frames can also be utilized as records to conduct further assessment of dynamic response of a SDOF or MDOF frames, as desired.

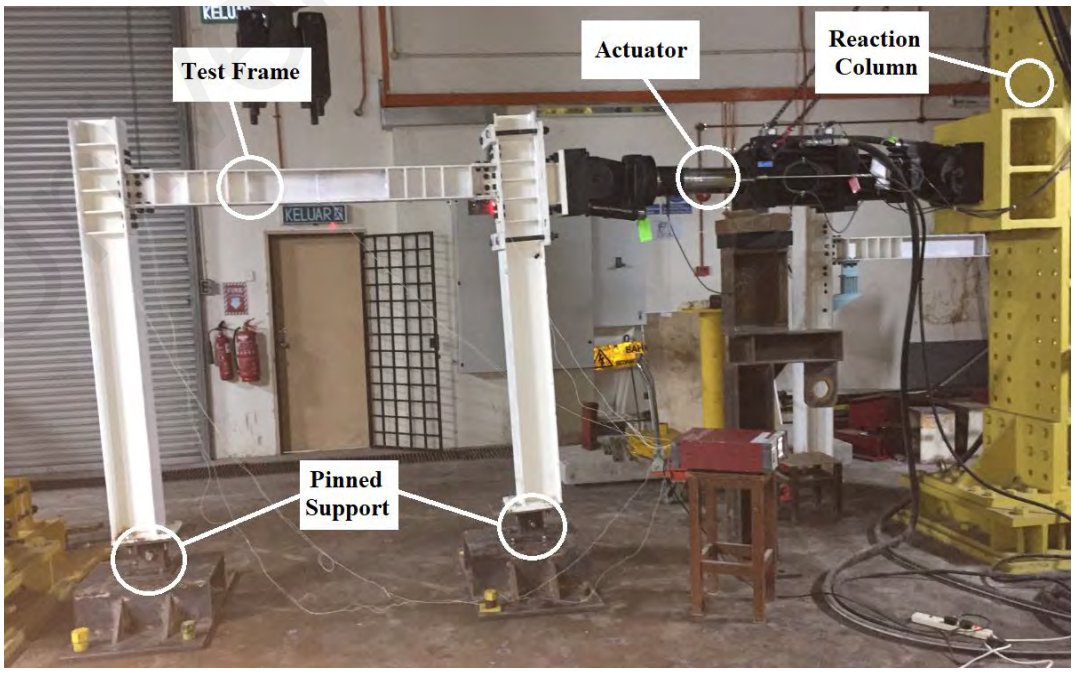

Figure 5.8: Details of the test setup (bare frame)

Figure 5.9: Test setup of the frame with BD

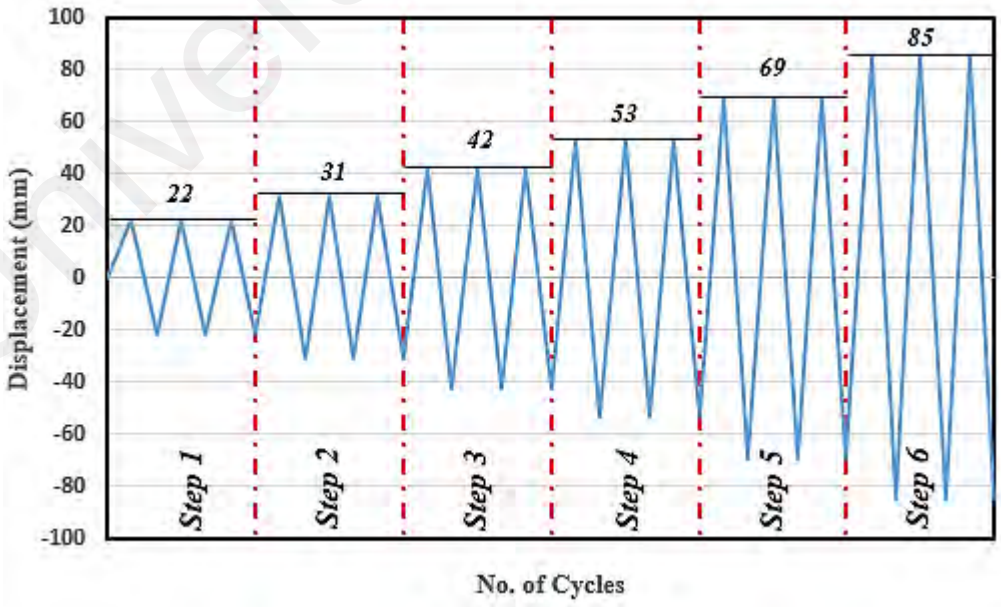

Figure 5.10: Designed cyclic loading

5.4 Experimental Results

5.4.1 Failure Mechanisms

For moment frames, failure often occurs at the connecting flanges of beams or columns. This happens due to flange yielding following by local buckling once the story drift is enlarged under lateral loading (Hsu & Halim, 2017). For a semi-rigid structural frame subjected to the lateral force, failure was initiated at the connected angles. In this study, yielding was primarily observed at the angles bolted to the beam and columns in the semi-rigid frame as shown in Figure 5.11. Progressive plastic deformation of the connected angles caused fracture once the frame drift was increased. Although, the failure pattern of the tested semi-rigid frame with BD devices was commenced with the BD devices yielding but followed with the angles yielding as demonstrated in Figure 5.12. This figure displays that, the solid bars of the BD were the first components which were deformed. The yield zone of the BD devices proceeded at both ends of the bars which were fixed to the top and bottom plates as shown in Figure 5.13.

It is worth mentioning from the experiments that, no buckling nor deformation was observed in the plates attached to the BD devices, throughout the testing. This means that, the plates were relatively stiffer than the bars and the BD performance governed by the bars deformation. From this aspect it was assessed that, the BD device had an acceptable stability under the cycles of large deformations.

Figure 5.11: Failure pattern of the angles in the bare semi-rigid frame (zoom view)

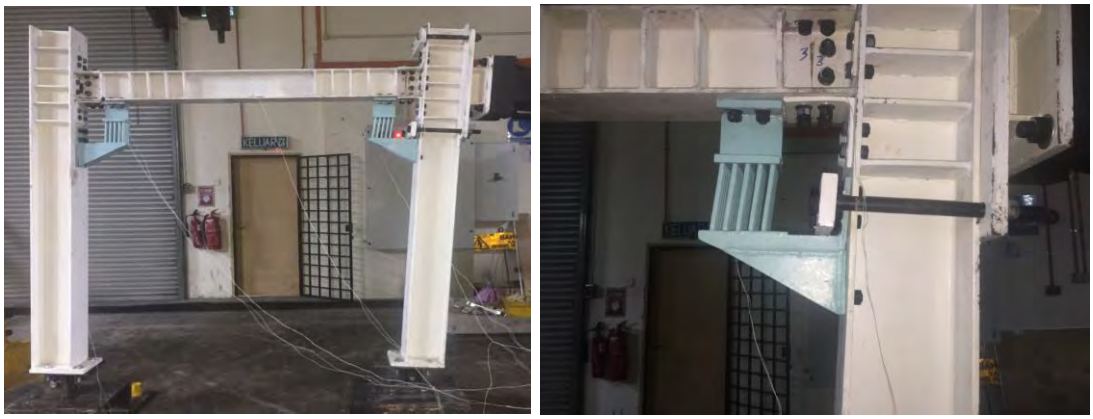

Figure 5.12: Failure pattern of the semi-rigid frame with BD devices (overall view and zoom view)

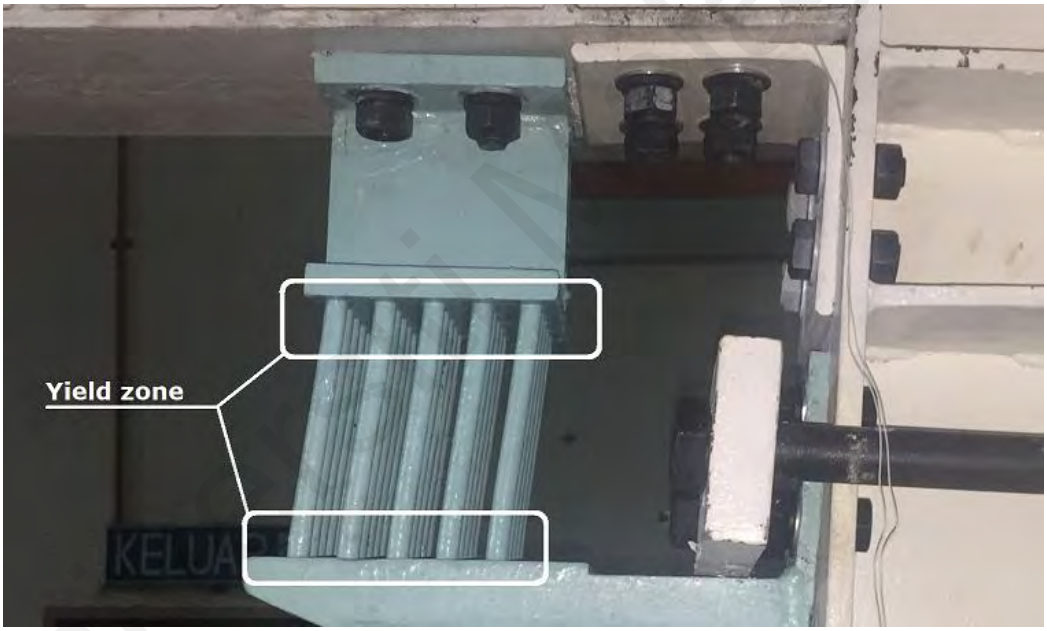

Figure 5.13: Yield zone of the bars

5.4.2 Deformation Capacity

The force-displacement hysteresis curves of both frames from the experiment are presented in Figure 5.14. The hysteresis loops of the semi-rigid frame with BD devices followed the pattern of the bare semi-rigid frame. However, the area under the hysteresis curves of the semi-rigid frame with BD devices was larger than the semi-rigid frame. This

indicates that the BD devices caused stiffness enlargement of the semi-rigid frame. This is because the BD added stiffness to the frame. This additional stiffness affects the natural vibration period of the structure before and after yielding of the devices. Consequently, the BD effect on the acceleration response must be taken into consideration in designing MDOF structures. Moreover, the expected effect in case of multi-story frames should also be discussed. For both the frames, a slight pinching effect was demonstrated in the first few cycles of force-displacement hysteresis curves. A smooth transition from the elastic to plastic state was observed in both the frames. Furthermore, the hysteresis curves of the frames shown the Bauschinger effect and kinematic hardening of the steel material while the plastic strength was increased gradually in each cycle without any sign of stiffness degradation. The bare frame and frame with BD devices showed a stable hysteretic response throughout the loading scheme. The maximum load of the frames was recorded at the last cycle of loading, however, it was not the ultimate load bearing of the frames due to limitation of the actuator head movement. It was observed from the experiments that, the semi-rigid frame with and without BD exhibited no structural failure, however, failure occurred for the angles of the connections. The replacement of the angles with simple sections at the beam-column connections significantly cut down the expenses as long as structural retrofitting is concerned, but it is difficult for a rigid frame to replace or rehabilitate the structural members subjected to dynamic loadings. This failure is generally followed by ongoing plastic deformation cumulated in the beams. When the deformation capacity is of importance, utilizing of rigid connections or rigid frame is unfeasible. For the semi-rigid test frame equipped with BD devices, the deformation trend was analogous to that of the semi-rigid frame with no BD devices. The BD devices showed stable action while providing continuous support to the test frame up to the inelastic level. Moreover, sufficient resistance capability of the BD devices efficiently increased the frame strength. In other words, the BD devices with its deformability could

inhibit structural members to approach yield point under the applied displacement; resulted in improving the frame performance. It should be noted that the ductility of the frames cannot be calculated as none of the frames reached to their ultimate bearing capacity due to the actuator head movement limitation.

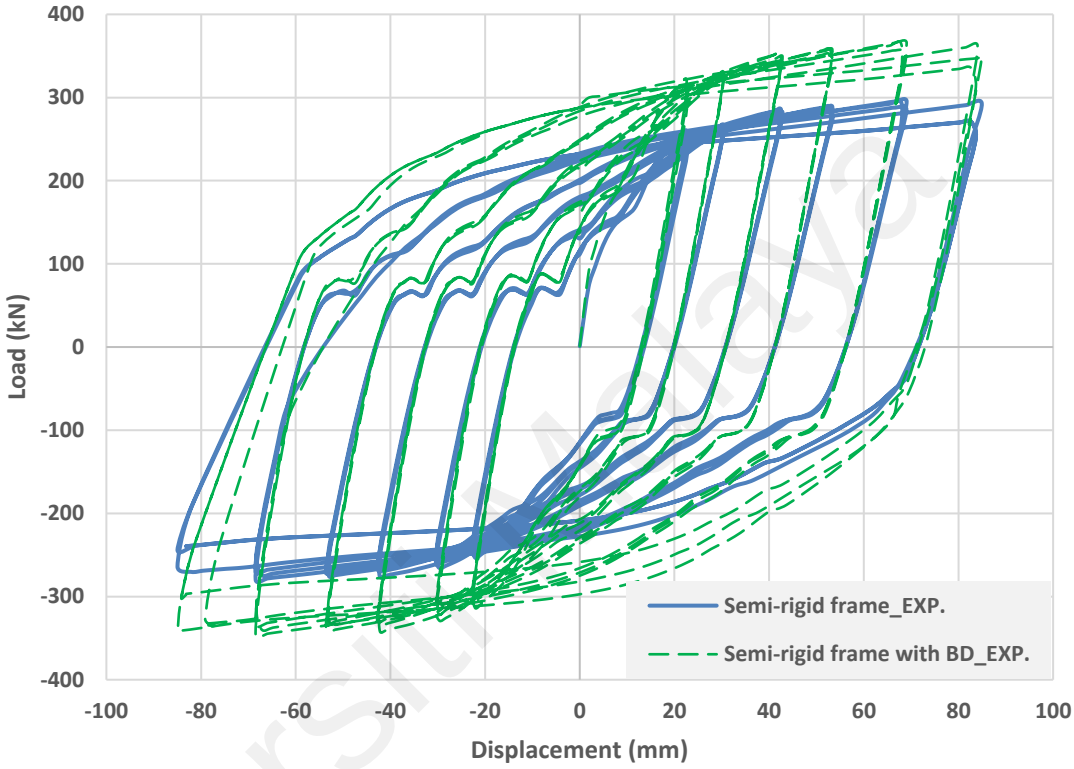

Figure 5.14: Hysteresis loops obtained from the experimental test frames with and without BD device

5.4.3 Stiffness and Strength

Figure 5.15 shows the strength of the frames in positive cycles with respect to the applied displacement for both semi-rigid frames with and without BD devices. Strength of the frame with BD devices was larger than the bare frame in both elastic and inelastic zones. The figure also demonstrates that, the BD devices significantly improved the structure strength of the frame. For instance, the yield strength of the bare frame was 222 kN which was increased to 276 kN in the frame with the BD devices. Meanwhile, the

maximum strength of the semi-rigid frame equipped with the BD devices was 375 kN which is much greater than 295 kN of the frame without dampers, showing 27% enhancement. Similarly, Figure 5.16 depicts the effective stiffness versus applied displacement for the tested frames. Stiffness of the frames were gradually decreased as the displacement increased. Nonetheless, the stiffness of the frame with BDs were larger than the bare frame throughout the loadings scheme. As it can be observed from the figure, the initial stiffness of the frame increased by 23.1 % when the BD devices utilized in the semi-rigid frame. The effective stiffness of the frame with BD devices was about 24.3% higher than the frame without dampers at the end of loading protocol. It should be noted that, the BD configuration including arrangement of the solid bars, diameter and height of the solid bars and even the selected materials of the solid bars and attached plates can have a significant impact on the overall performance of structures, i.e. strength, stiffness, ductility and energy dissipation. Some of these effects were examined, and briefly discussed in the previous chapters.

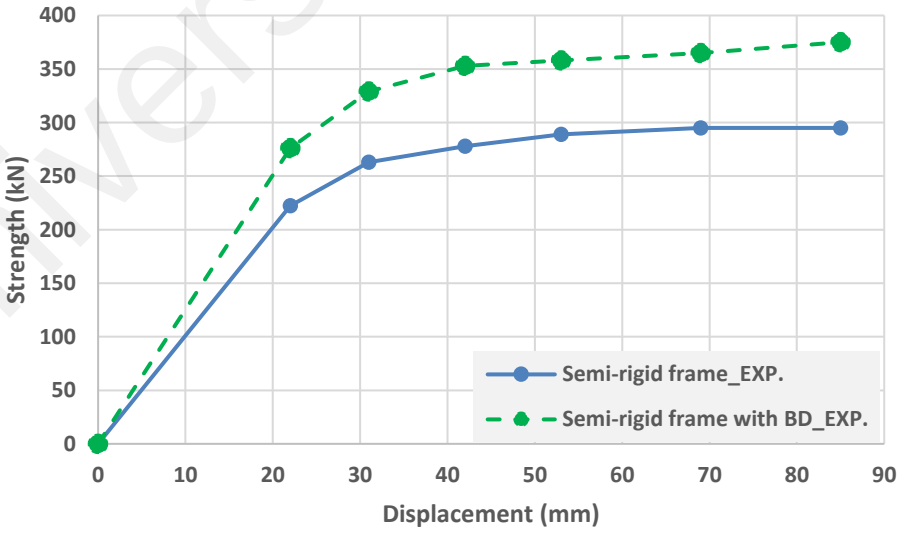

Figure 5.15: Force-displacement relationship for the tested frames

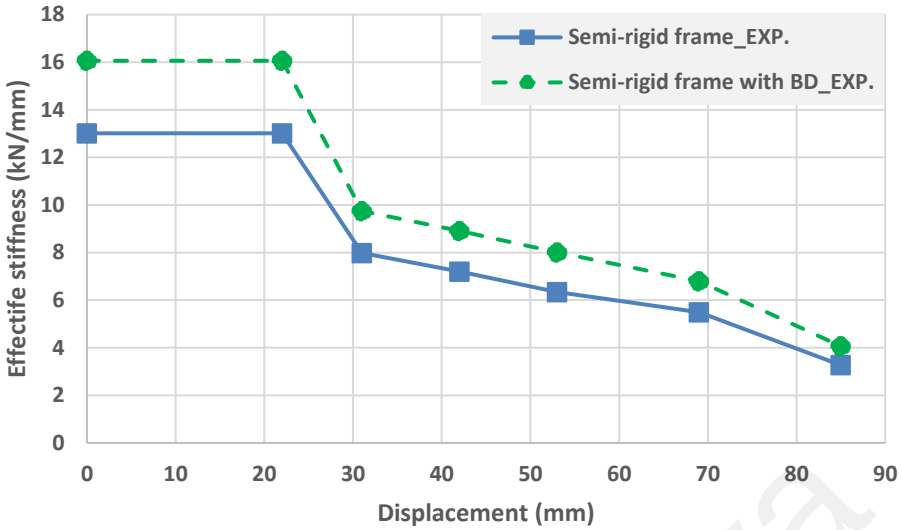

Figure 5.16: Normalized stiffness versus displacement for the tested frames

5.4.4 Energy Dissipation

Energy dissipation capability of the frames was assessed through the hysteresis curves obtained from the test. Figure 5.17 illustrates the cumulative dissipated energy over the total displacement of the semi-rigid frames with and without BD devices loaded to the maximum displacement. At a glance the comparison demonstrated that, a remarkable enhancement in dissipating energy was attained when the BD devices were implemented in the semi-rigid frame. The cumulative dissipated energy of the bare frame linearly increased until the end of the loading scheme. The semi-rigid frame with BD devices also exhibited similar energy dissipation behavior, however, the cumulative dissipated energy dissipation enlarged more significantly at each increment of the displacement loading. At the first cumulative displacement, the cumulative dissipated energy of the semi-rigid frame with BD devices was about two times higher than the bare frame. As the cumulative displacement increased, the dissipated energy of the frame with BD devices remarkably raised until the end of the test as compared with the semi-rigid frame. The total dissipated energy of the frame with BD devices was 228081 kNmm while it was only 180197 kNmm for the bare semi-rigid frame at the cumulative displacement of 3624 mm. This shows an

overall dissipation capability of the semi-rigid frame increased by 27% after implementation of the BD devices at the end of testing. It should be noted that, with an increase of the damper height and bars diameter, energy dissipation capacity may improve efficiently.

Figure 5.18 shows the comparison of cyclic energy dissipation over the applied cycles of load for the semi-rigid frame with and without BD devices. It can be seen from the figure that, the bare frame dissipated more energy in all cycles of displacement loading. The energy dissipation of the frame with BD devices was 90% higher than the semi-rigid frame in first 3 cycles of loading. In second 3 cycles of loading the energy dissipation of frame with BD devices improved by 32%. Similarly, the energy dissipation of the semi-rigid frame with BD devices in fourth and fifth steps was 21% and 24% higher than the semi-rigid frame, respectively. In the last step of cyclic loading the energy dissipation of the frame with and without BD devices was 93840 kNmm and 75480 kNmm, respectively; showing a 24% improvement after implementation of the dampers.

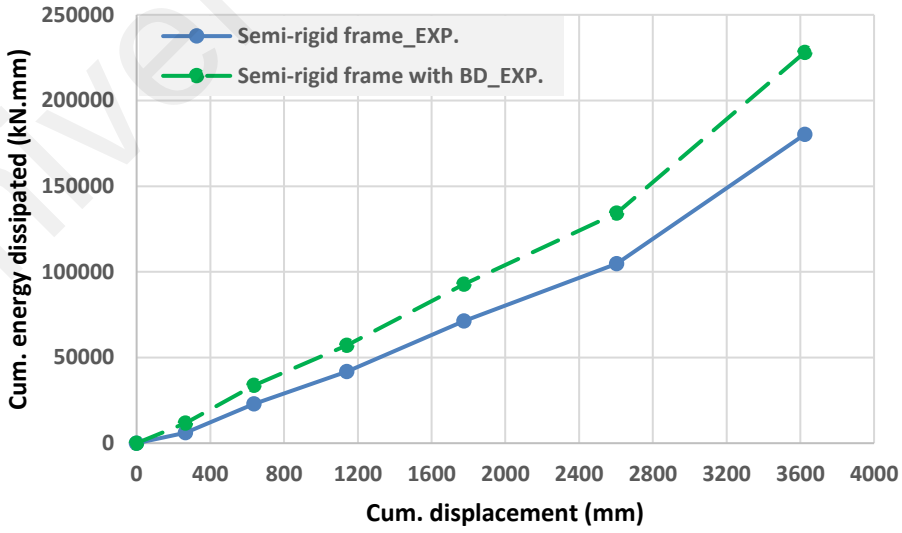

Figure 5.17: Cumulative energy dissipation versus cumulative displacement

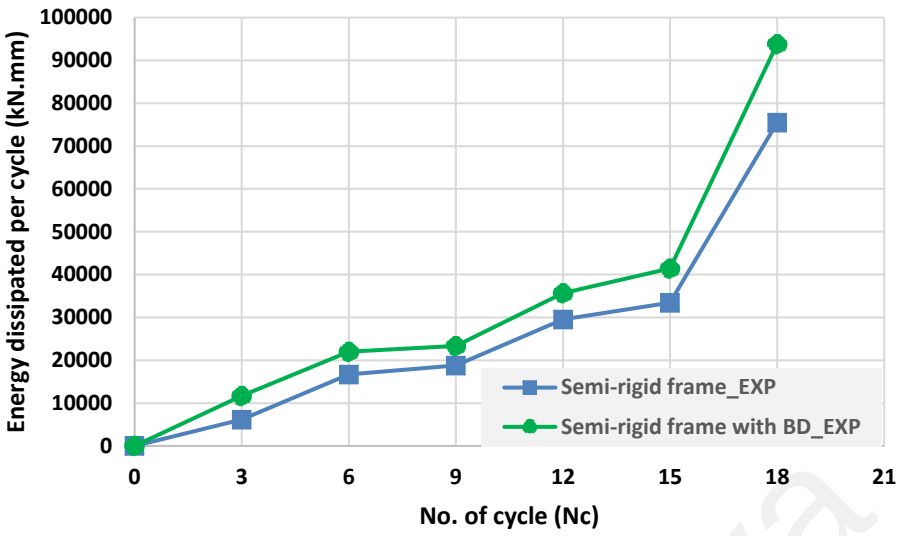

Figure 5.18: Cyclic energy dissipation versus number of undergone cycles

Figure 5.19 shows the strength capacity versus the total energy dissipation for semi-rigid frames with and without BD devices. It can be observed from this comparisons that, the frame performance with the BD devices was remarkably enhanced in terms of strength and energy dissipation capacity. The strength of both frames increased linear over the cumulative dissipated energy in the first step of loading. Thereafter the frames dissipated the energy gradually as the strength increased. The strength and cumulative dissipated energy of the frame with BD device were improved 27%, respectively. It can surely be predicted that, the other BD parameters such as diameter, height and number. Further, the overall behavior of the frame equipped with the proposed BD devices was compared with the frame without BD device. The comparison including dissipated energy, deformation, strength and stiffness of both tested frames is presented in Figure 5.20. As shown from this figure, a superior performance of the frame equipped with the proposed device was attained. Higher performance can even be achieved when a suitable BD device is adopted taking the most appropriate parameters into consideration. These appearances can confirm the usability of the proposed BD device for engineering design applications. It is

noted from the evaluation of tested frames that, stiffness and strength of the semi-rigid frame equipped with BD devices were generally more than that of the frame with no damper device. Consequently, the period of vibration for frames with proposed damper may be shortened and result in further seismic action. As a result, a feasible solution to this matter is to provide a gap between the beam-column joint as implemented in this study for application of BD devices. Therefore, one of the advantages of using BD is controlling of the system stiffness (about 23%), whereas, the system strength can be significantly enhanced (about 27%), as shown in Figure 5.20.

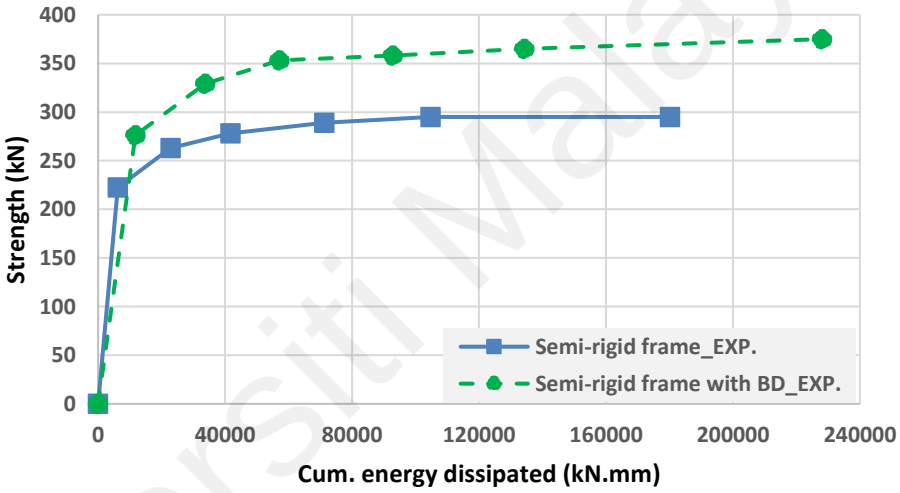

Figure 5.19: Dissipated energy and strength relationship for tested frames

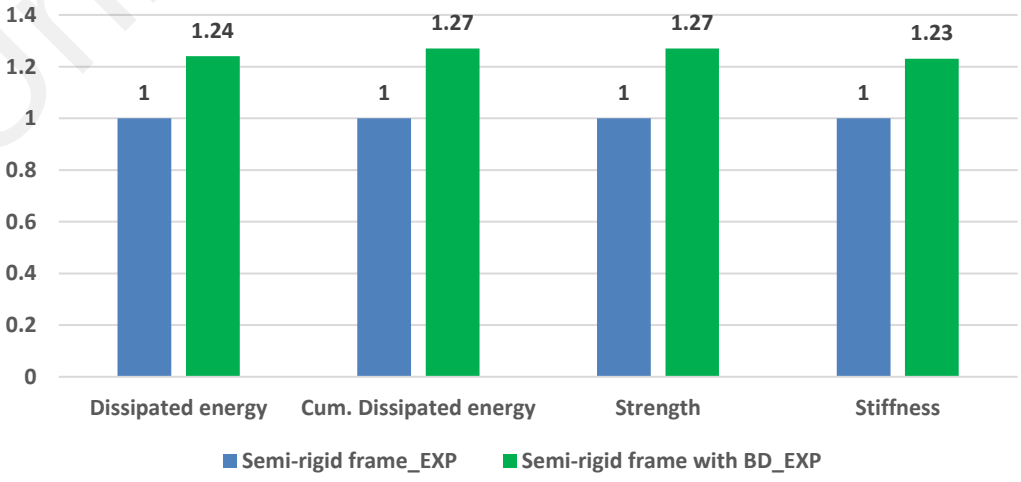

Figure 5.20: Improved performance of the frame with BD devices

5.5 Finite Element Analysis of the Frames under Cyclic Loading

FE modeling of the tested semi-rigid frames was carried out in order to make comparison with the experimental results. The FE modeling of the frames is shown in Figure 5.21. ABAQUS software was used to model the frames where the described specifications of the elements as discussed in Section 4.3. Furthermore, a pinned-support was defined at the base of the columns to represent the boundary condition of the columns as designed for the experimental test. The cyclic displacement load was applied to the right column as demonstrated in Figure 5.21(a). The same loading scheme of the experimental test was used in the FE analysis. By assuming that the bolts had negligible energy dissipation during the testing due to their higher stiffness than the plate angles and BD devices, the tie constrain was used to connect the frame elements i.e. angles well as the BD parts to the main frame. The tie constrain integrates the frame as a whole and enables the load transfer between the frame elements. It should be noted that material and geometry nonlinearities were deliberated in the FE analysis. The beam and columns were meshed coarsely while the steel angles, stiffeners and BD devices were finely meshed. The detail of FE mesh discretization of the frames is shown in Figure 5.21(b).

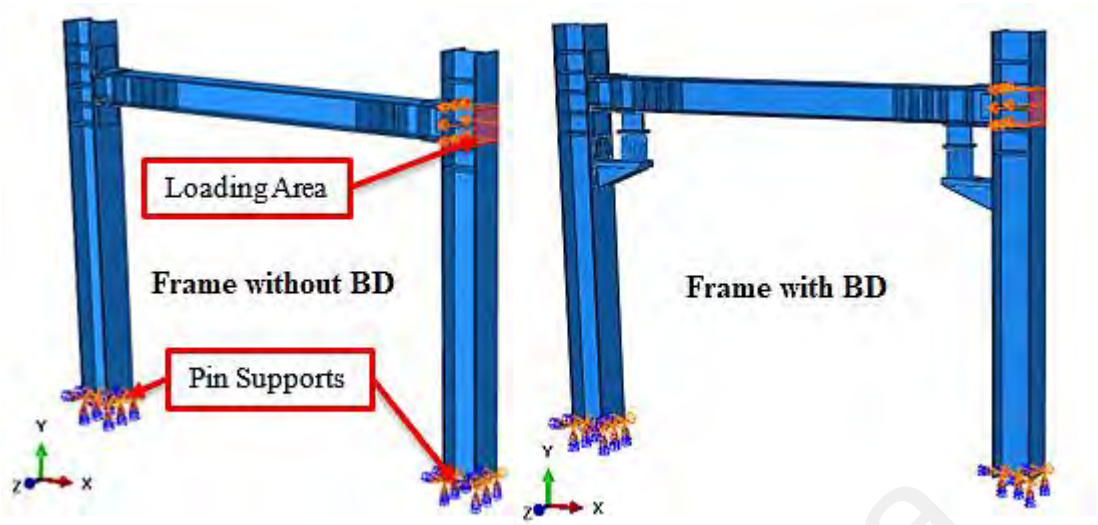

a)

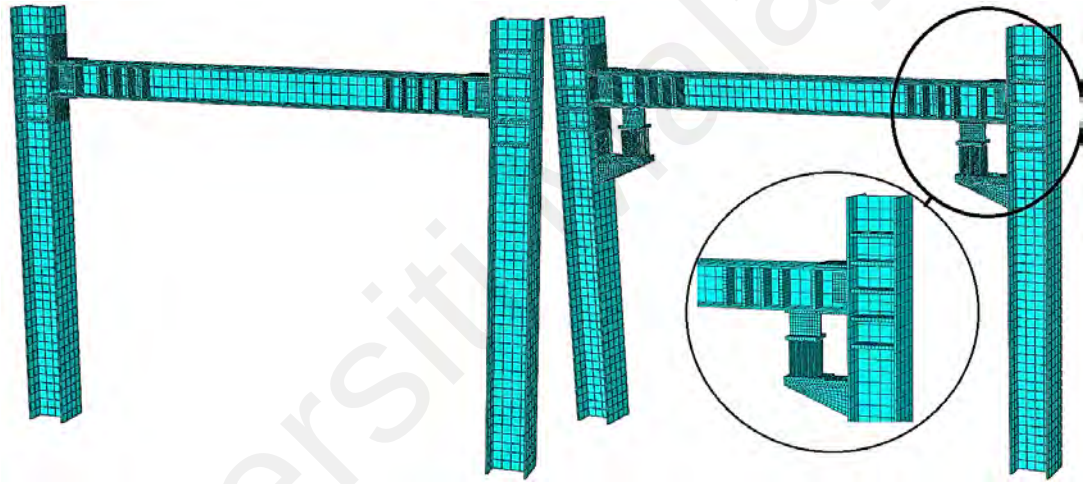

b)

Figure 5.21: FE discretization of the semi-rigid modeled frames; a) the FE criteria and b) the FE discretization

Figure 5.22 shows the Von Mises stress propagation of the analyzed frames. As it is shown in the figure, a significant stress reduction was observed for the semi-rigid frame with BD devices, especially at the panel zones and columns base as displayed in Figures 5.22(a) and 5.22(b). It was because, the stress concentration occurred at the end sides of the solid bars. In contrast, the frame without BD devices reached the yield stress at the aforementioned regions. This phenomenon confirmed the favorable effect of the proposed

damper device on mitigation of stresses of frame structures subjected to cyclic or dynamic loads. Furthermore, a comparison of deformed shape between the FE model and the experimental test for the semi-rigid frame with the BD device at the beam-column connection at the last cycle of loading is shown in Figure 5.23. The figure illustrates that the deformation of the FE model is well matched with the experimental deformation of the semi-rigid frame with BD devices. Under such deformation, the stress was equally propagated in entire the frame due to the effect of the BD devices on the frame. This simply means that, another advantage of using BD device is to increase plastic capacity of the entire frame section in order to contribute in the hysteresis performance of the frame with no sign of instability.

The hysteresis behavior of the FE models was also obtained and compared to those obtained from the experimental tests as shown in Figures 5.24 and 5.25 for semi-rigid frame without and with BD devices, respectively. As these figures demonstrated, the maximum positive and negative load values of the FE analysis were fairly closed to the experimental results at the last cyclic of displacement loading. Furthermore, the hysteresis curves obtained from the FE models showed a good agreement with the results from the experiments. To avoid repetition, no further discussions were made to extract the effective stiffness, strength, energy dissipation, and deformation capacity parameters from the FE hysteresis loops.

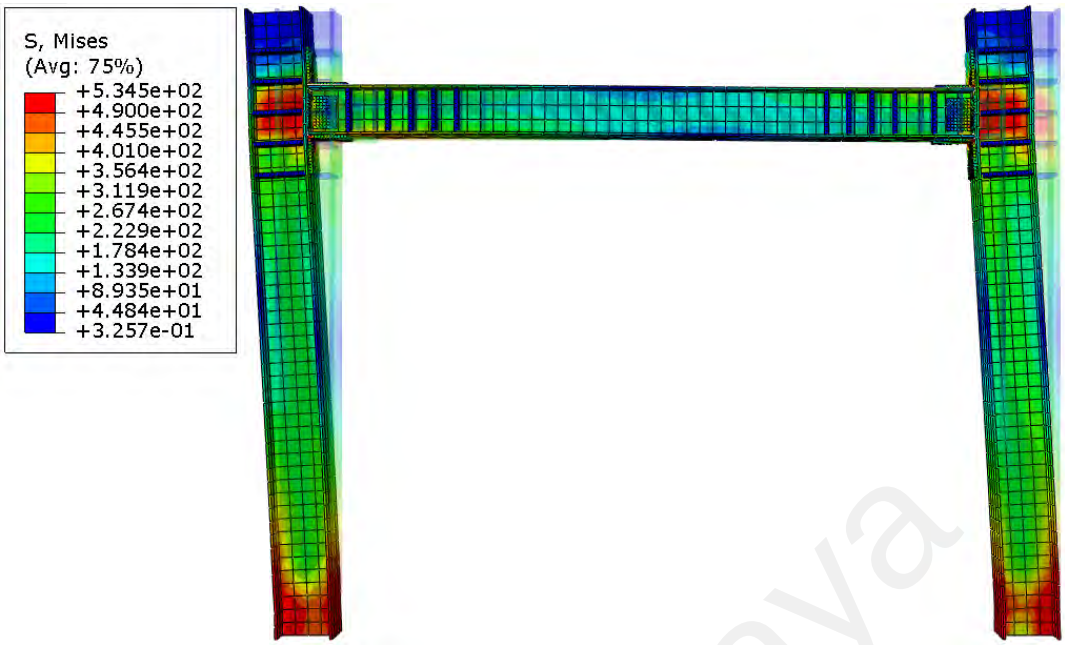

a)

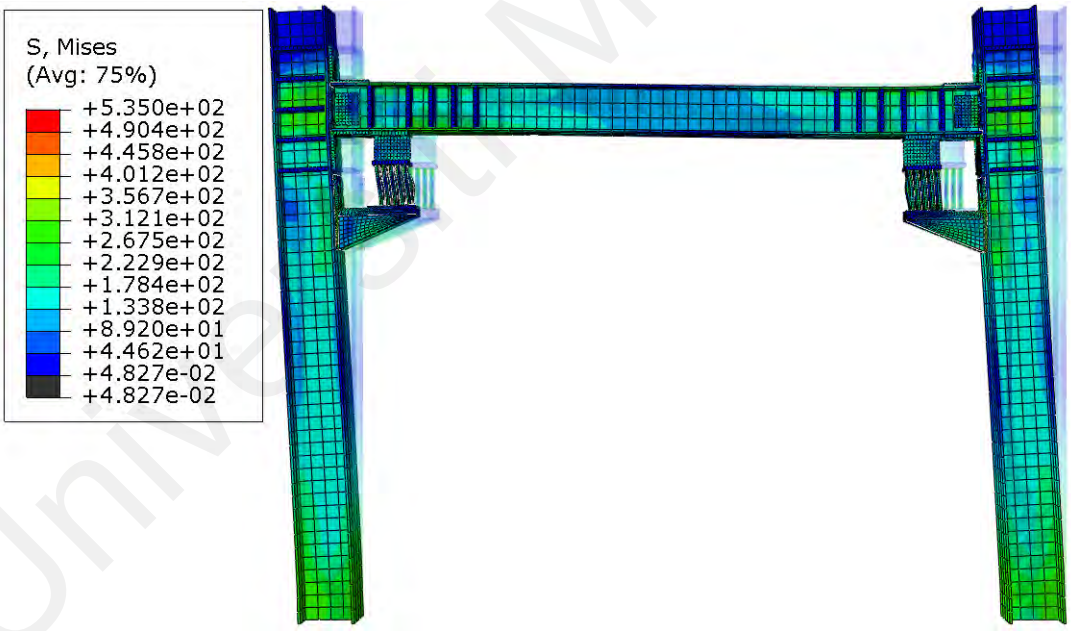

b)

Figure 5.22: Von Mises stress contour of the semi-rigid frame a) without BD devices and b) with BD devices (unit: MPa)

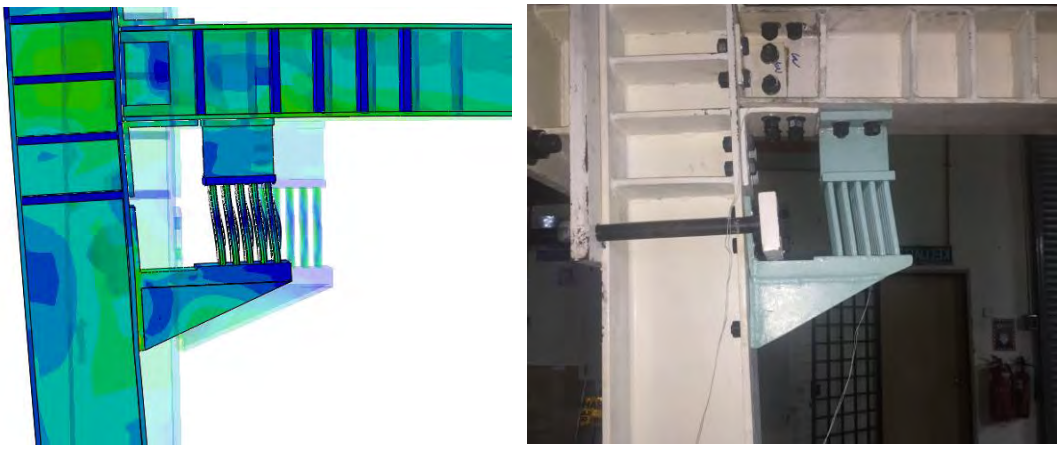

Figure 5.23: Comparison of deformed shape between FE model and experimental test of the semi-rigid frame equipped with BD devices

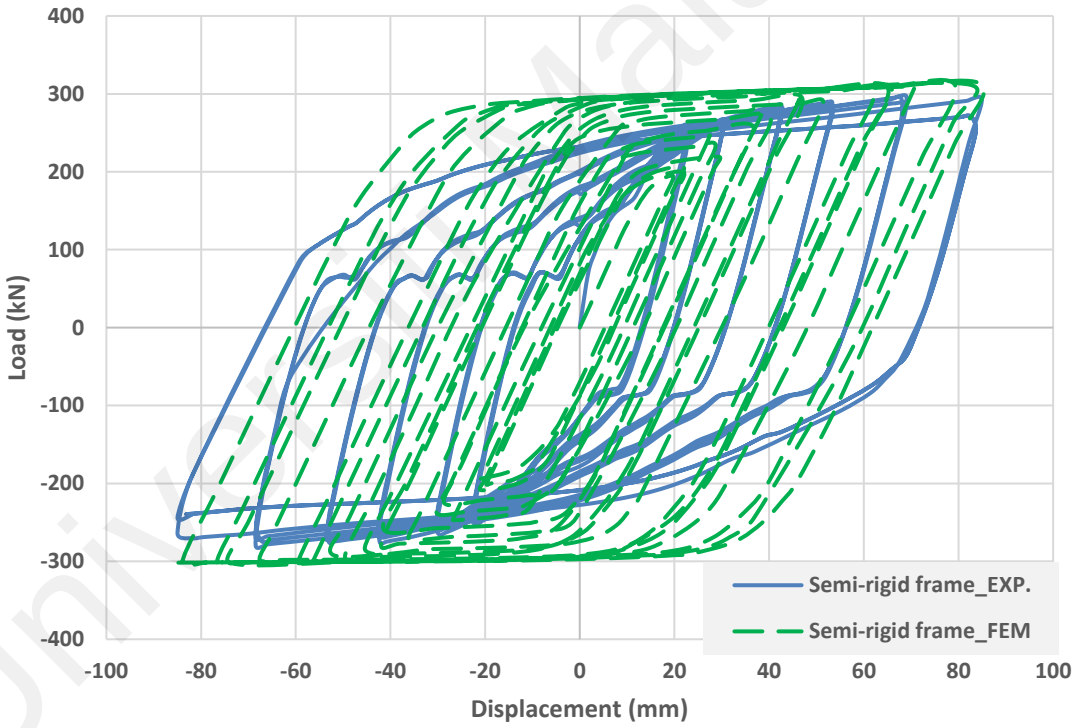

Figure 5.24: Comparison of hysteresis loops between experimental test and FE model for semi-rigid frame without BD devices

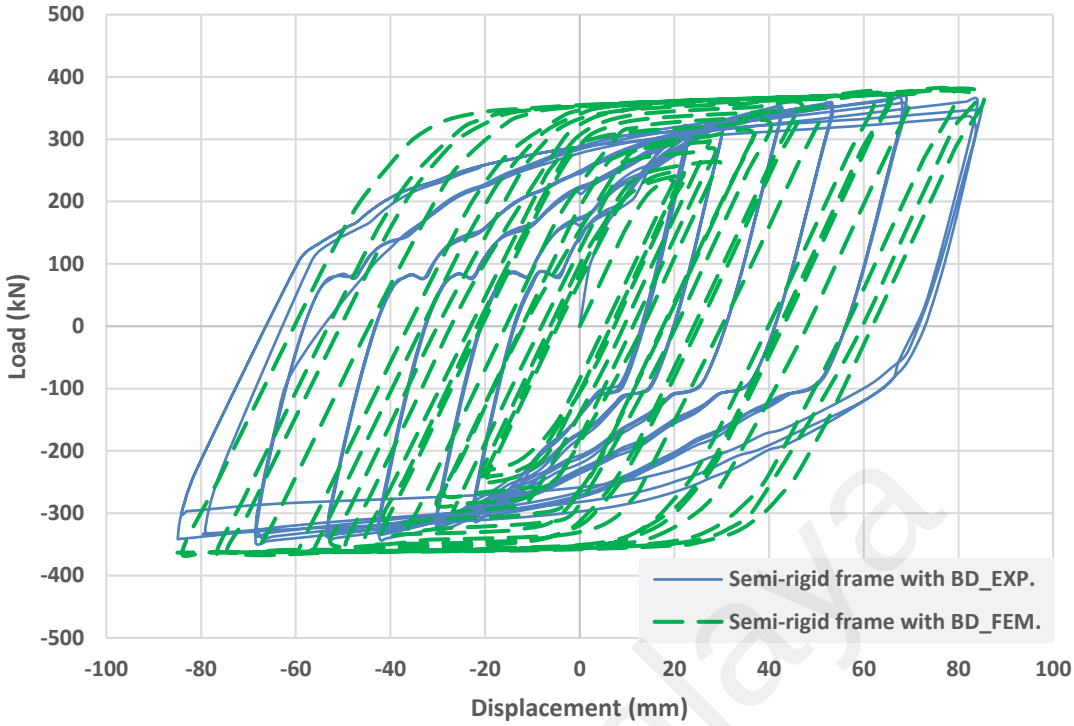

Figure 5.25: Comparison of hysteresis loops between experimental test and FE model for semi-rigid frame with BD devices

Eventually, to have satisfactory structural design under seismic actions, the structures must have substantial energy dissipation capacity, adequate strength as well as a good deformation capacity. To satisfactorily assess the effectiveness of the proposed BD device in enhancements of the structural performance, the aforementioned parameters were obtained from the experimental tests. Moreover, the FE analysis of the frames with and without BD devices was developed and investigated. It was shown from both the experimental and the FE results that, the proposed device can remarkably enhance the performance of the frame structures under cyclic loading.

5.6 Summary and Conclusions

This chapter investigated the performance improvement of a structural frame equipped with the BD devices under cyclic loadings. Initially, a preliminary performance assessment of the structural frames with and without BD devices was performed under the pushover loading by using FE analysis. It was observed from this analysis that, the stress concentration was in the panel zone and base of the columns of the frames without BD devices, which was unfavorable. On the contrary, the stresses were ideally propagated in the entire semi-rigid frame when the BD devices were utilized. Furthermore, the semi-rigid frames with and without BD devices were experimentally tested under a sequence of cyclic displacement loading. The failure mechanism of the frame with BD devices initiated and propagated in the device which prevented the failure of the connection angle plates. The BD devices demonstrated stable behavior and improved the hysteresis performance of the semi-rigid frame. Further comparisons of the test frames illustrated that, satisfactory improvements was achieved in terms of deformation capacity, strength, stiffness and dissipated energy for the test frame with BD devices. It was also noted that, the strength of the semi-rigid frame with BD devices was enhanced by 25%, while the stiffness was increased around 23%. This was desirable to control the stiffness of the system by adjusting the damper parameters. An overall energy dissipation of the semi-rigid frame improved by 27% when the BD devices used. In addition, the three-dimensional FE model of the tested semi-rigid frames was developed and analysis. The FE models were subjected to the same loading protocol of the test to demonstrate the accuracy of the study. It was shown that the FE analysis results were well-agreed with the results obtained from experimental tests and can be used for future studies. It was shown from both the experimental and the FE analysis results that, the proposed device can remarkably enhance the performance of the frame structures under dynamic loading.

CHAPTER 6: CONCLUSIONS

6.1 Summary of the Research

A new structural passive vibration control system, called bar damper (BD), was proposed for protecting buildings and bridges subjected to dynamic loads. The device was made of a number of solid bars sandwiched between two steel plates, one at the top and one at the bottom. The top and bottom plates can be welded or bolted to the adjacent plates to connect the device to the structure. Depending on the design of the plates, a specific number of bolt holes can be drilled in the plates to attach the BD device to the target structural member. Energy dissipation by the BD device was achieved mainly through the inelastic cyclic flexural deformation of the bars. The proposed device was primarily meant to be installed at beam-column joints. Nevertheless, it can be installed in several configurations and can even be utilized as a base isolation system due to its design flexibility.

The efficiency of the BD device was evaluated experimentally, theoretically and numerically. To this end, the study was carried out in two main stages: i) assessment of the proposed damper device under displacement-controlled cyclic loading and ii) performance assessment of a semi-rigid structural frame equipped with the proposed damper device under applied cyclic loading. To achieve the aim in the first stage, twelve device specimens were prepared considering different parameters to assess the behavior of the device individually. The parameters were height, diameter and number of solid bars. To assess the height effect, the solid bars were designed with heights of 70 mm, 100 mm, 130 mm and 160 mm, and with diameter and number of 10 mm and 24, respectively. To evaluate the diameter effect, the solid bars were designed with diameters of 8 mm, 10 mm, 12 mm and 14 mm, and with height and number of 100 mm and 24, respectively. Next, the bar number effect was assessed for solid bars designed in 20, 24, 28 and 32, with height and diameter of 100 mm and 10 mm, respectively. It is noted that among all

three considered parameters, the common device specimen was the one with 24 solid bars, bars height of 100 mm and bars diameter of 10 mm. As a result, this specimen (BD-H100 or BD-D10 or BD-N24) was selected for implementation in the FE analysis. In order to carry out FE modelling of the device, the steel elements were modeled as eight-node quadrilateral reduced integration solid elements. To observe the real performance of the device, the steel elements' geometrical and material nonlinearities were also considered in the FE analysis. The von Mises yield criterion was utilized to take the inelastic deformation of the solid bars into consideration. The theoretical equations of the BD device were also derived based on its plastic mechanism and they were compared to the experiments and FE results. In the second stage, the proposed BD devices were installed in a semi-rigid frame and experimentally tested under quasi-static cyclic loading. The performance of the frame with a BD device was compared to a similar frame without a BD device. FE models of each frame were developed and analyzed under cyclic loading.

6.2 Conclusions

According to the abovementioned investigations and results obtained from the parametric experimental study as well as FE analyses, the following conclusions can be drawn:

1. A passive structural vibration control system called a bar damper (BD) was proposed and developed in the present study. The proposed BD device is simple, light in weight, cost-effective and easy to build with effective energy dissipation capability in a planar direction owing to its unique geometry. The device can also be made of other passive materials like aluminum, zinc, lead or a combination of dissipative materials. It can even be made from the aforementioned material waste.

2. The BD device performance was assessed experimentally under quasi-static cyclic displacement loading through three considered parameters; the height, diameter and number of the solid bars. The experimental test of the BD specimens showed that the height of the solid bars has the most effect on input energy dissipation and ductility, but the diameter parameter governed the strength and stiffness capacity. Although the changes in the bars number did not affect the yield displacement, but this showed noticeable capacity in cumulative energy dissipation and cumulative displacement.
3. Theoretical formulas of the BD device were derived based on its plasticity mechanism. The proposed formulas were then compared with the experimental and FE analysis results. It was shown that the proposed equations can predict the device performance acceptably, as the predicted yield force and displacement obtained with the equations were in suitable agreement with the experimental and FE results. The FE analysis results were also compared to the experimental tests and good agreement was observed. A simplified bi-linear model of the BD device was also proposed in order to enhance its practical use by structural engineers for implementation in structure design.
4. The performance of the proposed BD device was evaluated in a structural frame through the experimental test. Additionally, FE models of the frames were also developed to monitor the frames' behavior. It was shown that the FE results were well-agreed with the results obtained from the experiments. According to the results, the frame without BD device absorbed high stresses at the panel zone and base of the columns. However, the stresses were propagated optimally in the entire frame when BD devices were installed. Furthermore, compared to the bare frame (no BD device installed) the tested frame equipped with BD devices exhibited

finer performance with stable hysteretic behavior and satisfactory improvement in strength, deformation capacity and dissipated energy.

6.3 Recommendations for Future Research

1. The performance of the steel BD device specimens was evaluated using steel materials in this study. It is recommended to build the device using other suitable damping materials such as aluminum, copper, lead, zinc and brass or a combination of these materials to increase the energy dissipation capacity and decrease the cost of the device.
2. The BD device has potential to be installed in different locations of structures as shown. In the present study, the BD device was examined at the beam-column connection location. Therefore, further study can be done to investigate the optimal location of the device in order to achieve the maximum capacity of the device to improve the seismic performance of structures.
3. The BD devices can be tested under unidirectional or bidirectional motions using shaking tables to investigate the device performance in elastic and plastic zone under transient loading.
4. The proposed BD device can be designed in several forms and combined with many other available damper devices in the market. Ability to design the device as a base isolation system or a hybrid vibration control system can be considered as another feasible design phase.
5. Installing the BD devices in structural frames will add stiffness to the structure. This affects the natural vibration period of the structure before and after yielding of the devices. As a result, the BD effect on the acceleration response must be taken into consideration. Moreover, the expected effect in case of multi-story frames should also be discussed.

REFERENCES

ABAQUS, Inc., ABAQUS Analysis Reference Manual 2016, ABAQUS Analysis User's Manual, ABAQUS, Inc., 2016. (n.d.).

Akiyama, H. (1985). *Earthquake-Resistant Limit-State Design for Buildings*. Tokyo: University of Tokyo Press.

Alhamaydeh, M. H., Barakat, S. A., & Abed, F. H. (2013). Multiple regression modeling of natural rubber seismic-isolation systems with supplemental viscous damping for near-field ground motion. *Journal of Civil Engineering and Management*, *19*(5), 665–682.

Ali, H.-E., & Abdel-Ghaffar, A. (1995). Modeling of rubber and lead passive-control bearings for seismic analysis. *Journal of Structural Engineering*, *121*(7), 1134–1144.

Almeida, A., Ferreira, R., Proença, J. M., & Gago, A. S. (2017). Seismic retrofit of RC building structures with Buckling Restrained Braces. *Engineering Structures*, *130*, 14–22.

Alqado, T. E., & Nikolakopoulos, G. (2016). Posicast control of structures using MR dampers. *Structural Control and Health Monitoring*, *23*(8), 1121–1134.

Alqado, T. E., Nikolakopoulos, G., & Dritsas, L. (2017). Semi-active control of flexible structures using closed-loop input shaping techniques. *Structural Control and Health Monitoring*, *24*(5), e1913.

Amini, F., Hazaveh, N. K., & Rad, A. A. (2013). Wavelet PSO-Based LQR Algorithm for Optimal Structural Control Using Active Tuned Mass Dampers. *Computer-Aided Civil and Infrastructure Engineering*, *28*(7), 542–557.

Amini, F., & Samani, M. Z. (2014). A Wavelet-Based Adaptive Pole Assignment Method for Structural Control. *Computer-Aided Civil and Infrastructure Engineering*, *29*(6), 464–477.

Andersson, A., O'Connor, A., & Karoumi, R. (2015). Passive and Adaptive Damping Systems for Vibration Mitigation and Increased Fatigue Service Life of a Tied Arch Railway Bridge. *Computer-Aided Civil and Infrastructure Engineering*, *30*(9), 748–757.

Apostolakis, G., & Dargush, G. F. (2009). Optimal seismic design of moment-resisting steel frames with hysteretic passive devices. *Earthquake Engineering & Structural Dynamics*, (39), 355–376.

Arias-Montiel, M., Silva-Navarro, G., & Antonio-García, A. (2014). Active Vibration Control in a Rotor System by an Active Suspension with Linear Actuators. *Journal of Applied Research and Technology*, *12*(5), 898–907.

Arsava, K. S., & Kim, Y. (2015). Modeling of Magnetorheological Dampers under Various Impact Loads. *Shock and Vibration*, *2015*, 1–20.

ASTM E8M-00. Standard test methods for tension testing of metallic materials [metric]. (2002). West Conshohocken, PA, USA.

Attary, N., Symans, M., Nagarajaiah, S., Reinhorn, A. M., Constantinou, M. C., Sarlis, A. A., … Taylor, D. (2015). Performance Evaluation of Negative Stiffness Devices for Seismic Response Control of Bridge Structures via Experimental Shake Table Tests. *Journal of Earthquake Engineering*, *19*(2), 249–276.

Attary, Navid, Symans, M., Nagarajaiah, S., Reinhorn, A. M., Constantinou, M. C., Sarlis, A. A., … Taylor, D. P. (2015). Experimental Shake Table Testing of an Adaptive Passive Negative Stiffness Device within a Highway Bridge Model. *Earthquake Spectra*, *31*(4), 2163–2194.

Aumjaud, P., Smith, C. W., & Evans, K. E. (2015). A novel viscoelastic damping treatment for honeycomb sandwich structures. *Composite Structures*, *119*, 322–332.

Barmo, A., Mualla, I. H., & Hasan, H. T. (2015). The Behavior of Multi-Story Buildings Seismically Isolated System Hybrid Isolation (Friction, Rubber and with the Addition of Rotational Friction Dampers). *Open Journal of Earthquake Research*, *04*(01), 1–13.

Basu, D., & Reddy, P. R. M. (2016). A New Metallic Damper for Seismic Resilience: Analytical Feasibility Study. *Structures*, *7*, 165–183.

Bigdeli, Y., & Kim, D. (2014). Active Control of 3-D Irregular Building by using Energy Based Neuro-Controller. *Advances in Structural Engineering*, *17*(6), 837–850.

Briones, B., & De la Llera, J. . (2014). Analysis, design and testing of an hourglass-shaped ETP-copper energy dissipation device. *Engineering Structures*, *79*, 309–321.

Brodersen, M. L., Ou, G., Høgsberg, J., & Dyke, S. (2016). Analysis of hybrid viscous damper by real time hybrid simulations. *Engineering Structures*, *126*, 675–688.

Brown, H. M., Allen, R. M., Hellweg, M., Khainovski, O., Neuhauser, D., & Souf, A. (2011). Development of the ElarmS methodology for earthquake early warning: Realtime application in California and offline testing in Japan. *Soil Dynamics and Earthquake Engineering*, *31*(2), 188–200.

Calvi, P. M., Moratti, M., & Calvi, G. M. (2016). Seismic Isolation Devices Based on Sliding Between Surfaces with Variable Friction Coefficient. *Earthquake Spectra*, *32*(4), 2291–2315.

Camara, A., Cristantielli, R., Astiz, M. A., & Málaga-Chuquitaype, C. (2017). Design of hysteretic dampers with optimal ductility for the transverse seismic control of cable-stayed bridges. *Earthquake Engineering & Structural Dynamics*.

Cao, L., Downey, A., Laflamme, S., Taylor, D., & Ricles, J. (2015). Variable friction device for structural control based on duo-servo vehicle brake: Modeling and experimental validation. *Journal of Sound and Vibration*, *348*, 41–56.

Cha, Y.-J., Agrawal, A. K., Friedman, A., Phillips, B., Ahn, R., Dong, B., Christenson, R. (2014). Performance Validations of Semiactive Controllers on Large-Scale

Moment-Resisting Frame Equipped with 200-kN MR Damper Using Real-Time Hybrid Simulations. *Journal of Structural Engineering*, *140*(10), 04014066.

Chan, R. W. K., & Albermani, F. (2008). Experimental study of steel slit damper for passive energy dissipation. *Engineering Structures*, *30*(4), 1058–1066.

Chen, H.-Y., & Liang, J.-W. (2017). Adaptive wavelet neural network controller for active suppression control of a diaphragm-type pneumatic vibration isolator. *International Journal of Control, Automation and Systems*, *15*(3), 1456–1465.

Chen, X., Yang, H. T. Y., Shan, J., Hansma, P. K., & Shi, W. (2016). Bio-Inspired Passive Optimized Base-Isolation System for Seismic Mitigation of Building Structures. *Journal of Engineering Mechanics*, *142*(1), 04015061.

Chen, Z. H., Lam, K. H., & Ni, Y. Q. (2016). Enhanced damping for bridge cables using a self-sensing MR damper. *Smart Materials and Structures*, *25*(8), 085019.

Choi, H., & Kim, J. (2010). New installation scheme for viscoelastic dampers using cables. *Canadian Journal of Civil Engineering*, *37*(9), 1201–1211.

Chou, C. C., Tsai, W. J., & Chung, P. T. (2016). Development and validation tests of a dual-core self-centering sandwiched buckling-restrained brace (SC-SBRB) for seismic resistance. *Engineering Structures*, *121*, 30–41.

Chu, S.-Y., Yeh, S.-W., Lu, L.-Y., & Peng, C.-H. (2017). A leverage-type stiffness controllable mass damper for vibration mitigation of structures. *Structural Control and Health Monitoring*, *24*(4), e1896.

Collette, C., & Chesné, S. (2016). Robust hybrid mass damper. *Journal of Sound and Vibration*, *375*, 19–27.

Crusells-Girona, M., & Aparicio, Á. C. (2016). Active control implementation in cable-stayed bridges for quasi-static loading patterns. *Engineering Structures*, *118*, 394–406.

Cu, V. H., & Han, B. (2015). A stay cable with viscous damper and tuned mass damper. *Australian Journal of Structural Engineering*, *16*(4), 316–323.

Cu, V. H., Han, B., & Pham, D. H. (2017). Tuned mass-high damping rubber damper on a taut cable. *KSCE Journal of Civil Engineering*, *21*(3), 928–936.

Curadelli, O., & Amani, M. (2014). Integrated structure-passive control design of linear structures under seismic excitations. *Engineering Structures*, *81*, 256–264.

Dai, K., Wang, J., Mao, R., Lu, Z., & Chen, S.-E. (2017). Experimental investigation on dynamic characterization and seismic control performance of a TLPD system. *The Structural Design of Tall and Special Buildings*, *26*(7), e1350.

Dall'Asta, A., & Ragni, L. (2008). Dynamic systems with high damping rubber: Nonlinear behaviour and linear approximation. *Earthquake Engineering & Structural Dynamics*, *37*(13), 1511–1526.

De Domenico, D., & Ricciardi, G. (2019). Earthquake protection of structures with nonlinear viscous dampers optimized through an energy-based stochastic approach. *Engineering Structures*, *179*, 523–539.

De la Llera, J. C., Esguerra, C., & Almazán, J. L. (2004). Earthquake behavior of structures with copper energy dissipators. *Earthquake Engineering & Structural Dynamics*, *33*(3), 329–358.

De Matteis, G., Sarracco, G., & Brando, G. (2016). Experimental tests and optimization rules for steel perforated shear panels. *Journal of Constructional Steel Research*, *123*, 41–52.

Del Carpio R., M., Mosqueda, G., & Lignos, D. G. (2019). Experimental investigation of steel building gravity framing systems under strong earthquake shaking. *Soil Dynamics and Earthquake Engineering*, *116*, 230–241.

Demetriou, D., & Nikitas, N. (2016). A Novel Hybrid Semi-Active Mass Damper Configuration for Structural Applications. *Applied Sciences*, *6*(12), 397.

Deshmukh, S. N., & Chandiramani, N. K. (2014). LQR Control of Wind Excited Benchmark Building Using Variable Stiffness Tuned Mass Damper. *Shock and Vibration*, *2014*, 1–12.

Dimakogianni, D., Dougka, G., & Vayas, I. (2015). Seismic behavior of frames with innovative energy dissipation systems (FUSEIS1-2). *Engineering Structures*, *90*, 83–95.

Dolce, M., Filardi, B., Marnetto, R., & Nigro, D. (1996). Experimental tests and applications of a new biaxial elasto-plastic device for the passive control of structures. In *4th world congress on joint sealants and bearing systems for concrete structures, ACI SP-164, Sacramento, California*.

Dong, Y., & Zhang, Y. (1993). Cyclic plasticity constitutive model of structural steel. *Journal of Harbin University of Civil Engineering and Architecture*, *26*(5), 106–12.

Dougka, G., Dimakogianni, D., & Vayas, I. (2014). Innovative energy dissipation systems (FUSEIS 1-1) — Experimental analysis. *Journal of Constructional Steel Research*, *96*, 69–80.

Downey, A., Cao, L., Laflamme, S., Taylor, D., & Ricles, J. (2016). High capacity variable friction damper based on band brake technology. *Engineering Structures*, *113*, 287–298.

Elwardany, H., Seleemah, A., & Jankowski, R. (2018). Corrigendum to “Seismic pounding behavior of multi-story buildings in series considering the effect of infill panels.” *Engineering Structures*, *171*, 139–150.

Elwardany, H., Seleemah, A., Jankowski, R., & El-khoriby, S. (2019). Influence of soil–structure interaction on seismic pounding between steel frame buildings considering the effect of infill panels. *Bulletin of Earthquake Engineering*, *17*(11), 6165–6202.

Etedali, S., Sohrabi, M. R., & Tavakoli, S. (2013). Optimal PD/PID control of smart base

isolated buildings equipped with piezoelectric friction dampers. *Earthquake Engineering and Engineering Vibration*, *12*(1), 39–54.

Fateh, A., Hejazi, F., Jaafar, M. S., & Karim, I. A. (2016). Numerical and experimental evaluation of a developed nonlinear curved spring element under compression force. *Journal of Constructional Steel Research*, *117*, 115–125.

Fateh, A., Hejazi, F., Jaafar, M. S., Karim, I. A., & Adnan, A. Bin. (2016). Design of a variable stiffness bracing system: Mathematical modeling, fabrication, and dynamic analysis. *Soil Dynamics and Earthquake Engineering*, *80*, 87–101.

FEMA. (2007). *Federal Emergency Management Agency (FEMA). Interim protocols for determining seismic performance characteristics of structural and nonstructural components*. Washington, DC, USA.

Franco, J. M., Cahís, X., Gracia, L., & López, F. (2010). Experimental testing of a new anti-seismic dissipator energy device based on the plasticity of metals. *Engineering Structures*, *32*(9), 2672–2682.

Fu, & Johnson, E. A. (2014). Active Control for a Distributed Mass Damper System. *Journal of Engineering Mechanics*, *140*(2), 426–429.

Fu, Y., & Cherry, S. (2000). Design of friction damped structures using lateral force procedure. *Earthquake Engineering and Structural Dynamics*, *29*(7), 989–1010.

Garivani, S., Aghakouchak, A. A., & Shahbeyk, S. (2016). Numerical and experimental study of comb-teeth metallic yielding dampers. *International Journal of Steel Structures*, *16*(1), 177–196.

Garrido, H., Curadelli, O., & Ambrosini, D. (2016). Experimental and theoretical study of semi-active friction tendons. *Mechatronics*, *39*, 63–76.

Ghaedi, Khaled, Hejazi, F., Ibrahim, Z., & Khanzaei, P. (2018). Flexible Foundation Effect on Seismic Analysis of Roller Compacted Concrete (RCC) Dams Using Finite Element Method. *KSCE Journal of Civil Engineering*, *22*(4), 1275–1287.

Ghaedi, Khaled, Jameel, M., Ibrahim, Z., & Khanzaei, P. (2016). Seismic analysis of Roller Compacted Concrete (RCC) dams considering effect of sizes and shapes of galleries. *KSCE Journal of Civil Engineering*, *20*(1), 261–272.

Gong, S., & Zhou, Y. (2017). Experimental study and numerical simulation on a new type of viscoelastic damper with strong nonlinear characteristics. *Structural Control and Health Monitoring*, *24*(4), e1897.

Gordan, M., Razak, H. A., Z. Ismail, & Ghaedi, K. (2017). Recent developments in damage identification of structures using data mining. *Latin American Journal of Solids and Structures*, *14*(13), 2373–2401.

Guerrero, H., Ji, T., Teran-Gilmore, A., & Escobar, J. A. (2016). A method for preliminary seismic design and assessment of low-rise structures protected with buckling-restrained braces. *Engineering Structures*, *123*, 141–154.

Gur, S., Mishra, S. K., Bhowmick, S., & Chakraborty, S. (2014). Compliant liquid column damper modified by shape memory alloy device for seismic vibration control. *Smart Materials and Structures*, *23*(10), 105009.

Hansma, P. K., Fantner, G. E., Kindt, J. H., Thurner, P. J., Schitter, G., Turner, P. J., … Finch, M. M. (2005). Sacrificial bonds in the interfibrillar matrix of bone. *Journal of Musculoskeletal & Neuronal Interactions*, *5*(4), 313–315.

Hao, X.-Y., Li, H.-N., Li, G., & Makino, T. (2014). Experimental investigation of steel structure with innovative H-type steel unbuckling braces. *The Structural Design of Tall and Special Buildings*, *23*(14), 1064–1082.

Hashemi, S. M. A., Haji Kazemi, H., & Karamodin, A. (2016). Localized genetically optimized wavelet neural network for semi-active control of buildings subjected to earthquake. *Structural Control and Health Monitoring*, *23*(8), 1074–1087.

Hatzigeorgiou, G. D., & Pnevmatikos, N. G. (2014). Maximum damping forces for structures with viscous dampers under near-source earthquakes. *Engineering Structures*, *68*, 1–13.

He, H., Wang, X., & Zhang, X. (2016). Energy-Dissipation Performance of Combined Low Yield Point Steel Plate Damper Based on Topology Optimization and Its Application in Structural Control. *Advances in Materials Science and Engineering*, *2016*, 1–16.

Hejazi, F., Shoaei, M. D., Tousi, A., & Jaafar, M. S. (2016). Analytical Model for Viscous Wall Dampers. *Computer-Aided Civil and Infrastructure Engineering*, *31*(5), 381–399.

Hejazi, F., Toloue, I., Jaafar, M. S., & Noorzaei, J. (2013). Optimization of earthquake energy dissipation system by genetic algorithm. *Computer-Aided Civil and Infrastructure Engineering*, *28*(10), 796–810.

Heo, G., Kim, C., Jeon, S., Lee, C., & Seo, S. (2017). A study on a MR damping system with lumped mass for a two-span bridge to diminish its earthquake-induced longitudinal vibration. *Soil Dynamics and Earthquake Engineering*, *92*, 312–329.

Hsu, H.-L., & Halim, H. (2017). Improving seismic performance of framed structures with steel curved dampers. *Engineering Structures*, *130*, 99–111.

Hu, H. Y. (2004). Using delayed state feedback to stabilize periodic motions of an oscillator. *Journal of Sound and Vibration*, *275*(3–5), 1009–1025.

Huang, X., Liu, X., & Hua, H. (2014). On the characteristics of an ultra-low frequency nonlinear isolator using sliding beam as negative stiffness. *Journal of Mechanical Science and Technology*, *28*(3), 813–822.

Jalaeefar, A., & Asgarian, B. (2014). A simple hybrid damping device with energy-dissipating and re-centering characteristics for special structures. *The Structural Design of Tall and Special Buildings*, *23*(7), 483–499.

Javanmardi, A., Ibrahim, Z., Ghaedi, K., Benisi Ghadim, H., & Hanif, M. U. (2019).

State-of-the-Art Review of Metallic Dampers: Testing, Development and Implementation. *Archives of Computational Methods in Engineering*, 1–24.

Javanmardi, A. (2019). *Seismic behavior investigation of a cable-stayed bridge with hybrid passive control system*. PhD Thesis, University of Malaya.

Javanmardi, A., Abadi, R., Marsono, A. K., Tap, M., Ibrahim, Z., & Ahmad, A. (2015). Correlation of Stiffness and Natural Frequency of Precast Frame System. *Applied Mechanics and Materials Vol.*, *735*, 141–144.

Javanmardi, A., Ghaedi, K., Ibrahim, Z., Huang, F., & Xu, P. (2020). Development of a new hexagonal honeycomb steel damper. *Archives of Civil and Mechanical Engineering (2020)*, *9*, 1–19.

Javanmardi, A., Ghaedi, K., Ibrahim, Z., & Muthu, K. U. (2018). Seismic Pounding Mitigation of an Existing Cable-Stayed Bridge Using Metallic Dampers. In *IABSE Conference – Engineering the Developing World* (pp. 617–623). Kuala Lumpur, Malaysia: International Association for Bridge and Structural Engineering.

Javanmardi, A., Ibrahim, Z., & Ghaedi, K. (2018). Development of a new hybrid precast beam-to-column connection. *IOP Conference Series: Materials Science and Engineering*, *431*, 112002.

Javanmardi, A., Ibrahim, Z., Ghaedi, K., Jameel, M., Hanif, M. U., & Gordan, M. (2018). Seismic response of a base isolated cable-stayed bridge under near-fault ground motion excitations. *Scientific Research Journal*, *15*(1), 1–14.

Javanmardi, A., Ibrahim, Z., Ghaedi, K., & Khatibi, H. (2017). Numerical analysis of vertical pipe damper. In *39th IABSE SYMPOSIUM; Engineering the Future* (pp. 2974–2980). Vancouver, Canada: International Association for Bridge and Structural Engineering.

Javanmardi, A., Ibrahim, Z., Ghaedi, K., Jameel, M., Khatibi, H., & Suhatril, M. (2017). Seismic response characteristics of a base isolated cable-stayed bridge under moderate and strong ground motions. *Archives of Civil and Mechanical Engineering*, *17*(2), 419–432.

Javanmardi, A., Ibrahim, Z., Ghaedi, K., Khan, N. B., & Benisi Ghadim, H. (2018). Seismic isolation retrofitting solution for an existing steel cable-stayed bridge. *PLOS ONE*, *13*(7), e0200482.

Jin, X., Chen, M. Z. Q., & Huang, Z. (2016). Minimization of the beam response using inerter- based passive vibration control configurations. *International Journal of Mechanical Sciences*, *119*(October), 80–87.

Karimi, H. R. (2012). Semiactive – passive structural vibration control strategy for adjacent structures under, *349*, 3003–3026.

Kasagi, M., Fujita, K., Tsuji, M., & Takewaki, I. (2016). Automatic generation of smart earthquake-resistant building system: Hybrid system of base-isolation and building-connection. *Heliyon*, *2*(2), e00069.

Khalid, M., Yusof, R., Joshani, M., Selamat, H., & Joshani, M. (2014). Nonlinear identification of a magneto-rheological damper based on dynamic neural networks. *Computer-Aided Civil and Infrastructure Engineering*, *29*(3), 221–233.

Khanzaei, P., Abdulrazeg, A. a., Samali, B., & Ghaedi, K. (2015). Thermal and Structural Response of RCC Dams During Their Service Life. *Journal of Thermal Stresses*, *38*(6), 591–609.

Kim, J., & Jeong, J. (2016). Seismic retrofit of asymmetric structures using steel plate slit dampers. *Journal of Constructional Steel Research*, *120*, 232–244.

Koetaka, Y., Chusilp, P., Zhang, Z., Ando, M., Suita, K., & Inoue, K. (2005). Mechanical property of beam-to-column moment connection with hysteretic dampers for column weak axis. *Engineering Structures*, *27*, 109–117.

Lazar, I. F., Neild, S. A., & Wagg, D. J. (2014). Using an inerter-based device for structural vibration suppression. *Earthquake Engineering & Structural Dynamics*, *43*(8), 1129–1147.

Lee, C. H., Kim, J., Kim, D. H., Ryu, J., & Ju, Y. K. (2016). Numerical and experimental analysis of combined behavior of shear-type friction damper and non-uniform strip damper for multi-level seismic protection. *Engineering Structures*, *114*, 75–92.

Légeron, F., Paultre, P., & Mazars, J. (2005). Damage Mechanics Modeling of Nonlinear Seismic Behavior of Concrete Structures. *Journal of Structural Engineering*, *131*(6), 946–955.

Li, G., & Wong, K. K. F. (2014). Theory of Nonlinear Structural Analysis: The Force Analogy Method for Earthquake Engineering. *Theory of Nonlinear Structural Analysis: The Force Analogy Method for Earthquake Engineering*, (1970), 1–354.

Li, H. N., & Li, G. (2007). Experimental study of structure with "dual function" metallic dampers. *Engineering Structures*, *29*(8), 1917–1928.

LIN, C. C., SHEU, J. F., CHU, S. Y., & CHUNG, L. L. (1996). Time-Delay Effect and Its Solution for Optimal Output Feedback Control of Structures. *Earthquake Engineering & Structural Dynamics*, *25*(6), 547–559.

Lin, G.-L., Lin, C.-C., Chen, B.-C., & Soong, T.-T. (2015). Vibration control performance of tuned mass dampers with resettable variable stiffness. *Engineering Structures*, *83*, 187–197. 1

Ling, Y. H., & Ling, H. H. (2012). Progress on Study and Application of Shape Memory Alloy in Passive Energy Dissipation. *Applied Mechanics and Materials*, *198–199*, 3–8.

Liu, C., Jing, X., & Li, F. (2015). Vibration isolation using a hybrid lever-type isolation system with an X-shape supporting structure. *International Journal of Mechanical Sciences*, *98*, 169–177.

Liu, J., Chen, X., Gao, J., & Zhang, X. (2016). Multiple-source multiple-harmonic active vibration control of variable section cylindrical structures: A numerical study.

Mechanical Systems and Signal Processing, *81*, 461–474.

Lu, L.-Y. (2004). Semi-active modal control for seismic structures with variable friction dampers. *Engineering Structures*, *26*(4), 437–454.

Lu, X., Zhang, Q., Weng, D., Zhou, Z., Wang, S., Mahin, S. A., … Qian, F. (2017). Improving performance of a super tall building using a new eddy-current tuned mass damper. *Structural Control and Health Monitoring*, *24*(3), e1882.

Lu, Z., Chen, X., Zhang, D., & Dai, K. (2017). Experimental and analytical study on the performance of particle tuned mass dampers under seismic excitation. *Earthquake Engineering & Structural Dynamics*, *46*(5), 697–714.

Luo, J., Wierschem, N. E., Fahnestock, L. A., Spencer, B. F., Quinn, D. D., McFarland, D. M., … Bergman, L. A. (2014). Design, simulation, and large-scale testing of an innovative vibration mitigation device employing essentially nonlinear elastomeric springs. *Earthquake Engineering & Structural Dynamics*, *43*(12), 1829–1851.

Luu, M., Martinez-Rodrigo, M. D., Zabel, V., & Könke, C. (2014). Semi-active magnetorheological dampers for reducing response of high-speed railway bridges. *Control Engineering Practice*, *32*, 147–160.

Maddaloni, G., Caterino, N., Nestovito, G., & Occhiuzzi, A. (2013). Use of seismic early warning information to calibrate variable dampers for structural control of a highway bridge: evaluation of the system robustness. *Bulletin of Earthquake Engineering*, *11*(6), 2407–2428.

Maddaloni, G., Caterino, N., Nestovito, G., & Occhiuzzi, A. (2016). Exploring New Boundaries to Mitigate Structural Vibrations of Bridges in Seismic Regions: A Smart Passive Strategy. *Shock and Vibration*, *2016*, 1–13.

Maddaloni, G., Caterino, N., & Occhiuzzi, A. (2011). Semi-active control of the benchmark highway bridge based on seismic early warning systems. *Bulletin of Earthquake Engineering*, *9*(5), 1703–1715.

Maleki, S., & Bagheri, S. (2010). Pipe damper, Part I: Experimental and analytical study. *Journal of Constructional Steel Research*, *66*(8–9), 1088–1095.

Maleki, S., & Mahjoubi, S. (2013). Dual-pipe damper. *Journal of Constructional Steel Research*, *85*, 81–91.

Maleki, S., & Mahjoubi, S. (2014). Infilled-pipe damper. *Journal of Constructional Steel Research*, *98*, 45–58.

Marian, L., & Giaralis, A. (2014). Optimal design of a novel tuned mass-damper–inerter (TMDI) passive vibration control configuration for stochastically support-excited structural systems. *Probabilistic Engineering Mechanics*, *38*, 156–164.

Markou, A. A., & Manolis, G. D. (2016). A fractional derivative Zener model for the numerical simulation of base isolated structures. *Bulletin of Earthquake Engineering*, *14*(1), 283–295.

Mashal, M., & Palermo, A. (2019). Emulative seismic resistant technology for Accelerated Bridge Construction. *Soil Dynamics and Earthquake Engineering*, *124*, 197–211.

Meng, B., Zhong, W., Hao, J., & Tan, Z. (2019). Improved steel frame performance against progressive collapse with infill panels. *Journal of Constructional Steel Research*, *158*, 201–212.

Miguel, Leandro F.F., Lopez, R. H., Torii, A. J., Miguel, L. F. F., & Beck, A. T. (2016). Robust design optimization of TMDs in vehicle–bridge coupled vibration problems. *Engineering Structures*, *126*, 703–711.

Miguel, Letícia Fleck Fadel, Fadel Miguel, L. F., & Lopez, R. H. (2015). A firefly algorithm for the design of force and placement of friction dampers for control of man-induced vibrations in footbridges. *Optimization and Engineering*, *16*(3), 633–661.

Min, K.-W., Kim, J., & Lee, H.-R. (2014). A design procedure of two-way liquid dampers for attenuation of wind-induced responses of tall buildings. *Journal of Wind Engineering and Industrial Aerodynamics*, *129*, 22–30.

Mitchell, R., Cha, Y.-J., Kim, Y., & Mahajan, A. A. (2015). Active control of highway bridges subject to a variety of earthquake loads. *Earthquake Engineering and Engineering Vibration*, *14*(2), 253–263.

Miyamoto, K., She, J., Imani, J., Xin, X., & Sato, D. (2016). Equivalent-input-disturbance approach to active structural control for seismically excited buildings. *Engineering Structures*, *125*, 392–399.

Mualla, I. H., Jakupsson, E. D., & Nielsen, L. O. (2010). Structural behaviour of 5000 kN damper. *14th European Conference on Earthquake Engineering, Ohrid, Republic of Macedonia*, *2*, 1–8.

Murase, M., Tsuji, M., & Takewaki, I. (2013). Smart passive control of buildings with higher redundancy and robustness using base-isolation and inter-connection. *Earthquakes and Structures*, *4*(6), 649–670.

Muresan, C. I., Dulf, E. H., & Prodan, O. (2016). A fractional order controller for seismic mitigation of structures equipped with viscoelastic mass dampers. *Journal of Vibration and Control*, *22*(8), 1980–1992.

Nazarimofrad, E., & Zahrai, S. M. (2016). Seismic control of irregular multistory buildings using active tendons considering soil–structure interaction effect. *Soil Dynamics and Earthquake Engineering*, *89*, 100–115.

Nigdeli, S. M., & Boduroğlu, M. H. (2013). Active Tendon Control of Torsionally Irregular Structures under Near-Fault Ground Motion Excitation. *Computer-Aided Civil and Infrastructure Engineering*, *28*(9), 718–736.

Omidi, E., Mahmoodi, S. N., & Shepard, W. S. (2016). Multi positive feedback control method for active vibration suppression in flexible structures. *Mechatronics*, *33*, 23–33.

Ozbulut, O. E., & Hurlebaus, S. (2011). Re-centering variable friction device for vibration control of structures subjected to near-field earthquakes. *Mechanical Systems and Signal Processing*, *25*(8), 2849–2862.

Pantidis, P., & Gerasimidis, S. (2018). Progressive collapse of 3D steel composite buildings under interior gravity column loss. *Journal of Constructional Steel Research*, *150*, 60–75.

Papalou, A., Strepelias, E., Roubien, D., Bousias, S., & Triantafillou, T. (2015). Seismic protection of monuments using particle dampers in multi-drum columns. *Soil Dynamics and Earthquake Engineering*, *77*, 360–368.

Papalou, Angeliki, & Strepelias, E. (2016). Effectiveness of particle dampers in reducing monuments' response under dynamic loads. *Mechanics of Advanced Materials and Structures*, *23*(2), 128–135.

Pardo-Varela, J., & de la Llera, J. C. (2015). A Semi-active piezoelectric friction damper. *Earthquake Engineering & Structural Dynamics*, *44*(3), 333–354.

Park, H.-Y., & Oh, S.-H. (2020). Structural performance of beam system with T-stub type slit damper. *Engineering Structures*, *205*, 109858.

Patil, D. M., & Sangle, K. K. (2015). Seismic Behaviour of Different Bracing Systems in High Rise 2-D Steel Buildings. *Structures*, *3*, 282–305.

Pereira, E., Díaz, I. M., Hudson, E. J., & Reynolds, P. (2014). Optimal control-based methodology for active vibration control of pedestrian structures. *Engineering Structures*, *80*, 153–162.

Pham, M.-N., & Ahn, H.-J. (2015). Horizontal active vibration isolator (HAVI) using electromagnetic planar actuator (EPA). *International Journal of Precision Engineering and Manufacturing-Green Technology*, *2*(3), 269–274.

Qian, H., Li, H., Song, G., & Guo, W. (2013). Recentering Shape Memory Alloy Passive Damper for Structural Vibration Control. *Mathematical Problems in Engineering*, *2013*, 1–13.

Qu, B., Dai, C., Qiu, J., Hou, H., & Qiu, C. (2019). Testing of seismic dampers with replaceable U-shaped steel plates. *Engineering Structures*, *179*, 625–639.

Qu, C., Li, H.-N., Huo, L., & Yi, T.-H. (2017). Optimum Value of Negative Stiffness and Additional Damping in Civil Structures. *Journal of Structural Engineering*, 04017068.

Ramberg, W., & Osgood, W. (1943). *NACA-TN-902*. *National Advisory Committee for Aeronautics*. Washington, DC, United States.

Ranaei, O., & Aghakouchak, A. A. (2019). A new hybrid energy dissipation system with viscoelastic and flexural yielding strips dampers for multi-level vibration control. *Archives of Civil and Mechanical Engineering*, *19*(2), 584–597.

Ras, A., & Boumechra, N. (2016). Seismic energy dissipation study of linear fluid viscous

dampers in steel structure design. *Alexandria Engineering Journal*, *55*(3), 2821–2832.

Richiedei, D., & Trevisani, A. (2017). Simultaneous active and passive control for eigenstructure assignment in lightly damped systems. *Mechanical Systems and Signal Processing*, *85*, 556–566.

Ruiz, R. O., Taflanidis, A. A., & Lopez-Garcia, D. (2016). Characterization and design of tuned liquid dampers with floating roof considering arbitrary tank cross-sections. *Journal of Sound and Vibration*, *368*, 36–54.

Saaed, T. E., Nikolakopoulos, G., Jonasson, J.-E., & Hedlund, H. (2015). A state-of-the-art review of structural control systems. *Journal of Vibration and Control*, *21*(5), 919–937.

Seleemah, A. A., & El-Sharkawy, M. (2011). Seismic analysis and modeling of isolated elevated liquid storage tanks. *Earthquakes and Structures*, *2*(4), 397–412.

Serror, M. H., Diab, R. A., & Mourad, S. A. (2014). Behavior of steel moment resisting frames with supplemental damping devices. *Journal of Advanced Research*.

Shen, W., & Zhu, S. (2015). Harvesting energy via electromagnetic damper: Application to bridge stay cables. *Journal of Intelligent Material Systems and Structures*, *26*(1), 3–19.

Shen, W., Zhu, S., & Zhu, H. (2016). Experimental study on using electromagnetic devices on bridge stay cables for simultaneous energy harvesting and vibration damping. *Smart Materials and Structures*, *25*(6), 065011.

Shi, X., & Zhu, S. (2015). Magnetic negative stiffness dampers. *Smart Materials and Structures*, *24*(7), 072002.

Shi, Y., Becker, T. C., Furukawa, S., Sato, E., & Nakashima, M. (2014). LQR control with frequency-dependent scheduled gain for a semi-active floor isolation system. *Earthquake Engineering & Structural Dynamics*, *43*(9), 1265–1284.

Sigaher, A. N., & Constantinou, M. C. (2003). Scissor-Jack-Damper Energy Dissipation System. *Earthquake Spectra*, *19*(1), 133–158.

Silva Lobo, P., Almeida, J., & Guerreiro, L. (2015). Semi-active Damping Device Based on Superelastic Shape Memory Alloys. *Structures*, *3*, 1–12.

Silwal, B., Michael, R. J., & Ozbulut, O. E. (2015). A superelastic viscous damper for enhanced seismic performance of steel moment frames. *Engineering Structures*, *105*, 152–164.

Soleymani, M., & Khodadadi, M. (2014). Adaptive fuzzy controller for active tuned mass damper of a benchmark tall building subjected to seismic and wind loads. *The Structural Design of Tall and Special Buildings*, *23*(10), 781–800.

Soong, T. T., & Spencer Jr, B. F. (2002). Supplemental energy dissipation : state-of-the-art and state-of-the- practice. *Engineering Structures*, *24*, 243–259.

Spak, K. S., Agnes, G. S., & Inman, D. J. (2015). Modeling vibration response and damping of cables and cabled structures. *Journal of Sound and Vibration*, *336*, 240–256.

Stiemer, S. F. (1981). *Experimental behavior of a spatial piping systemwith steel energy absorbers subjected to a simulated differential seismic input (UCB/EERC-81/09)*. Berkeley: Earthquake Engineering Research Center, University of California.

Sun, C., & Nagarajaiah, S. (2014). Study on semi-active tuned mass damper with variable damping and stiffness under seismic excitations. *Structural Control and Health Monitoring*, *21*(6), 890–906.

Tafsirojjaman, T., Fawzia, S., Thambiratnam, D., & Zhao, X. L. (2019). Seismic strengthening of rigid steel frame with CFRP. *Archives of Civil and Mechanical Engineering*, *19*(2), 334–347.

Takeya, K., Sasaki, E., & Kobayashi, Y. (2016). Design and parametric study on energy harvesting from bridge vibration using tuned dual-mass damper systems. *Journal of Sound and Vibration*, *361*, 50–65.

Tan, P., Xu, K., Wang, B., Chang, C., Liu, H., & Zhou, F. (2014). Development and performance evaluation of an innovative low-cost seismic isolator. *Science China Technological Sciences*, *57*(10), 2050–2061.

Teng, J., Xing, H. B., Lu, W., Li, Z. H., & Chen, C. J. (2016). Influence analysis of time delay to active mass damper control system using pole assignment method. *Mechanical Systems and Signal Processing*, *80*, 99–116.

Teng, J., Xing, H. B., Xiao, Y. Q., Liu, C. Y., Li, H., & Ou, J. P. (2014). Design and implementation of AMD system for response control in tall buildings. *Smart Structures and Systems*, *13*(2), 235–255.

Tinkir, M., Kalyoncu, M., & Şahin, Y. (2013). Deflection Control of Two-Floors Structure Against Northridge Earthquake by Using PI Controlled Active Mass Damping. *Applied Mechanics and Materials*, *307*, 126–130.

Titirla, M. D., Papadopoulos, P. K., & Doudoumis, I. N. (2018). Finite element modelling of an innovative passive energy dissipation device for seismic hazard mitigation. *Engineering Structures*, *168*, 218–228.

Ubertini, F., Venanzi, I., & Comanducci, G. (2015). Considerations on the implementation and modeling of an active mass driver with electric torsional servomotor. *Mechanical Systems and Signal Processing*, *58*, 53–69.

Van Khang, N., Seils, A., An, T. N., Dien, N. P., & Nghia, N. T. (2016). An improvement of the step-by-step analysis method for study on passive flutter control of a bridge deck. *Archive of Applied Mechanics*, *86*(3), 557–573.

Walsh, K. K., Sallar, G., & Steinberg, E. P. (2017). Modeling and Validation of a Passive Resettable Stiffness Damper. *Journal of Engineering Mechanics*, *143*(2), 04016114.

Wang, N., & Adeli, H. (2015a). Robust vibration control of wind-excited highrise

building structures. *Journal of Civil Engineering and Management*, *21*(8), 967–976.

Wang, N., & Adeli, H. (2015b). Self-constructing wavelet neural network algorithm for nonlinear control of large structures. *Engineering Applications of Artificial Intelligence*, *41*, 249–258.

Weber, F. (2014). Semi-active vibration absorber based on real-time controlled MR damper. *Mechanical Systems and Signal Processing*, *46*(2), 272–288.

Weber, F, & Distl, H. (2015). Semi-active damping with negative stiffness for multi-mode cable vibration mitigation: approximate collocated control solution. *Smart Materials and Structures*, *24*(11), 115015.

Weber, F, & Maślanka, M. (2014). Precise stiffness and damping emulation with MR dampers and its application to semi-active tuned mass dampers of Wolgograd Bridge. *Smart Materials and Structures*, *23*(1), 015019.

Weber, Felix, & Distl, H. (2015). Amplitude and frequency independent cable damping of Sutong Bridge and Russky Bridge by magnetorheological dampers. *Structural Control and Health Monitoring*, *22*(2), 237–254.

Wu, W., Chen, X., & Shan, Y. (2014). Analysis and experiment of a vibration isolator using a novel magnetic spring with negative stiffness. *Journal of Sound and Vibration*, *333*(13), 2958–2970.

Xiang, N., Goto, Y., Obata, M., & Alam, M. S. (2019). Passive seismic unseating prevention strategies implemented in highway bridges: A state-of-the-art review. *Engineering Structures*, *194*, 77–93.

Xu, Q., Chen, J., Liu, X., Li, J., & Yuan, C. (2017). An ABC-BP-ANN algorithm for semi-active control for Magnetorheological damper. *KSCE Journal of Civil Engineering*, *21*, 2310–2321.

Xu, Y. L., & Teng, J. (2002). Optimum design of active/passive control devices for tall buildings under earthquake excitation. *Structural Design of Tall Buildings*, *11*(2), 109–127.

Yamamoto, M., & Sone, T. (2014). Damping systems that are effective over a wide range of displacement amplitudes using metallic yielding component and viscoelastic damper in series. *Earthquake Engineering & Structural Dynamics*, *43*(14), 2097–2114.

Yan, W., Xu, W., Wang, J., & Chen, Y. (2014). Experimental Research on the Effects of a Tuned Particle Damper on a Viaduct System under Seismic Loads. *Journal of Bridge Engineering*, *19*(3), 04013004.

Yang, J. N., Agrawal, A. K., Samali, B., & Wu, J.-C. (2004). Benchmark Problem for Response Control of Wind-Excited Tall Buildings. *Journal of Engineering Mechanics*, *130*(4), 437–446.

Yang, Shin, J.-H., Lee, H., Kim, S.-K., & Kwak, M. K. (2017). Active vibration control of structure by Active Mass Damper and Multi-Modal Negative Acceleration

Feedback control algorithm. *Journal of Sound and Vibration*, *392*, 18–30.

Yanik, A., Aldemir, U., & Bakioglu, M. (2014). A new active control performance index for vibration control of three-dimensional structures. *Engineering Structures*, *62–63*, 53–64.

Yavuz, Ş., Malgaca, L., & Karagülle, H. (2016). Analysis of active vibration control of multi-degree-of-freedom flexible systems by Newmark method. *Simulation Modelling Practice and Theory*, *69*, 136–148.

Yongjiu, S., Meng, W., & Yuanqing, W. (2011). Experimental and constitutive model study of structural steel under cyclic loading. *Journal of Constructional Steel Research*, *67*(8), 1185–1197.

Zare, A. R., & Ahmadizadeh, M. (2014). Design of viscous fluid passive structural control systems using pole assignment algorithm. *Structural Control and Health Monitoring*, *21*(7), 1084–1099.

Zeinali, M., Mazlan, S. A., Abd Fatah, A. Y., & Zamzuri, H. (2013). A phenomenological dynamic model of a magnetorheological damper using a neuro-fuzzy system. *Smart Materials and Structures*, *22*(12), 125013.

Zhou, Y., Zhang, C., & Lu, X. (2017). Seismic performance of a damping outrigger system for tall buildings. *Structural Control and Health Monitoring*, *24*(1), e1864.